A Thesis Submitted for the Degree of PhD at the University of Warwick

Spectroelectrochemical techniques for the conservation of metallic artefacts

by

Rosie Ann Grayburn

Thesis

Submitted to the University of Warwick

for the degree of

Doctor of Philosophy

Department of Physics

May 2015

Spectroelectrochemical techniques for the conservation of metallic artefacts

Thesis submitted to Universiteit Gent in fulfilment of the requirements for the degree of

Doctor of Science: Chemistry

by

Rosie Ann Grayburn

Supervisor: Emeritus Professor Mark Dowsett

Co-supervisor: Professor Dr. Annemie Adriaens

Contents

Acknowledgements ix

Declarations xii

Abstract xiv

Nederlandstalige samenvatting xvi

Abbreviations xviii

1. Introduction 1

1.1 Conservation principles 1
1.2 Conservation of metallic objects 3
1.3 Lead as a cultural heritage material 5
1.4 Studying materials *in situ* in a controlled environment – the eCell 7
1.5 Scope of the thesis 11
1.6 References 13

2. Methods 20

2.1 Scattering methods 20
  2.1.1 Surface powder X-ray diffraction 20
  2.1.2 Synchrotron X-ray diffraction 23
2.2 Electrochemical methods 26
  2.2.1 Open circuit potential 28
  2.2.2 Cyclic voltammetry 29
  2.2.3 Electrochemical impedance spectroscopy 30
2.3 Microscopy 31
  2.3.1 Optical microscopy 32
  2.3.2 Scanning electron microscopy 32
2.4 Gas chromatography – mass spectrometry 34
2.5 References 36

3. Synthesis and spectroelectrochemical analysis of lead carboxylates 39

3.1 Introduction 39
  3.1.1 Synthesis and spectroelectrochemical analysis of metal carboxylates 39
  3.1.2 Lead soap identification in oil paintings 40

3.2 Experimental 42
3.2.1 Synthesis 42
3.2.2 Instrumentation..43
3.2.3 Sample preparation (voltammetry) 43
Working electrodes 43
Reference samples..44
Paint facsimiles 45
3.3 Results and discussion 46
3.3.1 Synthesis 46
3.3.2 Spectroscopic identification of lead carboxylates 47
Elemental analysis..47
IR 48
XRD 50
3.3.3 Voltammetric identification of lead carboxylates 54
3.3.4 Assessment of voltammetry as a method for lead soap identification 58
3.3.5 Assessment of voltammetry as a method for lead soap identification – testing a paint facsimile 63
3.4 Conclusions 65
3.5 References 67

4. Spectroelectrochemical characterisation and performance of a new coating for heritage lead..73
4.1 Introduction 73
4.1.1 Carboxylates as coatings 73
4.2 Experimental..74
4.2.1 Sample preparation..74
4.2.2 Analytical methods..75
4.3 Results and discussion 78
4.3.1 Sample preparation..78
4.3.2 Time-lapse SR-XRD of coating formation 79
4.3.3 Coating mass thickness 82
4.3.4 Effectiveness against acidic pollutants and a longer chain solution 85
4.3.5 Coating corroded lead 90
GC-MS of the corrosive environment..90
Sample preparation..92
X-ray diffraction..93
Electrochemical impedance..96

4.4 Conclusions 98

4.5 References 100

5. Testing lead coatings in model and real museum environments 104

5.1 Introduction 104

5.1.1 VOCs in heritage environments 104

5.2 Experimental 106

5.2.1 Sample preparation 106

Lead coupon preparation 106

Coating preparation 107

5.2.2 Creating the oak environment – *in situ* and *ex situ* XRD 107

Ex situ experiments 107

Tests in a ‘real’ oak environment – het Museum voor de Geshiedenis van de Wetenschappen 108

In situ experiments 110

5.2.3 GC-MS of oak VOCs 113

GC-MS of oak VOC environment within the eCell 113

GC-MS of VOCs within the museum 114

5.3 Results and discussion 114

5.3.1 GC-MS results 114

Analysis of a model environment inside the eCell 114

Analysis of the museum environment 117

5.3.2 Long-term corrosion analysis by XRD 119

A model environment inside the eCell 119

Testing conservation coatings in a museum environment 125

5.3.3 Time-lapse SR-XRD of coating exposed to oak VOCs 130

5.4 Conclusions 140

5.5 Acknowledgements 142

5.6 References 143

6. A portable cell (peCell) for spectroelectroelectrochemical studies of heritage metals 148

6.1 Introduction 148

6.2 Design 149

6.2.1 Design brief 149

6.2.2 Design history 150

6.2.3 Design of the peCell 152

6.2.4 Materials 156

6.2.5 Fittings 157
6.2.6 Windows 157
6.2.7 Filling 158
6.2.8 Electrodes 159
6.2.9 Electrochemical measurements 159
6.2.10 Motors and movement 160
6.2.11 A working electrode position sensor for the eCell or peCell 160
6.3 Experimental 162
    6.3.1 Measuring the system impedance 162
    6.3.2 Optimising a working electrode position sensor for the eCell or peCell 162
6.4 Results and discussion 163
    6.4.1 Analysis of the peCell design 163
    6.4.2 A long-term voltage logger for OCP measurements 165
    6.4.3 Optimising a working electrode position sensor for the eCell or peCell 167
6.5 Conclusions 169
6.6 References 169

7. Testing the peCell prototype – SR-XRD study of a novel biomaterial 171
7.1 Introduction 171
7.2 Experimental 172
7.3 Results and discussion 176
    7.3.1 Open-circuit potential and temperature – monitoring the conditions inside the cell 176
    7.3.2 Corrosion product evolution – SR-XRD analysis 179
    7.3.3 Analysis of the peCell design in use 184
7.4 Conclusions 187
7.5 Acknowledgements 188
7.6 References 189

8. Conclusion 192
8.1 Project summary 192
8.2 Future work 195
8.3 Final thoughts 198

List of publications and activities 200

List of Tables

3.1 Long-chain carboxylic acids and abbreviations 42

3.2 Lead pigments commonly found in oil paintings...44

3.3 Oil absorption parameters for lead-containing pigments 45

3.4 Elemental analysis results 48

3.5 C-O stretching band characterisation - IR...50

3.6 Unit cell length calculations 52

4.1 List of VOCs detected within a corrosive oak environment 90

4.2 Coating properties 95

5.1 List of VOCs detected from oak within the eCell at 75% RH 115

5.2 List of VOCs detected from the Museum of Science History, UGent during 1 month 118

5.3 Summary of museum environment parameters collected over 7 months 126

6.1 Parts of the peCell (material or supplier) 155

6.2 Optimisation of the voltage difference and noise from Hall sensor.............168

List of Figures

1.1 The Mary Rose hull being stored in a controlled climate 2

1.2 Lead objects excavated from the Mary Rose 6

1.3 A pipe organ under construction after conservation 7

1.4 Laue and Bragg geometries 9

2.1 A primitive unit cell and an example of a crystal plane 21

2.2 Reflection of X-rays from a crystal plane 22

2.3 Schematic of a synchrotron light source 24

2.4 The experimental setup for SR-XRD at XMaS 26

2.5 Electrochemical behaviour of a metal substrate in solution (E_{corr}) 29

2.6 SEM image of the corroded surface of an iron anchor 32

2.7 Interaction volume in SEM 33

3.1 Lead soap formation from a 1632 canvas painting by Rembrandt 41

3.2 IR spectrum of $Pb(C14)_2$ and C14 49

3.3 IR spectrum of $Pb(C16)_2$ and C16 49

3.4 IR spectrum of $Pb(C18)_2$ and C18 49

3.5 XRD diffraction pattern of $Pb(C14)_2$ coated on lead 51

3.6 XRD patterns of all synthesised lead carboxylates 53

3.7 XRD patterns of unreacted carboxylic acids C14 - 18 54

3.8 Cyclic voltammograms of lead carboyxlates in an acetic acid buffer 55

3.9 Cyclic voltammograms of lead pigments in an acetic acid buffer 59

3.10 Cyclic voltammogram of a paint sample in an acetic acid buffer 64

4.1 The setup of the droplet coating experiment at DUBBLE within the eCell 76

4.2 Photograph of C14 and C18-coated lead samples compared with bare lead 79

4.3 Time-lapse SR-XRD of the $Pb(C14)_2$ coating process 79

4.4 Optical and scanning electron microscopy of the coated surface 82

4.5 Finding the optimal coating concentration using XRD 83

4.6 Coating effectiveness in acetic acid 87

4.7 The effect of increasing coating carbon-chain length 88

4.8 GC trace after 2 months exposure of active charcoal to an oak environment..........................91

4.9 Photograph and microscopy image of corroded and C14-coated lead 92

4.10 XRD diffraction patterns for C14 and C18 compared with corroded lead precursor 93

4.11 Impedance and phase plots of $Pb(C14)_2$ and $Pb(C18)_2$ coating on polished and corroded lead substrates 96

5.1 The experiment exhibition at The Museum of Science History, UGent 110

5.2 The set-up on DUBBLE for time-lapse XRD of the effect of oak VOCs on coated lead......111

5.3 The beam monitor values during the course of a time-lapse experiment..............................112

5.4 GC trace after 3 hours exposure of the SPME tip to an oak environment within the eCell...116

5.5 GC trace after 20 minutes expose of the SPME tip to 1 mM acetic acid 117

5.6 XRD pattern of the $Pb(C_{14})_2$ coating after exposure in air 119

5.7 Raw and reprojected XRD diffractograms from a $Pb(C_{14})_2$ coated coupon from the Mar camera, DUBBLE 120

5.8 XRD patterns of the $Pb(C_{14})_2$ coating after exposure in an oak environment for 2, 7 and 30 days...123

5.9 Relative humidity and temperature data recorded in the Museum of Science History, UGent for 7 months 125

5.10 Relative humidity and temperature data recorded in the Museum of Science History, UGent during September 2014 126

5.11 XRD patterns of samples before and after ‘exhibition’ in an oak display case 128

5.12 Corrosion of the $Pb(C_{14})_2$ coating in real time in oak and comparison with bare lead corrosion..131

5.13 Relative Pb peak areas for all Pb reflections collected from the corrosion of $Pb(C_{14})_2$ coating in real time..132

5.14 Thickness of hydrocerussite growing on coated and uncoated lead 137

5.15 Final SR-XRD patterns of $Pb(C_{14})_2$ coated and uncoated lead after exposure to oak VOCs within the eCell 138

5.16 Fractional mean difference on beam measurements calculated from raw data from DUBBLE 140

6.1 The assembled peCell..153

6.2 The assembled cell body with all attached parts 154

6.3 The environment generator 154

6.4 The eCell working electrode 154

6.5 Working electrode piston 154

6.6 Ag/AgCl reference electrode 154

6.7 3D drawing of cam assembly 154

6.8 peCell window assembly 158

6.9 Hall sensor test circuit 161

6.10 3D assembly of new eCell base incorporating the Hall sensor 163

6.11 Finding the output impedance of the eCell 166

6.12 Buffer circuit diagram integrated into voltage logger 167

6.13 Measuring the output voltage of the Hall sensor 168

7.1 Samples mounted with the peCell prior to filling with SUS 173

7.2 The pump-peCell setup on the XMaS beamline 174

7.3 Insulated transportation box containing the peCell 175

7.4 The peCell mounted on the XMaS beamline 175

7.5 The E_{corr} of Sample 1 and the temperature of the peCell during the experiment 177

7.6 Raw diffraction patterns from Samples 1-3 with the peCell 179

7.7 Summed diffraction patterns from across a 4 mm range on the sample surface 181

7.8 Photographs taken of the samples with the peCell after 7 days 183

7.9 peCell ready for XRD analysis on the XMaS beamline 185

This work would not have been possible without the help, guidance and support of all these people, and seeing as this is the part of thesis they will all read I'll try not to forget anyone.

Firstly, I have to thank Mark Dowsett for being the most wonderful, supportive supervisor. I count myself as very lucky to have had your guidance over the past 4 years. I will always remember your wicked sense of humour and occasional outburst of topical poetry ("His voice is a light tenor, which was a slight surprise; we gaze at him intently but he does not meet our eyes…" – an extract from An Ode to David Willetts MP).

Thanks go to Mieke Adriaens for co-supervising my Joint Ph.D – I have been very happy in Gent, so thank you for getting me there and allowing me to overstay my invitation. Thanks must also go to the Department of Physics at Warwick and Bijzonder Onderzoeksfonds (grant no. 01SF0112) for my funding.

I have been lucky enough to participate in seven beamtimes (so far at the time of writing) at the ESRF, Grenoble – all tiring but gratifying experiences. Thanks to the staff at DUBBLE for letting us do XRD on an XAS beamline, and for the staff at XMaS for always giving us the warmest welcome especially Laurence Bouchenoire, Tom Hase, Paul Thompson and Didier Wermieille.

Thanks must go to Mark Jones at the Mary Rose Museum for allowing me to spend two weeks getting to know the museum and its conservation studio during my Ph.D. It was an unforgettable experience and you must be so proud of the new museum.

For the GCMS experiments, thanks go to Eric Westenbrink (Warwick) and Kevin Roeleveld (UGent) for giving up their time to teach me the technique. Also thanks go to David Walker for helping me to tame Gwyneth (the PanAlytical Powder XRD) and Steve York for patiently training me on the SEM.

As part of my research I was able to set-up an experiment-exhibition at the Museum of History of Science (UGent). Thanks to all those who helped: Professor Segers, Kristel Wautier and Alexander Jonckheere at the museum, Kristof Ysabie (Provincie Oost-

Vlaanderen) for the loan of the RH/T logger and Davy De Pauw (UGent) for making a lovely museum-quality mount for my samples.

The design and assembly of the peCell prototype was my most challenging project during the past 3.5 years. For their limitless patience and guidance I would like to thank Jorge Anjos and Davy De Pauw (both UGent). Also thanks go to Dave Greenshields in the Electronic Workshop at Warwick for my first soldering lesson.

Nothing quite gets you through those difficult days and long synchrotron nights like great colleagues. I have been lucky enough to be part of two research groups filled with lovely people. Ricky, Matt, Pieter-Jan, Alice, Michel and Victoria, thanks for the laughs and the support over the years – it has been a pleasure to work with you all. Warm thanks go out to the rest of the ASP/ESA group for your friendliness and help over the years. Thanks also go to everyone in S12 for making me feel so welcome – it really means a lot ☺.

Finally I want to thank all my family and friends for being so interested in what I've been up to, and especially those who made my Anglo-Belgian transition so smooth: Mummy, Trevor, Bruno, Naomi, John&Agnes, the Westssons, Harriet, Shahania, Joe, Sarah, Lize, Anke, Mamie&Papie, Roemie… I think all of you have made me feel at home, either by sending over Cheddar in the post (or bringing it in person), being great company or simply keeping in touch. Finally, thank you to my darling Hans for sweeping me off my feet at the end of a beam time two years ago. Thank you for being such a wonderful partner. We are just at the start of our life-adventure! Next stop: California!

Declarations

I declare that this thesis and the work presented in it are my own and represent my own original research. Wherever contributions of others are included, I have endeavoured to ensure that this is stated clearly and attributed with explicit references. This thesis has been submitted as part of the requirements of the cotutelary Ph.D agreement between the universities of Warwick (UK) and Ghent (Belgium). The parts of this thesis which have been published by the author have been indicated within relevant chapters.

Abstract

The research presented in this thesis uses laboratory and synchrotron based structural techniques in combination with electrochemistry to test the durability of selected conservation methods. A new piece of portable spectroelectrochemical equipment (the peCell) is also described: the peCell was designed for the long-term monitoring of conservation treatments. Lead carboxylates were selected as the focal point of this research due to the interest in studying their deposition from ethanolic solution and the effectiveness of this type of coating on lead. Therefore the spectroscopic analysis, electrochemical testing in an electrolyte modelling atmospheric corrosion, short-term and long-term volatile organic compound (VOC) exposure, and museum testing of this inhibitor demonstrates an entire package of tests which might be used as a benchmark for testing conservation treatments prior to use on artefacts. In addition the contrasting effects of lead carboxylates in oil paintings and as conservation coatings are discussed.

Alongside laboratory spectroelectrochemical data, the corrosion by oak VOCs of a conserved lead sample was studied, (a) using a state-of-the-art *in situ* time-lapse technique on a synchrotron and (b) within a museum environment. Surface analysis by X-ray diffraction (XRD) was used to compare the growth of crystalline surface corrosion products over time: the extent of corrosion can be related to the effectiveness of the various conservation techniques.

The peCell is a portable electrochemical or environmental cell which was invented in order to provide a way of tracking the chemical changes occurring in a conserved sample *in situ* over a long period of time. The cell is capable of holding three samples which can be monitored continuously using open circuit potential and sporadically (i.e. whenever a synchrotron beam line is accessible) using SR-XRD. Other environmental parameters within the cell can also be monitored, such as temperature. The prototype cell was successfully trialled at the XMaS beamline, ESRF using an alternative copper corrosion system.

Nederlandstalige samenvatting

Het onderzoek, voorgesteld in deze thesis, maakt gebruik van labo- en synchrotrongebaseerde technieken in combinatie met elektrochemie om de duurzaamheid van enkele geselecteerde conservatiemethoden te testen. Tevens wordt een nieuwe draagbare spectro-elektrochemische cel (peCell) beschreven, welke ontwikkeld werd voor de lange-termijn bewaking van conservatiebehandelingen. Het werk heeft zich voornamelijk gericht op loodcarboxylaat-ethanoloplossingen met als doel deze af te zetten als beschermende deklaag op loden voorwerpen. Meerdere experimenten werden beoogd als maatstaf. Deze omvatten spectroscopische analysen, elektrochemische testen, korte en lange blootstelling aan vluchtige organische componenten en feitelijke testen in een museumomgeving. Daarnaast wordt in dit werk ook de contrasteren effecten van loodcarboxylaten in olieschilderijen besproken.

De corrosie door vluchtige organische componenten van een geconserveerd loden staal werd bestudeerd (a) gebruik makend van een state-of-the-art in-situ tijdsgeresolveerde synchrotrontechniek en (b) in een museumomgeving. X-straaldiffractie (XRD) werd gebruikt om de groei van het kristallijne corrosieproducten aan het oppervlak in functie van de tijd te volgen: de omvang van de corrosie kan ons informeren over de efficiëntie van verschillende conservatiemethoden.

De peCell is een draagbare elektrochemische of milieucel die ontwikkeld werd om chemische veranderingen te volgen over een langere periode en dit in-situ in een bepaalde omgeving. De cel kan drie stalen hanteren die tegelijkertijd en continu gevolgd kunnen worden via de openklempotentiaal en sporadisch (wanneer een synchrotron bundellijn beschikbar is) gebruik makend van synchrotron gebaseerde XRD. Andere parameters, zoals bv. de tempartuur in de cel, kunnen ook gevolgd worden. Het prototype van de cel werd met succes ingezet op de XMaS bundellijn (ESRF, Grenoble).

List of abbreviations

AC	Alternating current
CCD	Charge-coupled device
CV	Cyclic voltammetry
E_{corr}	Corrosion potential
EIS	Electrochemical impedance spectroscopy
FT-IR	Fourier transform infrared spectroscopy
GC-MS	Gas chromatography - mass spectrometry
GCE	Glassy carbon electrode
IUD	Intrauterine device
OCP	Open circuit potential
PCTFE	Polychlorotrifluoroethylene
PEEK	Polyetheretherketone
PTFE	Polytetrafluoroethylene
RH	Relative humidity
SEM	Scanning electron microscopy
SIMS	Secondary ion mass spectrometry
SPME	Solid-phase microextraction
SR-XRD	Synchrotron X-ray diffraction
SUS	Simulated uterine solution
VMP	Voltammetry of microparticles
VOC	Volatile organic compounds
XAS	X-ray absorption spectroscopy
XRD	X-ray diffraction

1. Introduction

The interface between art and science has been long discussed. In his influential 1959 Rede lecture entitled “The Two Cultures”, C. P. Snow famously claimed that the gap between the arts and sciences was the main reason why the world’s problems were not solved [1]. Thankfully the field of conservation (or more recently ‘heritage’) science brings together expertise in science and art in order to solve some smaller problems related to the preservation and understanding of our material cultural heritage. This could mean exploring reasons behind the discolouration of Van Gogh’s sunflowers [2], finding the best method to prolong the life of an historic ship whilst keeping it as a popular tourist attraction (e.g. the ss Great Britain [3,4] or the Mary Rose [5]) or even trying to digitally recreate vital cultural heritage which has been destroyed due to larger world problems (e.g. the Buddhas of Bamiyan which were destroyed during the 2001 Afghanistan war) [6].

1.1 Conservation principles

Conservation, in the context of cultural heritage, is the preservation or restoration of works of art, artefacts and historic architecture. One aim of conservation science is to study the chemical change occurring before, during and after conservation treatments take place. Conservation research adds to our understanding of how these treatments work on a molecular scale and therefore allows us to develop and improve them.

There are two types of conservation practice. Firstly, interventive conservation involves adding material to or removing material from a work of art. This is done in order to stabilise the surface, prevent corrosion or replace lost parts to improve aesthetics. For example during the current restoration of The Ghent Altarpiece the previous varnishes and retouchings will be removed and replaced by accurate, water-soluble facsimiles of the original paint [7]. Another example of interventive conservation is the impregnation of the remaining Mary Rose timbers using polyethylene glycol (PEG) to prevent shrinkage while drying [8]. This treatment has taken over twenty years and allows the ship to be displayed within a controlled environment in the new Mary Rose museum (Figure 1.1).

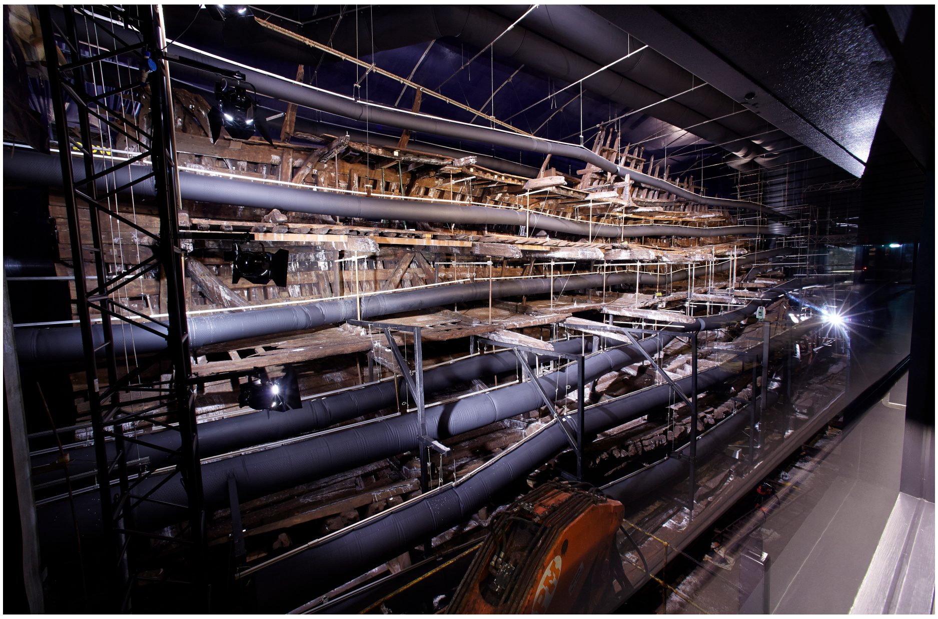

Figure 1.1 The Mary Rose hull stored in a controlled climate after being sprayed with PEG (Photo credit: zedphoto.com)

The second type of conservation, preventative conservation, aims to increase the lifespan of artefacts by controlling the environment within which the artefact is stored. This could involve temperature, UV, humidity or air content control within a display case, frame or storage location. For example, the ss Great Britain is an iron ship and popular tourist attraction in Bristol, UK. In order to keep the ship accessible to visitors for at least the next hundred years, the iron hull of the ship is now enclosed in a dry dock with a controlled environment wherein visitors can enter [4,9].

Conservators are not bound by set rules. However most national and international professional conservation organisations have a set of guidelines for good practice, which normally include the following [10]:

- Intervention should be kept to a minimum (i.e. preventive conservation is preferred);
- A treatment should be reversible (e.g. using water-soluble paints on The Ghent Altarpiece);
- A treatment should not alter the cultural value of the object and the information it contains.

Both interventive and preventive methods require an in-depth understanding of the physiochemical processes occurring between the material and the surrounding environment. In the context of metals conservation, this refers to the study of corrosion processes which occurred in the past to form existing corrosion products and which are also likely to occur during and after conservation.

1.2 Conservation of metallic objects

Both interventive and preventative conservation methods exist for heritage metals. The corrosion mechanisms of heritage metals with well-known corrosive agents (e.g. chlorides) have been at least partly elucidated [11–14]. Popular preventive conservation methods are based on information such as the relative humidity and oxygen concentration thresholds that cause corrosion [15]. The environment in which the artefact is stored (for display or otherwise) can be tuned to “turn off” corrosion. For example, at 12 % RH, chlorine-impregnated iron does not corrode, but at 15 – 20 % RH there is sufficient water concentration in the air to form β-FeOOH, which leads to slow corrosion [16,17]. Oxygen also accelerates the deterioration of metal artefacts, but the removal of oxygen (in a display case, for example) is very expensive and is only carried out for objects of very high cultural value [18].

If these preventative measures are not suitable, several interventive techniques exist for metallic objects. Firstly removing material (corrosive agents or corrosion products) from the artefact can be an effective way of preserving the metal surface. Soluble corrosion products or corrosive ions can be removed by soaking the object in an appropriate solution. For example, soaking chloride-contaminated copper/bronze in sodium sesquicarbonate solution has been shown to be an effective method of removing chlorides which cause bronze disease [19]. However, this process can take many years to complete and it is difficult to monitor the progress of ion removal within the entire volume of an artefact [20].

The removal of solid corrosion products requires some degree of dexterity. Care must be taken when removing corrosion products physically (by using a scalpel for example) so as to limit the damage to the original patina and its pattern/form.

Electrochemical techniques can be used to reduce corrosion products back to the original metal if the object is made the working electrode of the system. They can be used to conserve an entire metallic object by immersion [21] or more locally using an electrolytic pen [22]. These techniques have been often used for homogenous surfaces such as silver, wherewith they have been successful in removing tarnish (Ag_2S) [23].

The methods in the second category of interventive techniques require the addition of material in order to stabilise the object: for example a coating or an inhibitor. Inhibitors react chemically with the substrate to produce a stable surface. This can be especially useful to halt a destructive cyclic chemical reaction, such as bronze disease. In this particular case, benzotriazole (BTA) is used to react with copper to form a copper (I)-BTA film, which affords protection against ongoing corrosion by chlorides [24].

As opposed to inhibitors, coatings do not form a strong chemical bond with the substrate but their application may require surface pre-treatment. Practical conservation was carried out as part of the doctoral training for this thesis on a set of pewter recovered from the Mary Rose wreck. This particular set of pewterware belonged to Sir George Carew, the commanding officer of the Mary Rose, and his stamp still survives on each item (he did not survive the sinking) [25]. The pewter was tarnished after years of storage in an urban museum and required surface cleaning with a gentle abrasive (Pre-lim, Picreator, UK) with a microcloth prior to application of a microcrystalline wax coating (Renaissance wax, Picreator, UK).[1]

Other coatings and inhibitors originally developed for industrial use (e.g. silanes, acrylic resins) are also used in the conservation studio. Carboxylates, the subject of this thesis, have been long classed as a coating but can also be classed as inhibitors, depending on the reactivity of the substrate.

1.3 Lead as a cultural heritage material

Lead is a post-transition metal. It is dense and is toxic. As is common with post-transition metals, lead is soft and malleable with a low melting point of 327.5 °C. These properties have made it a popular material for building, infrastructure and

---

[1] It is worth mentioning that very little research has been done on the effects of these waxes and surface cleaners on heritage materials, and the author found them difficult to use due to the extensive visible residue left behind.

cultural objects for thousands of years [26]. A well-known historic example of lead use was in Roman water pipes (known as *fistulæ*).

Lead metal has also been a popular material for munitions throughout history due to its high density and ease of casting due to the low melting point. On Henry VIII's flagship, the Mary Rose, lead shot (Object 83A5018, Figure 1.2) was customised for deadly purpose: an inner core of iron made sure the shot pierced the armour of the enemy [27]. In the wreck of the Mary Rose, as well as the large number of lead shot, there were other lead artefacts which showed the 'living' side of the ship: sounding weights, tokens and trade weights which would have been personal belongings of the crew in preparation for their voyage which never came about (for example, Object 79A0476, Figure 1.2). These objects were surprisingly well preserved due to the passivating corrosion products that form in the marine environment of the Solent [25].

Figure 1.2 Lead objects from the Mary Rose ship: a lead shot (L) and sounding weight (R). Object identifiers relate to the date and area of excavation. (Copyright: Mary Rose Museum)

Lead also lends itself to musical cultural heritage; the sound of pressurised air flowing through lead organ pipes is a familiar sound across Europe's cities and villages (Figure 1.3). Organ music is mostly affiliated with religious music (e.g. Bach, Parry) but secular organ music is increasingly popular in concert halls [28], which can house huge organs with thousands of pipes. The particular construction of the pipe organ also makes the lead vulnerable to corrosion in heated churches: the wooden windchest emits organic acids which attack the lead metal pipes to cause cracking and subsequent loss of timbre [29–32]. In modern organ building, in order to prevent the emission of organic acids, the wooden holes within which the pipes sit are burnt. Other methods of prevention alongside organic acid interaction with lead will be explored to some extent in this thesis.

Figure 1.3 A pipe organ in construction after conservation at Orgel Lapelgebouw, Diksmuide, Belgium (Copyright: Rosie Grayburn)

1.4 Studying materials *in situ* in a controlled environment – the eCell

If samples are removed from a controlled environment for measurement, the surface could react with the ambient and give misleading results. Therefore the most accurate way to model real corrosion or other chemical transformations is to examine the samples of interest while they reside within the created conditions. This requires a piece of equipment which allows surface analysis to occur *in situ*, such as the eCell [33] which allows simultaneous surface analysis within an electrochemical (or VOC-saturated) environment. The cell window must be transparent to the electromagnetic radiation to be used and the material of the cell must be resistant to the generated environment. Also, the thickness of the electrolyte between the sample and the window must be sufficiently thin (100 µm) to allow penetration of the incident radiation and avoid scattering of signal from the liquid.

In this research we are interested in *in situ* synchrotron X-ray techniques for tracking corrosion and/or electrochemical behaviour. Spectroelectrochemical cells for use in synchrotron beamlines were first pioneered by Fleischmann, Robinson and co-workers, as they defined these requirements for *in situ* analytical instrumentation for corrosion studies [34] and spectroelectrochemistry. The authors applied a SR-XRD technique to a lead-dioxide layer deposited on platinum in a sulphuric acid electrolyte within a Bragg-type cell [34–36]. The X-rays with a wavelength of 1.307 Å were incident at 4° and cyclic voltammetry was performed using the lead-dioxide sample as a working electrode during surface analysis. In addition the cell was used for *in situ* EXAFS of samples pre-passivated within the electrochemical cell [34]. Since the development of these first cells, *in situ* cells have been designed by many other researchers for similar purposes [37–41].

There are principally two types of cell: Bragg and Laue cells (Figure 1.4). Bragg cells work in reflection mode whereas Laue cells work in reflection or transmission mode. For a Bragg-type cell, the window of the cell must be parallel to the surface of interest. In a Laue-type cell, the incoming X-rays pass through a window perpendicular to the surface of interest and outgoing X-rays pass through a second perpendicular window. In order to reduce scattering from the electrolyte in a Laue-type cell it is possible to reduce the thickness of the cell [42].

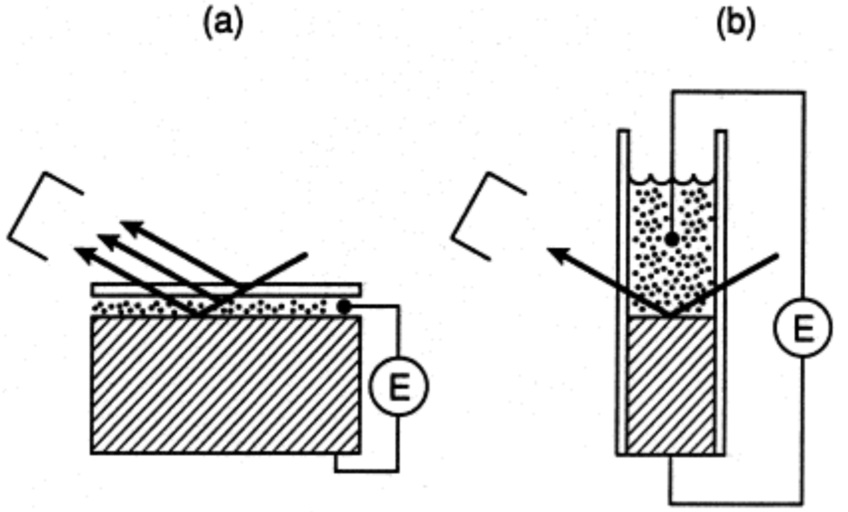

Figure 1.4 (a) Reflection geometry in a Bragg cell, and (b) transmission geometry in a Laue cell. Reprinted from reference [42] with permission from Elsevier.

The Electrochemistry and Surface Analysis (ESA) and Analytical Science Projects (ASP) groups at Ghent and Warwick Universities have designed four iterations of an environmental/electrochemical cell (eCell) for the examination of conservation processes simultaneously by electrochemical and synchrotron X-ray methods [33]. The eCell is a Bragg cell used in reflection mode for surface analysis but remote control of the working electrode ensures movement between this position and a “dwell’ position which allows the electrode to be immersed in electrolyte. The eCell environment can be customised depending on the experimental conditions required: gas flow, liquid flow, synchrotron radiation and/or electrochemistry. The first system to be studied was chlorine-contaminated copper [43,44]. Copper-containing marine artefacts become impregnated with chloride ions during their residence in seawater. After removal from this low-oxygen environment into ambient conditions, the nantokite formed by reaction of copper with chlorine reacts with oxygen and water to form powdery copper hydroxychlorides [45]. These compounds can cause structural damage to the artefact due to loss of metallic structure, a process more commonly known as "bronze disease" [14,46,47]. As previously mentioned, a common method of chloride removal for the prevention of bronze disease is soaking in water or a sodium sesquicarbonate solution [18]. In addition, a weak polarising potential could be applied to reduce copper chloride species thus removing chlorides from the metal [48–50].

Using XRD and X-ray absorption spectroscopy (XAS) in a time-lapse experiment, the growth and disappearance of copper corrosion products were monitored with time [20,51–53]. The corrosion potential of the electrochemical cell (E_{corr}) (the copper sample being the working electrode) was also measured using open circuit potential (OCP). The results from the spectroscopy and diffraction were compared with the E_{corr} to see if a relationship between corrosion product removal and E_{corr} could be established. If such a relationship existed, E_{corr} could possibly be used as a simple monitoring tool for chloride removal during soaking. It was found that E_{corr} could only track the removal of chemically bound chlorides. If chlorides were adsorbed to the surface, monitoring by OCP was not possible even though they would still pose a threat to the metallic surface after conservation.

Also using the eCell, the effectiveness of electrolytic reduction of a chloride-impregnated sample was investigated. XRD patterns were extracted while the conservation treatment was taking place [54]. In this way, the transformation of nantokite to cuprite was visualised, thus showing the successful removal of chlorides using this technique. Other copper corrosion transformations have also been observed by exposing reference materials to reactants of interest and tracking the crystalline transformations with time without electrochemical intervention [11,12].

Lead decanoate ($Pb(CH_3(CH_2)_8COO)_2$) was studied as a possible conservation coating on lead using spectroelectrochemical techniques within the eCell: the growth of the crystalline coating was studied over time using SR-XRD alongside EIS to measure the effectiveness directly of the growing layer [53,55]. This layer was then exposed to acetic acid vapour within the cell and the resulting crystalline corrosion products were recorded over time using XRD [56]. More recently the eCell has also been used to study the growth and deterioration of lead dodecanoate ($Pb(CH_3(CH_2)_{10}COO)_2$) spectroelectrochemically using cyclic voltammetry (CV) and linear sweep voltammetry with SR-XRD [57].

The eCell is capable of providing a wide variety of environments for many different samples. The portable cell described in this thesis (Chapter 6 and 7) aims to provide multi-sample capability for longer-term experiments.

1.5 Scope of the thesis

The aim of the research presented in this thesis was to use electrochemistry in combination with laboratory and synchrotron based structural techniques to test the long-term viability of conservation methods. Specifically a new piece of portable spectroelectrochemical equipment (the peCell) was designed for the long-term monitoring of conservation treatments. Lead carboxylates were selected as the focal point of this research due to the interest in studying the coating mechanism and efficacy of this type of coating on lead.

Chapters 1 and 2 give a background to the research and an overview of the experimental techniques used. In Chapter 3, contrasting effects of lead carboxylates in oil paintings and as conservation coatings are discussed: in one case their inhibition of corrosion when applied to a lead surface, and in the other the damage they cause to oil paintings. We aimed to synthesise and spectroelectrochemically characterise three lead carboxylates. Then, using the electrochemical information we collected, we briefly assessed the viability of voltammetry as a method for finding lead soaps in oil paint samples.

However the focus of the research was the investigation of the protective characteristics of lead carboxylates (14 – 18 carbons per chain) when deposited from an ethanolic solution. Previous work has focussed on deposition from aqueous solution, which limits the length of carbon chain that can be deposited on lead [58,59]. By using ethanol as a solvent, longer chain carboxylic acids can be dissolved and therefore the protection characteristics can possibly be improved. In Chapter 4 the coating process is described through the use of time-lapse synchrotron X-ray methods and the optimum inhibitor concentration in solution is investigated. By applying the chosen inhibitor to a polished lead coupon and using this as the working electrode in an electrochemical setup modelling a corrosive VOC environment, the effectiveness of the two chosen inhibitors is tested. Electrochemical impedance spectroscopy (EIS) can give quantitative data relating to the effectiveness of a coating on a conductive substrate, in this case the conserved lead sample compared with an unconserved sample. In addition, more realistic substrates for testing conservation inhibitors (i.e. pre-corroded lead) were screened.

The real-time corrosion by oak VOCs of a conserved lead coupon is described in Chapter 5 using a state-of-the-art *in situ* technique on a synchrotron. Coupled with this study, an experiment/exhibit erected at the Museum for the History of Science, Gent is described. Within the exhibit, the longevity of a range of conserved lead coupons was tested by placing conserved and unconserved control samples in an oak display case for 7 months. Surface analysis by X-ray diffraction was used to compare the growth of crystalline surface corrosion products during this time: the extent of corrosion can tell us about the effectiveness of the various conservation techniques.

The peCell was invented as part of this project in order to provide a way of tracking the chemical changes occurring in a conserved sample over a long period of time. It is described in Chapter 6. The cell is capable of holding three samples which can be monitored continuously using open circuit potential and sporadically (i.e. whenever a synchrotron beam line is accessible) using SR-XRD. The prototype cell was tested using an alternative copper corrosion system as described in Chapter 7.

1.6 References

[1] C.P. Snow, The Two Cultures, Cambridge University Press, London, 1959.

[2] L. Monico, G. Van der Snickt, K. Janssens, W. De Nolf, C. Miliani, J. Dik, M. Radepont, E. Hendriks, M. Geldof, M. Cotte, Degradation process of lead chromate in paintings by Vincent van Gogh studied by means of synchrotron X-ray spectromicroscopy and related methods. 2. Original paint layer samples., Analytical Chemistry. 83 (2011) 1224–31.

[3] D. Watkinson, M. Tanner, R. Turner, M. Lewis, ss Great Britain: Teamwork as a platform for innovative conservation, The Conservator. 29 (2005) 73–86.

[4] D. Watkinson, M. Tanner, ss Great Britain: conservation and access – synergy and cost, Studies in Conservation. 53 (2008) 109–114.

[5] G. Mcconnachie, R. Eaton, M. Jones, A Re-evaluation of the Use of Maximum Moisture Content Data for Assessing the Condition of Waterlogged Archaeological Wood, E-Preservation Science. (2008) 29–35.

[6] M. Petzet, ed., The Giant Buddhas of Bamiyan: Safeguarding the remains, ICOMOS, Paris, 2009.

[7] KIK/IRPA, The Ghent Altarpiece, http://closertovaneyck.kikirpa.be/, Date accessed: August 11, 2014.

[8] J. Evans, Preserving the Mary Rose, Chemistry World. (2014) 46–49.

[9] D. Watkinson, M. Lewis, ss Great Britain iron hull : modelling corrosion to define storage relative humidity, in: D. Hallam, J. Ashton (Eds.), Metal 04: Proceedings of the Interim Meeting of the ICOM-CC Metal Working Group, National Museum of Australia, Canberra, 2004: pp. 88–103.

[10] The Institute of Conservation, Standards in conservation, www.icon.org.uk, Date accessed: November 21, 2014.

[11] M. Dowsett, A. Adriaens, C. Martin, L. Bouchenoire, The Use of Synchrotron X-rays To Observe Copper Corrosion in Real Time, Analytical Chemistry. 84 (2012) 4866–4872.

[12] R. Grayburn, M. Dowsett, M. Hand, P.-J. Sabbe, P. Thompson, A. Adriaens, Tracking the progression of bronze disease – A synchrotron X-ray diffraction study of nantokite hydrolysis, Corrosion Science. 91 (2015) 220–223.

[13] L. Robbiola, J. Blengino, C. Fiaud, Morphology and mechanisms of formation of natural patinas on archaeological Cu–Sn alloys, Corrosion Science. 40 (1998) 2083–2111.

[14] I.D. Macleod, Bronze disease: An electrochemical explanation, Bulletin ICCM. 7 (1981) 16–26.

[15] R. Wiesinger, I. Martina, C. Kleber, M. Schreiner, Influence of relative humidity and ozone on atmospheric silver corrosion, Corrosion Science. 77 (2013) 69–76.

[16] M.R.T. Lewis, D. Watkinson, Desiccated Storage of Chloride-Contaminated Iron: A Study of the Effects of Loss of Environmental Control, in: E. May, M. Jones, J. Mitchell (Eds.), Heritage Microbiology and Science: Microbes, Monuments and Maritime Materials, Royal Society of Chemistry, Cambridge, 2008: pp. 279–289.

[17] D. Watkinson, M.T. Lewis, Desiccated Storage of Chloride-Contaminated Archaeological Iron Objects Desiccated Contaminated Objects Storage of Chloride Iron Archaeological, Studies in Conservation. 50 (2005) 1–12.

[18] D. Watkinson, Preservation of Metallic Cultural Heritage, in: T.J.A. Richardson, B.R.A. Cottis, R. Lindsay, S. Lyon, D.J.D. Scantlebury, H. Stott, M. Graham (Eds.), Shreir's Corrosion, Volume 4, Elsevier, Amsterdam, 2009: pp. 3307–3340.

[19] K. Leyssens, A. Adriaens, C. Degrigny, E. Pantos, Evaluation of corrosion potential measurements as a means to monitor the storage and stabilization processes of archaeological copper-based artifacts., Analytical Chemistry. 78 (2006) 2794–801.

[20] A. Adriaens, M. Dowsett, In-situ spectroelectrochemical studies of the removal of chlorides from copper, in: C. Degrigny, R. van Langth, I. Joosten, B. Ankersmit (Eds.), Metal 07: Proceedings of the Interim Meeting of the ICOM-CC Metal Working Group, Rijksmuseum, Amsterdam, 2007: pp. 10–14.

[21] C. Degrigny, Use of electrochemical techniques for the conservation of metal artefacts: a review, Journal of Solid State Electrochemistry. 14 (2009) 353–361.

[22] C. Degrigny, The Pleco, http://www.fablab-neuch.ch/pleco/plus.php?id=1, Date accessed: August 13, 2014.

[23] D. Scott, J. Podany, B.B. Considine, J.P.G. Museum, G.C. Institute, Ancient & Historic Metals: Conservation and Scientific Research: Proceedings of a Symposium Organized by the J. Paul Getty Museum and the Getty Conservation Institute, November 1991, Getty Conservation Institute, Los Angeles, 1994.

[24] R.B. Faltermeier, A Corrosion Inhibitor Test for Copper-Based Artifacts, Studies in Conservation. 44 (1998) 121–128.

[25] M. Jones, For Future Generations: Conservation of a Tudor Maritime Collection (The Archaeology of the Mary Rose: Volume 5), Mary Rose Trust Ltd, Portsmouth, 2011.

[26] S. Hong, J. Candelone, C. Patterson, C. Boutron, Greenland Ice Evidence of Hemispheric Lead Pollution Two Millennia Ago by Greek and Roman Civilizations, Science. 265 (1994) 1841–1843.

[27] S. Kilcoyne, Strain analysis of 15th century guns and projectiles, Institute Laue Langevin Experimental Reports. (2012).

[28] E.H.B., King of Instruments, back on stage, The Economist. (2013).

[29] A. Åslund, J. Speedstra, The COLLAPSE Project: Corrosion of organ pipes - causes and recommendations, Publications Office of the European Union, Luxembourg, 2011.

[30] A. Niklasson, S. Langer, K. Arrhenius, Air pollutant concentrations and atmospheric corrosion of organ pipes in European church environments, Studies in Conservation. 53 (2008) 24–40.

[31] C. Chiavari, C. Martini, D. Prandstraller, A. Niklasson, L.-G. Johansson, J.-E. Svensson, A. Åslund, C.J. Bergsten, Atmospheric corrosion of historical organ pipes: The influence of environment and materials, Corrosion Science. 50 (2008) 2444–2455.

[32] F. Deflorian, M. Fedel, Electrochemical analysis of the degradation of lead alloy organ-pipes due to acetic acid, Journal of Cultural Heritage. 14 (2013) 254–260.

[33] M.G. Dowsett, A. Adriaens, Cell for simultaneous synchrotron radiation X-ray and electrochemical corrosion measurements on cultural heritage metals and other materials., Analytical Chemistry. 78 (2006) 3360–5.

[34] J. Robinson, F.C. Walsh, In situ synchrotron radiation X-ray techniques for studies of corrosion and protection, Corrosion Science. 35 (1993) 791–800.

[35] N. Barlow, C. Brennan, S.E. Doyle, G.N. Greaves, M. Miller, a. H. Nahle, K.J. Roberts, J. Robinson, J.N. Sherwood, F.C. Walsh, Instrumentation and data acquisition for in situ electrochemistry at the Daresbury SRS, Review of Scientific Instruments. 60 (1989) 2386.

[36] M.E. Herron, S.E. Doyle, K.J. Roberts, J. Robinson, F.C. Walsh, Instrumentation and cell design for in situ studies of electrode surfaces using x-ray synchrotron radiation, Review of Scientific Instruments. 63 (1992) 950.

[37] C. Kleber, M. Schreiner, Multianalytical in-situ investigations of the early stages of corrosion of copper, zinc and binary copper/zinc alloys, Corrosion Science. 45 (2003) 2851–2866.

[38] R. Springell, S. Rennie, L. Costelle, J. Darnbrough, C.A. Stitt, E. Cocklin, C. Lucas, R. Burrows, H.E. Sims, D. Wermeille, J. Rawle, C. Nicklin, W. Nuttall, T. Scott, G. Lander, Water corrosion of spent nuclear fuel: radiolysis driven dissolution at the UO2/water interface, Faraday Discuss. (2015).

[39] R. Wiesinger, U. Schade, C. Kleber, M. Schreiner, An experimental set-up to apply polarization modulation to infrared reflection absorption spectroscopy for improved in situ studies of atmospheric corrosion processes., The Review of Scientific Instruments. 85 (2014) 064102.

[40] K.-S. Yun, S. Joo, H.-J. Kim, J. Kwak, E. Yoon, Silicon Micromachined Infrared Thin-Layer Cell for In Situ Spectroelectrochemical Analysis of Aqueous and Nonaqueous Solvent System, Electroanalysis. 17 (2005) 959–964.

[41] T. Rayment, A.J. Davenport, A.J. Dent, J.-P. Tinnes, R.J.K. Wiltshire, C. Martin, G. Clark, P. Quinn, J.F.W. Mosselmans, Characterisation of salt films on dissolving metal surfaces in artificial corrosion pits via in situ synchrotron X-ray diffraction, Electrochemistry Communications. 10 (2008) 855–858.

[42] Z. Nagy, H. You, Applications of surface X-ray scattering to electrochemistry problems, Electrochimica Acta. 47 (2002) 3037–3055.

[43] K. Leyssens, Monitoring the conservation treatment of corroded cupreous artefacts: The use of electrochemistry and synchrotron radiation based spectroelectrochemistry., PhD Thesis, Universiteit Gent, 2006.

[44] K. Leyssens, a. Adriaens, M.G. Dowsett, B. Schotte, I. Oloff, E. Pantos, a. M.T. Bell, S.P. Thompson, Simultaneous in situ time resolved SR-XRD and corrosion potential analyses to monitor the corrosion on copper, Electrochemistry Communications. 7 (2005) 1265–1270.

[45] A.A.M. Pollard, R. Thomas, P. Williams, T. Drayman-Weisser, The copper(II) chloride system and corrosion: a complex interplay of kinetic and thermodynamic factors., in: T. Drayman-Weisser (Ed.), The Conservation of Bronze Sculpture in the Outdoor Environment: A Dialogue among Conservators, Curators, Environmental Scientists, and Corrosion Engineers. Edited by Terry Drayman-Weisser., National Association of Corrosion Engineers, Houston, Texas, United States, 1983: pp. 123–133.

[46] L. Robbiola, La corrosion de bronzes archéologiques, la maladie du bronze: un aperçu scientifique, in: Journées Sur La Conservation, Restauration Des Biens Culturels: Recherches et Techniques Actuelles, 1987: pp. 9–13.

[47] D.A. Scott, Bronze disease: A review of some chemical problems and the role of relative humidity, Journal of the American Institute for Conservation. 29 (1990) 193–206.

[48] J.C. Coelho, C.M. Oliveira, M.D. Carvalho, I.T.E. Fonseca, The efficiency of electrochemical methods for the removal of chloride ions from iron marine archaeological objects: A comparative study, Materials and Corrosion. 65 (2014) 38–44.

[49] M. Uminski, V. Guidetti, The removal of chloride ions from artificially corroded bronze plates, Studies in Conservation. 40 (1995) 274–278.

[50] F. Dalard, Y. Gourbeyre, C. Degrigny, Chloride Removal from Archaeological Cast Iron by Pulsating Current, Studies in Conservation. 47 (2002) 117.

[51] M.G. Dowsett, A. Adriaens, G.K.C. Jones, N. Poolton, S. Fiddy, S. Nikitenko, Optically detected X-ray absorption spectroscopy measurements as a means of monitoring corrosion layers on copper., Analytical Chemistry. 80 (2008) 8717–24.

[52] A. Adriaens, M. Dowsett, The coordinated use of synchrotron spectroelectrochemistry for corrosion studies on heritage metals., Accounts of Chemical Research. 43 (2010) 927–35.

[53] A. Adriaens, M. Dowsett, Time resolved spectroelectrochemistry studies for protection of heritage metals, Surface Engineering. 24 (2008) 84–89.

[54] A. Adriaens, M. Dowsett, K. Leyssens, B. Van Gasse, Insights into electrolytic stabilization with weak polarization as treatment for archaeological copper objects., Analytical and Bioanalytical Chemistry. 387 (2007) 861–8.

[55] M. Dowsett, A. Adriaens, B. Schotte, G. Jones, L. Bouchenoire, In-situ spectroelectrochemical study of the growth process of a lead decanoate coating as corrosion inhibitor for lead surfaces, Surface and Interface Analysis. 41 (2009) 565–572.

[56] M. Dowsett, A. Adriaens, B. Schotte, G. Jones, Real time spectroelectrochemical growth and corrosion resistance monitoring of lead carboxylate coatings in an environmental cell (eCell), in: C. Degrigny, R. van Langth, I. Joosten, B. Ankersmit (Eds.), Metal 07: Proceedings of the Interim Meeting of the ICOM-CC Metal Working Group, Rijksmuseum, Amsterdam, 2007: pp. 26–31.

[57] M. De Keersmaecker, M. Dowsett, R. Grayburn, D. Banerjee, A. Adriaens, In-situ spectroelectrochemical characterization of the electrochemical growth and breakdown of a lead dodecanoate coating on a lead substrate., Talanta. 132 (2015) 760–8.

[58] K. De Wael, M. Keersmaecker, M. Dowsett, D. Walker, P.A. Thomas, A. Adriaens, Electrochemical deposition of dodecanoate on lead in view of an environmentally safe corrosion inhibition, Journal of Solid State Electrochemistry. 14 (2009) 407–413.

[59] E. Rocca, J. Steinmetz, Inhibition of lead corrosion with saturated linear aliphatic chain monocarboxylates of sodium, Corrosion Science. 43 (2001) 891–902.

2 Methods

This chapter describes the analytical techniques used to carry out this research. X-ray diffraction and electrochemical methods were the primary tools used to study coating effectiveness and peCell capabilities. However, microscopy and gas chromatography mass spectrometry (GC-MS) were also used to answer other questions regarding sample topography and environmental composition, respectively.

2.1 Scattering methods

2.1.1 Surface powder X-ray diffraction

The atoms in a crystalline material are arranged in repeating structures called unit cells. These cells are classified into 14 distinct categories, known as Bravais lattices [1]. Bravais lattices can be distinguished by their symmetry. A triclinic lattice has the least symmetry and a cubic lattice has the most symmetry [2]. Three length units (a, b, c) and three angles (α, β, γ) are the lattice parameters which define the type of Bravais lattice and describe the location of lattice points and basis (the repeated molecule or atom) in a crystal structure. Figure 2.1 shows the simplest unit cell called a primitive lattice whereby the basis is found on lattice points at the corners of a cube only. More complex lattices find the basis in the middle of a face or at the centre of the lattice.

Crystal planes are characterised using Miller indices (h k l) to show where they are located, in terms of the reciprocal of multiples of the lattice length parameters. A (110) plane is shown in Figure 2.1.

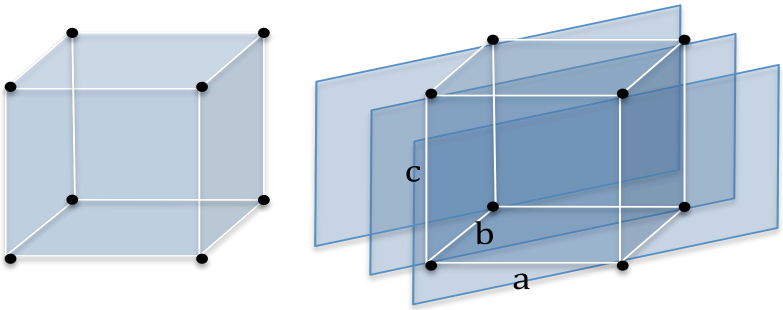

Figure 2.1 A primitive unit cell and an example of a crystal plane, (110). Black dots represent the basis which can be single atoms or molecules. In the case of this primitive cubic lattice, lattice parameters a, b **and** c **are all equal and can be referred to as** a **only.**

When electromagnetic radiation such as X-rays interacts with an atom, the electrons within the atom oscillate and as a result, emit X-rays in all directions. The scattered waves from the interaction with a plane of atoms can interfere constructively or destructively. Constructive interference of the scattered waves results in diffracted beams in specific directions. According to the Bragg condition (Equation 2.1) when n is an integer, these specific directions are related to the incident beam's wavelength (λ) and the interplanar spacing:

$$2d\sin\theta = n\lambda \,, \tag{2.1}$$

where θ is the angle of incidence, and d is the spacing between the layers in the lattice. The angle of incidence can be measured as the angle between the beam and the planes of a single crystal. In this work, θ is referred to as the angle between the beam and the surface containing a random powder (crystalline) sample. As shown in Figure 2.2, incident X-rays can be scattered (or reflected) from crystal planes below the surface of the sample: crystal planes act as a partially silvered mirror.

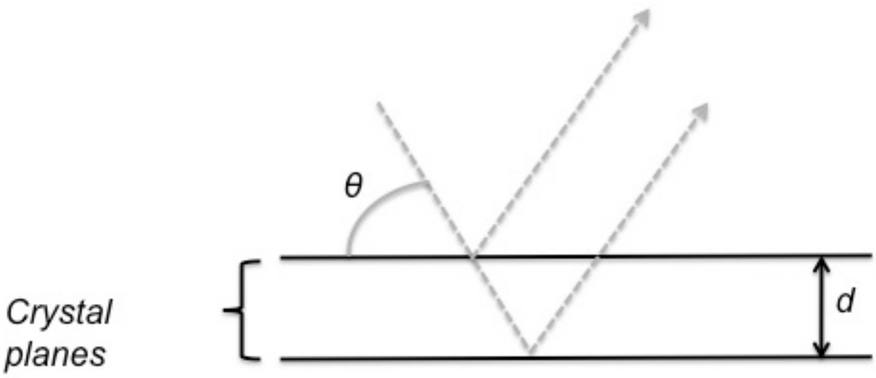

Figure 2.2 Incident X-rays (dotted line) are reflected from crystal planes at all values of n but constructive interference only occurs when n is an integer (Equation 2.1).

When the Bragg condition is fulfilled, the Miller indices can be derived from the interplanar spacing, *d*:

$$d_{hkl} = \frac{a}{\sqrt{h^2 + k^2 + l^2}} , \tag{2.2}$$

where *a* is the length of the unit cell for a cubic lattice. This equation can be adapted for any Bravais lattice [2].

The Bravais lattice and the basis are uniquely identified by the diffraction pattern through peak positions, the presence or absence of a peak (due to destructive interference in non-primitive cells) and the relative peak intensities. This allows the structural characterisation of the material directly from the pattern and the identification of the compound and crystal structure by comparison with relevant references.

In this work two different types of surface powder X-ray diffraction were used: laboratory X-ray diffraction and synchrotron X-ray diffraction. Firstly the laboratory diffractometer uses a Bragg-Brentano geometry to obtain a diffraction pattern. While an X-ray source (normally Cu-K_α) is stationary, the sample scans a range of θ while a detector scans the same range at twice the rate of the sample (both with respect to the beam axis). This is known as a theta-two theta scan. X-ray wavelengths are selected using a monochromator and the beam is reduced in size using a slit. These instruments are laboratory based and can produce excellent resolution diffraction patterns (see Chapters 3 and 5) which display the counts per second from the detector for each 2θ value. Bragg reflections take the form of peaks in the pattern. A disadvantage of this technique is the long time scale required to obtain such a pattern.

Several diffractometers have been used in this work: an ARL X' TRA Powder Diffractometer and D5000 Siemens diffractometer using Cu-K_α X-rays with a wavelength of 1.5405 Å and scintillation counter detectors was used for coating and corrosion product characterisation; a PANalytical X'Pert Pro X-Ray MRD X-Ray powder diffractometer equipped with a curved Johansson monochromator giving pure Cu-K_α X-rays at a wavelength of 1.540598 Å and a PIXcel detector was used for high resolution pattern acquisition.

2.1.2 Synchrotron X-ray diffraction

Synchrotron radiation is produced by accelerating electrons to close to the speed of light in an arc so that they exhibit relativistic properties [3]. Electron acceleration is controlled in a storage ring hundreds of metres diameter (Figure 2.3). The orbit of electrons within the ring is controlled by bending magnets and undulators. In this work two bending magnet beamlines were used, BM28 [4] and BM26A [5] at the European Synchrotron Radiation Facility (ESRF). The bending magnet bends the accelerated electrons in their orbit. As the electrons bend they emit synchrotron light at a tangent to the orbit. Bending magnet beamlines are placed at such an angle as to receive this light. The optics in the beamline then modify the beam to the requirements of the experimental hutch i.e.

focussing and selecting the appropriate wavelength [6]. For example, the XMaS beamline has access to a range of X-ray energies from 2.4 – 15 keV and a range of beam footprint sizes from 20 x 20 μm^2 – 0.8 x 0.8 mm^2 [4].

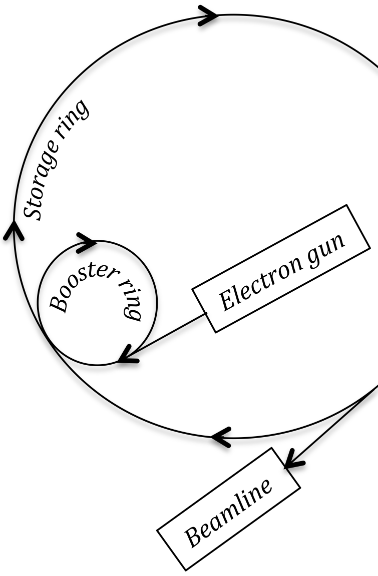

Figure 2.3 The ESRF synchrotron has a circumference of 844 m and stores electrons travelling at close to the speed of light. The 300 m long booster ring accelerates the electrons to be injected into the storage ring twice a day. Electrons are produced by an electron gun and accelerated to 2 x 10^8 eV for injection into the booster ring. There are more than 40 beamlines at the ESRF, each with their own specialism.

In this work synchrotron (SR) X-rays were used, which display the same diffraction properties as X-rays used in a laboratory. However, due to the high power of SR-X-rays, diffractograms of an adequate resolution can be obtained in a much smaller space of time (seconds) than laboratory XRD patterns. This enables data sets to be collected in quick succession and allows us to record time-lapse patterns.

The X-ray beam flux fluctuates according to some statistical rules special to the production of X-rays in a synchrotron. A particular detector monitors these fluctuations; in this case an ion chamber [7]. The ion chamber samples the beam by the detection of electrons resulting from the ionisation of a gas inside the detector by the beam. The resulting current is measured by an ammeter, which outputs a proportional voltage. Finally the voltage is converted to counts using a voltage-frequency converter. The resulting value, the beam monitor, is used to normalise data. Most of the steps in the measurement by the beam monitor value introduce an error, although it is not known which is more dominant in the context of this work.

The SR-XRD set-up used in this work (see Figure 2.4 for the setup at the XMaS beamline) was different to that of the laboratory XRD described previously. This setup was possible due to the quasi-parallel nature of synchrotron X-rays [8]. The X-ray beam used in laboratory XRD diverges from the source in Bragg-Brentano geometry. A diffraction pattern was collected from a fixed 2D detector (Mar CCD camera) for a fixed incident angle of X-rays. The camera axis was positioned at the correct angle to the beam for the reflected X-rays to be collected over the desired range of 2θ. In this case the angle of the camera axis to the beam was from 35° to 40° (sample dependent) in order to obtain a 2θ range of 5° – 65°. The camera plane intersects the diffraction cones to produce a section of the elliptical rings of a powder diffraction pattern (see Chapters 5 and 7).

The resulting 2D diffraction images from the camera are processed using the esaProject software [9]. esaProject (© EVA Surface Analysis) is a software package which can extract patterns from a variety of data formats and perform subsequent analysis. The elliptical rings of the 2D diffraction pattern are transformed to straight lines. In this form, the image rows can be summed and integrated. The resulting pattern shows the intensity recorded by the camera at all 2θ values. This can be done with single patterns or in a batch process. esaProject is also capable of processing a range of file formats and formatting them into a publishable state.

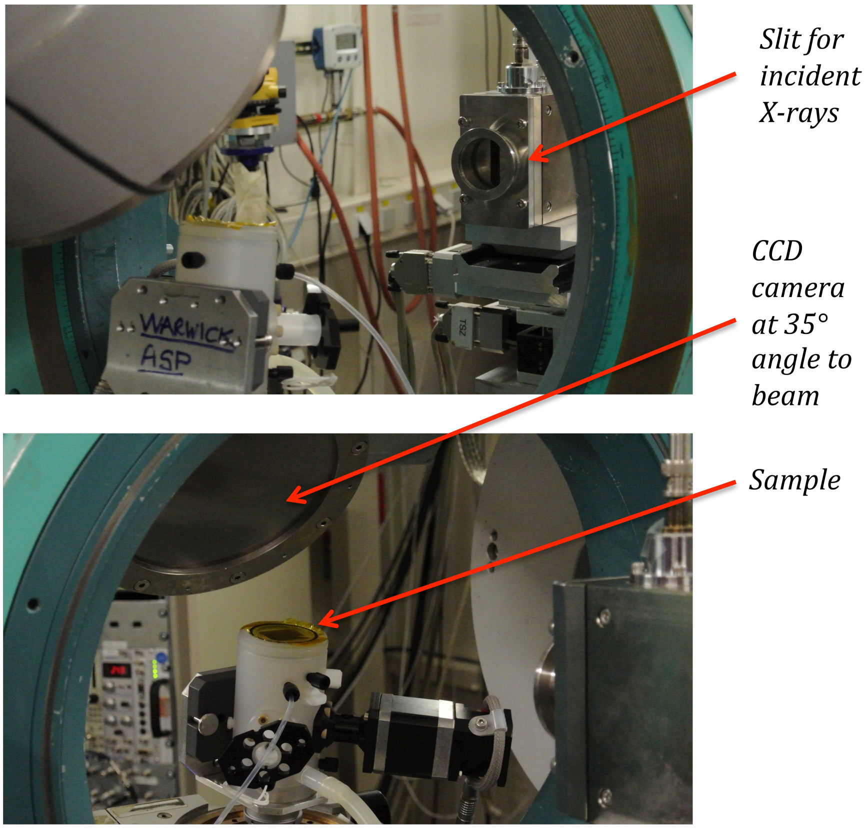

Figure 2.4 Experimental setup for synchrotron X-ray diffraction at the XMaS beamline

2.2 Electrochemical methods

Electrochemistry is the coupling of chemical changes to the passage of electricity. The starting point for any electrochemical experiment is the electrochemical cell in which the conditions one wishes to study are created. A standard electrochemical experiment consists of at least two electrodes (the working and reference electrodes) with addition of a counter electrode in a three-electrode cell [10]. All electrodes are immersed in an electrolyte. The electrode reaction of interest occurs at the working electrode, so this should consist of the material of interest e.g. a coated lead coupon. Working electrodes can be active (they are involved in the reaction) or inert (they act as a support for the reactants) [10]. In order for a reaction to take place at the working electrode a conducting pathway is needed. If necessary there should also be exclusivity at the working electrode, i.e. no other electrode reactions should occur, except those to be studied.

Because potential is a relative concept, the voltage on the working electrode must be referred to a reference electrode,

$$\Delta E = E_{WE} - E_{RE} \tag{2.3}$$

Reference electrodes therefore are required to supply a stable potential therefore the species involved must be in constant supply. A silver|silver chloride (Ag|AgCl) reference electrode was used in this work, which consists of a silver wire coated with silver chloride immersed in a chloride-rich aqueous solution.

$$\mathrm{AgCl_{(s)} + e^- \Leftrightarrow Ag_{(s)} + Cl^-_{(aq)}} \tag{2.4}$$

This electrode reaction has a potential of +0.210 V if a 3M KCl solution is used, and is successful as an electrode due to the fast kinetics of the system and porous nature of the AgCl coating [10]. In the three-electrode cell, a counter electrode made of an inert material is used as a source or sink for any current produced so as not to disturb the potential difference between the working and reference electrodes; a carbon counter electrode was used in the laboratory and a platinum counter electrode was used in the eCell [11] (described in Chapters 1, 6 and 7). The electrolyte completes the circuit between the three electrodes. The electrolyte is chosen in order to provide the appropriate environment for the working electrode (e.g. corrosive, chloride, biological) but must have a high ionic conductivity so that the electrode reaction can take place.

Once the three-electrode cell is set up, a potentiostat can set the potential difference between the reference and working electrode to the required value or measure it. Using a potentiostat, small changes in current can be measured which can give information about redox processes within materials. Alternatively the electrical resistance of a protective layer can be assessed. In this thesis three techniques have been used to study chemical processes and properties. A PGSTAT20 potentiostat with GPES (v4.9) or Nova software (all Autolab, Eco Chemie B.V., The Netherlands; Department of Analytical Chemistry, Universiteit Gent) was used to record electrochemical data.

2.2.1 Open circuit potential

OCP is the technique used to measure the E_{corr} of a system. At the E_{corr} the electrochemical system is at a steady state i.e. no external current is flowing through the system. Several reactions can occur at the working electrode spontaneously and simultaneously, despite the lack of external current which can give information about the corrosion or passivation of the surface of the working electrode [12]. In this research the precise value of E_{corr} is not important, rather its behaviour with time. As shown in Figure 2.5, the monitoring of E_{corr} can tell us whether the working electrode is corroding or passivating, either due to the electrolyte or the chemical history of the sample [13]. The rate of decay of the open-circuit vs. time curves can give information regarding corrosion rate, electrode kinetics and double layer capacitance [14]. The E_{corr} can also be related to the activity of the reactive species via the Nernst equation (Equation 2.5), where E_0 is the electrode potential (standard conditions), R is the gas constant, T

is temperature, *n* is the number of moles of electrons transferred in the reaction, *F* is Faraday's constant, a is the activity of the products or reactants and *v* is the stoichiometric coefficient. One example of E_{corr} in practice is its use as a parameter to gauge the stability of a metal artefact during conservation or after excavation [15–19].

$$E_{corr} = E_0 - \frac{RT}{nF} \ln \frac{\prod a_{prod}^{v_{prod}}}{\prod a_{react}^{v_{react}}} \tag{2.5}$$

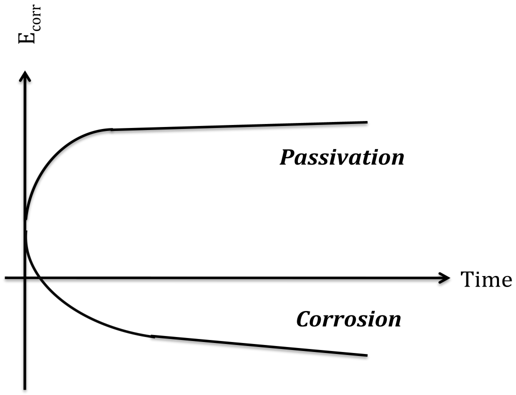

Figure 2.5 Electrochemical behaviour of a metal substrate in solution through the monitoring of E_{corr} vs time

2.2.2 Cyclic voltammetry

The potential difference of the cell can be ramped with time up to a point, then reversed back to the starting potential: this is known as cyclic voltammetry. On the application of a potential to the cell, the polarised working electrode yields a current which is collected and interpreted. Oxidation and reduction reactions which occur due to the cyclic voltammetry conditions imposed by the potentiostat produce a voltammetric trace which can give information about oxidation and reduction reactions in the form of positive or negative peaks, respectively. The location of these peaks can be used to identify compounds in a sample [20] or identify reaction mechanisms by the order of peaks found [21].

2.2.3 Electrochemical impedance spectroscopy

In direct current electricity, Ohm’s law defines resistance. In alternating current (AC) electricity, resistance takes a complex form to include the phase shift, *Φ* [10]:

$$Z = \frac{E(t)}{I(t)} = \frac{E_0}{I_0} e^{-j\phi} , \tag{2.6}$$

where Z is impedance, E*(t)* is the complex potential, I*(t)* is the complex current and *j* is √-1. Impedance is the tendency of a circuit to impede the flow of AC current.

Electrochemical impedance spectroscopy is carried out in a normal three-electrode cell. In an EIS measurement, a swept frequency potential is applied and the resulting current is measured. The resulting modulus of the impedance is plotted, which is the ratio of the magnitude of the voltage sine wave to the current sine wave. This value is normally plotted logarithmically (y-axis) due to the large range of impedance possible in EIS experiments and so that certain circuit behaviour can be observed in the plot. The frequency is also plotted logarithmically (0.001 – 100,000 Hz range) on the x-axis. Along with the phase (y-axis), this makes up a Bode plot, which is the customary way to plot impedance data [22] (see Chapter 4 for example plots). Impedance data can also be plotted as a Nyquist plot which is the real versus imaginary impedance. This data treatment has not been carried out as part of this research due to the ample conclusions that can be drawn from the Bode plot.

A Bode plot can provide sufficient information regarding the properties of a coated sample. For example, the magnitude of the phase part of the plot can give information about the properties of the coating in the electrolyte e.g. is the coating capacitive or resistive? In addition, the modulus of the impedance can tell us about how effective the coating is in the electrolyte, when compared against a reference i.e. a non-coated sample. The impedance at low frequency gives information about the coating resistance and the impedance at high frequency gives information about the electrolyte resistance [23]. Although EIS is non-destructive, the electrolyte could alter the sample surface over time, even before a measurement is completed. This source of error should be acknowledged when analysing impedance data.

2.3 Microscopy

In order to create a 2D representation of the sample surface at various magnifications, two types of microscopy were used: optical microscopy and scanning electron microscopy.

Image imperfections arise due to aberrations in the lens system. Astigmatisms and aberrations due to spherical and chromatic aberration can be corrected for, but it is more difficult for diffraction limits to be overcome. Because of lens aberrations, blurring occurs when signals from adjacent regions are mixed together [24]. The smallest distance that can be resolved (Δl) can be approximated to:

$$\Delta l \approx \frac{\lambda}{2\mathrm{NA}}, \tag{2.7}$$

where λ is the probe wavelength and NA is the numerical aperture. In scanning electron microscopy (SEM), the resolution limit is not related to the electron wavelength but the beam diameter. Signal to noise ratio (mostly random Poisson noise) and sample drift (movement of the sample) can also cause image imperfections.

2.3.1 Optical microscopy

Optical microscopy uses visible light to interact with the specimen of interest. All signals resulting from the interaction of visible light with the object are processed and magnified by a lens to produce the image. Filters and diffraction objectives can also be used. In this work, compound optical microscopes were used in reflection mode: images were collected on a Nikon SM2800 microscope (Universiteit Gent).

2.3.2 Scanning electron microscopy

Scanning electron microscopy uses electrons to produce an image of high magnification through interaction of electrons with a conductive sample. The image is formed by moving the electron beam in synchronised raster scans. The signal resulting from the object-electron interaction goes to a detector and is subsequently amplified to prevent the loss of signal. An example SEM image is shown in Figure 2.6.

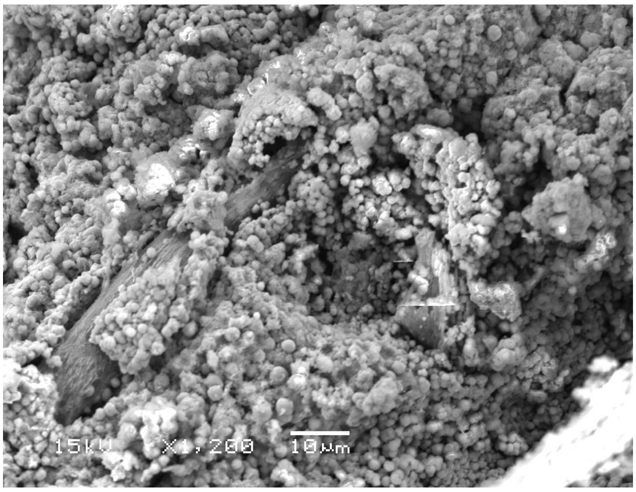

Figure 2.6 SEM image of the corroded surface of an iron anchor from the Mary Rose recorded by the author using the Trust's JEOL JSM-6610LV microscope

The probe used in SEM is an accelerated electron beam. Momentum is imparted onto the electron by accelerating it through a potential difference drop V (the accelerating voltage of the microscope) to give the desired wavelength, λ [25] (m is the electron mass and e is the charge on the electron). This is described by the de Broglie equation:

$$\lambda = \frac{h}{\sqrt{2meV}}. \tag{2.8}$$

In the optical column of the SEM, electrons are extracted from a sharp-tipped electron source using a high electric field [24]. Good electron sources must have a low work function, and are heated to reduce the work function further due to thermionic emission (e.g. LaB_6). Scanning electron microscopes use magnetic lenses to focus the electron beam.

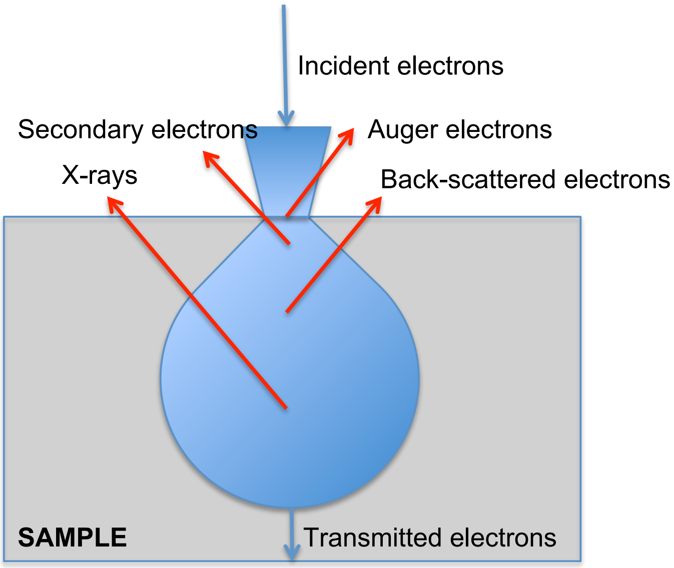

Figure 2.7 Signals resulting from the interaction of an electron beam with a sample.

Figure 2.7 describes the interaction volume resulting from the contact of the electron beam with a sample. The penetration depth of the electrons with the incident beam perpendicular to the surface is approximately equal to the diameter of the interaction volume, which determines the resolution and can be larger in size than the electron beam itself. Secondary and Auger electrons can only escape from the first few nm of the sample due to their low energy (<100 eV); backscattered electrons are higher in energy and can therefore escape from deeper in the sample. Backscattered electrons give information about atomic number contrast and surface orientation [24]. In this research, secondary electron images were collected to give information about the surface topography of coated samples. SEM images were collected on a ZEISS SUPRA 55-VP microscope (Department of Physics, University of Warwick) at 20 kV accelerating voltage.

2.4 Gas chromatography – mass spectrometry

In order to analyse the volatile organic compounds (VOCs) emitted from oak, GC-MS was used. In this technique, gas chromatography separates the molecular species and feeds them in a time sequence according to their transport rate in the GC column to the mass spectrometer for characterisation based on fragmentation patterns and mass of the ions. Additionally, species can be characterised based on their chromatographic retention.

In gas chromatography, the gas (mobile phase) passes through a solid column (stationary phase) and the interaction of the mobile phase with the stationary phase determines the separation of the gas mixture. The analytes within the mobile phase are transported using an inert carrier gas (e.g. helium) through the column. Molecules are separated as they dissolve and re-dissolve with different frequencies in the stationary phase [26]. Molecules with a higher vapour pressure will have a higher concentration of molecules in the gas phase than the stationary phase, and will therefore move through the column more rapidly. By tuning the column temperature, the vapour pressures can be changed. In addition the separation characteristics can be controlled by the properties of the column: its diameter, length, and the chemical composition of the stationary phase. For example, a polar stationary phase (containing ionic headgroups for example) will reduce the vapour pressure of polar solutes through additional intermolecular bonding.

Once the separated molecules reach the detector (the mass spectrometer) they enter a vacuum. For the coupling of the GC to the MS side, there must be a sufficient pressure drop through the column. This can be achieved by a long column (up to 30 m) [26].

A mass spectrometer consists of an ion source, mass analyser and detector [27]. The ion source ionises the molecules in order of arrival at the MS side. The resulting ion fragments are separated by their mass-to-charge ratios typically in a quadrupole mass filter. A mass spectrum then displays the abundance of the ions as a function of the mass-to-charge ratio. This allows the molecule to be characterised by its fragmentation pattern or (more simply) the weight of its most abundant ion.

In this work two GC-MS instruments were used: a SCION-SQ^{TM}, Bruker (School of Engineering, University of Warwick) and an Agilent 6890 GC equipped with an Agilent 5973 MS (Department of Organic Chemistry, Universiteit Gent). Using the integrated software and NIST databases, volatile organic molecules from oak could be characterised.

2.5 References

[1] P. Atkins, J. De Paula, Physical Chemistry, 8th ed., Oxford University Press, Oxford, 2006.

[2] C. Suryanarayana, M. Grant Norton, X-Ray Diffraction: A Practical Approach, Plenum Press, New York, 1998.

[3] G. Margaritondo, A Primer in Synchrotron Radiation: Everything You Wanted to Know about SEX (Synchrotron Emission of X-rays) but Were Afraid to Ask., Journal of Synchrotron Radiation. 2 (1995) 148–54.

[4] S.D. Brown, L. Bouchenoire, D. Bowyer, J. Kervin, D. Laundy, M.J. Longfield, D. Mannix, D.F. Paul, A. Stunault, P. Thompson, M.J. Cooper, C.A. Lucas, W.G. Stirling, The XMaS beamline at ESRF: instrumental developments and high-resolution diffraction studies, Journal of Synchrotron Radiation. 8 (2001) 1172–1181.

[5] S. Nikitenko, A.M. Beale, A.M.J. van der Eerden, S.D.M. Jacques, O. Leynaud, M.G. O'Brien, D. Detollenaere, R. Kaptein, B.M. Weckhuysen, W. Bras, Implementation of a combined SAXS/WAXS/QEXAFS set-up for time-resolved in situ experiments., Journal of Synchrotron Radiation. 15 (2008) 632–40.

[6] P. Willmott, An Introduction to Synchrotron Radiation, 1st ed., John Wiley & Sons, Ltd, Chichester, UK, 2011.

[7] C. Chantler, C. Tran, D. Paterson, Monitoring fluctuations at a synchrotron beamline using matched ion chambers: 1. modelling, data collection, and deduction of simple measures of association, X-Ray Spectrometry. 29 (2000) 449–458.

[8] B. He, U. Preckwinkel, K. Smith, Fundamentals of two-dimensional X-ray diffraction (XRD2), Advances in X-Ray Analysis. 43 (2000) 273–280.

[9] M. Dowsett, A. Adriaens, B. Schotte, G. Jones, L. Bouchenoire, In-situ spectroelectrochemical study of the growth process of a lead decanoate coating as corrosion inhibitor for lead surfaces, Surface and Interface Analysis. 41 (2009) 565–572.

[10] K.B. Oldham, J.C. Myland, A.M. Bond, Electrochemical Science and Technology: Fundamentals and Applications, 1st ed., John Wiley & Sons, Ltd, Chichester, UK, 2011.

[11] M.G. Dowsett, A. Adriaens, Cell for simultaneous synchrotron radiation X-ray and electrochemical corrosion measurements on cultural heritage metals and other materials., Analytical Chemistry. 78 (2006) 3360–5.

[12] C. Degrigny, Use of electrochemical techniques for the conservation of metal artefacts: a review, Journal of Solid State Electrochemistry. 14 (2009) 353–361.

[13] M. Dowsett, A. Adriaens, EC188 Final Report: Time-resolved XRD and XAS for the conservation / protection of heritage and other metals using XMaS, 2011.

[14] P.C. Milner, Interpretation of Measurements of Potential Decay on Open Circuit, Journal of The Electrochemical Society. 107 (1960) 343.

[15] D. Watkinson, Preservation of Metallic Cultural Heritage, in: T.J.A. Richardson, B.R.A. Cottis, R. Lindsay, S. Lyon, D.J.D. Scantlebury, H. Stott, M. Graham (Eds.), Shreir's Corrosion, Volume 4, Elsevier, Amsterdam, 2009: pp. 3307–3340.

[16] E. Rocca, F. Mirambet, The electrochemical techniques for the diagnosis and restoration treatments of technical and industrial heritage: three examples of metallic artefacts, Journal of Solid State Electrochemistry. 14 (2009) 415–423.

[17] J.C. Coelho, C.M. Oliveira, M.D. Carvalho, I.T.E. Fonseca, The efficiency of electrochemical methods for the removal of chloride ions from iron marine archaeological objects: A comparative study, Materials and Corrosion. 65 (2014) 38–44.

[18] A. Doménech-Carbó, V. Costa, M.T. Doménech-Carbó, Electrochemistry in Treatment and Conservation of Metal Artifacts, in: A. Doménech-Carbó, M.T. Doménech-Carbó, V. Costa (Eds.), Electrochemical Methods in Archaeometry, Conservation and Restoration, Springer Berlin Heidelberg, Berlin, Heidelberg, 2009: pp. 135–140.

[19] A. Doménech, M.T. Doménech-Carbó, H.G.M. Edwards, Quantitation from Tafel analysis in solid-state voltammetry. Application to the study of cobalt and copper pigments in severely damaged frescoes., Analytical Chemistry. 80 (2008) 2704–16.

[20] A. Elia, Application of electrochemical methods for the study and protection of heritage copper alloys, PhD thesis, Universiteit Gent, 2013.

[21] A.J. Bard, L.R. Faulkner, Electrochemical methods: fundamentals and applications, Wiley, New York, 1980.

[22] D. Loveday, P. Peterson, B. Rodgers, Evaluation of Organic Coatings with Electrochemical Impedance Spectroscopy Part 1 : Fundamentals of Electrochemical Impedance Spectroscopy, JCT CoatingsTech. (2004) 46–52.

[23] D. Loveday, P. Peterson, B. Rodgers, Evaluation of Organic Coatings with Electrochemical Impedance Spectroscopy Part 2 : Application of EIS to Coatings, JCT CoatingsTech. (2004) 88–93.

[24] P.J. Goodhew, J. Humphreys, R. Beanland, Electron Microscopy and Analysis, CRC Press, London and New York, 2000.

[25] C.E. Hall, Introduction to Electron Microscopy, 2nd ed., McGraw-Hill, USA, 1966.

[26] W. Jennings, Analytical Gas Chromatography, Academic Press INC, Orlando, Florida, 1987.

[27] J.H. Gross, Mass Spectrometry, Springer, Berlin, Heidelberg, 2011.

Chapter 3 – Synthesis and spectroelectrochemical analysis of lead carboxylates

3.1 Introduction

Lead carboxylates have two very contrasting effects: in one case they can protect a lead surface from attack by atmospheric pollutants; in the other they are the scourges of the painting conservator. In this chapter three lead carboxylates are synthesised and characterised spectroelectrochemically. Then, using the electrochemical information collected, the viability of voltammetry as a method for finding lead soaps in oil paint samples is assessed.

3.1.1 Synthesis and spectroelectrochemical analysis of metal carboxylates

Metal carboxylates are composed of a metal ion bound in coordination to one or more carboxylic acid groups. The resulting compound is ambiphillic: the carbon chain being hydrophobic while the metal ion head has the ability to attract water molecules [1].

The compounds can be synthesised in a variety of ways. The easiest and most common method is precipitation using aqueous solutions of metal salts and the sodium carboxylate of interest [2–4]. In oil paintings, lead carboxylates are also produced by a precipitation reaction, although the carboxylate source is unreacted fatty acids within the oil binder [5–8], and the reactive lead salt can be a lead or lead-tin pigment e.g. red lead, lead white or lead-tin yellow (see Table 3.2 for chemical details). This reaction can be observed at room temperature over a period of months [9] or can be tracked over 2 hours by heating to 100°C [10].

Hydrothermal synthesis at high pressure can also produce metal carboxylates with higher purity [3,11].

The physical properties of metal carboxylates have been widely reported due to the application of these compounds in colloidal chemistry and associated industries. Although not relevant to this thesis, the liquid crystal properties of melted metal carboxylates have been studied in depth, especially regarding the changing crystalline phases with temperature [12,13]. At room temperature, characterisation of metal carboxylates has been carried out using a variety of analytical techniques in connection to the compound's presence in oil paintings [2,4,9,10,14,15].

The structures of smaller-chain carboxylates [16,17] and diacids [2] have been solved from single crystals, but due to the difficulty to produce single crystals of longer chain carboxylates X-ray diffraction patterns of crystalline products can only be used to approximate the unit cell size. There is often a large discrepancy in c-axis length (the longest side of the unit cell, consisting of the length of two carbon chains and the metal ion) between various results [2,3,11]. This issue will be addressed in the following work.

The reaction of the carboxylic acid functionality with metal ions causes a change in carbon-oxygen bonding structure, which can be detected by infrared (IR) spectroscopy [10,18,19]. IR spectroscopy can therefore be a useful tool to check the completion of the reaction between the metal ion and the acid.

3.1.2 Lead soap identification in oil paintings

Lead carboxylates (also known as lead soaps) are formed in oil paintings and cause large, white surface protrusions. These protrusions are invariably thought of as a sign of deterioration in the paint film but their origins are not wholly understood as they do not form on all paint surfaces containing the correct 'ingredients' for soap formation. Conditions of storage [20] and previous conservation treatments [21] have been cited as reasons for formation.

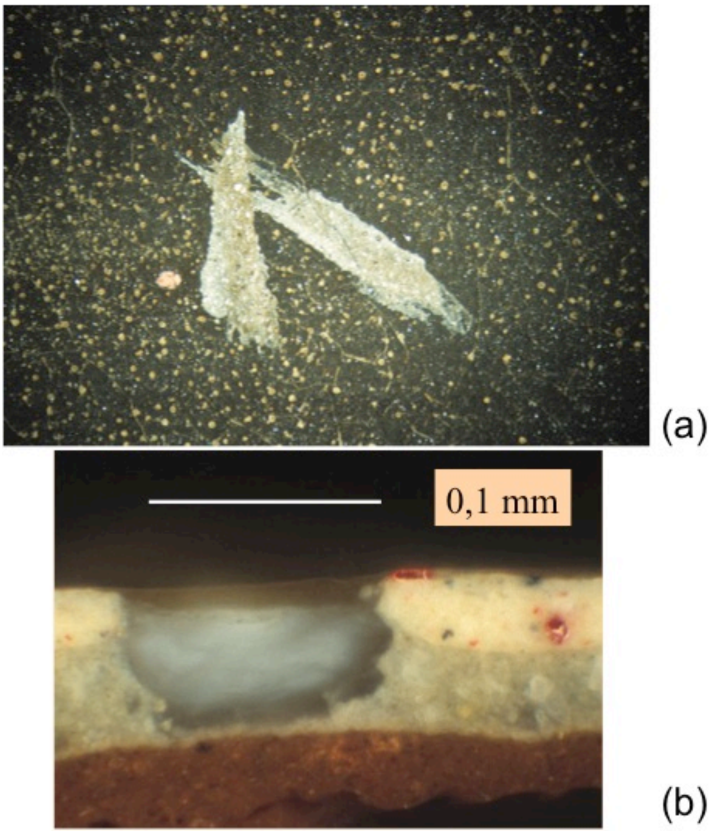

Figure 3.1 Lead soaps from a 1632 canvas painting by Rembrandt, *De anatomische les van Dr Nicolaes Tulp*: (a) is a macrophoto of lead soap protrusions in the far left of the canvas (no scale given) and (b) shows the microscope image of a cross section taken from the painting. The opaque well is the lead soap. (Image credit: Petria Noble, Mauritshuis, The Hague)

The most common method of identifying the presence of lead soaps within oil paintings is optical microscopy of painting cross sections removed from the painted layer. Figure 3.1 shows an example of such a cross section. The white, transparent colour of lead soaps and the smooth texture of the protrusions makes them easy to differentiate from pigment particles and oil medium [21–23]. In addition, secondary ion mass spectrometry (SIMS) and FT-IR maps of the cross sections can be used to verify this characteristic 'texture' [5,15,24,25] by targeting ions or specific bond vibration frequencies specifically found in lead carboxylates.

Electrochemical techniques have been studied for the identification of pigments but not metal carboxylates. Voltammetric analysis of microparticles (VMP) taken from facsimiles or actual paint samples has been successful in studying the difference in voltammetric signal between pigments containing the same element [26–30]. In this chapter, VMP will be trialled as a possible lead soap identification method using synthesised lead carboxylates commonly found in oil paintings [2,4,14,15].

3.2 Experimental

Lead ditetradecanoate, lead dihexadecanoate and lead dioctadecanoate were prepared from their constituent acids (Table 3.1) and characterised in various ways.

3.2.1 Synthesis

Table 3.1 Long-chain carboxylic acids and abbreviations used in this work.

Carbon atoms	Common name	IUPAC name	Chemical formula	Short formula in text	Short formula for coating in text
14	Myristic acid	Tetradecanoic acid	$CH_3(CH_2)_{12}COOH$	C14	$Pb(C14)_2$
16	Palmitic acid	Hexadecanoic acid	$CH_3(CH_2)_{14}COOH$	C16	$Pb(C16)_2$
18	Stearic acid	Octadecanoic acid	$CH_3(CH_2)_{16}COOH$	C18	$Pb(C18)_2$

The lead carboxylates were made using a precipitation method. Lead acetate trihydrate ($Pb(CH_3COO)_2.3H_2O$, 1 g, Merck, Germany, 2.6 mMol, 1 eq., dissolved in 15 mL of deionised (DI) water) was added to the required carboxylic acid (2 eq., dissolved in 100 mL ethanol, VWR Belgium). On mixing a white precipitate immediately formed. The resulting crystals were filtered, rinsed with ethanol and DI water and dried in air.

3.2.2 Instruments

The lead carboxylates were characterised by infrared spectroscopy (Perkin-Elmer Spectrum1000 with HATR cell, Pike Technologies), elemental analysis (Thermo Flash 2000 CHN analyser) and powder X-ray diffraction (ARL X' TRA Powder Diffractometer).

Voltammetric analysis of glassy carbon-mounted samples was carried out using a PGSTAT20 potentiostat with GPES software version 4.9 (Autolab, Eco Chemie B.V., The Netherlands). A three-electrode set-up was used: a working electrode (details below), a AgCl/Ag reference electrode (Radiometer Analytical, France) and a carbon counter electrode immersed in an acetic acid buffer (pH 5.5, 5 mg L^{-1}). Cyclic voltammograms were collected from 0 – -1 V with a scan rate of 5 mV/s. Measurements were repeated three times.

3.2.3 Sample preparation (voltammetry)

Working electrodes

Several commercially available and custom-made glassy carbon electrodes (GCEs) were trialled. Finally a custom-made GCE (8 mm ⌀) encapsulated in epoxy resin and secured with a brass thread was tested. This working electrode was chosen due to the large surface area of the electrode and secure electrical connection between the glassy carbon and the output.

Reference samples

The voltammetric response of lead soaps was measured by depositing samples on to a glassy carbon surface on the selected electrode. This was first polished using a MicroCloth® impregnated with 1 μm alumina (both Buehler, USA). The surface was then rinsed with DI water and dried using a TechniCloth (Texwipe, USA) in preparation for the dispersion of reference samples.

The samples were prepared by suspending approximately 10 mg of the lead carboxylate powder in 1 mL ethanol inside a sample tube (Eppendorf, Germany). The tubes were then placed in an ultrasonic bath for one minute to break up larger particles and disperse the insoluble carboxylate in the solution. Reference samples for some important lead-containing pigments were measured in the same way. Details of the reference chemicals used are described in Table 3.2.

Table 3.2 Lead pigments commonly found in oil paintings.

Compound	***Abbreviation***	***Supplier***
Lead oxide (PbO)	PbO	UCB, Belgium
Basic lead carbonate or lead white $(PbCO_3)_2.Pb(OH)_2)$	PbWh	VWR, Belgium
Minium or red lead (Pb_3O_4)	Min	Kremer, Germany
Lead tin oxide (Pb_2SnO_4)	PbSn	Kremer, Germany

Using a micropipette (Eppendorf, Germany), 2 μL of the suspension was delivered to the centre of the glassy carbon electrode. The ethanol was left to dry in air leaving a thin layer of particles on the glassy carbon. Larger volumes of suspension were attempted (100 μL, 20 μL) but in these cases the film was repelled from the glassy carbon surface and simply dried on the epoxy resin casing.

Paint facsimiles

A paint facsimile is a sample which aims to reproduce the contents and characteristics of paint. The main difference between the reference samples and paint facsimiles is the addition of an artists' oil to possibly recreate the conditions of an oil paint and lead soap formation.

Paint facsimiles were prepared using oil absorption parameters [31] (Table 3.3). The oil (1 g) was added to 0.15 g of each lead pigment. The paints were ground for 1 minute using a pestle and mortar then spread thinly on glass slides and left to dry for 1 month.

Table 3.3 Examples of oil absorption parameters for lead-containing pigments

Name	***Chemical formula***	***Oil Absorption (wt/100 wt)***	***Suggested oil***	***Reference***
Basic lead carbonate, lead white	$2PbCO_3.Pb(OH)_2$	11-15	Linseed or walnut	[31]
Lead-tin yellow	Pb_2SnO_4	15-25	Linseed or walnut	[32]

After this drying period, IR spectroscopy was performed to check the reaction of carboxylate groups in the paint. A small flake of paint (10 mg) was removed from the glass slide using a spatula, was suspended in ethanol and sonicated for 5 minutes to break up the sample. Then 2 μL of the suspension was delivered to the glassy carbon surface and left to dry for 1 minute before testing using the same electrochemical parameters as used for the reference chemicals.

In order to improve characterisation of the lead components in the paint layers, the layers were swollen after drying. Swelling of the paint layer using an organic solvent causes the paint structure to break down due to leaching of soluble oil components. In an electrochemical sense, this should facilitate better penetration of the electrolyte into the film resulting in an improved signal from electroactive components. When the paint samples were dried, the holder was dipped into 10 mL xylene (99.9 %, UCB, Belgium) for 10 minutes to allow sufficient time for the solvent to act on the layer [33]. The layer was then dried for 24 hours prior to testing.

3.3 Results and discussion

3.3.1 Synthesis

On combination of the Pb^{2+} solution (acetate salt) and the ethanolic carboxylate in a 1:2 ratio, the soap forms instantaneously and precipitates out of the solution. The formation of this 1:2 complex is consistent with charge neutralisation [12]. When this occurs, the solvent is a mix of ethanol (solvent for the carboxylic acid) and a small amount of water (solvent for the lead salt), so it is possible that some carboxylic acid precipitates out of the solution due to its hydrophobicity. However due to the strong electrostatic interaction between Pb^{2+} and the carboxylate [1] and the high stability of the complex due to the long carbon chain, the precipitation of unreacted carboxylate is minimal.

Previously, the association of the complex has been described as a two-step process involving the reaction of Pb^{2+} in aqueous solution with the two dissociated carboxylate anions C_nCOO^- consecutively [1]. One can look more closely at the dissociation of these species in ethanol by studying the pK_a values of the acids. Ethanol has a similar pK_a value to water [34] (pK_a 15.9) so the pK_a values for the acids (usually calculated in water) can be approximated to the standard values.

Increasing the chain length of carboxylic acids from C14 to C18 has little effect on the pK_a values so the pK_a of C14 – C18 can be approximated to 4.94 – 4.96 [35]. The dissociation of tetradecanoic acid in ethanol and the subsequent pK_a equations are shown below:

$$CH_3(CH_2)_{12}COOH + EtOH <-> CH_3(CH_2)_{12}COO^- + EtOH_2^+ \tag{3.1}$$

$$K = [EtOH_2^+][CH_3(CH_2)_{12}COO^-]([CH_3(CH_2)_{12}COOH][EtOH])^{-1} \tag{3.2}$$

$$pK_a\,(C14) = pK_a\,(EtOH) + \log\,([CH_3(CH_2)_{12}COO^-]/[CH_3(CH_2)_{12}COOH]) \tag{3.3}$$

$$[CH_3(CH_2)_{12}COO^-]/[CH_3(CH_2)_{12}COOH] = 1.1\text{x}10^{-11} \tag{3.4}$$

In solution, the carboxylic acid reacts with ethanol (acting as a base) and dissociates to form the carboxylate ion and protonated ethanol (Equation 3.1); equilibrium constant, K (Equation 3.2) results. Using known pK_a values the ratio of concentrations at standard conditions can be calculated. Therefore at standard conditions, the acid is sometimes in a dissociated state in ethanolic solution and the association of the lead carboxylate complex can be assumed to proceed in a similar way as described in reference [1]. The weak dissociation of the acid is also evidenced by the low conductivity measured in such solutions (~ 1 μS).

3.3.2 Spectroscopic identification of lead carboxylates

Elemental analysis

In order to test the purity of the synthesised lead soaps, elemental analysis was carried out in a CHN analyser. This instrument uses dynamic flash combustion to break down the sample into simple compounds which are then separated by chromatography and quantified. Table 3.4 shows the results from elemental analysis and shows that the synthesis method for $Pb(C14)_2$, $Pb(C16)_2$ and $Pb(C18)_2$ is effective due to the low error (E%) between the theoretical (T%) and measured (M%) percentage weight. However, the error may exist due to the presence of some unreacted carboxylate (see also IR data). This could be prevented by additional purification or recrystallisation [36]. The presence of equal amounts of nitrogen in each sample could be background signals.

Table 3.4 Results from elemental analysis where T is the theoretical mass percentage, M is the measured mass percentage and E is the error on the measured mass based on theoretical prediction (E=(| T-M |/T).

Compound	MW	C%			H%			N%		
		T%	*M%*	*E%*	*T%*	*M%*	*E%*	*T%*	*M%*	*E%*
$Pb(CH_3(CH_2)_{12}COO)_2$	661.9	50.7	50.6	0.2	8.2	8.4	2.4	0	0.2	100
$Pb(CH_3(CH_2)_{14}COO)_2$	718.0	53.5	53.6	0.2	8.6	8.9	3.5	0	0.2	100
$Pb(CH_3(CH_2)_{16}COO)_2$	774.1	55.8	55.9	0.2	9.0	9.3	3.3	0	0.2	100

IR

Reference compounds for each lead carboxylate were synthesised as described. Infrared spectra were recorded from the starting materials (carboxylic acids) and the lead soaps. This method was chosen as a simple way of showing that the lead carboxylate had formed - the COO^- stretching doublet at 1514 cm^{-1} and 1420 cm^{-1} is characteristic of a bidentate ligand [37]. In previous work, IR spectra taken from a dodecanoate coated lead coupon show this same spectral feature [19].

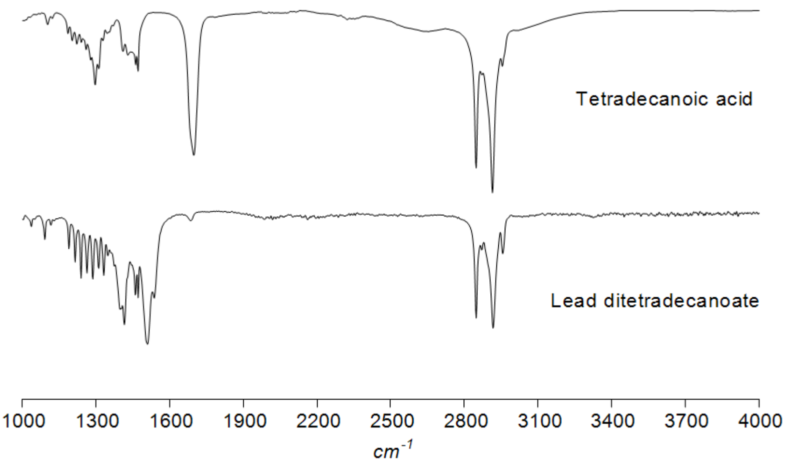

Figure 3.2 IR spectrum of Pb(C14)$_2$ and C14

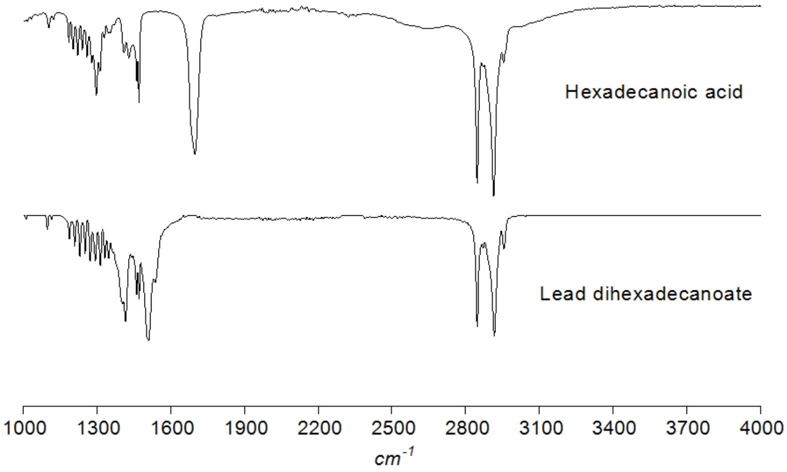

Figure 3.3 IR spectrum of Pb(C16)$_2$ and C16

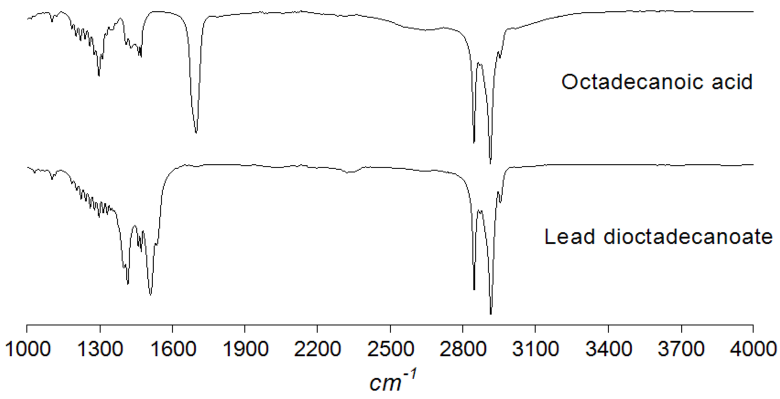

Figure 3.4 IR spectrum of Pb(C18)$_2$ and C18

Figures 3.2 - 3.4 show the IR results from the synthesised lead carboxylates and the corresponding starting materials. In all spectra, the four symmetric/asymmetric C-H stretching peaks at ~ 2900 cm^{-1} are present thus showing the long carbon chain plays no role in the carboxylate formation, and is relatively unchanged in the product. The carboxylate functionality gives most information about the complex formation. The carbon-oxygen double bond in the starting material disappears, demonstrating full complexation with the lead. Table 3.5 shows that the peaks in the IR spectra for differing complexes can barely be distinguished from each other because the carbon chain length has no effect on the stretching characteristics of the carboxylate moiety. A small peak for C=O in the $Pb(C14)_2$ and $Pb(C18)_2$ spectra shows that some acid was unreacted, despite the fact that the product had been rinsed repeatedly with ethanol. The presence of a small amount of acid could explain the errors in the elemental analysis.

Table 3.5 C-O stretching band characterisation.

	C=O stretch, cm^{-1}	**ΔνC-O, cm^{-1}**	**Form of complex**
$Pb(C18)_2$	1699	94.46	Bidentate
$Pb(C16)_2$	1699	95.06	Bidentate
$Pb(C14)_2$	1699	95.06	Bidentate

XRD

Figure 3.5 shows the XRD pattern of a tetradecanoate coated lead coupon measured on the PANalytical X-ray diffractometer. The fifteen peaks with a uniform spacing of 0.156 Å^{-1} are the even reflections in the series 002, 004, …, 0030 etc. which arise because the c-axis d-spacing is much larger than one wavelength. The odd reflections have a much lower intensity and the 001 peak is not visible, probably because of surface roughness. Although no comparably high quality reference pattern for this compound can be found, Figure 3.5 shows a reasonable similarity to International Centre for Diffraction Database (ICDD) reference no. 00-049-1964 (lead tetradecanoate) and strong qualitative similarity to ICDD references for other long chain lead carboxylates such as lead hexadecanoate (No. 00-055-1624) and octadecanoate (No. 00-055-1625). Work on fully indexing this pattern is incomplete, but the reflections labelled with asterisks between 1.4 and 1.8 Å^{-1} are probably higher order reflections from the lead tetradecanoate lattice rather than from residual tetradecanoic acid [38].

The same compounds formed as coatings were synthesised and characterised. Figure 3.6 shows the X-ray diffraction patterns for the three lead carboxylates. The characteristic 0.156 Å^{-1} spacing between peaks of the Pb(C14)$_2$ carboxylate is present in the powder and the coating, showing the similarity between the crystalline structure in coating and powder form.

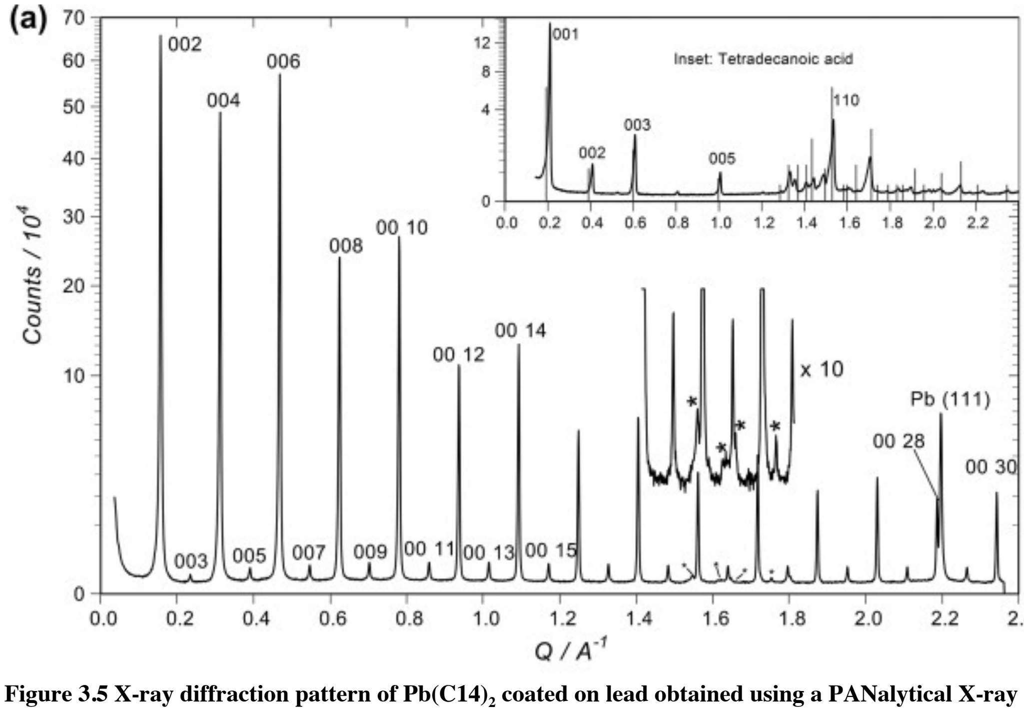

Figure 3.5 X-ray diffraction pattern of Pb(C14)$_2$ coated on lead obtained using a PANalytical X-ray diffractometer at the University of Warwick

In the powder diffraction patterns, the odd reflections are not observed, possibly due to the different instrumental setup. The spacing between peaks decreases with increasing carbon chain length: 0.1375 Å^{-1} and 0.125 Å^{-1} for the hexadecanoate and octadecanoate salt respectively. This is in line with the corresponding increase in the c-axis of the complex as carbon chain length increases.

Although the odd peaks or the 002 peak in $Pb(C18)_2$ and $Pb(C16)_2$ patterns cannot be seen, the size of the unit cell can still be deduced by calculating the 001 reflection. In previous studies, this reflection has commonly been forgotten in calculations of unit cell size [39] leading to many incorrect estimations for this value. By reducing the 004 reflection by 1.5 times the spacing, and calibrating to d-space, this would equate to the unit cell size in the c-direction as shown in Table 3.6. This calculation would not be correct if the first peak was assumed to be the 001 peak because the lattice parameter would not be equal at all reflections according to Equation (3.5) [40].

$$a = \frac{\lambda}{2\sin\theta}\sqrt{h^2 + k^2 + l^2} \tag{3.5}$$

Table 3.6 Unit cell length, c, calculations.

	q-space/Å^{-1}			Unit cell length, Å
	004	*Even peak spacing*	*001*	*001*
Pb(C18)$_2$	0.253	0.125	0.0660	95.2
Pb(C16)$_2$	0.280	0.140	0.0703	89.4
Pb(C14)$_2$	0.314	0.159	0.0760	82.7

At q-space higher than 1.5 Å^{-1}, the evenly spaced pattern stops, due to inward scattering of X-rays. The remaining unindexed peaks refer to reflections from the a/b direction and are common for all lead carboxylates because the determining functional group for these axes are common for all synthesised compounds i.e. the lead carboxylate functionality.

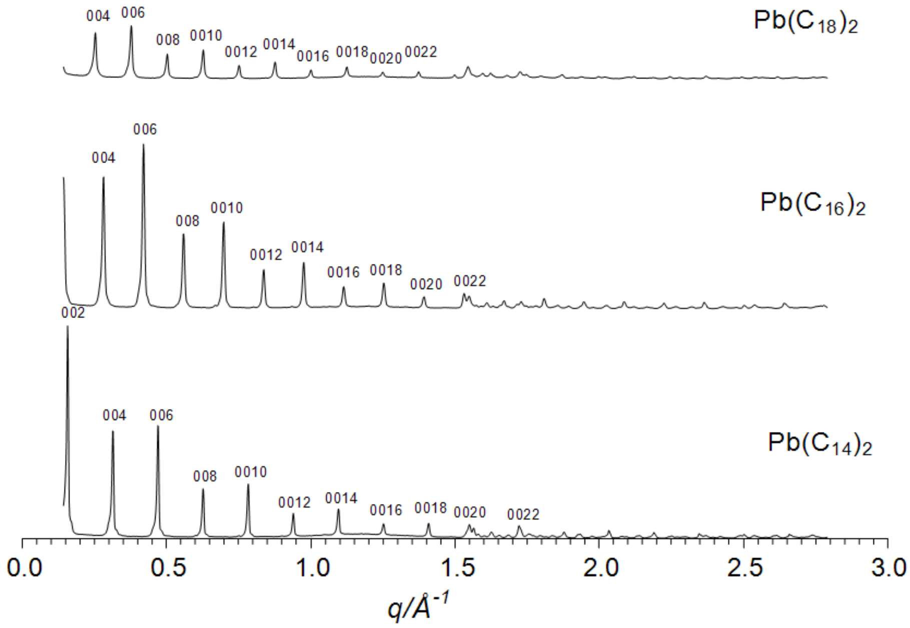

Figure 3.6 XRD patterns for all synthesised lead carboxylates

Figure 3.7 shows the diffraction patterns obtained from the starting carboxylic acids. These patterns have been indexed (ICDD Numbers 008-0806, 003-0250 and 038-1923 for C14 to C18 respectively). Compared to the lead complex, a similar pattern of uniform spacing between the first three peaks is observed. The first and third peaks correspond to the 001 and 003 reflections, whereas the second, smaller peak corresponds to the 002 reflection. In fact, this pattern continues for two further detectable reflections: reflection 004 is visible barely in the C18 pattern. A decrease in the peak heights of the even c-axis reflections is observed corresponding to the decreased distance travelled by scattered X-rays of higher q-spacing. The uniform spacing observed in the first 3 peaks is higher compared to the associated lead carboxylate due to the lack of complexation. As with the lead carboxylates, the spacing (corresponding to a lower c-axis length and therefore molecular size) decreases with increasing carbon chain length. The peaks at 1.5 and 1.7 Å^{-1} are common for all the carboxylic acids and are reflections from the a or b axes perpendicular to the long c-axis.

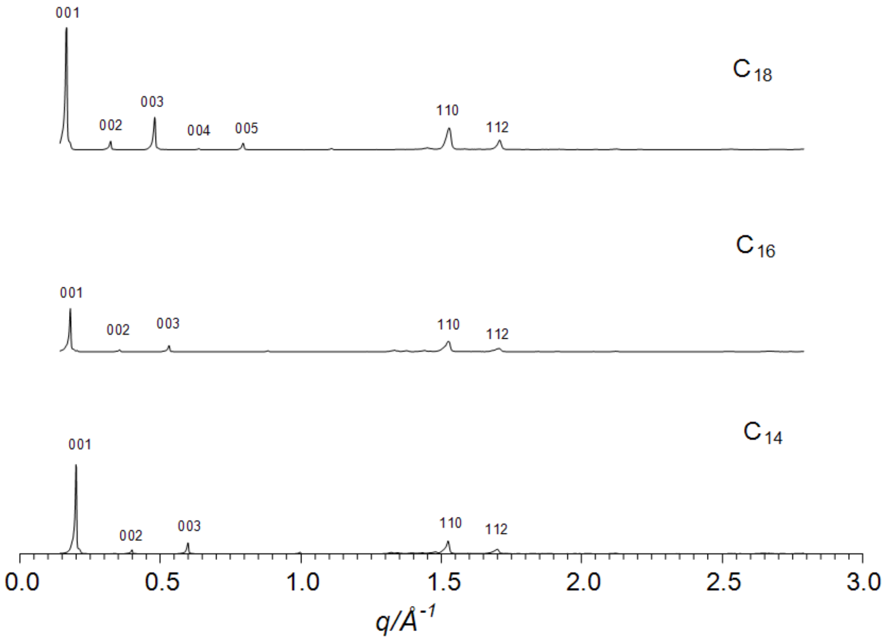

Figure 3.7 XRD patterns of unreacted carboxylic acids C14 – 18

3.3.3 Voltammetric identification of lead carboxylates

An acetic acid buffer (pH 5.5, 5 mg L^{-1}) was used for identification purposes only, not to simulate a particular environment. The buffer provides a relatively low pH thus favouring the proton-assisted reduction processes of lead compounds. Also the electrolyte has a high enough ionic strength and a sufficiently stable pH to give a reproducible voltammetric response. A range of 0 - -1 V was used in order to study the oxidation of lead (II) compounds without over-oxidation to form lead (IV) oxides [41].

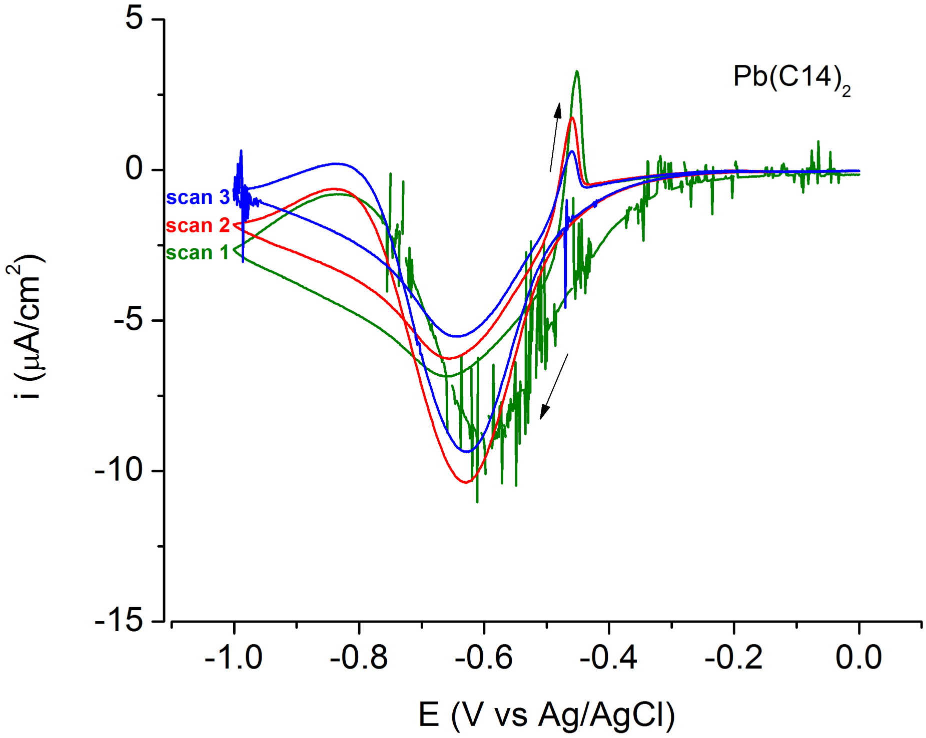
Pb(C14)$_2$
scan 3
scan 2
scan 1
5
0
-5
-10
-15
i (μA/cm^2)
-1.0
-0.8
-0.6
-0.4
-0.2
0.0
E (V vs Ag/AgCl)

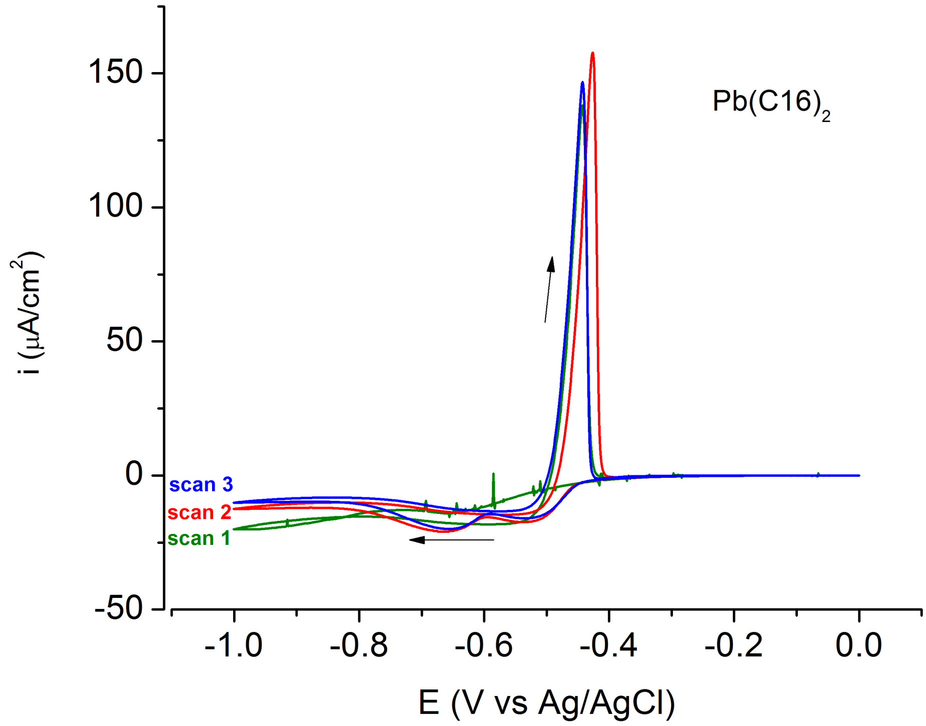
Pb(C16)$_2$
scan 3
scan 2
scan 1
150
100
50
0
-50
i (μA/cm^2)
-1.0
-0.8
-0.6
-0.4
-0.2
0.0
E (V vs Ag/AgCl)

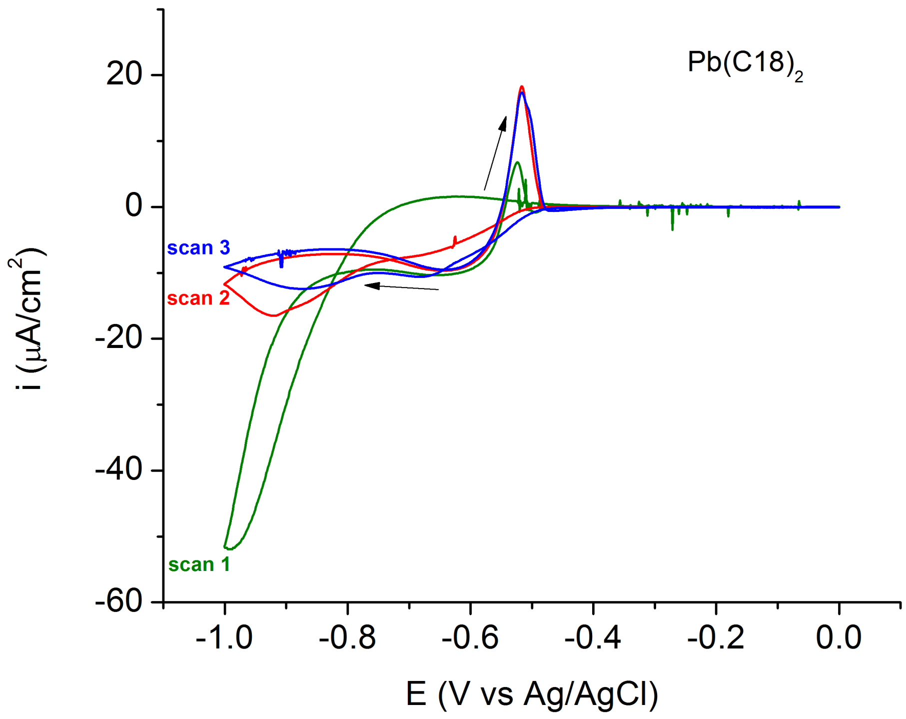

Figure 3.8 Cyclic voltammograms of lead carboxylates in an acetic acid buffer.

Figure 3.8 shows three consecutive voltammograms of all the synthesised lead carboxylates. The CVs show a broad reductive peak which corresponds to the reduction of the lead carboxylate to lead metal. The CVs show a single distinctive oxidation peak at around -0.45 V corresponding to the reaction in the following electrochemical equation, which uses lead ditetradecanoate as an example [42].

$$Pb_{(s)} + 2CH_3(CH_2)_{12}COOH_{(s)} \rightarrow Pb(CH_3(CH_2)_{12}COO)_{2\ (s)} + 2H^+_{\ (aq)} + 2e^- \qquad (3.6)$$

Although Pb(C14)$_2$ and Pb(C16)$_2$ show very similar oxidation peaks, Pb(C18)$_2$ has the most negative oxidation peak potential compared to Pb(C14)$_2$ and Pb(C16)$_2$. This could be an indication of the lesser stability imparted by the longer chain carboxylate, although the $Pb(C16)_2$ does not show an intermediate value between $Pb(C14)_2$ and $Pb(C18)_2$. After the oxidation peak (-0.4 – 0 V), the current drops to a value close to zero. This corresponds to a passive state at which no reactions occur [42].

For all lead carboxylates the oxidation peaks are narrow (0.05 V width) whereas the reduction peaks are broad and flat. The peak position, height and peak area do not change to a great extent over the course of three scans. $Pb(C16)_2$ gave the clearest results, possibly due to the superior quality of layer formed on the GCE. This may also explain why equal reductive and oxidative peak areas were found for $Pb(C16)_2$ only.

Cyclic voltammetry of the lead carboxylates can provide an initial indication of the stability of the compounds compared to other Pb(II) compounds. Figure 3.8 shows that after 3 successive CV scans, $Pb(C16)_2$ still gives a reproducible peak at approximately -0.45 V, 150 $\mu A\ cm^{-2}$. This is due to the insolubility of the soap film on the GCE. The reproducibility of the signal during several cyclic voltammetric scans could also suggest that the complex would perform well as a coating.

In comparison to their respective lead soaps, unreacted carboxylates (in oil or pure substances) would not have a measurable voltammetric response within this potential range, and previous work showed that the anodic oxidation peak is indeed small [43], thus being less useful for characterisation. However, if necessary IR spectroscopy can be used to identify these unreacted components as previously discussed.

3.3.4 Assessment of voltammetry as a method for lead soap identification

With cyclic voltammetric data from lead carboxylates, it is possible that preparing and measuring a paint sample in the same way could lead to the identification of these compounds within the sample. In order to test this hypothesis, a range of lead pigments was similarly measured and studied to determine whether differentiation between lead species is possible.

Most of the pigments do not show a reproducible signal during the course of the three consecutive scans. The progression of signals is clearly different compared to the lead carboxylates. For example, in Figure 3.9 the height of the peaks of lead white (PbWh) decreases by a factor of n^2 for each cycle observed. The reduction peak is 0.55 V wide and has an onset potential at -0.44 V, which could be due to the following reduction reactions occurring:

$$\mathrm{PbCO_{3\ (s)} + 2H^+_{\ (aq)} + 2e^- \rightarrow Pb_{\ (s)} + CO_{2\ (g)} + H_2O} \tag{3.7}$$

$$\mathrm{Pb(OH)_{2\ (s)} + 2H^+_{\ (aq)} + 2e^- \rightarrow Pb_{\ (s)} + 2H_2O} \tag{3.8}$$

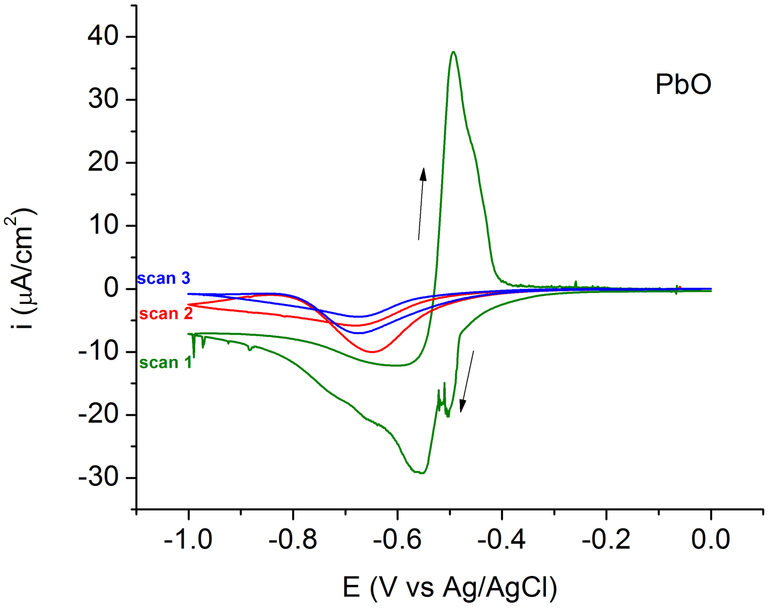
40
30
20
10
0
-10
-20
-30
i (μA/cm²)
-1.0
-0.8
-0.6
-0.4
-0.2
0.0
E (V vs Ag/AgCl)
PbO
scan 3
scan 2
scan 1

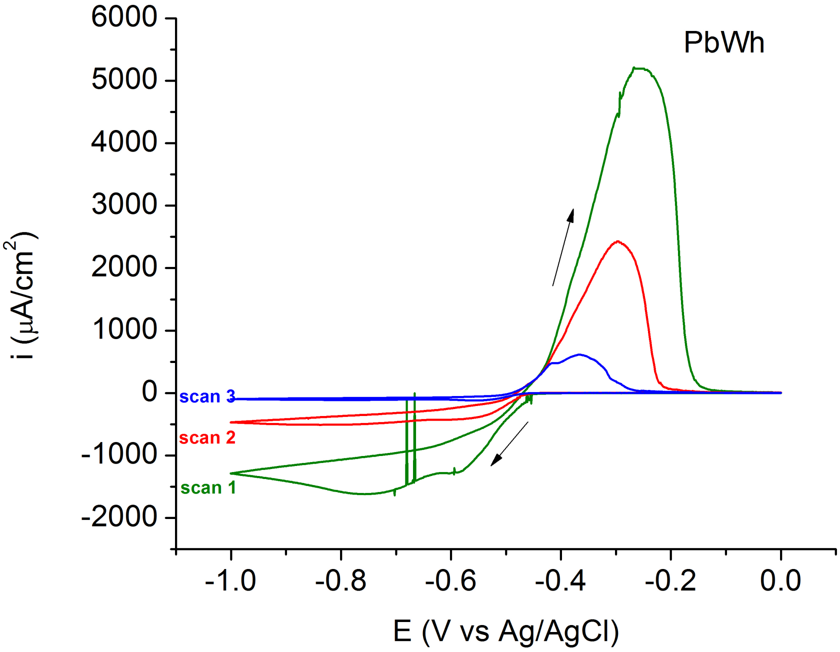
6000
5000
4000
3000
2000
1000
0
-1000
-2000
i (μA/cm²)
-1.0
-0.8
-0.6
-0.4
-0.2
0.0
E (V vs Ag/AgCl)
PbWh
scan 3
scan 2
scan 1

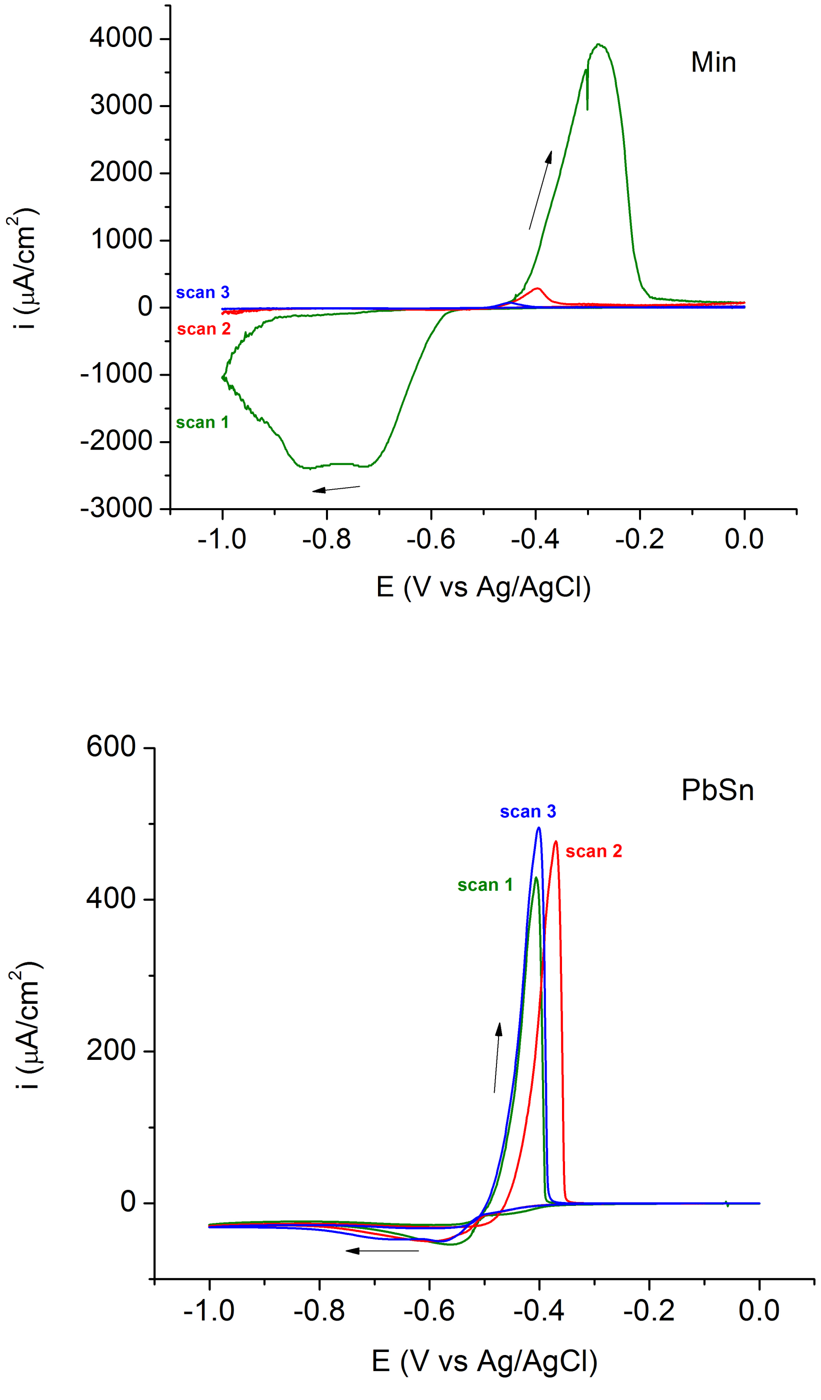

Figure 3.9 Cyclic voltammograms of lead pigments in an acetic acid buffer.

The difference between reactions (3.7) and (3.8) and reaction (3.6) is the formation of products which diffuse readily away from the electrochemically active surface: the reverse reduction reaction does not occur and the analyte is completely reduced to lead after scan 3. In addition, the production of gaseous carbon dioxide may cause swelling of the delicate GCE film, thus detaching particles of analyte from the surface and decreasing the electrochemical signal. The oxidation peak (onset 0.44 V, peak width 0.3 V) could correspond to the oxidation of lead by OH^- ions in solution [42]. Similar reactions must also occur in the minium and lead oxide sample because the CV trace is similarly irreproducible after the first scan. However, it is also possible that the acetic acid electrolyte is reacting with these pigments [44] to produce soluble products. The stability of the PbSn peaks is observed by the reproducible scans. This stability is due to the formation of a SnO_2 film which passivates the surface [45].

Cyclic voltammetric results for the lead carboxylates will now be compared with a range of other Pb(II) compounds which may be found in oil paintings [15]. All the compounds shown in Figure 3.9 are potentially targets for identification. Minium, lead-tin yellow and lead white are common pigments and precursors to lead soap formation [7,9,26], whereas lead oxide can be a precursor to lead soap formation through degradation of other oxide-containing pigments [46]. The peak heights (current densities) can be studied for this work due to the consistency in sample preparation. However, due to the dependence of current density on the concentration of the substance and quality of the sample, this parameter could not be used in the analysis of an unknown mixture such as a paint sample.

From studying Figures 3.8 and 3.9, two groups of compounds having similar voltammetric fingerprints can be formed (from the non-carboxylate reference compounds). In the first group, lead white and minium have large identifiable peaks with high current densities. In addition, the anodic and cathodic peaks have a larger peak separation than lead oxide and lead-tin oxide, these being

0.35 V and 0.5 V for lead white and minium respectively. Secondly, lead oxide and lead-tin oxide are less easily identifiable due to the small current density of the anodic and cathodic peaks. However, these compounds are characterised by a small peak separation.

Overall, the data show that two groups of compounds can be easily separated from the initial parameters described above. However, the identification of individual compounds may be less accurate. Comparing the lead reference compounds to the lead carboxylates, there is a similarity in the anodic peak for the carboxylates and lead oxide. Although when measured alone the carboxylates can be identified due to the broad reductive peak, a mixture of lead compounds in a sample would prevent this conclusion from being drawn.

The errors measured in this initial examination of the technique are due to the irreducibility of sample deposition onto the glassy carbon surface. This arises from separation of the mixture prior to deposition and uncontrolled spreading of the droplet. However these errors are smaller for certain pigment mixtures, such as lead-tin yellow.

Comparing this data to VMP results obtained by Doménech-Carbó *et al.* shows the sensitivity of peak data to the experimental conditions: the sample preparation techniques differ in their work [27]. One might speculate that this possibly causes different crystal orientations to be present in the sample, which leads to a difference in reactivity.

Most current pigment and lead soap identification practices involve the analysis of prepared cross sections using various analytical techniques [2,5,7,9,25,47]. These existing techniques and the method proposed use a very small amount of sample although with common methods the sample is embedded in resin for analysis, whereas this method uses a suspension of material in a chosen solvent. The encapsulation in resin ensures the longevity of the sample once it is removed from the painted surface. Although the cross sections may not appear visually damaged post-analysis, the interaction of electromagnetic radiation of varying energies with the sample will alter the sample at some level. The technique of voltammetry proposed here is destructive, although the extent of destruction compared to other techniques has not been analysed.

3.3.5 Assessment of voltammetry as a method for lead soap identification – testing a paint facsimile

A test was devised to compare the reference data from lead-containing pigments with pigments in a paint facsimile, in order to further investigate the effectiveness of this technique. A sample of lead white and walnut oil was prepared (Table 3.3), left to dry for one month then swollen in xylene. IR spectroscopic data from this dry sample showed that no lead soaps had formed during this time. This was entirely expected because the appearance of lead soaps in oil paintings is unpredictable and has been observed in time scales from weeks to decades [2,5,7,8,10]. Although lead soaps had not formed in the facsimile, the preparation and testing of this sample is still important to examine the viability of the technique for detecting lead-containing compounds.

On detachment from the glass slide, it was easy to observe by eye that the sample had a distinct oil film that lay on top of the lead white under layer. This formation is also observed in paint cross sections [2,4,5,9,25], and the region of interest for lead soap formation is the interface between these two layers [24,25].

It was difficult to form a suspension of the oil paint film in ethanol because of the insolubility of the dried, cross-linked oil. Adding a small amount of acetone to the suspension caused the sample to disintegrate slightly, and allowed the detachment of the lead white from the bulk of the oil film. After the addition of acetone, some dried oil film remained undissolved, while the unreacted carboxylic acids in the oil dissolved in the acetone [48] and the lead white formed a suspension in solution. On deposition of the sonicated sample onto the GCE, the surface gave the appearance of oil microdroplets.

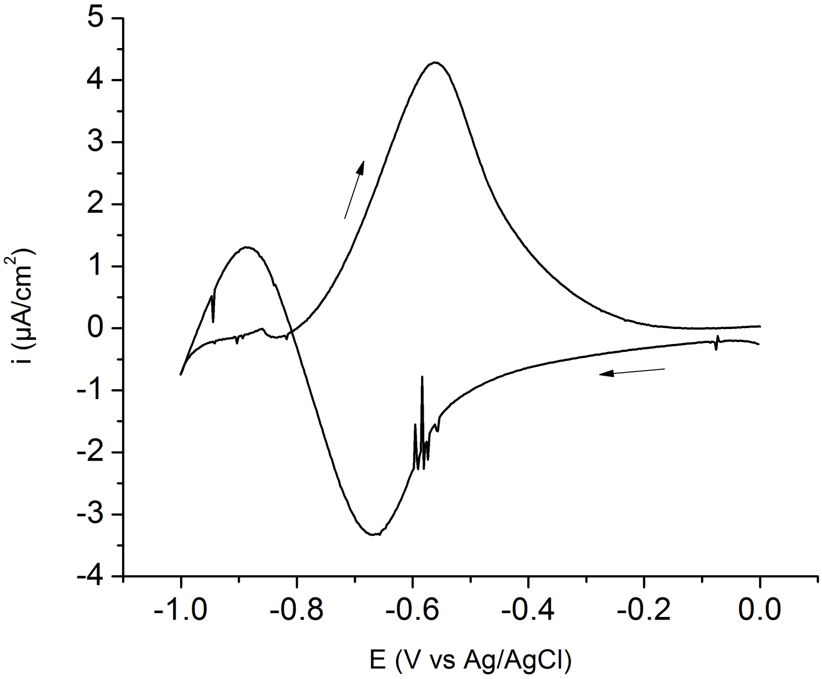

Figure 3.10 Lead white/walnut oil paint facsimile "PbWh_WO_1month" peak potential location compared with reference lead compounds

Figure 3.10 shows the result from the CV scans of the lead white in walnut oil sample. The technique proved to be highly irreproducible: the data obtained with the first deposition of the 'paint sample' onto the GCE gave the results shown. After this first scan, the results of subsequent depositions showed no anodic or cathodic peaks. This could be attributed to the oxidation of lead white which was previously observed in the lead white reference scans (Figure 3.9, Equations 3.7 and 3.8).

Comparing the anodic and cathodic potential peaks of lead white in the walnut oil binder and the reference sample, a shift to lower potentials is observed with the addition of binder. This behaviour has been observed previously [27] and is attributed to lead pigment-binder interaction and the association of lead ions with the binder during electrochemical reduction.

The measured current is three orders of magnitude below the expected range for lead white. This is presumed to be due to the oil binder having an insulating effect on the electrochemical signal, and preventing charge diffusion from the lead to the GCE surface. Doménech-Carbó *et al.* did not observe the same decrease in current with addition of binder to lead pigment samples [27]. This could be due to the ability to control sample thickness more accurately using completely dry samples.

3.4 Conclusions

In this chapter the dual role of lead carboxylates in conservation has been compared: they can be an unwanted product in oil paintings and used as a protective coating for lead artefacts. Lead carboxylates were synthesised successfully using a precipitation method with lead acetate. These complexes were subsequently characterised in order to inform further study of these compounds as coatings for lead. However, there may be some source of inaccuracy in the characterisation because it has been recently found that the formation of lead soaps in aqueous solution occurs via a basic lead soap complex containing two additional bridging oxygen atoms [49]. In this work by Hermans *et al.*, it was shown that the XRD patterns of the basic and non-basic lead soaps can be differentiated at all chain lengths apart from C14 [50]. Therefore further work is needed to determine which compound is synthesised using the precipitation method in this thesis. Work is ongoing elsewhere [51] to more accurately study the molecular structure of metal carboxylates.

By investigating the cyclic voltammetric characteristics of the synthesised lead soaps, the stability of the compounds is first seen: peak area did not decrease after multiple scans. The cyclic voltammetric patterns from lead soaps were also compared with other lead-containing pigments for the purpose of ascertaining whether the technique could be used for the identification of lead compounds in paint samples. The reference voltammograms showed a clear difference between lead soaps and other lead compounds. Furthermore, additional characterisation information can be gained from using the data from consecutive CV scans. Lead soaps give a consistent peak area whereas other lead compounds, such as lead oxide, show a reduction in peak area with each consecutive scan.

Despite this, it is unlikely that using cyclic voltammetry and GCE electrodes to mount samples would give an accurate picture of lead compounds within a paint sample at present. Further work needs to be carried out in the following areas:

- Sample preparation needs to be more controlled and standardised. This could be done by measuring the particle/micelle size of the suspension using a light scattering technique before applying the solution to the GCE. Also, prolonged sonication of the sample would reduce particle size if necessary.
- The effect of the binder in the paint sample is apparently limiting the current due to insulating properties of the oil, which exist on the GCE surface in the form of microdroplets and cause restricted conduction.

Sample preparation could be modified to separate the binder from the lead completely. In this way the sample eventually deposited on the GCE surface would more closely resemble the reference materials and the effect of the binder (a shift in anodic and cathodic peaks) would be reduced or even eliminated.

If these problems were addressed it might become possible to differentiate lead soaps from other lead pigments in paint samples. Samples are straightforward to make and the experiment is easy to carry out if the equipment is available. Cyclic voltammetry by [cyclic] nature in part is non-destructive, in returning the sample to its original oxidation state at the end of the scan. However, the technique is destructive due to the nature of sample preparation. Despite this the benefit of clear analysis of lead carboxylate formation may outweigh use of a destructive technique, if compared to the damaging nature of these compounds in oil paintings.

3.5 References

[1] R.F.P. Pereira, A.J.M. Valente, H.D. Burrows, The interaction of long chain sodium carboxylates and sodium dodecylsulfate with lead(II) ions in aqueous solutions., Journal of Colloid and Interface Science. 414 (2014) 66–72.

[2] M.J. Plater, B. De Silva, T. Gelbrich, M.B. Hursthouse, C.L. Higgitt, D.R. Saunders, The characterisation of lead fatty acid soaps in “protrusions” in aged traditional oil paint, Polyhedron. 22 (2003) 3171–3179.

[3] R.W. Corkery, Artificial biomineralisation and metallic soaps, PhD thesis, Australian National University, 1998.

[4] L. Robinet, M. Corbeil, The Characterization of Metal Soaps, Studies in Conservation. 48 (2003) 23–40.

[5] J. Boon, F. Hoogland, Chemical processes in aged oil paints affecting metal soap migration and aggregation, in: AIC Paintings Specialty Group, Annual Meeting in Rhode Island Conference Proceedings, 2007.

[6] L. Carlyle, M. Witlox, Historically accurate reconstructions of artists' oil painting materials, Tate Papers. Spring (2007) 1–9.

[7] A. Higgitt, M. Spring, D. Saunders, Pigment-medium interactions in oil paint films containing red lead or lead-tin yellow, The National Gallery Technical Bulletin. 24 (2003) 75–95.

[8] D. Erhardt, C. Tumosa, Long-term chemical and physical processes in oil paint films, Studies in Conservation. 50 (2005) 143–150.

[9] M. Cotte, E. Checroun, J. Susini, P. Walter, Micro-analytical study of interactions between oil and lead compounds in paintings, Applied Physics A. 89 (2007) 841–848.

[10] M. Cotte, E. Checroun, J. Susini, P. Dumas, P. Tchoreloff, M. Besnard, et al., Kinetics of oil saponification by lead salts in ancient preparations of pharmaceutical lead plasters and painting lead mediums., Talanta. 70 (2006) 1136–42.

[11] M.R.S.J. Foreman, M.J. Plater, J.M.S. Skakle, Synthesis and characterisation of polymeric and oligomeric lead(II) carboxylates, Journal of the Chemical Society, Dalton Transactions. (2001) 1897–1903.

[12] M.S. Akanni, E.K. Okoh, H.D. Burrows, H.A. Ellis, The thermal behaviour of divalent and higher valent metal soaps: a review, Thermochimica Acta. 208 (1992) 1–41.

[13] M.S. Akanni, N.A. Abass, Solution behaviour in alcohols and phase transitions of cadmium(II), mercury(II) and lead(II) carboxylates, Liquid Crystals. 6 (2006) 597–608.

[14] K. Keune, J. Boon, Analytical Imaging Studies of Cross-Sections of Paintings Affected by Lead Soap Aggregate Formation, Studies in Conservation. 52 (2007) 161–176.

[15] K. Keune, J.J. Boon, Imaging secondary ion mass spectrometry of a paint cross section taken from an early Netherlandish painting by Rogier van der Weyden., Analytical Chemistry. 76 (2004) 1374–85.

[16] F. Lacouture, M. François, C. Didierjean, J.P. Rivera, E. Rocca, J. Steinmetz, Anhydrous lead(II) heptanoate, Acta Crystallographica Section C Crystal Structure Communications. 57 (2001) 530–531.

[17] C.M. Mauck, T.W.P. van den Heuvel, M.M. Hull, M. Zeller, C.M. Oertel, Synthesis and structures of Pb3O2(CH3COO)2·0.5H2O and Pb2O(HCOO)2: two corrosion products revisited., Inorganic Chemistry. 49 (2010) 10736–43.

[18] V. Zelenák, Z. Vargová, K. Györyová, Correlation of infrared spectra of zinc(II) carboxylates with their structures., Spectrochimica Acta. Part A, Molecular and Biomolecular Spectroscopy. 66 (2007) 262–72.

[19] K. De Wael, M. Keersmaecker, M. Dowsett, D. Walker, P.A. Thomas, A. Adriaens, Electrochemical deposition of dodecanoate on lead in view of an environmentally safe corrosion inhibition, Journal of Solid State Electrochemistry. 14 (2009) 407–413.

[20] J. Berg, Analytical chemical studies on traditional linseed oil paints, PhD Thesis, Universiteit van Amsterdam, 2002.

[21] J. Townsend, R. Jones, K. Stoner, Lead soap aggregates in sixteenth-and seventeenth-century British paintings, AIC Paintings Specialty Group, Annual Meeting in Rhode Island. (2007).

[22] J. Townsend, K. Keune, Microscopical techniques applied to traditional paintings, Infocus Magazine. (2006) 54–65.

[23] R. Jones, J. Townsend, Drying crackle in early and mid-eighteenth-century British paintings: an explanation of the phenomenon of microcissing, Paper Presented at 5th International Symposium Painting Techniques, Amsterdam. (2013).

[24] A. van Loon, Color Changes and Chemical Reactivity in Seventeenth-century Oil Paintings, PhD Thesis, Amsterdam, The Netherlands, 2008.

[25] K. Keune, Binding medium, pigments and metals soaps characterised and localised in paint crosssections, PhD Thesis, University of Amsterdam, 2005.

[26] A. Doménech, M. Domenech-Carbo, X. Mas, J. Ciarrocci, Simultaneous identification of lead pigments and binding media in paint samples using voltammetry of microparticles, Arché. (2007) 121–124.

[27] A. Doménech-Carbó, M.T. Doménech-Carbó, X. Mas-Barberá, Identification of lead pigments in nanosamples from ancient paintings and polychromed sculptures using voltammetry of nanoparticles/atomic force microscopy., Talanta. 71 (2007) 1569–79.

[28] A. Elia, M. Dowsett, A. Adriaens, Electrochemical characterization of bronze historical objects using voltammetry of microparticles, Applied Physics A. 118 (2014) 449–455.

[29] A. Doménech-Carbó, M.T. Doménech-Carbó, M.A. Peiró-Ronda, L. Osete-Cortina, Electrochemistry and authentication of archaeological lead using voltammetry of microparticles: Application to the Tossal de Sant Miquel Iberian plate, Archaeometry. 53 (2011) 1193–1211.

[30] A. Doménech-Carbó, M.T. Doménech-Carbó, J. V Gimeno-Adelantado, F. Bosch-Reig, M.C. Saurí-Peris, M.J. Casas-Catalán, Electrochemical analysis of the alterations in copper pigments using charge transfer coefficient/peak potential diagrams. Application to microsamples of baroque wall paintings attached to polymer film electrodes, Fresenius' Journal of Analytical Chemistry. 369 (2001) 576–581.

[31] R. Mayer, The Artist's Handbook of Materials and Techniques, 5th ed., Faber and Faber, London, 1991.

[32] H. Kühn, Lead-Tin Yellow, Studies in Conservation. 13 (1968) 7.

[33] A. Phenix, The Swelling of Artists ' Paints in Organic Solvents . Part 2 , Comparative Swelling Powers of Selected Organic Solvents and Solvent Mixtures, Journal of the American Institute for Conservation. 41 (2002).

[34] P. Ballinger, F.A. Long, Acid Ionization Constants of Alcohols. II. Acidities of Some Substituted Methanols and Related Compounds 1,2, Journal of the American Chemical Society. 82 (1960) 795–798.

[35] D.D. Perrin, B. Dempsey, E.P. Serjeant, pKa Prediction for Organic Acids and Bases, Springer Netherlands, Dordrecht, 1981.

[36] C.G. Bazuin, D. Guillon, A. Skoulios, A.M. Amorim Da Costa, H.D. Burrows, C.F.G.C. Geraldes, et al., Thermotropic Polymorphism in Liquid-Crystalline Lead(II) Alkanoates, Liquid Crystals. 3 (1988) 1655–1670.

[37] N.W. Alcock, V.M. Tracy, T.C. Waddington, Acetates and acetato-complexes. Part 2. Spectroscopic studies, Journal of the Chemical Society, Dalton Transactions. (1976) 2243.

[38] Personal Communication from M. G. Dowsett, (2014).

[39] H.A. Ellis, N.A.S. White, R.A. Taylor, P.T. Maragh, Infrared, X-ray and microscopic studies on the room temperature structure of anhydrous lead (II) n-alkanoates, Journal of Molecular Structure. 738 (2005) 205–210.

[40] C. Suryanarayana, M. Grant Norton, X-Ray Diffraction: A Practical Approach, Plenum Press, New York, 1998.

[41] D. Pavlov, N. Iordanov, Growth processes of the anodic crystalline layer on potentiostatic oxidation of lead in sulfuric acid, Journal of The Electrochemical Society. 117 (1970) 1103.

[42] M. De Keersmaecker, M. Dowsett, R. Grayburn, D. Banerjee, A. Adriaens, In-situ spectroelectrochemical characterization of the electrochemical growth and breakdown of a lead dodecanoate coating on a lead substrate., Talanta. 132 (2015) 760–8.

[43] P. Cañizares, J. García-Gómez, J. Lobato, M.A. Rodrigo, Electrochemical Oxidation of Aqueous Carboxylic Acid Wastes Using Diamond Thin-Film Electrodes, Industrial & Engineering Chemistry Research. 42 (2003) 956–962.

[44] N. De Laet, S. Lycke, J. Van Pevenage, L. Moens, P. Vandenabeele, Investigation of pigment degradation due to acetic acid vapours: Raman spectroscopic analysis, European Journal of Mineralogy. 25 (2013) 855–862.

[45] M.C. Bernard, S. Joiret, Understanding corrosion of ancient metals for the conservation of cultural heritage, Electrochimica Acta. 54 (2009) 5199–5205.

[46] J.J. Boon, E.S.B. Ferreira, eds., Reporting Highlights of the De Mayerne Programme, NWO, The Hague, 2006.

[47] M. Odlyha, D. Thickett, L. Sheldon, Minerals associated with artists' paintings and archaeological iron objects, Journal of Thermal Analysis and Calorimetry. 105 (2011) 875–881.

[48] R. White, A. Roy, GC-MS and SEM Studies on the Effects of Solvent Cleaning on Old Master Paintings from the National Gallery, London, Studies in Conservation. 43 (1998) 159.

[49] J.J. Hermans, K. Keune, A. van Loon, Elucidating the molecule structure of metal soaps in oil paintings, Paper Presented at Chem CH 2014. (2014).

[50] S.M. Polvino, Accuracy, Precision, and Resolution in Strain Measurements on Diffraction Instruments, PhD Thesis, University of Colombia, 2011.

[51] J.J. Hermans, K. Keune, A. van Loon, R.W. Corkery, P.D. Iedema, The molecular structure of three types of long-chain zinc(II) alkanoates for the study of oil paint degradation, Polyhedron. 81 (2014) 335–340.

Chapter 4 Spectroelectrochemical characterisation and performance of a new coating for heritage lead

This chapter is based in part on a published article: R. Grayburn, M. Dowsett, M. De Keersmaecker, D. Banerjee, S. Brown, A. Adriaens, Towards a new method for coating heritage lead, Heritage Science. 2 (2014) 14.

4.1 Introduction

In Chapter 3 the damage of lead carboxylates to some cultural heritage objects was described. However long-chain carboxylic acids can also be applied to various metals as a conservation treatment. The resulting thin film of metal carboxylate forms a protective layer against atmospheric pollutants.

4.1.1 Carboxylates as coatings

Long-chain carboxylic acids have been studied as possible corrosion inhibiting coatings for lead [1–6] and other heritage metals such as copper [7,8], iron [9] and limestone [10]. In the context of lead (the most widely studied application) these coatings are usually formed by the immersion of the lead sample into an aqueous solution of the sodium salt of the carboxylate [1]. Sodium carboxylate has also been shown to deposit multiple layers of lead carboxyate on a lead surface using cyclic voltammetry [4,5]. For lead samples, a lead dicarboxylate coating forms on the surface, the carboxylic acid having reacted with the lead surface. Typically, studies have focussed on chain lengths up to the decanoate because the sodium salts are reasonably water soluble to that point.

Long-chain carboxylic acids are cheap and readily available. As opposed to conservation waxes, which are derived from crude oil, these coatings are derived from natural fatty acids, thus making these coatings the most 'environmentally-friendly' option. However, the solubility of the sodium carboxylates above the decanoate becomes too low for use in aqueous deposition. In addition, decanoic acid has a distinctive odour, which deters use.

In this chapter multi-technique studies on the deposition of tetradecanoic acid (or myristic acid, C14) $CH_3(CH_2)_{12}COOH$ and octadecanoic acid (or palmitic acid, C18) $CH_3(CH_2)_{16}COOH$ on lead are reported. We exploit the solubility of these long chain carboxylates in ethanol and use this property to move towards a new method of coating lead metal samples. The longer chains are expected to improve coating effectiveness due to increased coating stability with chain length [11]. Impedance measurements are used to determine coating effectiveness, whereas time-lapse synchrotron and laboratory XRD are used to study coating formation and thickness respectively. The work in this chapter also aims to show the effectiveness of the same ethanolic-deposited coatings on a more apt substrate for the context of conservation practice: corroded lead.

4.2 Experimental

4.2.1 Sample preparation

The lead coupon and coating preparation is described in detail in Chapter 5. Ethanolic octadecanoic acid (C18) solution (0.05 mol L^{-1}) and ethanolic solutions of tetradecanoic acid (C14) (1 mol L^{-1}, 0.5 mol L^{-1}, 0.25 mol L^{-1}, 0.1 mol L^{-1}, 0.05 mol L^{-1} and 0.01 mol L^{-1}) were similarly prepared. Coupons were immersed in the appropriate solution for 24 hours and left to dry in air.

The pre-corroded samples were prepared in such a way as to simulate the corrosion of lead due to oak-emitted volatile organic compounds (VOCs) when displayed or stored in an oak display cabinet. Therefore lead coupons were kept in an oak environment to model the oak display case for 9 months. The lead coupon, coating preparation and creation of an oak environment are described in Chapter 5. Polished lead coupons were enclosed within the oak environment at 50% RH for 9 months in order to develop a layer of corrosion products [12]. After corrosion, coupons were coated in the same manner as previously described, after mounting in a working electrode holder [13] (see Section 6.2.8).

4.2.2 Analytical methods

Time-lapse SR-XRD of coating formation

The real-time growth of lead ditetradecanoate ($Pb(C14)_2$) was studied on the Belgian-Dutch CRG beamline DUBBLE (BM26a) [14] at the ESRF in order to confirm that the coating formed from C14 on evaporation of the ethanol solvent. Previous work with sodium decanoate showed that the lead didecanoate layer formed during immersion [2,3], whereas this was reported not to be the case for ethanolic solutions [15]. The setup of SR-XRD experiments on DUBBLE using this equipment is detailed in Chapter 5.

A 0.05 mol L^{-1} solution of C14 was flowed in 2 mL droplets from a syringe across a polished lead sample surface in ambient air (Figure 4.1). The sample was held within the cell's sample holder (also known as the working electrode holder). The syringe was driven by a stepper motor, which was controlled remotely. The droplets readily wetted the surface and started evaporating immediately. Using Mar CCD 165 (Mar USA Inc., Evanston, IL, USA) camera a sequence of 10 surface powder diffraction images were recorded with a collection time of 15 seconds and an interval of 30 seconds between scans.

During the first four scans 4 x 2 mL aquilots of the solution were flowed over the surface using the Teflon FEP piping fixed to the top of the sample inside the eCell Mk IV [13] (Figure 4.1). The remaining six scans observed the drying and coating formation, although some evaporation occurred during the first four scans. SR-XRD patterns were extracted and analysed using the esaProject software [16] which can produce images such as those shown in Figure 4.3.

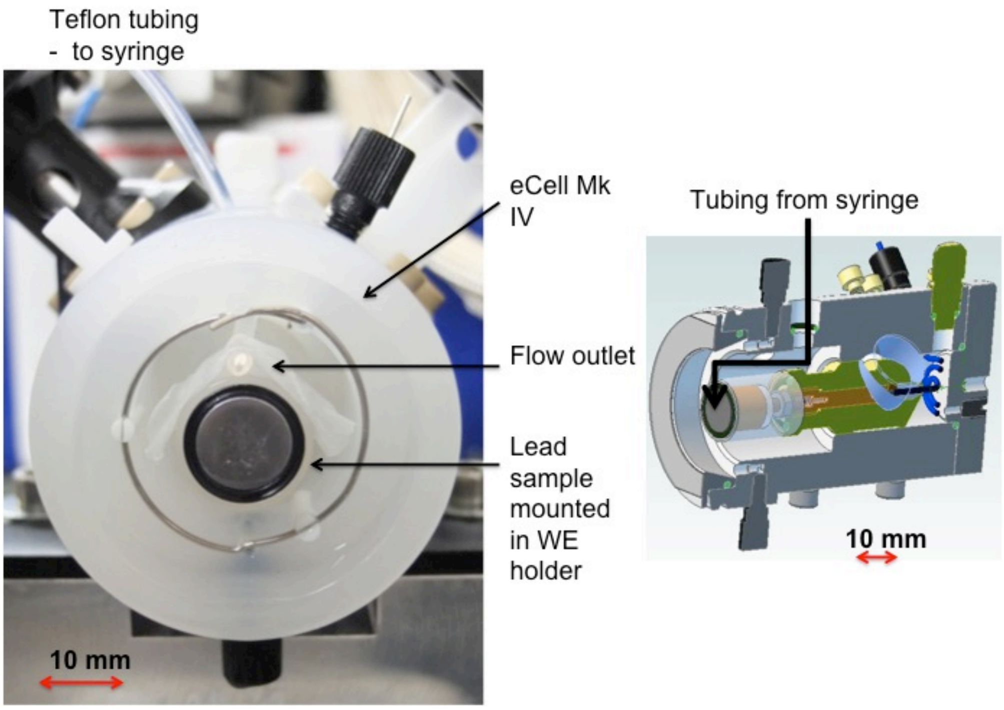

Figure 4.1 Front view of the droplet experiment (l) and a cross-section of the experiment (r). The eCell is used without its window for this experiment to allow for evaporation and to prevent the contact of the ethanol solution with the window material. eCell Mk IV ports are used to deliver solution via Teflon FEP tubing to the surface of the sample. Tubing outlet is held in place to the topside of the WE holder using scotch tape. The tubing is upwards of 1 m in length to allow for the automated syringe to be placed in a convenient location within the hutch.

Laboratory XRD of coated lead samples

XRD analysis of lead coupons coated with coating solutions of varying concentrations was carried out to determine the optimum coating solution concentration and to study coating corroded lead. XRD measurements were performed by Tom Planckaert at Universiteit Gent using an ARL X'TRA diffractometer using Cu-K_α X-rays with a wavelength of 1.5405 Å with a scintillation counter detector. A scan from 2 - 67° 2θ was performed on each sample at a scan rate of 0.8 °/minute and a step size of 0.02 °. One sample per solution concentration was measured.

GC-MS of the corrosive environment

The corrosive environment was sampled using a RAD130 Radiello® (Padova, Italy) cartridge which was placed in the closed environment alongside the samples inside a diffusive body [17]. After 2 months, the cartridge was removed and sampled as described in Section 5.2.3 (Museum Testing).

Microscopy

Surface topography of coated samples was investigated using SEM. SEM images of 0.05 mol L^{-1} C14 coated coupons were collected on a ZEISS SUPRA 55-VP microscope at 20 kV acceleration voltage at the University of Warwick's microscopy facilities. Optical microscope images were collected on a Nikon SM2800 microscope.

EIS

The electrical resistance of the coatings on lead was measured by EIS and compared to bare lead samples to assess performance. Impedance measurements were performed using a PGSTAT20 potentiostat with a FRA2 frequency response analysis module (both Metrohm Autolab B. V., The Netherlands). Data were acquired over a frequency range of 100 mHz to 10 kHz (0.1 V signal amplitude). The frequency range 10 kHz – 1 Hz was distributed logarithmically across the first 40 points and from 1 Hz – 100 mHz logarithmically over the last

10 points. Measurements were controlled by the Nova software (also Metrohm, version 1.8).

For all experiments a three-electrode system in a glass cell was used. The set-up consisted of a saturated calomel electrode (Radiometer Analytical, France), a carbon counter electrode and the lead coupon mounted in a working electrode holder. The electrolyte used was taken from the ASTM D 1384–87 standard [18], and is an aqueous solution used as a standard electrolyte for corrosion inhibition tests to model an atmospheric environment. The solution contains 148 mg L^{-1} Na_2SO_4, 138 mg L^{-1} $NaHCO_3$ and 165 mg L^{-1} NaCl (all Sigma Aldrich). For the immersion tests, bare and coated coupons were tested for impedance before and after immersion in 0.01 mol L^{-1} acetic acid solution for 10 minutes. Samples were rinsed with deionised water before and after immersion. All EIS measurements were repeated three times.

4.3 Results and discussion

4.3.1 Sample preparation

Coating polished lead samples

C14 was originally chosen as a candidate for coating development due to its high solubility in ethanol compared to longer chain carboxylates. A concentration of 0.05 mol L^{-1} was initially used for direct comparison to previous work using sodium carboxylates in aqueous solution [2,3,5,6].

Several methods of application to the lead surface were attempted. The solution can be applied to the surface by immersion or spraying, which makes it easy to use over large surface areas. Brush coating is impractical due to the low viscosity of the solution. Upon drying, the coating forms immediately to give a matt appearance and the surface often appears darker than when freshly polished (Figure 4.2).

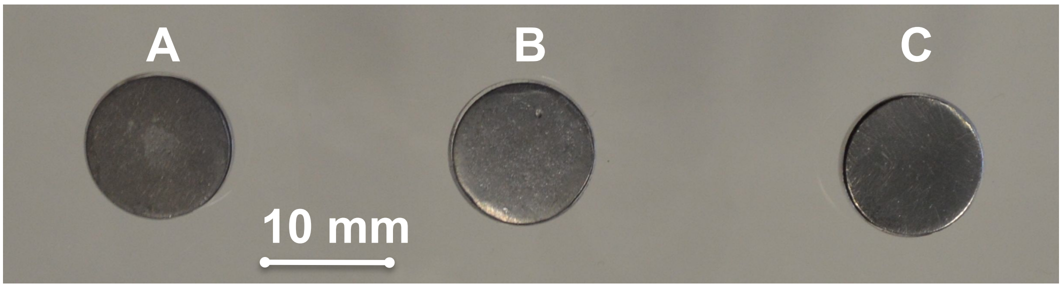

Figure 4.2 Photograph of C14 coated (A), C18 coated (B) and bare lead samples (C)

4.3.2 Time-lapse SR-XRD of coating formation

Figure 4.3 shows the SR-XRD results from a coating experiment using a C14 ethanolic solution on bare lead to investigate the coating formation mechanism.

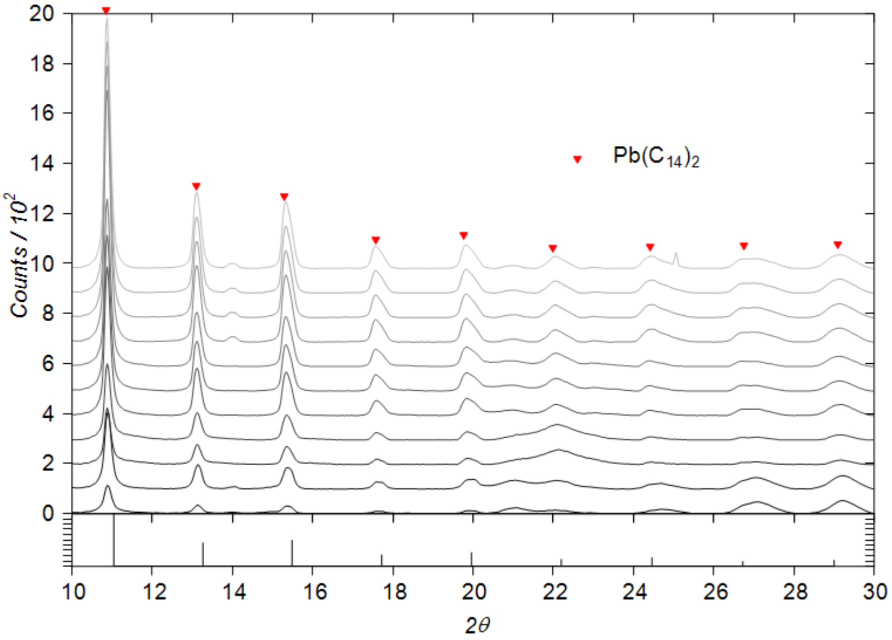

Figure 4.3 Time-lapse SR-XRD of the coating process. $Pb(C14)_2$ growth on a bare lead substrate during drying is shown. Patterns were collected every 45 seconds for 7.5 minutes. The development of the coating is shown from the first scan (bottom) to last scan (top).

In Figure 4.3 ten consecutive patterns for the drying sequence from an experiment are shown, where drops of the coating solution were flowed across the lead surface during surface analysis, allowing quick evaporation. Patterns were collected every 45 seconds, which consisted of 15 seconds of collection time plus 30 seconds of dwell time between measurements. The figure shows the $Pb(C14)_2$ layer forming within the first 15 seconds of contact with the inhibitor solution. The reflections labeled 0 0 10 to 0 0 26 are from preliminary indexing of this pattern, which was discussed in Chapter 3. However, the results show that peak areas have not yet reached a steady state during the final scans. This is due to incomplete drying. There is still ethanol present in the layer. Peak broadening occurs only at peaks of higher 2θ due to the experimental geometry. This is due to the beam footprint: reflections at higher 2θ are extended over more of the camera face. Other reflections in these patterns may be higher order reflections from the lead carboxylate structure or unreacted carboxylic acid.

From Figure 4.3 it can be seen that the lead tetradecanoate coating forms immediately on the application and evaporation of the solution thus providing a rapid treatment. No soaking is required. To confirm this rapid treatment a simple mass gain experiment was conducted: a lead coupon was soaked in 0.05 mol L^{-1} C14 ethanolic solution, dried, rinsed with deionised water and weighed (using 4 decimal place balance) every hour for 5 hours. No increase in weight was detected thus verifying the futility of a long soaking regime. In similar experiments with aqueous carboxylic acid treatments the mass gain is parabolic [2], which is due to a difference in coating mechanism. In aqueous solution the carboxylate forms in a dissolution-precipitation cycle, whereby precipitation occurs as the product crystallizes onto the lead surface to form the protective barrier [5,19,20]. Lead carboxylates are more soluble in ethanol than water [21] so therefore the crystallization of the layer from ethanolic solution only occurs when the ethanol evaporates. A dissolution-precipitation cycle does not exist when using ethanol as a solvent. Instead it is an evaporation-precipitation cycle. Although both solvents are polar, ethanol has a non-polar moiety (a short hydrocarbon chain, CH_3CH_2-) which aids solvation of the aliphatic chain of the lead carboxylate. This could explain the difference in coating mechanisms between the aqueous and ethanolic deposition methods.

The coating crystallises rapidly on evaporation of the solvent. In solution, the lead carboxylate forms as a gel layer [15], making use of the oxygen adsorbed on the lead surface. The adsorbed oxygen layer forms on the lead immediately after polishing due to lead's high reactivity in air [22]. SR-XRD is unable to detect monolayers of lead oxide so its involvement cannot be deduced in the mechanism of formation, but it may be inferred:

$$\mathrm{PbO(ads)} + 2\mathrm{CH_3(CH_2)_{12}COO^-} + 2\mathrm{H^+} -> \mathrm{Pb(CH_3(CH_2)_{12}COO)_2} + \mathrm{H_2O} \tag{4.1}$$

Figure 4.4a shows an optical microscopy image taken of a coupon coated by immersion for 24 hours in an ethanolic solution of tetradecanoic acid. The surface appears smooth but cracks show that the coating is soft and easily scratched. Figure 4.4b shows a scanning electron micrograph of the coated lead surface. The coating is not smooth at this scale and is formed of a layer of 1 μm length microcrystals. These differ in morphology from the lamellar crystal growth observed from lead carboxylate growth from aqueous solutions of sodium carboxylate [2]. The thickness of this layer can be calculated semi-quantitatively using XRD.

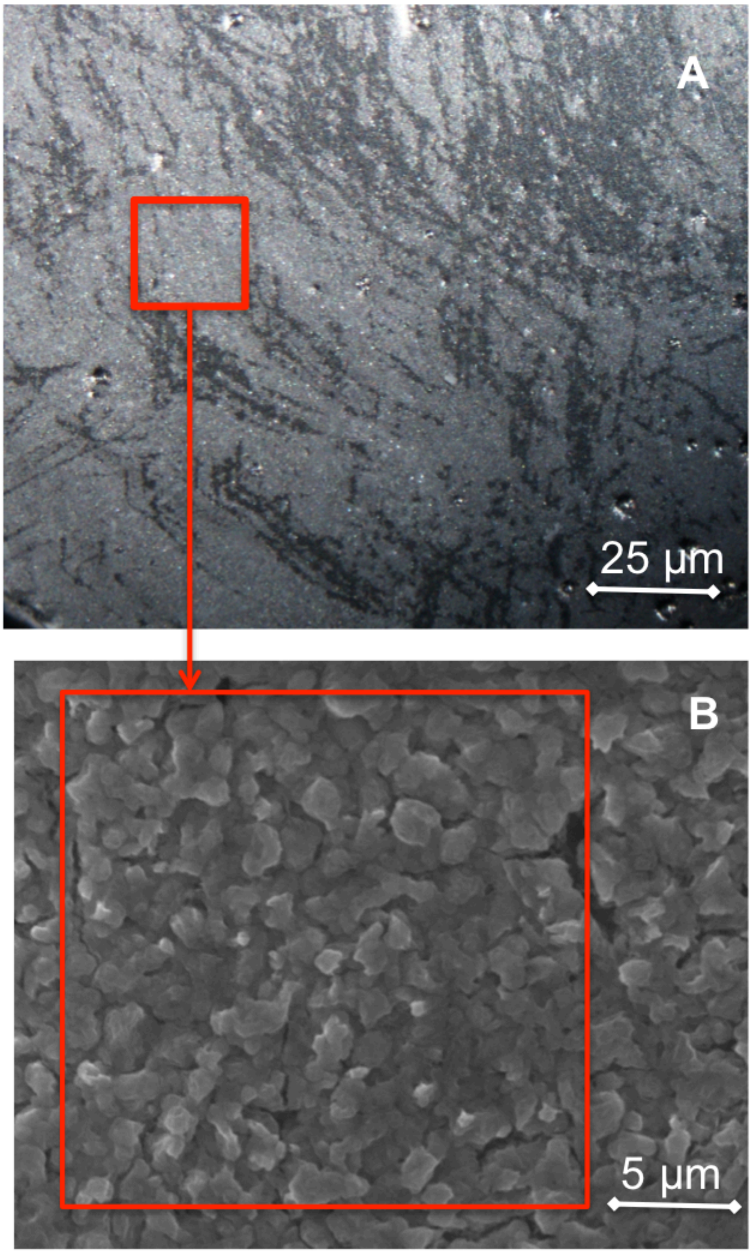

Figure 4.4 Microscopy of the coated surface. An optical microscopy image (A) and SEM (B) image of a C14 coated lead coupon was recorded after bare lead was coated by immersion for 24 hours.

4.3.3 Coating mass thickness

The XRD pattern of the lead tetradecanoate coating deposited from 0.05 mol L^{-1} tetradecanoic acid solution has been studied in Chapters 3 and 5 of this thesis. Patterns from lead samples coated with a range of concentrations of tetradecanoic acid are shown in Figure 4.5a. Although only one sample was used per concentration, the data (peak locations) are in agreement with previous

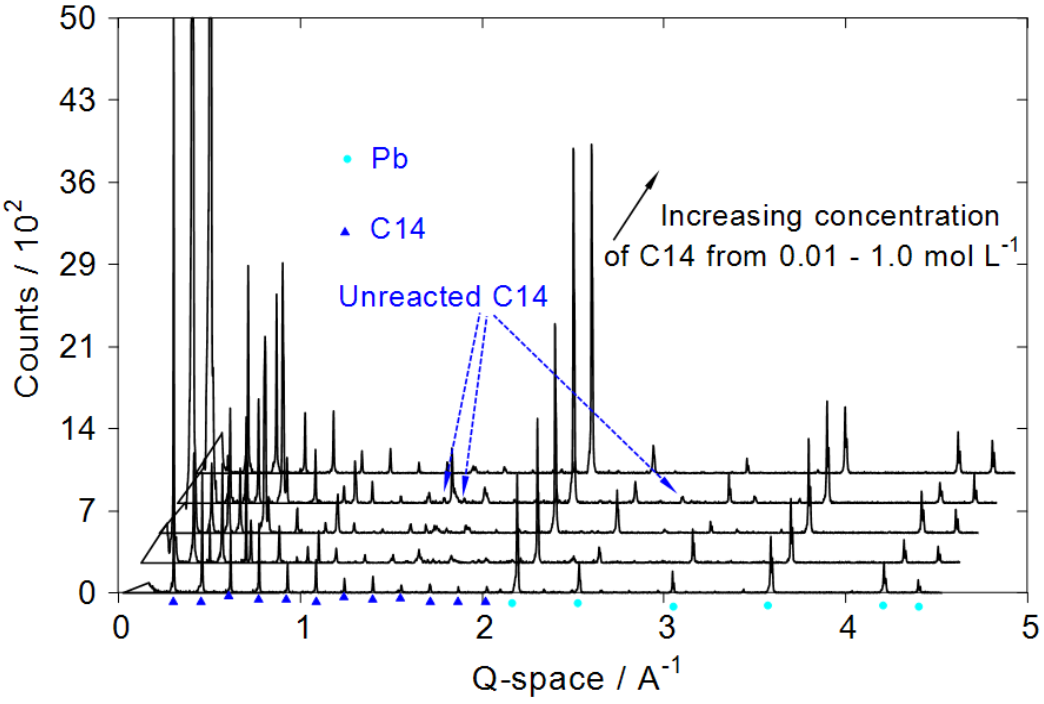

(a)

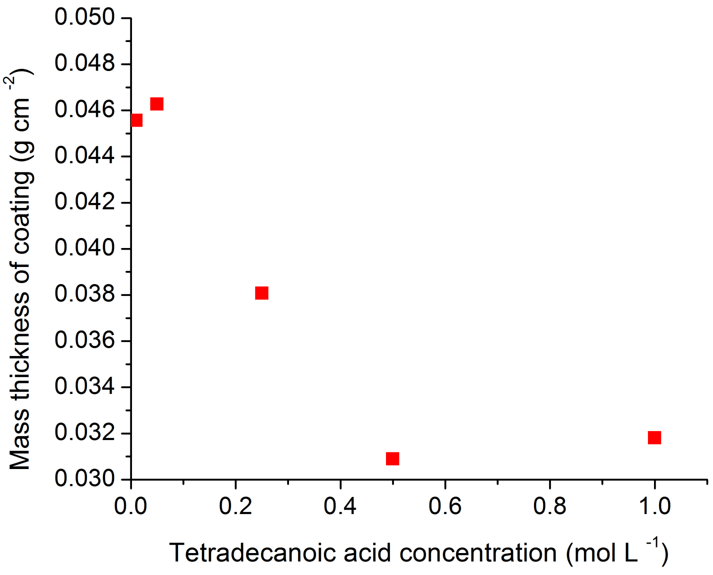

(b)

Figure 4.5 Finding the optimal coating concentration. XRD patterns of a coated lead coupon with increasing inhibitor concentrations were recorded (a). The mass thickness of the coating was calculated using an adapted version of the Beer-Lambert law and the extracted peak area of Pb 111 (see Chapter 5 for calculations). Mass thickness is plotted versus C14 concentration (b).

results (see Chapters 3 and 5). The evenly spaced peaks of the lead carboxylate are visible alongside the lead metal peaks. At all concentrations from 0.01 mol L^{-1} – 1 mol L^{-1}, the coating forms although at higher inhibitor concentrations unreacted tetradecanoic acid is also detected. On samples with unreacted tetradecanoic acid, the unreacted acid forms a white crust which can be removed easily with ethanol. The XRD pattern with the least contamination is given by the lead coated with a 0.01 mol L^{-1} solution in which only lead and lead tetradecanoate peaks feature. It is uncertain whether excess tetradecanoic acid on the surface would afford improved protection from atmospheric pollutants, but the unaesthetic appearance resulting from excess acid means higher inhibitor concentrations are not recommended.

The lead metal reflections are smaller for samples coated with lower inhibitor concentrations indicating that the coating of lead tetradecanoate is thicker for low concentrations. A thicker superficial lead compound will absorb more of the X-rays arriving at and reflected from the underlying lead surface leading to a reduction in lead signal. The extent of absorption by compounds can be measured using the mass attenuation coefficient and this leads directly to a method for estimating average layer thickness using the Beer-Lambert law, described in detail in Chapter 5.

Figure 4.5b shows the results for coating mass thickness calculated using the peak areas for the strongest lead signal in Figure 4.5a (attributed to the 111 reflection). The mass thickness is the mass of the lead ditetradecanoate coating per unit area (and the thickness is this divided by the density). Using this calculation the observations from Figure 4.5a can be quantified. The mass thickness of the coating from 0.01 mol L^{-1} and 0.05 mol L^{-1} solutions of the acid is the greatest at 0.045 g cm^{-2}. The mass thickness of the coating formed from higher concentrations of the acid is up to 30% lower. Deposition of mixed coatings of acid and lead carboxylate form for the higher concentrations, but the attenuation of the crystalline tetradecanoic acid will be significantly lower than that for the same thickness of lead tetradecanoate due to the lower density of the constituent atoms.

4.3.4 Effectiveness against acidic pollutants and a longer chain solution

Electrochemical impedance spectroscopy (EIS) can give quantitative data relating to the effectiveness of a coating on a conductive substrate. Acetic acid has been previously used as the electrolyte in electrochemical tests with carboxylates to model an atmosphere polluted with oak VOCs [19,20]. Here EIS is used to compare the impedance and phase data before and after immersion for 10 minutes in 0.01 mol L^{-1} acetic acid to see the corrosive effects of the acid modelling VOC emission by oak independently from the corrosion effects of the electrolyte during EIS analysis.

In the microscopy data, the coating can be seen to be easily scratched making it difficult not to damage the coating during mounting into the working electrode holder. Therefore the only reproducible results come from undamaged coatings.

Figure 4.6a shows the Bode impedance plot of the sample measured in an ASTM D 1384–87 electrolyte solution over a specified frequency range before and after immersion in acetic acid. The coated samples maintain a higher impedance than the bare samples at all frequencies: this shows the coating has improved the coating resistance compared to bare lead.

After immersion in acetic acid, the magnitude of impedance of the coating at low frequency decreased by 15%. The decrease in impedance suggests the aggressive corrosion through the coating by acetic acid. The ASTM D 1384–87 electrolyte initiates corrosion if in contact with lead. As it is used to model atmospheric corrosion, lead oxides and carbonates may form. As a consequence of acetic acid immersion the protection from the coating and from the oxide layer decreases and the electrolyte can penetrate to the metal surface to initiate corrosion more readily. The corrosion products formed by acetic acid immersion do not impart further protection, unlike the passivating lead oxide. This is due to the solubility of the corrosion product (lead acetate) in aqueous solutions such as the electrolyte used here [23]. In ambient atmospheric conditions, surface water caused by relative humidity can act as a solvent for soluble corrosion products [24]. The same decrease in impedance is seen with the bare lead as the acetic acid easily penetrates the passivation layer and forms lead acetate.

Figure 4.6b shows the corresponding Bode phase plots for the coated samples. These plots clearly show two maxima, corresponding to different time constants: the maximum at ~10 Hz corresponds to the double layer, which includes the surface oxide, and that at ~1000 Hz to the coating. The presence of two time constants indicates the penetration of the electrolyte into the coating and double layer, which increases the surface area of metal exposed to electrolyte.

The time constants shown in the phase plots shift to lower frequencies as a result of immersion in acetic acid. This can be linked to the observed decrease in impedance of the coated samples in Figure 4.6a, which occurs as a result of the formation of soluble corrosion products by the electrolyte after acetic acid infiltrates the protective coating layer.

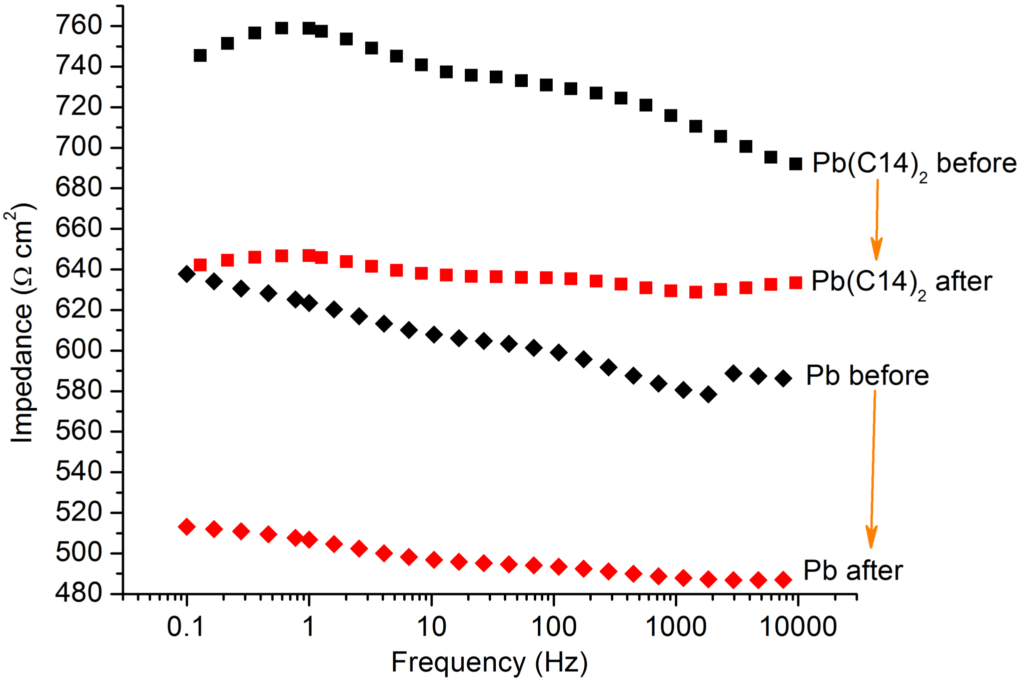

(a)

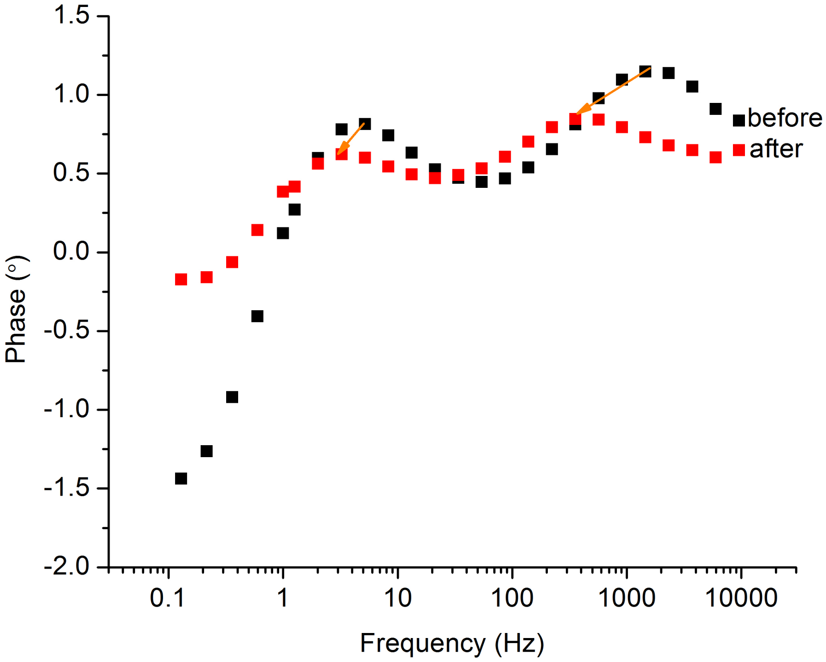

(b)

Figure 4.6 Coating effectiveness in acetic acid. Impedance (a) and phase (b) plots of $Pb(C14)_2$ coating and bare lead samples were recorded before and after immersion in acetic acid.

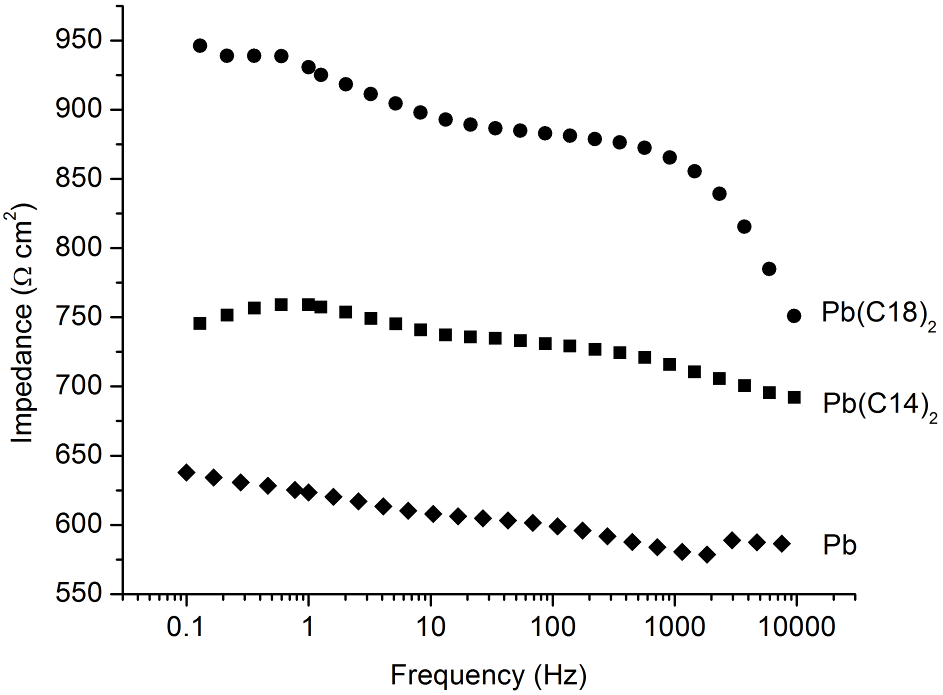

(a)

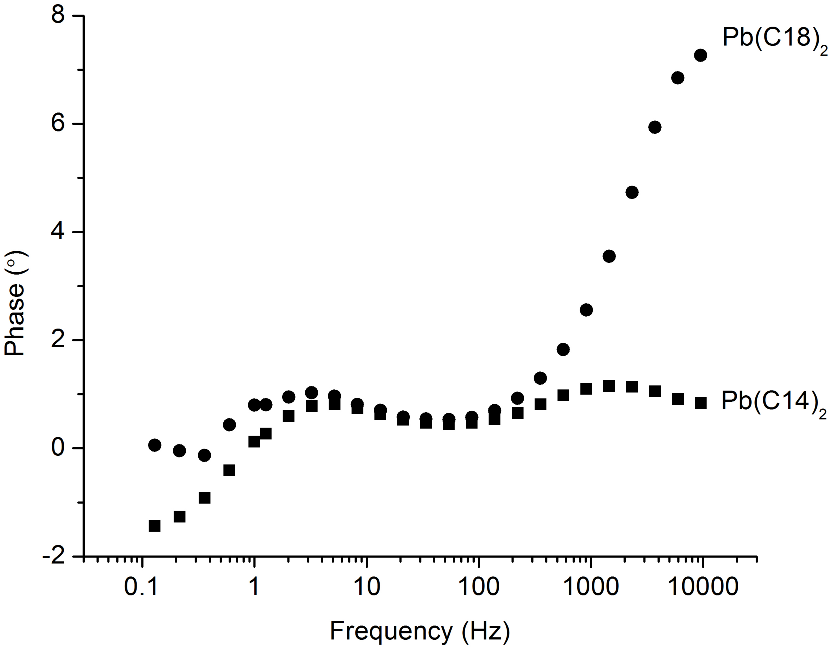

(b)

Figure 4.7 The effect of increasing coating carbon chain length. Impedance (a) and Bode phase plots (b) were recorded of bare lead and Pb(C14)$_2$ and Pb(C18)$_2$ coating on lead.

Figure 4.7a compares the impedance of a $Pb(C14)_2$ coating against a longer chain lead carboxylate $Pb(C18)_2$ coating deposited from the same concentration of ethanolic octadecanoic acid solution across the same range of frequencies. The magnitude of impedance at low frequencies is 20% higher for the longer chain carboxylate and 75% higher than bare lead, thus demonstrating its capacity for improved corrosion resistance. In comparison to C14, the phase plot (Figure 4.7b) shows the second time constant (~1000 Hz) shifted to higher frequencies. This suggests that the $Pb(C18)_2$ coating is reducing the rate of electrolyte penetration and therefore corrosion. This is presumably due to the longer carbon chains providing a greater area of hydrophobicity to repel aqueous electrolytes from reaching the metal substrate below.

Figure 4.7b shows an area of negative phase shift at very low frequencies. This can be related to inductive behaviour due to adsorption processes such as water uptake [25]. Negative phase shifts are found at low frequencies of the $Pb(C14)_2$ plots before immersion in acetic acid. Figure 4.4b shows the crystals on the coated surface of this sample – the gaps between crystals could allow for water-uptake into the coating [26]. There is less negative phase shift in the $Pb(C18)_2$ coating due to increased hydrophobicity, as previously mentioned.

The low phase angles observed in these data show that the lead tetradecanoate is mostly resistive. In addition, Figure 4.6a shows that the change in impedance of bare lead before and after immersion in acetic acid is the same (~15%) as the coated lead. In this way it can be concluded that the lead tetradecanoate coating is passivating the surface [27], not merely providing a barrier against pollutants.

4.3.5 Coating corroded lead

GC-MS of the corrosive environment

Thermal desorption GC-MS of the VOCs within the corrosive environment was carried out in order to inform conclusions regarding the corrosion products on lead exposed to this particular environment. The activated charcoal sampling tube was exposed to a thermal desorption regime in order to release VOCs for analysis within the GC column.

Table 4.1 List of VOCs detected within the oak environment at 75% RH using GC–MS.

Time (minutes)	**VOC (peak label)**	**Peak area / 10^8**
5.128	Acetic acid (A)	0.39
6.869	Ethyl acetate (B)	0.72
9.863	Methyl acrylate (C)	0.27
13.183	Furfural (D)	0.17

Table 4.1 and Figure 4.8 show the extracted compounds from the oak environment. Acetic acid and furfural are known degradation products of oak and were observed 18 months previously using the same piece of oak (see Chapter 5). Formic acid was not detected because its molecular weight was below the range of the gas chromatograph. The area labelled E has a parent peak molecular weight of 61 which does not correspond to a known VOC. It is possible that this region is an artefact of acid absorption onto the column. The lack of other VOCs originally detected in the sample could be due to the ongoing aging of the wood since the last analysis, or due to limitations of the activated charcoal after acidic exposure.

The region before E is background noise due to the GC column. Compound B has not been observed in previous oak VOC analyses (it is sometimes detected due to polyurethane coating emission [28]) but due to the consequent reappearance acetic acid 0.2 minutes later, it is possible that the ethyl acetate is a product of a reaction of acetic acid with active charcoal over a prolonged period of exposure. In addition, the peak labelled C could also be a result of prolonged exposure to the extreme acidic environment and subsequent degradation of the activated charcoal. This peak is still observed if the analysis is repeated using the VOC-free charcoal sample.

Overall, the detection of acetic acid is the most important observation for this study [12].

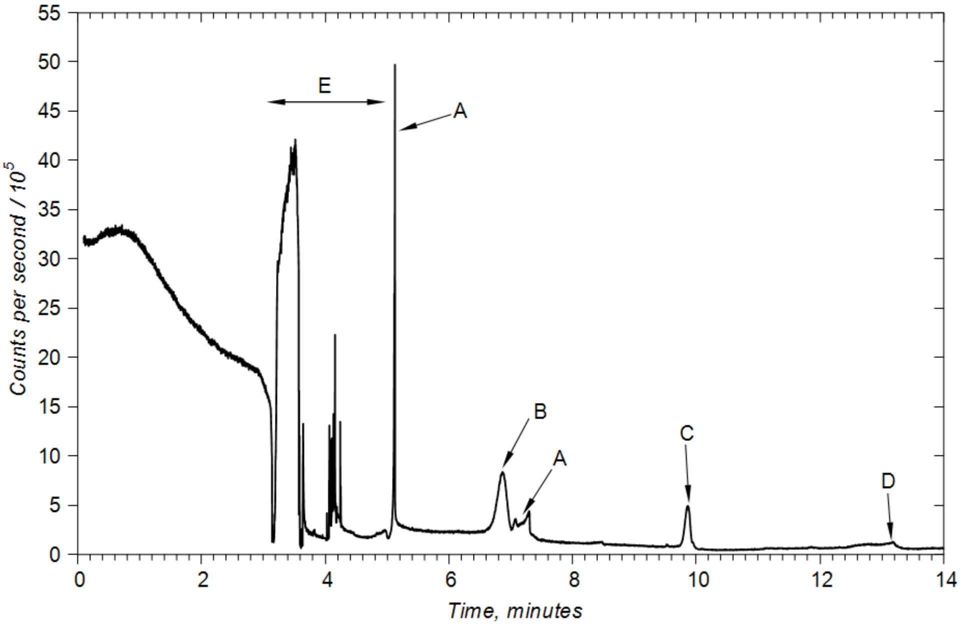

Figure 4.8 GC trace after 2 months exposure of the active charcoal sample to the oak environment. Peak labels are explained in Table 4.1. The peak labelled C is attributed to degradation of the activated charcoal.

Sample preparation

Figure 4.9 shows images of the corroded coupons before and after coating with tetradecanoic acid. Figure 4.9 (a) shows a coupon corroded by the 9 months exposure to the oak environment. The surface is covered with patches of pale-coloured corrosion products. The optical microscopy image more clearly shows the smaller spots of white corrosion products, around 0.4 mm diameter. After immersion in the ethanolic carboxylate solution the tarnish colour does not change, as evidenced in Figure 4.9 (b). The lead soap provides a waxy, opaque coating which does not alter the appearance of the surface. The microscopy image shows that the coating method covers the entire surface, up to the edge of the coupon meaning the entire exposed surface will be coated. This even coating provides a distinct aesthetic advantage over conservation microcrystalline wax, which can appear lumpy and streaky on application. The appearance is characteristic of a relatively uniform coating.

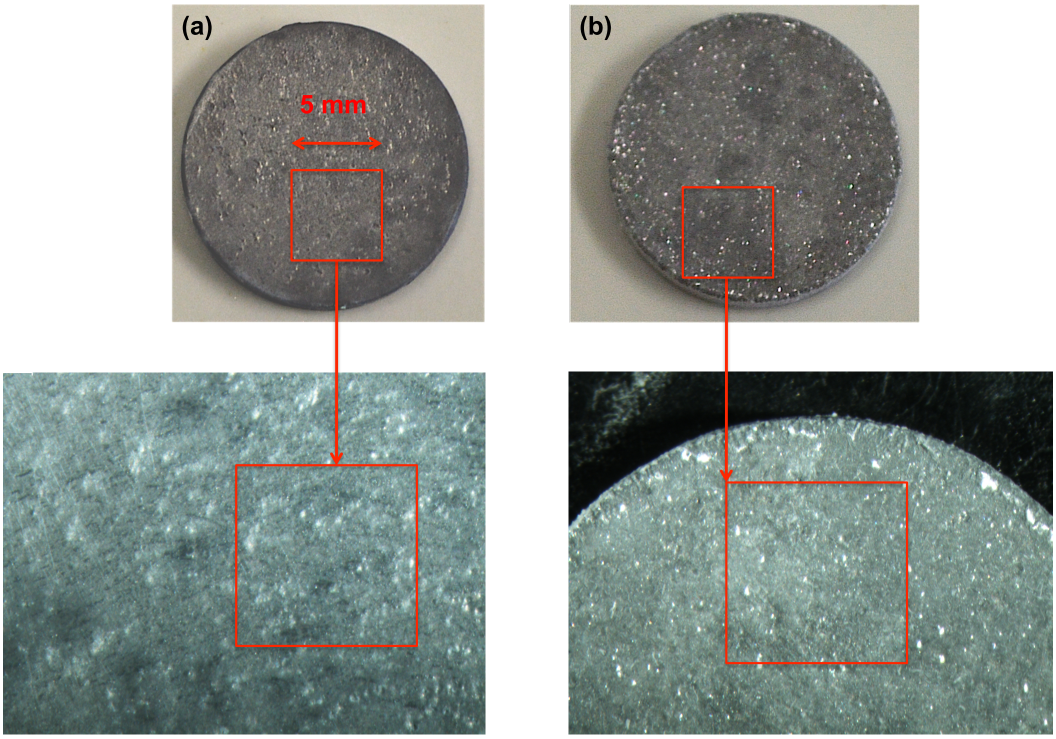

Figure 4.9 Photograph and microscopy image of corroded (a) and C14 coated corroded (b) lead.

X-ray diffraction

Figure 4.10 shows the X-ray diffraction patterns for coating corroded lead compared to the corroded precursor. Fluctuations in the background signal are due to statistical noise. Reference data was acquired from the ICDD database.

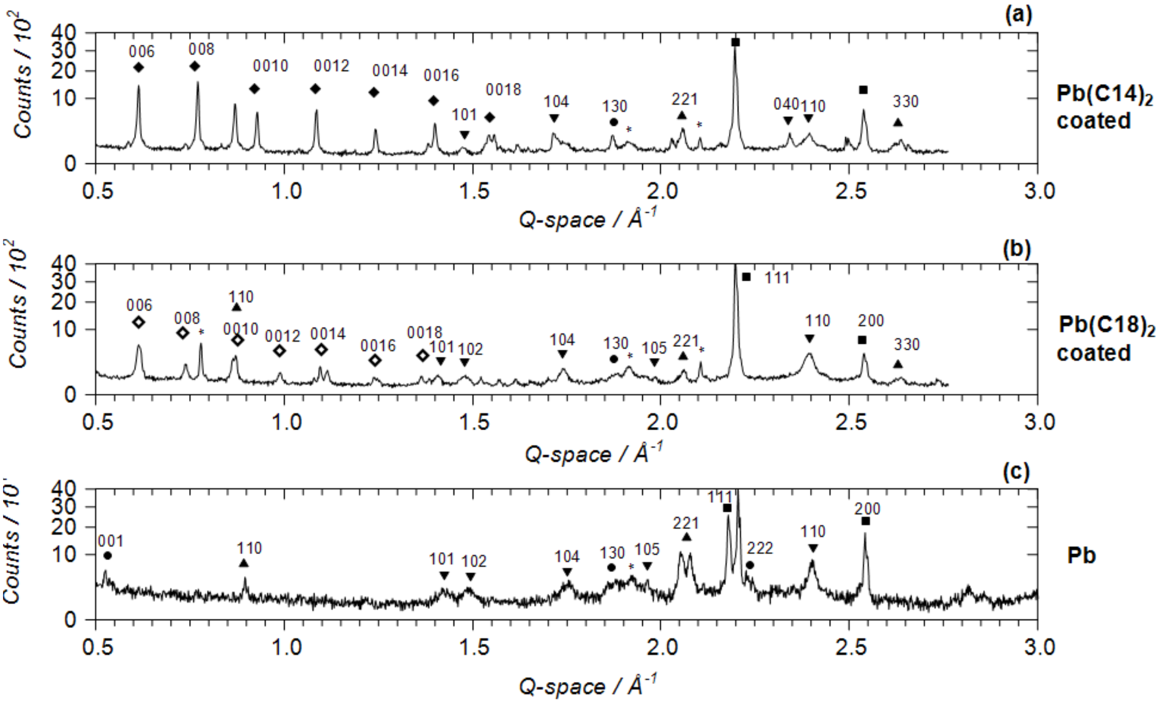

Figure 4.10 XRD diffraction patterns for C14 (a) and C18 (b) coated corroded lead compared with the corroded lead precursor (c). All peaks are indexed apart from unidentified peaks (*): lead acetate •, lead formate ▲, hydrocerussite ▼, lead ■, lead ditetradecanoate ◆ and lead dioctadecanoate ◇.

In both Figure 4.10 (a) and Figure 4.10 (b), crystalline corrosion products are detected, namely lead formate (ICDD No. 014-0825) and hydrocerussite (ICDD No. 13-0131). Lead formate is a reaction product of the lead oxide and formic acid [29], which is emitted from the oak [30] as a biodegradation product derived from formaldehyde. Lead acetate (ICDD No. 001-0028) has been found to be the main precursor to hydrocerussite (see Chapter 5) but equally lead formate can form this corrosion product [29,31,32]. In the GC-MS analysis of the VOCs emitted from this sample, no formic acid was detected due to low molecular weight limits of the detector. However, lead formate could not have formed from any material except formic acid: the presence of lead formate confirms the emission of formic acid from the oak. Acetic acid and possible acetic acid reaction products were detected using GC-MS but due to the lack of lead acetate peak at 0.55 $Å^{-1}$, we cannot deduce which short chain lead carboxylate was responsible for hydrocerussite formation. However it is possible that both lead acetate and lead formate acted as intermediates [32].

Most peaks detected from the coated samples area also found in the non-coated sample and appear sharper compared to the corroded lead. However, key lead acetate reflections are not seen in the coated corroded samples (001, 222). Lead acetate is soluble in water and ethanol [29] and so could have dissolved during coating. Other crystalline species observed in this experiment are not soluble in water.

The mass thickness of the layers of lead ditetradecanoate ($Pb(C14)_2$) have been previously calculated for polished samples (Section 4.3.3) and the related thickness values are shown in Table 4.2. The thicknesses calculated are semi-quantitative values based on the absorption of x-rays reflected from the lead surface by a coating on lead and the density of the coating (see Chapter 5). A literature thickness of the microcrystalline wax coating is comparable to the carboxylate coating on polished lead. It is expected that the polished sample would provide a thinner layer than the coated corroded sample due to the smaller amount of precursor oxide on the surface.

The calculation for thickness involves the mass attenuation coefficient, which quantifies the absorption of X-rays by the compounds covering the lead (corrosion products or coating). The thickness calculation for the corroded lead and polished coated lead use the mass attenuation coefficients for hydrocerussite (162.8 cm^2 g^{-1}) and lead ditetradecanoate (65.9 cm^2 g^{-1}), respectively. We cannot calculate the thickness of the layer on the lead in the coated corroded sample because the proportions of these compounds on the surface are not known.

Comparing Figure 4.10 (c) to Figure 4.10 (a) and (b) we can see that the height of the lead peak increases by one order of magnitude on coating. This could be due to the coating formation reaction: amorphous corrosion products [23] could dissolve and react with the carboxylate in solution to produce a thinner total layer of corrosion products plus coating compared to the initial corroded substrate.

Table 4.2 shows the peak area of the lead ditetradecanoate coating on the corroded lead sample has a greater intensity than the polished sample (the Pb 111 peak heights are comparable in both cases). This suggests that the layer of lead ditetradecanoate is thicker on the corroded sample compared to the polished sample, possibly due to the greater availability of Pb^{2+} ions from the pre-corrosion of the substrate. Furthermore, thick coatings, like those observed here, are formed on rough surfaces for simple morphological reasons. Electrochemical impedance data will be able to inform us as to the effectiveness of the coating on the corroded lead.

Table 4.2 Coating properties.

Coating	Thickness, µm	Peak area PbC14 002/Pb 111 ratio
$Pb(C14)_2$, polished lead	39.7	0.43
$Pb(C14)_2$, corroded lead	-	1.48
Corroded lead	23.8	-
Microcrystalline wax	40 [33]	-

Electrochemical impedance spectroscopy of corroded and polished coated samples

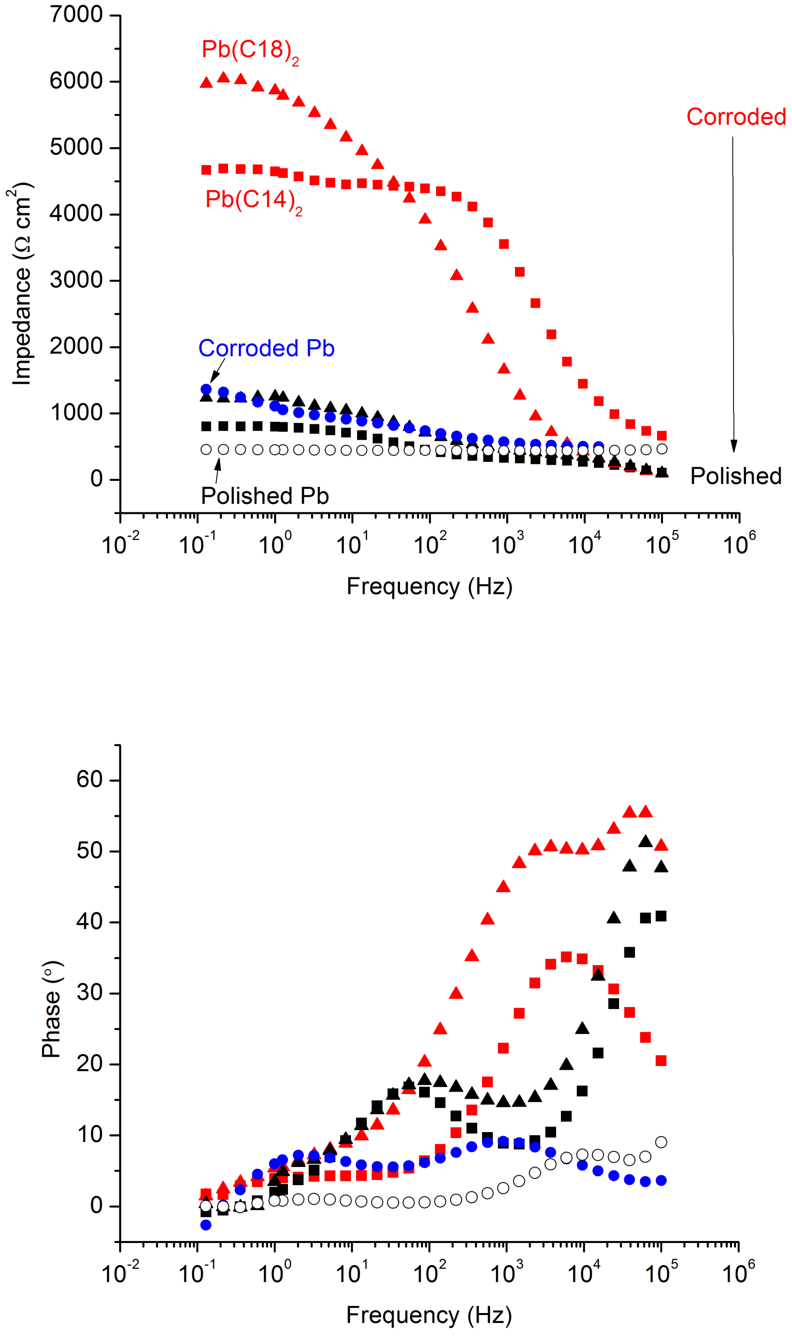

Figure 4.11 Impedance (a) and phase (b) plots of Pb(C14)$_2$ (squares) and Pb(C18)$_2$ (triangles) coatings on polished (black) and corroded (red) lead substrates. Bare lead (open circles) and corroded lead (blue circles) are also shown.

Figure 4.11a shows the impedance of the polished and corroded coated samples over a specified frequency range. The ASTM D electrolyte models atmospheric corrosion so the higher the impedance values at low frequencies, the greater the resistance of the coating to atmospheric corrosion. The difference in impedance between the corroded and polished coated samples is considerable. The data at low frequencies show an 83 % increase in coating impedance for lead dioctadecanoate ($Pb(C18)_2$) and 79 % increase for $Pb(C14)_2$ corroded samples compared to polished samples. The XRD results show that the corroded surface allows a thicker coating to form. This increased thickness of the coating could be the source of vastly improved impedance and resistance to the corrosive electrolyte.

The impedance of the polished coated samples is larger than bare lead, but not larger than corroded lead. As calculated previously, there is a significant layer of corrosion products on the surface of the corroded coupon which provides a protective layer against the electrolyte compared to bare lead. However by coating the samples, the improved impedance effect is not simply additive (polished coated sample plus corroded sample). This implies a significant improvement of the coating properties by forming the coating on a corroded sample possibly due to the thicker layer formed. This result is promising for future trials with real lead artefacts.

Figure 4.11b shows the corresponding Bode phase plots. For polished, corroded and bare samples, two maxima (time constants) are shown showing the freely corroding nature of the metal substrate by the corrosive electrolyte. The corroded coated samples show a single maximum due to a lack of significant corrosion of the underlying lead. For the polished samples, the first maximum at ~70 Hz is the same for both samples. This maximum corresponds to the double layer and surface oxide and demonstrates the reproducibility of the polishing technique. The second maximum at ~10000 Hz corresponds to the coating. For the $Pb(C18)_2$ coating this maximum is approximately 10° higher due to the improved corrosion resistance provided by the longer carbon chain. The corroded coated samples show a single time-constant at ~10000 Hz. This is due to the combined corrosion and coating layer providing greater corrosion resistance from the electrolyte. The $Pb(C18)_2$ coating is 15° higher than $Pb(C14)_2$ for the same reasons as the polished samples. However, the improved capacitive properties compared to the polished sample could be due to the improved thickness of the coating due to coating deposition on the corroded surface, as observed in the impedance plots.

4.4 Conclusions

In this chapter it has been shown that long chain carboxylates are easy to prepare and quick to apply to lead surfaces when the carboxylic acid is dissolved into an ethanolic solution. Evaporation of the solvent leaves behind the $Pb(C14)_2$ coating only, if the correct inhibitor concentration is used. For this lead surface preparation method, a concentration of between 0.01 and 0.05 mol L^{-1} is optimal. This will afford a coating mass thickness of approximately 0.045 g cm^{-2}.

Impedance tests showed that the coating is susceptible to electrolyte penetration, especially by acetic acid. Coatings prepared using longer chain carboxylates, are less susceptible to electrolyte penetration, although the compounds become progressively less soluble in ethanol.

Further work should include a review of the sample coating process. At present the mounting of the coated sample within the working electrode holder can cause damage to the coating (as seen in the optical microscopy results). The result of this damage is irreproducibility in the impedance data. Coating bare samples after mounting in the working electrode holder is possible, and demonstrates the ease of application of this coating. In Chapter 5, the long-term stability of these coatings in atmospheres polluted with oak VOCs will be tested.

Lead samples were artificially aged within an oak environment and coated with ethanolic solutions of tetradecanoic and octadecanoic acid. By coating a corroded sample instead of a polished surface, the effects of real artefact conservation by immersion in ethanolic carboxylate solution could be observed. XRD data showed an order of magnitude greater intensity if the carboxylate was applied to a corroded coupon, which implies a thicker coating. This improved coating was also shown in impedance and phase plots, where the effectiveness of the coating on corroded coupons was approximately 80% higher than polished and corroded coupons. These results are encouraging for future trials with real lead artefacts, seeing as corroded lead coupons are a more accurate representation of objects likely to be conserved.

4.5 References

[1] E. Rocca, J. Steinmetz, Inhibition of lead corrosion with saturated linear aliphatic chain monocarboxylates of sodium, Corrosion Science. 43 (2001) 891–902.

[2] M. Dowsett, A. Adriaens, B. Schotte, G. Jones, L. Bouchenoire, In-situ spectroelectrochemical study of the growth process of a lead decanoate coating as corrosion inhibitor for lead surfaces, Surface and Interface Analysis. 41 (2009) 565–572.

[3] M. Dowsett, A. Adriaens, B. Schotte, G. Jones, Real time spectroelectrochemical growth and corrosion resistance monitoring of lead carboxylate coatings in an environmental cell (eCell), in: C. Degrigny, R. van Langth, I. Joosten, B. Ankersmit (Eds.), Metal 07: Proceedings of the Interim Meeting of the ICOM-CC Metal Working Group, Rijksmuseum, Amsterdam, 2007: pp. 26–31.

[4] K. De Wael, M. Keersmaecker, M. Dowsett, D. Walker, P.A. Thomas, A. Adriaens, Electrochemical deposition of dodecanoate on lead in view of an environmentally safe corrosion inhibition, Journal of Solid State Electrochemistry. 14 (2009) 407–413.

[5] M. De Keersmaecker, K. De Wael, A. Adriaens, The use of lead dodecanoate as an environmentally friendly coating to inhibit the corrosion of lead objects: Comparison of three different deposition methods, Progress in Organic Coatings. 74 (2012) 1–7.

[6] A. Adriaens, F. De Bisschop, M. Dowsett, B. Schotte, Growth and real time corrosion resistance monitoring of lead decanoate coatings, Applied Surface Science. 254 (2008) 7351–7355.

[7] A. Elia, M. Dowsett, A. Adriaens, On the use of alcoholic carboxylic acid solutions for the deposition of protective coatings on copper, in: P. Mardikian, C. Chemello, P. Hull, C. Watters (Eds.), Metal 10: Proceedings of the Interim Meeting of the ICOM-CC Metal Working Group, Clemson University, 2010: pp. 144–150.

[8] A. Elia, K. Wael, M. Dowsett, A. Adriaens, Electrochemical deposition of a copper carboxylate layer on copper as potential corrosion inhibitor, Journal of Solid State Electrochemistry. 16 (2011) 143–148.

[9] F. Mirambet, S. Reguer, E. Rocca, S. Hollner, D. Testemale, A complementary set of electrochemical and X-ray synchrotron techniques to determine the passivation

mechanism of iron treated in a new corrosion inhibitor solution specifically developed for the preservation of metallic artefacts, Applied Physics A. 99 (2010) 341–349.

[10] R.A. Walker, K. Wilson, A.F. Lee, J. Woodford, V.H. Grassian, J. Baltrusaitis, G. Rubasinghege, G. Cibin, A. Dent, Preservation of York Minster historic limestone by hydrophobic surface coatings., Scientific Reports. 2 (2012) 880.

[11] S. Mauchauffee, E. Meux, M. Schneider, Determination of the Solubility Products in Water at 20 °C of 32 Metallic Carboxylates, Industrial & Engineering Chemistry Research. 47 (2008) 7533–7537.

[12] J. Tètreault, J. Sirois, E. Stamatopoulou, Studies of lead corrosion in acetic acid environments, Studies in Conservation. 43 (1998) 17–32.

[13] M.G. Dowsett, A. Adriaens, Cell for simultaneous synchrotron radiation X-ray and electrochemical corrosion measurements on cultural heritage metals and other materials., Analytical Chemistry. 78 (2006) 3360–5.

[14] S. Nikitenko, A.M. Beale, A.M.J. van der Eerden, S.D.M. Jacques, O. Leynaud, M.G. O'Brien, D. Detollenaere, R. Kaptein, B.M. Weckhuysen, W. Bras, Implementation of a combined SAXS/WAXS/QEXAFS set-up for time-resolved in situ experiments., Journal of Synchrotron Radiation. 15 (2008) 632–40.

[15] M. Dowsett, A. Adriaens, EC188 Final Report: Time-resolved XRD and XAS for the conservation / protection of heritage and other metals using XMaS, 2011.

[16] A. Adriaens, M. Dowsett, K. Leyssens, B. Van Gasse, Insights into electrolytic stabilization with weak polarization as treatment for archaeological copper objects., Analytical and Bioanalytical Chemistry. 387 (2007) 861–8.

[17] P. Sacco, F. Quaglio, Validation of the Radiello® Diffusive Sampler for the Measurement of Formic and Acetic Acids in Museum Environments, The Reporter. 26 (2008) 22–23.

[18] D15.06 Subcommittee, ASTM D1384-87 Standard Test Method for Corrosion Test for Engine Coolants in Glassware, in: Engine Coolants; Halogenated Organic Solvents and Fire Extinguishing Agents; Industrial and Specialty Chemicals, West Conshohocken, PA, 1988.

[19] M. De Keersmaecker, M. Dowsett, R. Grayburn, D. Banerjee, A. Adriaens, In-situ spectroelectrochemical characterization of the electrochemical growth and breakdown of a lead dodecanoate coating on a lead substrate., Talanta. 132 (2015) 760–8.

[20] M. De Keersmaecker, K. Verbeken, A. Adriaens, Lead dodecanoate coatings for the protection of lead and lead–tin alloy artifacts: Two examples, Applied Surface Science. 292 (2014) 149–160.

[21] H.D. Burrows, M.D.G. Miguel, R.P.C. Pereira, N.M.B. Proença, S.M.C. Cardoso, C.F.G.C. Geraldes, M.H. Gil, W. Brown, Solution behaviour of lead(II) carboxylates in organic solvents, Colloids and Surfaces A: Physicochemical and Engineering Aspects. 250 (2004) 459–465.

[22] M.C. Bernard, S. Joiret, Understanding corrosion of ancient metals for the conservation of cultural heritage, Electrochimica Acta. 54 (2009) 5199–5205.

[23] A. Niklasson, L.-G. Johansson, J.-E. Svensson, The influence of relative humidity and temperature on the acetic acid vapour-induced atmospheric corrosion of lead, Corrosion Science. 50 (2008) 3031–3037.

[24] R. Wiesinger, I. Martina, C. Kleber, M. Schreiner, Influence of relative humidity and ozone on atmospheric silver corrosion, Corrosion Science. 77 (2013) 69–76.

[25] D. Loveday, P. Peterson, B. Rodgers, Evaluation of Organic Coatings with Electrochemical Impedance Spectroscopy Part 2 : Application of EIS to Coatings, JCT CoatingsTech. (2004) 88–93.

[26] R.W. Corkery, S.T. Hyde, On the Swelling of Amphiphiles in Water, Langmuir. 12 (1996) 5528–5529.

[27] C.M. Oertel, S.P. Baker, A. Niklasson, L.-G. Johansson, J.-E. Svensson, Acetic Acid Vapor Corrosion of Lead–Tin Alloys Containing 3.4 and 15% Tin, Journal of the Electrochemical Society. 156 (2009) C414.

[28] J. Tétreault, E. Stamatopoulou, Determination of concentrations of acetic acid emitted from wood coatings in enclosures, Studies in Conservation. 42 (1997) 141–156.

[29] C.M. Mauck, T.W.P. van den Heuvel, M.M. Hull, M. Zeller, C.M. Oertel, Synthesis and structures of Pb3O2(CH3COO)2·0.5H2O and Pb2O(HCOO)2: two corrosion products revisited., Inorganic Chemistry. 49 (2010) 10736–43.

[30] E. Roffael, Volatile organic compounds and formaldehyde in nature, wood and wood based panels, Holz Als Roh- Und Werkstoff. 64 (2006) 144–149.

[31] A. Niklasson, L.-G. Johansson, J.-E. Svensson, Atmospheric Corrosion of Lead, Journal of the Electrochemical Society. 154 (2007) C618.

[32] J. Tétreault, E. Cano, M. van Bommel, D. Scott, M. Dennis, M.G. Barthés-Labrousse, L. Minel, L. Robbiola, Corrosion of copper and lead by formaldehyde, formic and acetic acid vapours, Studies in Conservation. 48 (2003) 237–250.

[33] P. Pouli, K. Melessanaki, a. Giakoumaki, V. Argyropoulos, D. Anglos, Measuring the thickness of protective coatings on historic metal objects using nanosecond and femtosecond laser induced breakdown spectroscopy depth profiling, Spectrochimica Acta Part B: Atomic Spectroscopy. 60 (2005) 1163–1171.

Chapter 5 – Testing lead coatings in model and real museum environments

This chapter is based in part on a published article: R. Grayburn, M. Dowsett, M. De Keersmaecker, E. Westenbrink, J.A. Covington, J.B. Crawford, M. Hand, D. Walker, P.A. Thomas, D. Banerjee, A. Adriaens, Time-lapse synchrotron X-ray diffraction to monitor conservation coatings for heritage lead in atmospheres polluted with oak-emitted volatile organic compounds, Corrosion Science. 82 (2014) 280–289.

5.1 Introduction

Coatings such as carboxylates, waxes and acrylics [1] are often applied to museum objects to protect them against corrosion caused by VOCs [2–5], anthropogenic gases [6,7] and humid conditions [8]. This is vital for the preservation of historic and cultural information held on the visible surface of an object, or for tone preservation in the context of organ pipes and other musical instruments [9,10]. In this chapter, carboxylate coatings are tested in model and real museum environments and compared with uncoated samples to gauge the effect of VOCs on the coating performance.

5.1.1 VOCs in heritage environments

The release of VOCs from oak is a result of the biodegradation and metabolic processes within the wood [11,12]. The interaction between lead (and its alloys) and oak can be found in many cultural heritage contexts where the materials co-exist in the same environment. For example, within a pipe organ the lead-rich pipes can react with VOCs emitted by the oak wind chest [7,13–16] causing degradation of the pipe structure through pitting and cracking. As a consequence this can lead to a substantial loss of timbre within the instrument and ultimately the loss of the affected pipe [13].

Other examples of VOC sources in cultural heritage contexts are found within museum display cases. Although many modern display cases attempt to explicitly omit wood and other VOC sources from their structure [17–20], antique wooden cases which have their own heritage value can still be found in use. In addition, wood coatings within these cases can be the source of VOCs such as acetic acid, which is known to corrode metallic surfaces [2,21]. Archival collections also suffer from self-degradation due to acetic and formic acid emissions from paper. Paper, being a product of wood, is liable to the same acid-producing degradation mechanism as display cases [22].

Passive and active sampling techniques exist to qualify the VOCs in heritage environments and have been used widely to help to understand the corrosion of cultural heritage materials [23–25]. Both categories of technique involve the adsorption of VOCs onto a material, which is then used to identify the VOCs. The difference between active and passive techniques lies in the way the atmosphere is moved to the sampling material: active sampling requires the pumping of air from the source (e.g. within an organ windchest) over the sampling material surface whereas passive techniques rely on the diffusion of gases to the sampling material. The adsorption of VOCs commonly found in museum collections onto carbon or polymer-based materials is a popular method to qualify VOCs when used alongside GC-MS as there is no need for expensive active sampling pumps. Thermal desorption of the VOCs from the adsorbent material occurs within the gas chromatograph and is able to detect masses as low as formic acid accurately [3,14,24–26]. In this work two passive GC-MS sampling techniques are used.

Due to the noted destructive effect of acidic VOCs, it is important to test the effectiveness of the proposed conservation coating when exposed to a museum environment. Previously, an oak-polluted environment has been modelled by using vapour from pure acetic acid to study the deterioration of carboxylate coatings [27,28]. In this work, real volatile organic compounds emitted from wood were used to react with the coated surface. The resulting crystalline corrosion products were monitored using X-ray diffraction.

5.2 Experimental

5.2.1 Sample preparation

Lead coupon preparation

Lead coupons with a diameter of 13 mm were pressed from 2 mm thick 99.95% lead metal sheet (Goodfellow Ltd., Cambridge, UK) and machined in an oil-free environment to a diameter of 12.5 mm.

One surface was then polished and cleaned using a protocol designed to eliminate as much preparation-related contamination as possible. This is as follows: The lead surface was polished by hand using a damp abrasive disc (BuehlerMet II ®, Germany) to remove visible surface defects and to expose a fresh metal surface. Coupons were then polished using a sequence of diamond polishes with decreasing particle sizes (6 µm, 3 µm, 1 µm Buehler MetaDi ® polycrystalline diamond suspension). A polishing cloth (Buehler MicroCloth ®) was saturated with the appropriate diamond suspension. A custom-made jig fitted to an automatic polisher (Buehler Minimet ® 1000) was used to hold the coupons in place during automated polishing. Coupons were polished for 15 minutes using each diamond suspension followed by rinsing with 2-propanol (99.5%, reagent grade) and cleaning in 2-propanol for 5 minutes in an ultrasonic bath. After polishing with the 1 μm diamond suspension, the coupons were ultrasonically cleaned in 2-propanol for 3 x 5 minutes, with fresh propanol for each cleaning cycle. Polished coupons were stored in 2-propanol until required.

Coating Preparation

Tetradecanoic acid (1.14 g, 5 mmols, ≥ 98% purum, Fluka Analytical) was dissolved in ethanol (100 mL, 99.99% reagent grade) to make a 0.05 mol L^{-1} solution. Octadecanoic acid (1.42 g, 5 mmols, ≥ 98% purum, Fluka Analytical) was dissolved in ethanol (100 mL, 99.99% reagent grade) to make a 0.05 mol L^{-1} solution. Polished lead coupons were coated by immersing them in this solution overnight in a sealed beaker and then allowing them to dry naturally in air.

For the museum tests, coupons were also coated with Renaissance wax (Picreator Enterprises Ltd, London UK) which is a microcrystalline wax commonly used by conservators for a range of heritage materials [1,29]. The wax was simply applied using a dry cloth (TechniCloth, Texwipe, USA) and left to dry for 1 hour before testing.

5.2.2 Creating the oak environment – *in situ* and *ex situ* XRD

Ex situ experiments

To study some longer-term effects of oak VOCs on the coated lead, an oak polluted environment was created within a desiccator with a total volume of 800 cm^3. A total of 150 cm^3 of a saturated solution of sodium chloride at the base of the desiccator created an elevated relative humidity (RH): up to 75% for the ambient test temperatures (18 - 20 °C) [30]. Coated and uncoated lead samples were placed on a shelf alongside thirteen 1 cm^3 oak cubes within the desiccator for 2, 7 and 30 days. Coated and uncoated reference samples were simply left covered in air for the same period of time. The 2 and 7-day sample preparation was carried out by Michel de Keersmaeker from the ESA group, UGent. The oak cubes were cut from a piece of contemporary oak (*Quercus sp.*) on a fine band saw to expose a fresh oak surface. The ratio of the oak surface area to air volume was 0.12 cm^{-1}.

Ex situ XRD measurements of samples exposed for 30 days to oak and laboratory air were carried out at the University of Warwick on a PANalytical X'Pert Pro X-Ray MRD X-Ray powder diffractometer equipped with a curved Johansson monochromator giving pure Cu-K_α X-rays at a wavelength of 1.540598 Å and a PIXcel detector allowing for faster data acquisition. The X-ray beam width was controlled using an automatic divergence slit to give a fixed 9 mm by 5 mm footprint on the sample. A 70 minute θ - 2θ scan from 1° - 70° 2θ with a step size of 0.0132° 2Θ was performed on each sample. Samples exposed for 2 and 7 days were analysed at Universiteit Gent using a Siemens D5000 diffractometer using Cu-K_α X-rays with a wavelength of 1.5405 Å with a scintillation counter detector. A 185-min scan from 1° to 70° 2θ with a step size of 0.02° 2Θ was performed on each sample. The D5000 measurements were carried out by Olivier Janssens (Department of Solid State Sciences, UGent).

Tests in a 'real' oak environment – het Museum voor de Geschiedenis van de Wetenschappen

The University of Ghent's History of Science museum houses not only an impressive collection of historic scientific instruments: the display cases themselves are also artefacts in their own right. The display case used in this work houses a collection of Bakelite artefacts but was originally an old library or office case in the Plateau building of the university. It is not inconceivable that the case was part of the original furniture of that building, and therefore would date back to the late 19th century [31].

In order to test the effectiveness of the coatings in a real environment, the coated samples were mounted on a custom-made sample holder made from polycarbonate and placed inside the display case (Figure 5.1, labels 1-4). Bare lead coupons were also mounted to compare the rate of corrosion with coated samples. Polycarbonate was deemed suitable for use in this study as it is benign in a heritage context and is sometimes used for display case glazing [32]. The humidity and temperature were logged continuously (hourly) using a Hanwell ML4106 datalogger (Letchworth, UK) within the cabinet (Figure 5.1, label 5) and the environment was qualified using GC-MS (Figure 5.1, label 6, see description in following section). X-ray diffraction patterns from bare lead coupons and the coupons coated with $Pb(C14)_2$, $Pb(C18)_2$ and microcrystalline wax were recorded before and after placement inside the display case. Samples were placed for seven months under these conditions. XRD analyses were performed before and after placement in the display case using an ARL X' TRA Powder Diffractometer using Cu-K_α X-rays with a wavelength of 1.5405 Å with a scintillation counter detector. A 185-minute scan from 2 - 40° 2θ with a step size of 0.02° 2Θ was performed on each sample. These measurements were carried out by Tom Planckaert (Department of Inorganic and Physical Chemistry, UGent).

Figure 5.1 The Experiment Exhibition. Nine 'conserved' coupons and three 'unconserved' coupons were displayed on a custom-made polycarbonate mount. The environment was continuously monitored and a small interpretation panel was erected (inset). (Copyright: Rosie Grayburn)

In situ experiments

Time-lapse *in situ* XRD measurements took place on the DUBBLE beam line, ESRF within the eCell Mk III, whose prototype is described elsewhere [33]. The eCell was created for *in situ* measurements on a synchrotron beam line and is designed to host a range of liquid or gaseous environments.

Oak annuli were made to the largest size which would fit the cell without obstructing the mechanism (Figure 5.2). The objective was to achieve the highest partial pressure of VOCs in the shortest time with an oak surface area to cell volume ratio of 0.6 cm^{-1} so as to observe the effects on a time-scale compatible with a synchrotron experiment. The dimensions were: outside diameter 4.1 cm, inside diameter 2 cm, height 0.7 cm. After machining, the annuli were stored in a sealed container. A separate annulus was used for each experiment described below. A relative humidity of up to 75% was produced within the eCell by attaching a specially designed environment generator containing the saturated sodium chloride solution to one of the cell ports (see Figure 5.2 and Figure 6.3). Two experiments are reported here: In the first, a coated lead coupon was exposed to oak VOCs from the annulus for 14 hours with humidity controlled by the environment generator described above. In the second, a similar experiment was carried out on bare lead for 7 hours. In this case oak VOC exposure was at the ambient RH of around 50%. Samples were placed on a sample holder within the cell, so that they could be automatically positioned around 200 μm from the X-ray window during XRD acquisition and then retracted to allow the environment unrestricted access to the surface.

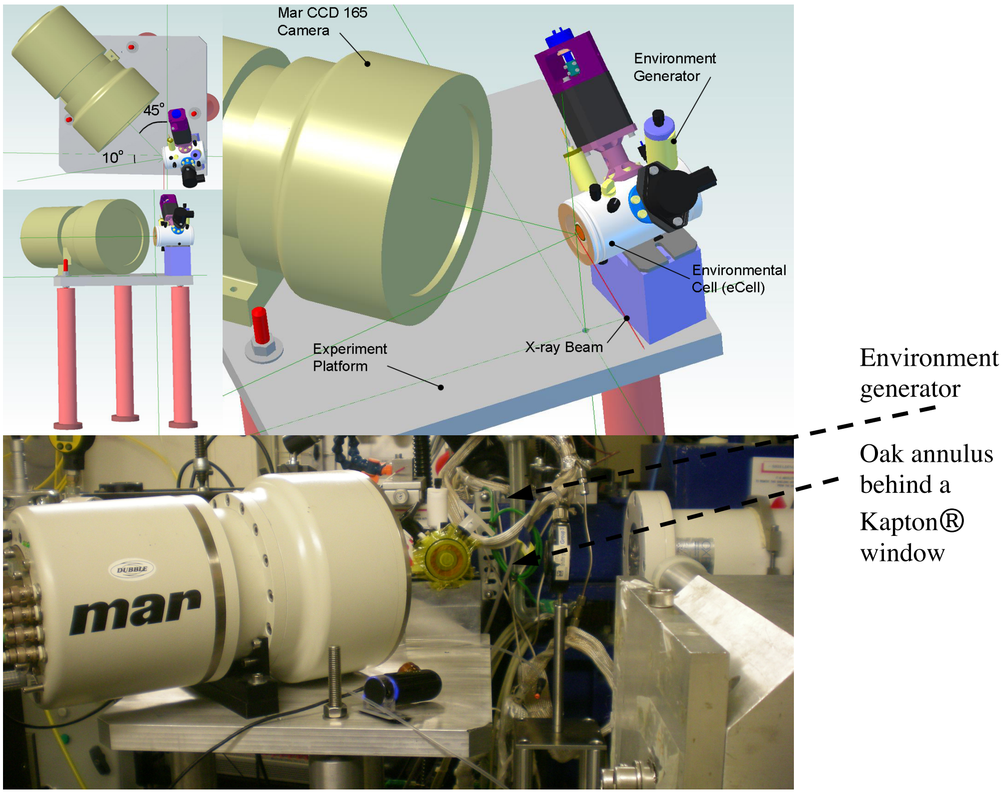

Figure 5.2 The set-up on the DUBBLE beamline for time-lapse XRD of the effect of oak VOCs on the lead tetradeconate coating using the eCell MkIII and the Mar camera. The eCell is shown here with a Kapton® window held in place by an O-ring. An oak annulus and an environment generator provide the corrosive environment. See Figure 6.3 for environment generator assembly.

Time-lapse interactions of lead samples with oak VOC atmospheres were studied using SR-XRD at DUBBLE [34] (station BM26A, ESRF, Grenoble, France). X-rays with a wavelength of 1.5498 Å were incident at 10° to the surface producing a footprint of 6 mm x 200 µm. A Mar CCD 165 (Mar USA Inc., Evanston, IL, USA) 2D detector was used to record 2D diffraction patterns of the corroding lead surface. The axis of the CCD camera was at 40.5° to the incident X-ray beam. The axial distance between the face of the detector and the beam center on the sample surface was 130 mm. Time-lapse sequences of images were collected, comprising XRD patterns with a 15-second exposure time recorded every 10 minutes for 14 hours (coated lead) and 7 hours (bare lead). A fast shutter was used to shield the sample from the X-rays between exposures.

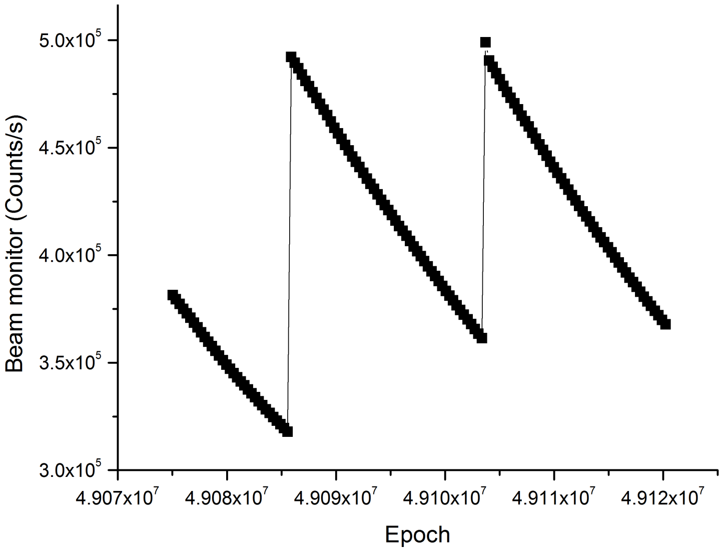

Figure 5.3 Beam monitor changes during the course of the time-lapse SR-XRD experiment detailed in this section. The beam was refilled twice during the experiment. Epoch is recorded in the spec file for the data. The beam monitor is recorded through an ion chamber via a frequency-count converter.

All XRD data were processed using the group's esaProject 2013 software [35]. All extracted patterns from SR-XRD were normalized to the beam monitor (from an ion chamber) in order to account for beam decay (Figure 5.3). Patterns are given as intensity or counts vs. wave number Q ($=2\pi/d$ where d is the d-spacing), so that they can be compared on a common scale.

5.2.3 GC-MS of Oak VOCs

GC-MS of oak VOC environment within the eCell

The eCell was set-up with an acrylic dummy sample holder in lieu of a lead sample and the oak environment created as described in the previous section with the humidity generator providing a relative humidity of 75%. The closed eCell environment was allowed to equilibrate for one hour prior to sampling. A custom-made septum plug attached a Restek IceBlue® Septa to the cell allowing collection of VOCs using a solid-phase microextraction (SPME) tip assembly (DVB/CAR/PDMS; 24 ga needle size; RS 57348-U, Restek, US). The tip was cleaned prior to exposure in the cell by running it three times through the GC-MS procedure. It was then exposed to the environment within the cell for 5 minutes, 20 minutes or 3 hours before being manually injected into the GC-MS (SCION-SQ ™, Bruker). This involved exposing the fiber tip within the GC injector, which was kept at a constant temperature of 250 °C.

The resulting VOC gas sample was then split in the injector with a ratio of 1:10, allowing only one tenth of the sample through the column in order to sharpen the peaks on the eventual chromatogram. An initial column temperature of 50 °C was held for the first minute of the sample run, following which it was heated at a constant rate of 20 °C per minute to a maximum of 280 °C before being held constant for a further 2.5 minutes. This temperature profile was used to separate the different VOCs desorbed from the SPME fiber tip according to molecular weight, volatility and polarity before they were transmitted to the detectors.

The headspace from a 1 mM acetic acid (>99.85%, Sigma Aldrich no. 695084) solution was also sampled in an attempt to quantify the concentration of acetic acid emitted.

GC-MS of VOCs within the museum

The atmosphere was sampled using a RAD130 Radiello® (Padova, Italy) cartridge which was placed in the cabinet alongside the samples inside a diffusive body (Figure 5.1, label 6) [26]. After a recorded time, the cartridge was removed from the cabinet. The activated charcoal within the cartridge was removed and a weighed portion was placed within a Gerstel TDS2 desorption tube, held in place by two Gerstel screens. The GC-MS used in this work was an Agilent 6890 equipped with an Agilent 5973 MS, a Gerstal TDS 2 desorption system and a Gerstel CIS4 cooled injection system. The same temperature regime was used as for the eCell tests, except the initial column temperature was held for 2 minutes.

5.3 Results and discussion

5.3.1 GC-MS results

Analysis of a model environment inside the eCell

All peaks over 5×10^7 counts per second (cps) were identified (Table 5.1), using the NIST 2012 library. The compounds identified have been found in previous studies of oak emissions and museum environments [3,11,36–38] although the experimental methods are not directly comparable.

Table 5.1 List of VOCs detected from oak within the eCell at 75% RH at various tip exposure times using GC–MS.

Time (minutes)	VOC (peak label)	SPME Tip exposure time at which VOC is observed
1.320	Acetone (A)	5 minutes, 20 minutes, 3 hours
1.914	2-butanone (B)	5 minutes, 20 minutes, 3 hours
2.270	Acetic acid (C)	5 minutes, 20 minutes, 3 hours
2.645	2H-pyran-2-one (D)	3 hours only
2.858	Pentenal (E)	3 hours only
3.413	Toluene (F)	3 hours only
3.880	Acetic acid butyl ester (G)	5 minutes, 20 minutes, 3 hours
4.420	Furfural (H)	20 minutes, 3 hours
> 4.420	Styrene (I), Heptenal (J), benzaldehyde (K), octanal (L), limonene (M), nonanal (N), dodecanal (O), various other long-chain hydrocarbons	3 hours only

As VOC concentrations were allowed to accumulate in the oak VOC environment within the cell, the number of identifiable compounds increases according to the longer exposures of the SPME tip. However, the dominant component from all tip exposure-times is acetic acid. Figure 5.4 shows that three times more acetic acid is emitted compared to any other compound. The high prevalence of acetic acid is probably due to its active production via a known degradation pathway [39,40]. Therefore lead is susceptible to interaction with acetic acid even during short periods of exposure to oak within the eCell.

Acetone, 2-butanone and acetic acid butyl ester also feature at all exposure times. Acetone was detected from reference solutions of acetic acid so it is presumed to originate from the ambient atmosphere, although it is also known to have biosynthetic origins [11].

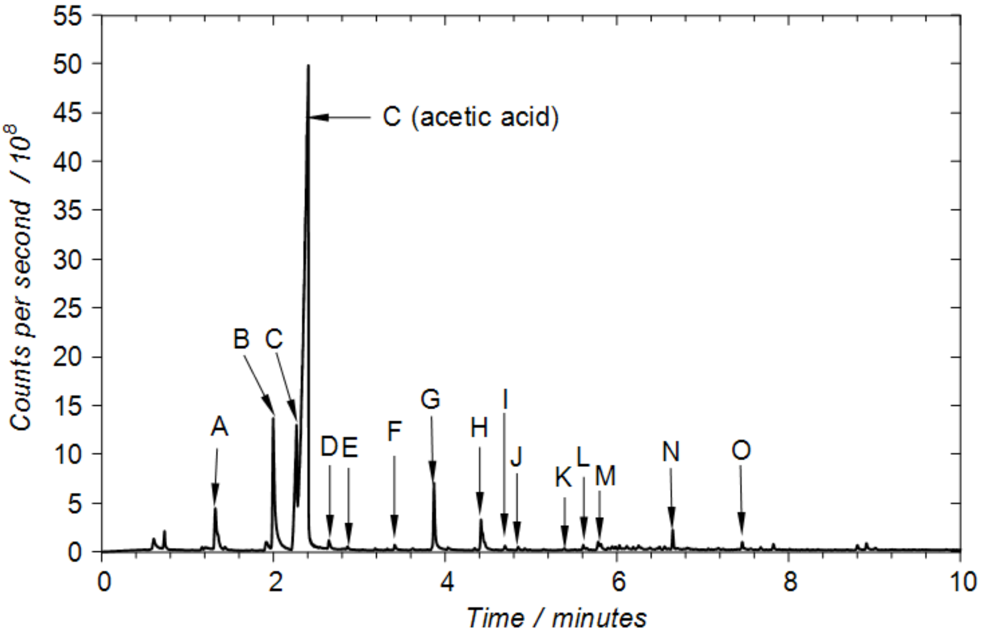

Figure 5.4 GC trace after 3 h exposure of the SPME tip to the oak environment within the eCell. Peak labels are explained in Table 1. The peaks below 1 min are attributed to carbon dioxide.

Over twenty VOCs were identified from the GC trace after 3 hours exposure to the oak environment, including an entire spectrum of saturated aldehydes from pentanal to dodecanal. The origin of these shorter-chain aldehydes in VOCs is unclear in literature but they could be degradation products resulting from prior heat-treatment of our wood sample [40]. Similarly furfural was only detected after 3 hours tip exposure. This cyclic aldehyde is a product of cellulose dehydration, either from enzymatic action or as a result of prior heat-treatment of the wood sample [41]. Limonene, a common terpene biosynthesised in plants [42], was detected after 3 hours tip exposure. Limonene is not a degradation product of wood so low detection concentration suggests diffusion of limonene out of the wood rather than active production.

Although we attempted to quantify the amount of acetic acid, the attempt was unsuccessful - the utility of this system to quantify the acetic acid concentration from oak is in doubt, because the emission of acetic acid from oak is an active process whereas the diffusion of acetic acid from its aqueous solution into air is passive. The headspace sampled from a 1 mmol L^{-1} acetic acid solution yielded an increased concentration of acetic acid with tip exposure time. Trace amounts of acetone and carbon dioxide were also measured. Polymers of three to six siloxane monomers were observed due to apparent stripping of the SPME tip (Figure 5.5).

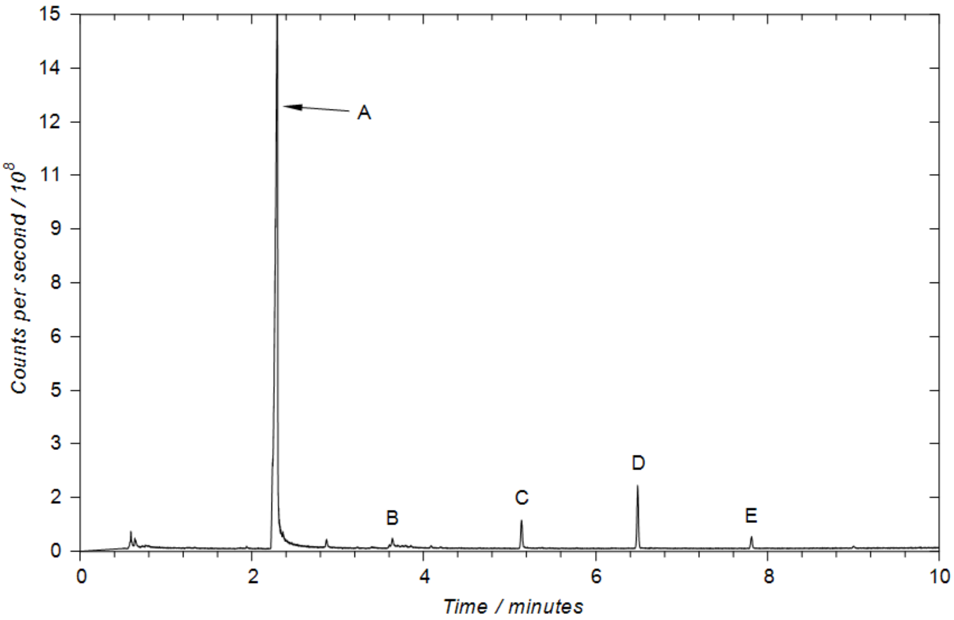

Figure 5.5 GC trace after 20 minutes exposure of the SPME tip to 1 mM acetic acid headspace. The peaks below 1 minute are attributed to carbon dioxide. Peaks identified as acetic acid (A), B (trisiloxane), C (tetrasiloxane), D (pentasiloxane) and E (hexasiloxane).

Analysis of the museum environment

Tests were carried out using a Radiello® cartridge which had been in place in the display case for 1 month. It was important to check if acetic acid was present within the museum environment so the corrosion mechanisms would be comparable with tests in the model oak VOC environments.

Trial GC-MS runs were designed to optimise the system prior to testing with a sample. A similar temperature program was used as in the SPME measurements but the method of extracting the VOCs from the adsorbent material was different, the volume of charcoal in the cartridge being larger than that of an SPME tip. The desorption regime required heating from 30 – 250 °C, and injection of the desorbed compounds into the column required the use of liquid nitrogen to achieve a temperature gradient from -150 – 300 °C.

Initial tests showed that the column was highly contaminated with fatty acids from previous measurements. Acetic acid and aldehydes were also detected. Therefore due to contaminants masking important VOC peaks, the GC-MS column was changed. The results from the new column are shown in Table 5.2. The Agilent software allows peak area determination and detection of trace amounts of VOCs, although the approximate location of the trace compounds must be known. In this case the SPME data can give information on the approximate locations of possible peaks. SPME and thermal desorption peak areas are non-comparable due to the different adsorbant materials used in each technique.

Table 5.2 List of VOCs detected from Museum of History of Science, Universiteit Gent over a 1 month period.

Time (minutes)	VOC	Peak area
3.956 – 4.136	Acetic acid	$(214 \pm 0.01) \times 10^6$
4.720 – 4.804	Furfural	trace
5.900	Octanal	$(1.9 \pm 0.001) \times 10^6$
6.727	Nonanal	$(1.7 \pm 0.001) \times 10^6$
7.481	Decanal	$(1.4 \pm 0.001) \times 10^6$

At first glance this data appears quite similar to the SPME data (Table 5.1, Figure 5.4) in the following ways: a large acetic acid signal compared to aldehydes, similar extraction times, similar VOCs detected. The results from longer-term museum exposure (4 months) gave unexpected results (no aldehydes, countless long chain and cyclic alkanes) due to the suspected degradation of the adsorbent active charcoal in the acidic museum environment. The source of error in these measurements originates from the Poisson noise on the counting detector. The VOC testing showed high concentrations of acetic acid which was presumed to come from the interior walls of the case, but due to the 'leakiness' of the cabinet it is possible there could have been an influence from other sources within the museum.

5.3.2 Long-term corrosion analysis by XRD

A model environment inside the eCell

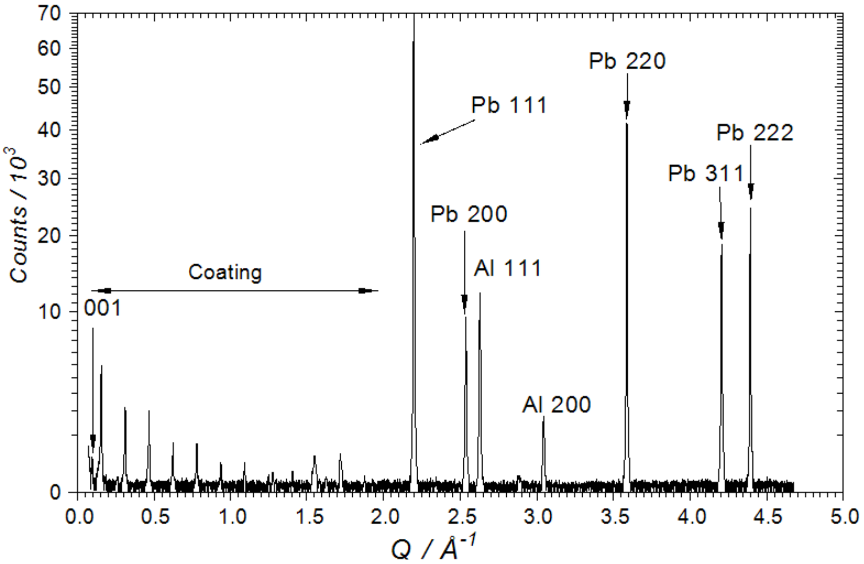

Figure 5.6 XRD pattern of the lead ditetradecanoate coating taken from a freshly prepared sample stored in laboratory air for 30 days (3 h scan). The Al peaks are from the sample holder and shifted by the height difference between the lead and aluminum surfaces. The y-axis of the XRD pattern in this figure is shown on a square-root scale in order to see the peaks of lower intensities.

An XRD pattern of a tetradecanoate coated lead coupon measured on the PANalytical X-ray diffractometer has been described previously in Figure 3.5. Figure 5.6 shows the XRD pattern of a tetradecanoate coated lead coupon after 30 days of storage in air measured on the PANalytical instrument. The data do not show any detectable crystalline corrosion products, thus demonstrating the effectiveness of the coating against appreciable corrosion in ambient conditions. The 001 reflection from the coating is visible in Figure 5.6. The other odd reflections are weak but just visible. The 00*n* reflection sequence in Figure 5.6 is consistent with a c-axis spacing of 80.5 ± 0.1 Å. Lead reflections are also identified. The other peaks in Figure 5.6 are due to the aluminum sample holder.

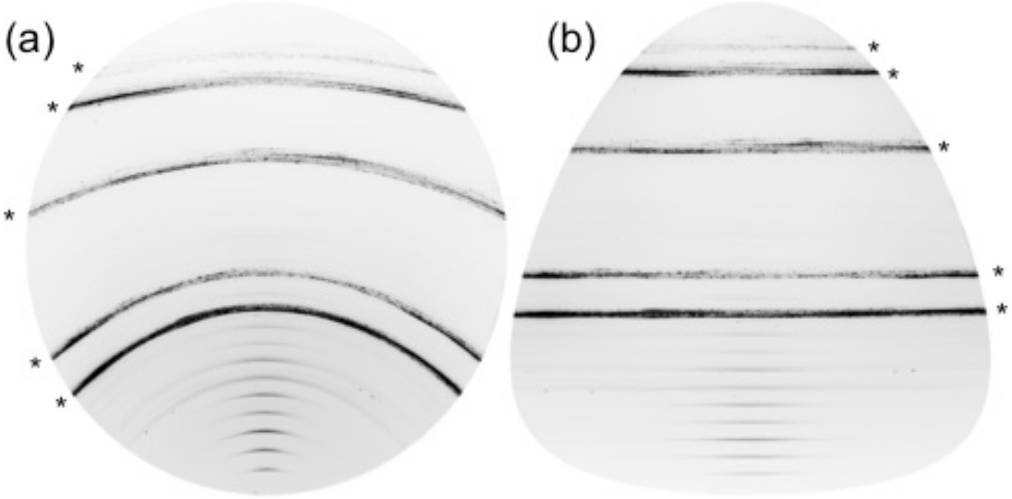

Figure 5.7 Raw (a) and reprojected [35] **(b) Mar SR-XRD diffractograms from a lead ditetradecanoate coated coupon acquired on DUBBLE beamline, ESRF. The acquisition time was 15 s. Lead reflections are denoted by a *.**

Figure 5.7 shows raw (a) and reprojected [35] (b) Mar diffractograms from a lead ditetradecanoate coated coupon acquired on DUBBLE. The acquisition time was 20 seconds. The lowermost ring is at Q = 0.7843 Å^{-1} (peak 5 in Figure 5.6). The coarse polycrystallinity of the lead coupon is demonstrated by the streaky and spotty nature of the lead rings. On the other hand, the evenly spaced rings which represent the lead ditetradecanoate are smooth and homogenous which shows that the coating is formed from small polycrystals [43] randomly oriented in 2 directions, but with strong c-axis alignment indicated by the intensification in the in-plane scattering direction. The 2D diffraction patterns from the Mar camera are simply integrated out of reprojected images, such as that shown in Figure 5.7 (b), by summing image rows.

Figure 5.8 summarizes the data from the exposure of lead to oak VOCs over periods of up to 30 days. In general, increased exposure times lead to increased backgrounds and loss of structure in the patterns. This can be attributed to four effects, viz: an increase in the number of peaks causing more overlap, broadening of peaks as long range order declines, the formation of amorphous phases, and deliquescence (frequently observed in environments with combined high RH and acetic acid concentrations [44]).

Figure 5.8a shows the progressive corrosion of the coated surfaces which were enclosed in the oak environment within a desiccator for 2, 7 (measured on the Siemens D5000 diffractometer) and 30 days respectively (measured on the PANalytical X-ray diffractometer). The most obvious effect of the oak environment after 2 days is the formation of lead acetate oxide hydrate ($Pb_3(CH_3COO)_6.PbO.H_2O$, ICDD No. 18-1739) (see peak at 0.55 $Å^{-1}$). The GC-MS data show that acetic acid is the main VOC emitted from oak (Figure 5.4), so it can presumed that this initial corrosion product derives from the reaction of acetic acid with the underlying lead, associated oxides and carbonates or with the coating itself.

Since these coatings are known to be hydrophobic we suppose that the reduction in pH of surface water through combination of water and acetic acid degrades this property. Then, the humid environment provides a thin film of water on the surface where acetate ions from dissolved gaseous acetic acid can form and react with lead. The association of these ions with the native oxide massicot, β-PbO (ICDD No. 38-1477) (peak at 2.0505 $Å^{-1}$) forms the lead acetate oxide hydrate compound. Massicot is formed during oak VOC exposure, but not on the protected surface left in air during the measurement period.

After 7 days in an oak environment the peak area of the lead acetate oxide hydrate has halved, whilst the background due to amorphous and/or unresolved scattering has increased significantly. This is presumably due to ongoing corrosion and the breakdown of the lead acetate oxide hydrate to produce lead carbonates and re-form acetic acid. The oak VOC polluted environment (i.e. elevated humidity and acetic acid concentration) allows the breakdown of the acetate to the carbonate. Tétreault and co-workers found that plumbonacrite ($6PbCO_3.3Pb(OH)_2.PbO$) was the favored corrosion product at 75% RH when lead was exposed to acetic acid, whereas hydrocerussite ($Pb_3(CO_3)_2(OH)_2$) was the preferred product at lower RH values and higher acetic acid concentrations [45]. In the oak polluted environment both hydrocerussite and plumbonacrite are formed because the elevated humidity causes a higher concentration of acetic acid to be released from oak [46,47]. This result is in agreement with Tétreault's findings.

(a) COATED SAMPLE

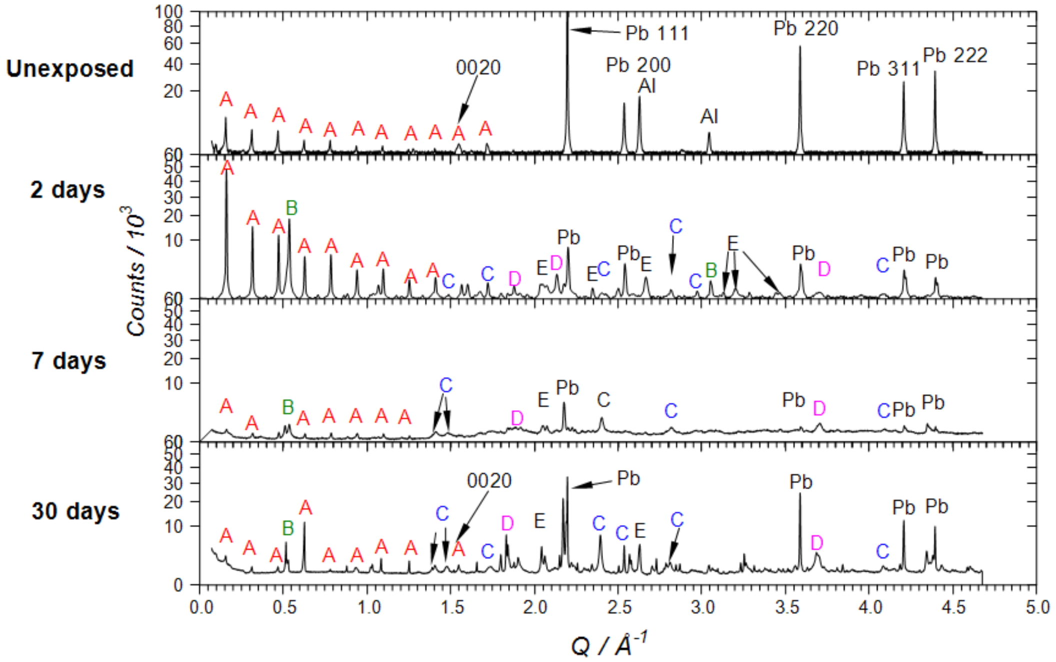

(b) BARE LEAD CONTROL

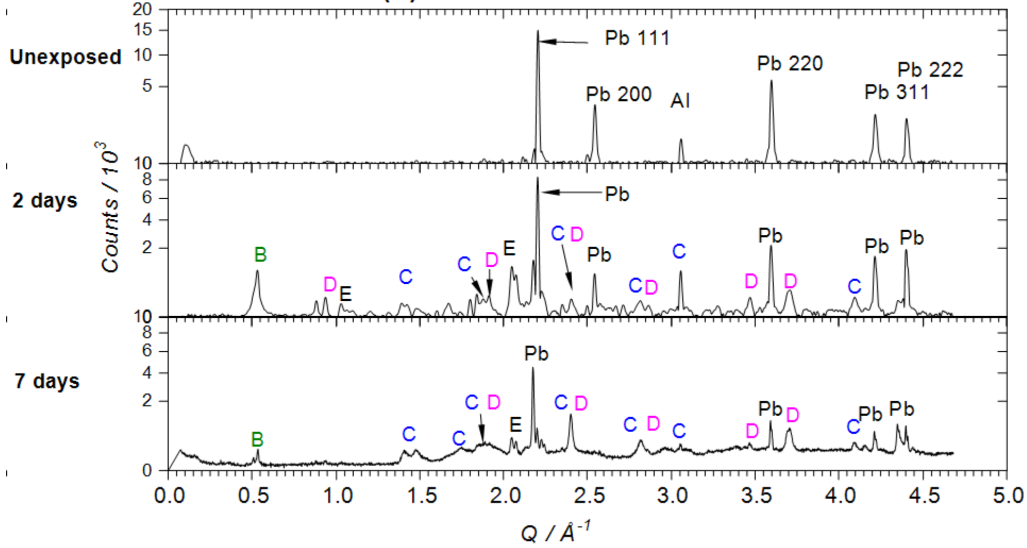

(c) REFERENCE PATTERNS

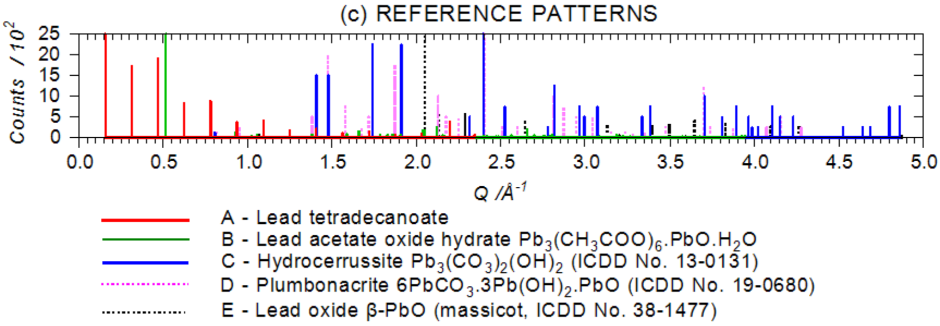

Figure 5.8 (a) XRD patterns of lead ditetradecanoate coated lead coupons after 2, 7 and 30 days within an oak environment; XRD pattern from an unexposed coated coupon. (b) XRD patterns of bare lead coupons after 2 and 7 days within an oak environment compared with an unexposed lead coupon. (c) Reference diffraction patterns.

All peaks of the lead ditetradecanoate coating decrease in height with oak exposure (2 days compared to 7 days), which suggests either that the lead ditetradecanoate layer is breaking down, or that it is being covered by the overgrowth of corrosion products, some of which may be amorphous [48]. Although a direct comparison between the 2 and 7 day data and the 30 day data cannot be made because the sensitivity and resolution of the PANalytical instrument are superior to the Siemens diffractometer, it can be seen that, even after 30 days, the 001 reflection and the even part of the 00*n* sequence are still visible (out to the 0010 reflection) and the sharp peaks are consistent either with coverage or the survival of a significant fraction of the coating intact.

Bare lead was also corroded within the same environment. A white layer of corrosion products formed within a few minutes exposure to the oak VOCs. Figure 5.8b shows the XRD results of bare lead kept with oak for 2 and 7 days measured on the Siemens D5000 diffractometer. The higher background for the 7-day exposure could be due to the formation of a large number of different corrosion products leading to the coalescence of unresolved small peaks, the growth of amorphous corrosion products, or even some deliquescence. Strong diminution in the lead reflections (e.g. 111 and 311) due to the coverage of corrosion products is evident. The small lead acetate peak (B) demonstrates advanced corrosion compared to the coated lead, and lead carbonate has formed already after 2 days. Lead acetate is an important intermediate to lead carbonate formation [44] therefore corrosion occurs more rapidly when lead is uncoated.

The source of error in these measurements originates from the Poisson noise on the counting detector.

Testing conservation coatings in a museum environment

The museum environment was continuously monitored during the placement of the samples in the display case. During the 7-month period a range of humidities and temperatures were recorded (Figure 5.9). A summary of the data is shown in Table 5.3. The mean temperature and relative humidity are comparable to the standard climate prescribed for VOC sampling (ISO 16000-6): 23 °C and 50 %RH. From March to the end of October, the relative humidity has increased from 28% to 40%. During this time the relative humidity rose to 63.4% in mid-July. The overall variation in humidity is due to local weather events and is not controlled in the museum or within individual display cases. The variation in temperature during the measurement period was smaller, due to the active temperature control within the museum and the passive temperature control imparted by the building structure i.e. the heat capacity of the building.

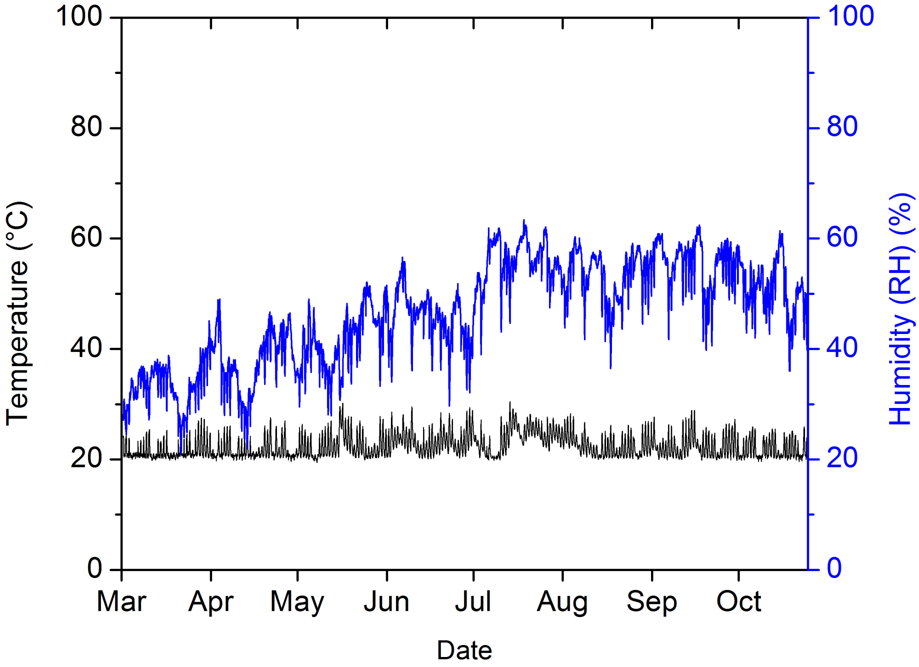

Figure 5.9 Relative humidity and temperature data recorded in the Museum for the History of Science, UGent for 7 months in 2014.

Table 5.3 Summary of museum environmental parameters collected over 7 months. Minimum and maximum temperatures were recorded on 11/5/2014 and 17/7/2014 respectively. Minimum and maximum relative humidities were recorded on 25/3/2014 and 22/7/2014 respectively.

	Temperature (°C)	**Relative Humidity (%)**
Mean	22.4	46.5
Minimum	19.4	20.9
Maximum	30.5	63.4
Standard deviation	2.1	9.3

Most variation occurs over a 24-hour period as evidenced in Figure 5.10, which shows the data measured over the course of 1 month. Temperature increased during the day and decreased over night – the opposite pattern is observed with relative humidity.

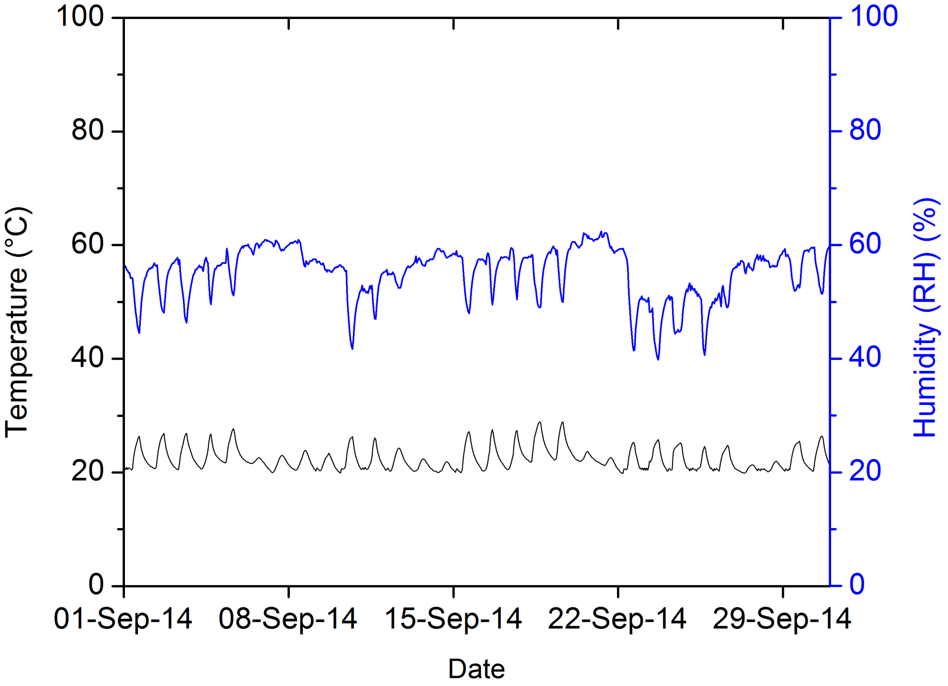

Figure 5.10 Relative humidity and temperature data recorded in the Museum for the History of Science, UGent during September 2014.

In comparison to the highly controlled environment of the eCell, the display case was clearly exposed to larger atmospheric changes due to cracks and gaps in the woodwork – the case was not a closed system. Despite these daily changes, the surface analysis part of the experiment was not time-resolved to this extent (i.e. only 'before' and 'after' surfaces were analysed) so the average environmental values are the most important in this study. This information can be used to compare the surface analysis results with other similar tests in musea.

Using the esaProject software, the three individual diffraction patterns obtained from each sample type were summed and divided by three to make an average pattern – there was no noticeable variation in the individual patterns from each set. Figure 5.11 shows the average XRD patterns obtained from the 4 different sample types displayed in the oak case.

All patterns (before and after placement) showed lead 111 and lead 200 peaks alongside peaks at 2.10 and 2.42 $Å^{-1}$. It is possible that these unidentified peaks are an artefact of the polishing process, although no firm match could be made with existing references. In addition for all samples after placement in the museum a single peak appears at 2.62 $Å^{-1}$. A wider 2θ range of analysis would perhaps shed some light on the characterisation of this unidentified compound.

The lead ditetradecanoate coated samples showed substantial amounts of unreacted tetradecanoic acid on the surface after treatment. The unreacted acid exists alongside the lead ditetradecanoate coating. After 7 months residence in the museum display case the unreacted tetradecanoic acid is no longer detected and the lead 111 peak height has increased by 50%. This suggests that the unreacted acid has completely reacted with the underlying lead during the 7-month period to produce more of the coating and that the coating has become more porous as more lead signal can escape.

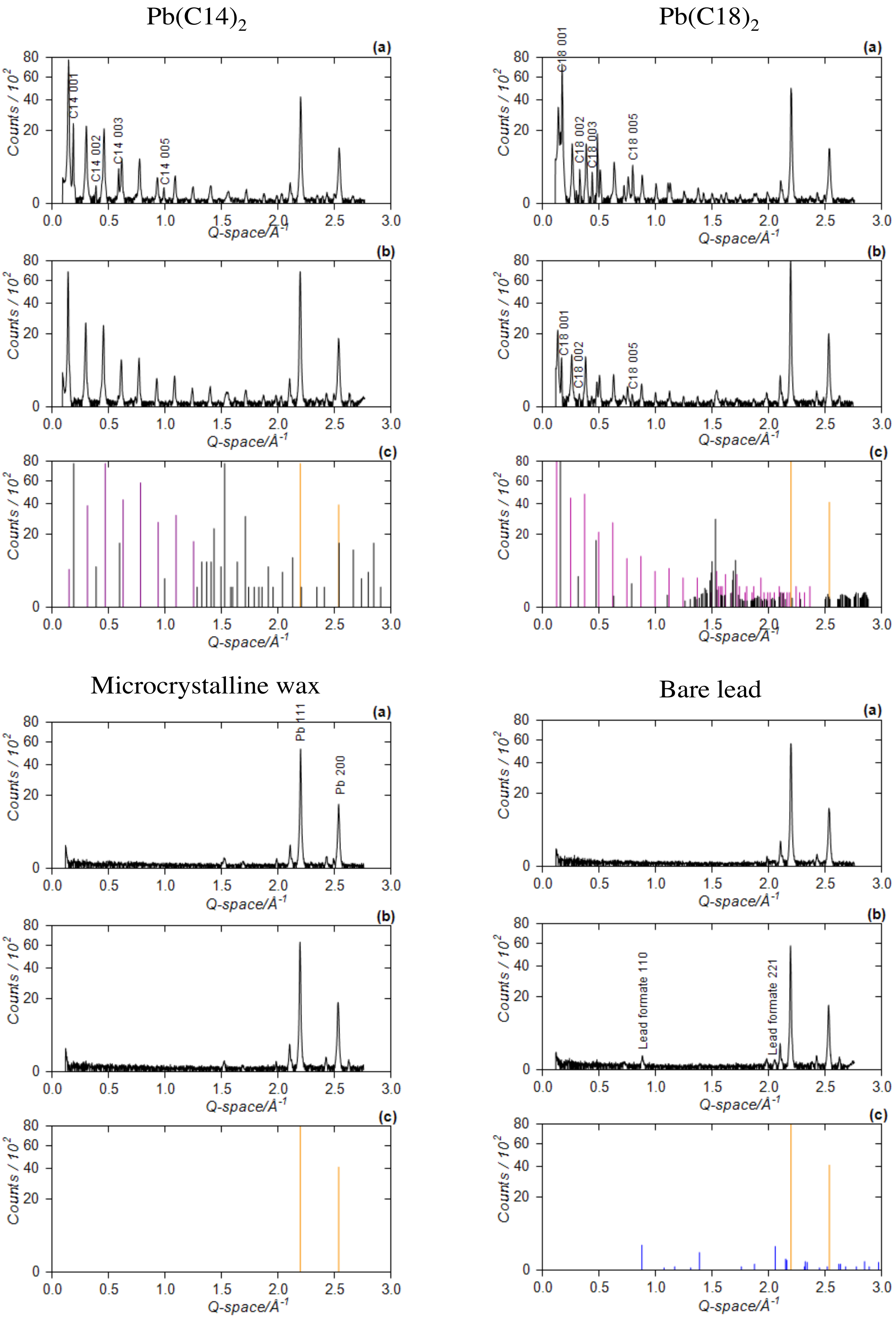

Figure 5.11 XRD patterns before and after ‘exhibition’ in an oak museum display case. References given are from lead (yellow), lead formate (blue, ICDD 014-0831), lead ditetradecanoate and lead dioctadecanoate (purple), and tetradecanoic acid and octadecanoic acid (black, ICDD 008-0786 and 038-1923 respectively). (a) Before, (b) after placement in museum, (c) references patterns.

The lead dioctadecanoate coated samples show a similar behaviour although after 7 months there is still unreacted acid remaining. This could be due to the seemingly higher concentration of unreacted acid prior to placement in the display case or due to the slower reaction of this acid with lead compared to tetradecanoic acid. This is evidenced by the greater peak height of the acid (7350 counts, C18 001) compared to the tetradecanoic acid (2300 counts, C14 001). The reason for this could be an inconsistency in sample preparation or a difference in reactivity between the two acids. In addition to the reacted and unreacted acid peaks, no corrosion products could be identified.

The samples coated with microcrystalline wax show no change in crystalline surface composition over the course of the 7-month exposure. The peak at 1.53 $Å^{-1}$ is unidentified but could be a result of the wax coating [49]. The bare lead samples were the only samples to demonstrate corrosion: lead formate peaks were clearly identified after 7 months of placement in the oak cabinet. No formic acid (the precursor to lead formate [25]) was detected in the GC-MS measurements due to detector limitations but the identification of lead formate verifies the presence of formic acid in the VOCs released from the oak. No advanced corrosion products are identified, such as lead carbonates or oxides. This suggests a far lower concentration of acidic VOCs in this environment compared to the month-long tests in the desiccator.

5.3.3 Time-lapse SR-XRD of coating exposed to oak VOCs

Figure 5.12 shows the background corrected peak areas of lead, massicot (β-PbO), hydrocerussite ($Pb_3(CO_3)_2(OH)_2$) and the lead ditetradecanoate coating extracted from the sequences of SR-XRD diffractograms recorded from the eCell containing the oak annulus to generate VOCs. The coated lead was exposed over a period of 14 hours (85 images) with RH rising to 75%. The bare lead was exposed for 7 hours (43 images) at ambient RH ~50%. The difference in relative humidity between experiments is important because increased relative humidity not only accelerates acetic acid emission from oak [46,47] but also enhances corrosion directly due to the presence of a thicker electrolyte layer. Data from coated lead are delineated in black, whilst those from bare lead are in grey.

Figure 5.12a shows the time dependence of the area of the lead 111 peak at 2.21 $Å^{-1}$. For each set, the areas have been normalized to that of the first peak in the set. Peak area data for the remaining lead reflections when manipulated in the same way give very similar results. Figure 5.13 shows that all lead reflections decrease on exposure the corrosive atmosphere. The peak from the bare lead in Figure 5.12a actually increases by 5% during the first 4 patterns: the polycrystalline lead surface re-orientates somewhat with the onset of corrosion. The observed overall decrease in the peak areas is due to increasing coverage by corrosion products, which absorb both the incoming beam and X-rays scattered from the lead surface. For both coated and bare lead the behaviour is characteristic of corrosion growth, which passivates somewhat, but there is appreciably less corrosion on the coated lead at any given time. Below, we use these data to obtain a semi-quantitative estimate of the corrosion layer thickness.

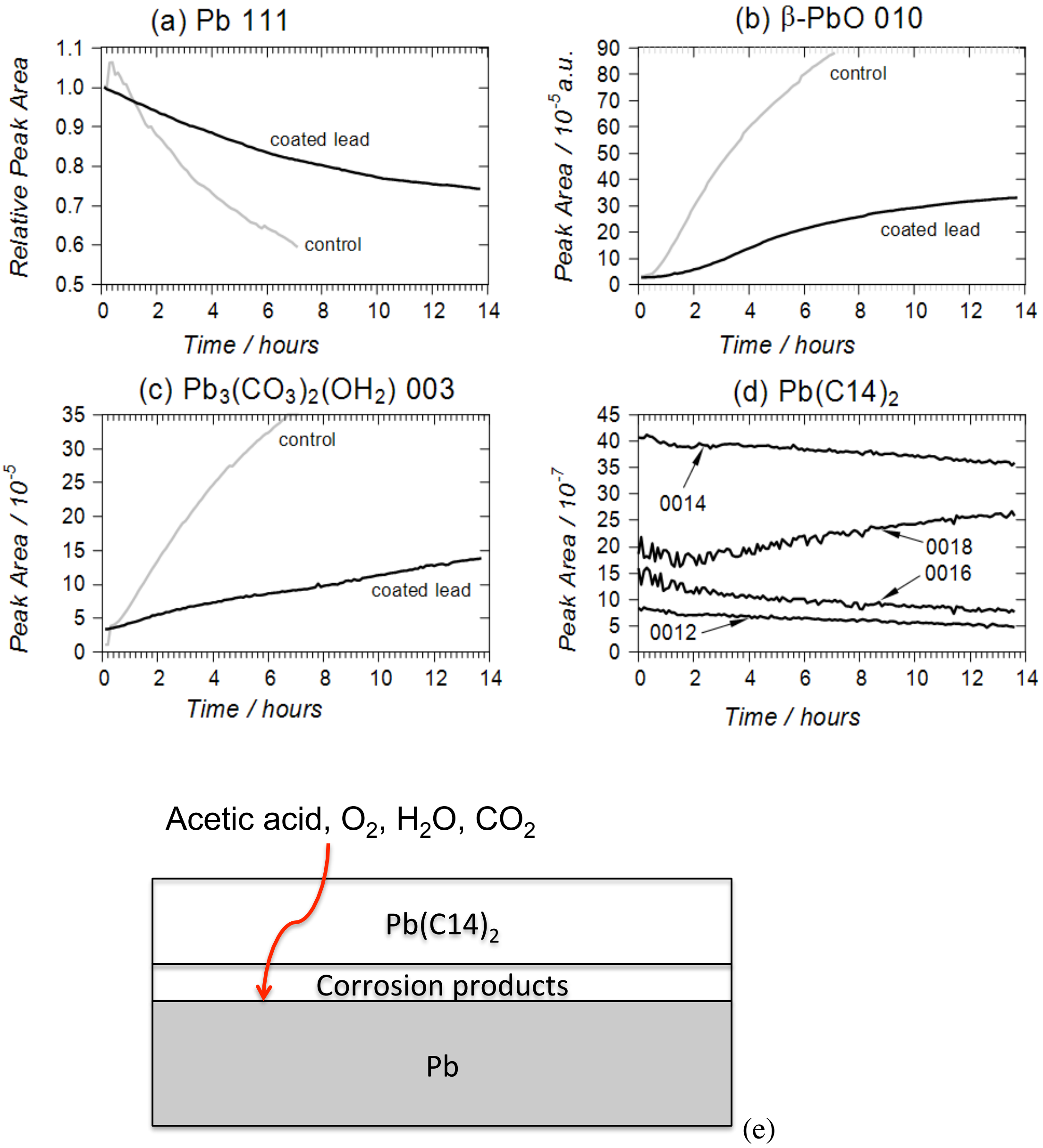

Figure 5.12 Corrosion of the coated lead in real time (elevated humidity, oak environment) and comparison with bare lead corrosion (ambient humidity, oak environment). Peak areas were extracted from (a) lead 111 @2.21 Å^{-1}, (b) massicot (β-PbO) 010 @2.07 Å^{-1}, (c) hydrocerussite ($Pb_3(CO_3)_2(OH)_2$) 003 @1.91 Å^{-1}, and (d) lead ditetradecanoate ($Pb(C14)_2$) even reflections from 0012 to 0018. Schematic (e) shows the presumed location of corrosion product growth and the diffusion of corrosive agents through the coating to the lead-coating interface.

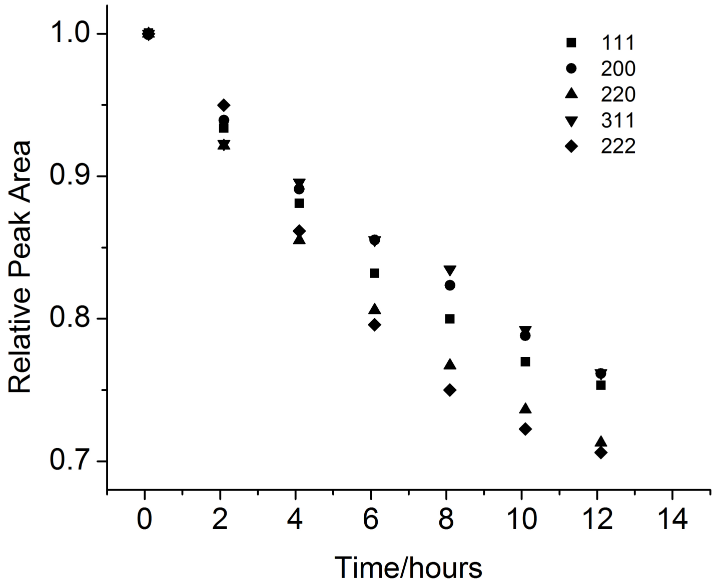

Figure 5.13 Relative Pb peak areas from the corrosion of the lead tetradecanoate coating in real time (elevated humidity, oak environment) experiment. Peak areas were extracted from lead 111, 200, 220, 311 and 222 peaks.

Peak areas from a surface layer which grows without structural change or being itself covered will increase to an asymptotic value because, once the corrosion layer is sufficiently thick to absorb or scatter all the incoming beam, no further increase in peak area (or height) will occur. This behavior is convolved with any tendency for growth to passivate, and cannot be modeled unless the growth law is known or assumed. Nevertheless, direct comparisons between the data from coated and bare lead can be made as follows.

Figure 5.12 b shows the change in lead (II) oxide (β-PbO, massicot) 010 peak at 2.07 Å^{-1} area over time. The amount of detectable lead oxide at any time after the first 30 minutes is around four times greater for the uncoated sample. Some oxide is present on both samples from the start as the polished lead surface has already been exposed to air for a few minutes. Rapid growth does not start for 20-30 minutes, possibly reflecting the time taken for the atmosphere (RH, oak VOCs) in the cell to stabilize. Although native oxide growth results from direct contact of lead with oxygen in the air (equation 5.1), its production can be increased as a result of acetic acid exposure [50]. This is due to the formation of lead acetate oxide hydrate, which uses the native PbO in its formation (equations 5.2 and 5.3): the dissolved acetate ions promote the reaction of the underlying lead with air to produce β-PbO.

$$2Pb + O_2 \rightarrow 2PbO \quad (5.1)$$

$$PbO + 2CH_3COOH \rightarrow Pb(CH_3COO)_2 + H_2O \quad (5.2)$$

$$3Pb(CH_3COO)_2 + PbO + H_2O \rightarrow Pb_3(CH_3COO)_6.PbO.H_2O \quad (5.3)$$

The concentration of acetic acid forming on the surface is not likely to be the same in the coated lead and uncoated lead and the position of the water film is different. At the least, the long carbon chains of the lead ditetradecanoate coating form a hydrophobic barrier on the surface of the lead which reduces the amount of water into which acetic acid vapor can dissolve whilst placing a barrier between this and the surface. It therefore takes longer for the corrosive agents to reach the lead surface promote the formation of β-PbO and the down-stream reaction products (Figure 5.12e).

Figure 5.12c shows the changes in peak area with time for the hydrocerussite 003 peak at 1.9 $Å^{-1}$. The peak areas of this corrosion product on coated lead are six times lower than for the bare lead 6 hours into exposure. These results demonstrate the protection afforded by the coating. Hydrocerussite growth results from the reaction of lead with acetic acid emitted from the oak. As discussed previously, lead acetate oxide hydrate breaks down to form carbonates and simultaneously reform acetic acid (equation 5.4).

$$3Pb_3(CH_3COO)_6.PbO.H_2O + 8CO_2 + 10H_2O \rightarrow 4Pb_3(CO_3)_2(OH)_2 + 18CH_3COOH \quad (5.4)$$

Lead acetate oxide hydrate cannot be seen on the diffraction patterns due to the low angle limitation of the instrumental setup – the lead acetate peak would be expected at 0.5 $Å^{-1}$ but the measurement limit with our Mar configuration is 0.6 $Å^{-1}$ (to prevent secondary scattering off the camera bezel). Despite the lack of an acetate peak it can be deduced from the longer-term oak exposure data (Figure 5.8) that lead acetate is the cause of hydrocerussite formation.

Figure 5.12d shows the change in peak areas of the even lead ditetradecanoate peaks from 0012 to 0018 over time within the oak environment. At longer oak exposure times (see Figure 5.8) it was found that the coating peaks apparently diminish over days, but this could be due to the eventual build up of corrosion products on the surface. Results from reflections 0012 to 0016 show the initial signs of this long-term behavior. The peak areas of the lead ditetradecanoate coating in Figure 5.12d suggests the location of corrosion is initially between the coating and the lead surface since the corrosion product growth seen in Figure 5.12a-c do not proportionally diminish the tetradecanoate reflections. The peak areas for the 0014 reflection are more than double that of the 0012 and 0016 reflections but the peak areas of the even reflections from 0012 to 0016 reduce by 6.25%, 11.25 and 46.7% respectively during the 14-hour measurement period. This shows that the higher order the reflection, the more sensitive the reflection is to surface coverage by corrosion products – this is due to the longer path length for higher order reflections. The 0018 reflection apparently increases by 30% during the measurement period due to proximity to the growing plumboacrite peak, which overlaps into the integration limit for this carboxylate reflection.

In order to obtain more quantitative information on the protection afforded by the coating, we proceed as follows: We assume that the X-ray absorption follows the Beer-Lambert law. Then, provided the lead peaks only cover a small range of angle so that the input and exit paths can be considered invariant over the peak we can write

$$A(t) = R(t) A_0 \exp\left(-\frac{\mu}{\rho} d(t) k\right) \qquad (5.5)$$

where $A(t)$ is the time dependence of the area of the lead 111 reflection, $R(t)$ corrects for changes in the reflection coefficient from the lead surface (e.g. due to changes in orientation as described above), A_0 is the peak area for no attenuation and for R=1, μ/ρ is a mean mass absorption coefficient for the corrosion layer, ρ is its mean density, $d(t)$ is the mean mass thickness (mass per unit area) of the corrosion, and k is a constant which accounts for the experimental geometry:

$$k = \frac{1}{\sin\theta_i} + \frac{1}{\sin(2\theta - \theta_i)} \qquad (5.6)$$

where θ_i is the incident angle of the beam to the surface (10°), and 2θ is the scattering angle for the 111 reflection. Clearly, this expression includes the simplifying assumption that μ/ρ remains constant over time.

The growth law for the corrosion $d(t)$ can be obtained directly by transforming the data in Figure 5.12a according to

$$d(t) = \frac{\rho}{\mu k} \ln\left(\frac{R(t)A_0}{A(t)} \right) \tag{5.7}$$

In general, the use of a 2-D detector followed by integration along the rings will make the data less sensitive to changes in R compared to a scanned point or linear detector, and, although the first 4 data points for the bare lead show an abrupt 5% increase which we attribute to a change in R this is relatively small. Therefore, for the purposes of obtaining an estimate of $d(t)$ we set R to 1.

By applying equation 5.7 to the data in Figure 5.12a, using the mass absorption coefficient for hydrocerussite calculated using NIST data [51] we can calculate the mass thickness of hydrocerussite on coated and uncoated lead. The values of mass absorption coefficients are similar for massicot (198 cm^2/g), plumbonacrite (191 cm^2/g) and hydrocerussite (179 cm^2/g) therefore the mass thicknesses calculated for all corrosion products are comparable. This quantification exercise also gives us information on the thickness of this corrosion product on the sample surface by simply dividing the mass thickness results by the density of hydrocerussite, 6.8 g/cm^3.

The behaviour of hydrocerussite thickness over time as deduced from the decrease in the lead signal is shown in Figure 5.14. As explained previously for Figure 5.12a, the initial decrease in thickness of the corrosion layer on lead due to the re-orientation of the polycrystalline lead with the onset of corrosion. After 4 hours, the thickness of hydrocerussite on coated lead is 2.0 μm whereas it grows to a thickness of 10 μm on bare lead after the same period of time. So, the coating (40 μm thick) is significantly retarding the growth of corrosion products on the lead surface. As with the data in Figure 5.12a, the thickness of hydrocerussite is tending towards asymptotic behavior due to passivation of the surface and absorption by the corrosion layer of incoming x-rays. However, the protective coating will reduce the hydrocerussite thickness on coated compared to bare lead by up to 75%.

Figure 5.15 shows the final diffraction patterns of bare and coated lead after exposure to oak within the eCell. As expected from Figure 5.12, the peak areas of lead oxide and lead carbonate corrosion products are greater for the bare lead sample, again demonstrating the protective nature of the coating. The peaks are broader than from a laboratory diffractometer because of the inherently low the angular resolution present in our experimental geometry on the synchrotron.

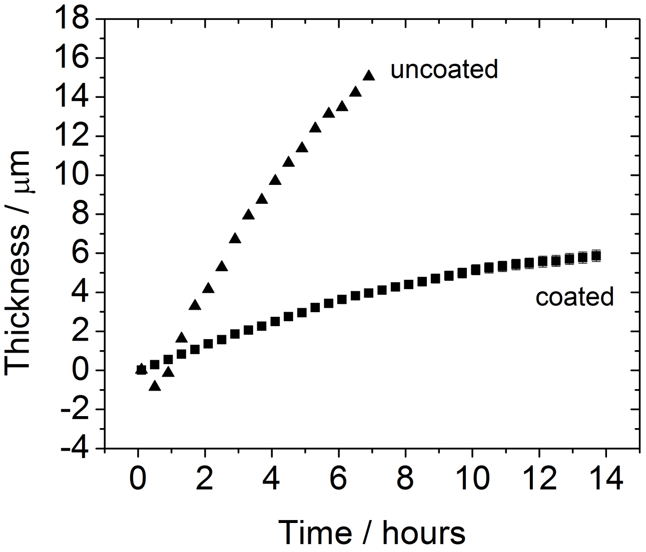

Figure 5.14 Thickness of hydrocerussite growing on coated (squares) and uncoated (triangles) lead with time. Mass thickness is calculated by translating Fig. 5.11a data into the Eq. (3). Thickness of the coating uses the mass thickness divided by the density of hydrocerussite.

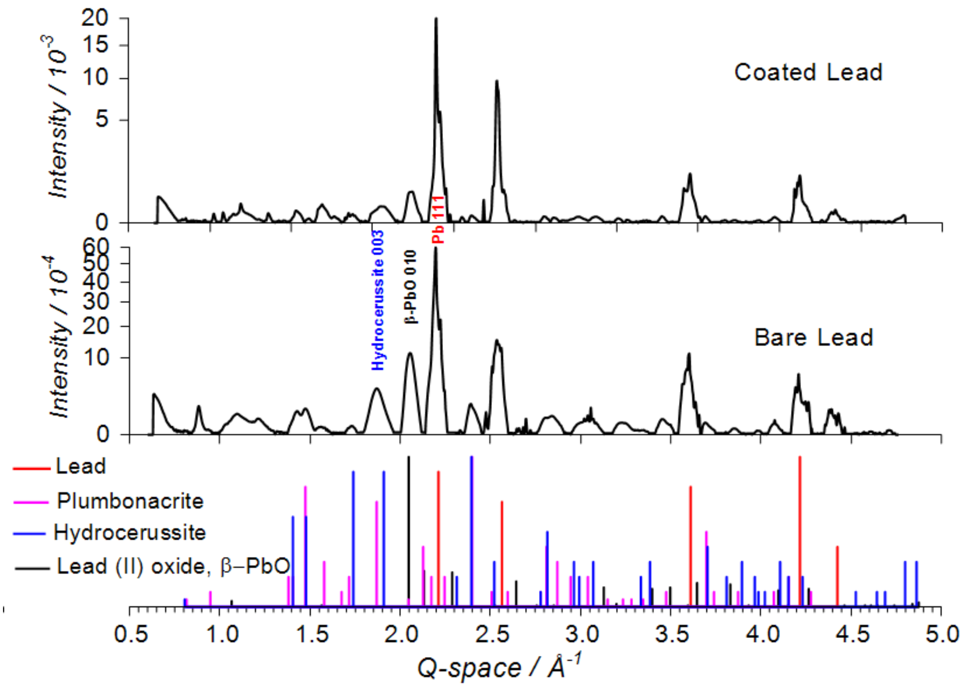

Figure 5.15 Final SR-XRD patterns of lead and tetradecanoate coated lead after exposure to oak VOCs within the eCell, i.e. the spectra used to calculate the last data point in Fig. 5.12. Diffraction patterns are compared against reference diffraction patterns for hydrocerussite (ICDD No. 13-0131), plumbonacrite (ICDD No. 19-0680), massicot (ICDD No. 38- 1477) and lead. The y-axis of the XRD patterns in this figure are shown on a square-root scale.

Errors in the normalised peak intensities (and therefore peak areas) can be calculated using equation 5.8 [52]. 'Normalised' refers to the division of intensity values by the appropriate beam monitor value. Equation 5.8 originates from simple propagation of errors and the counting detector used to measure the beam monitor (Figure 5.3), although this value goes through a frequency to count converter in order to display counts. The exact error on the ion chamber is not known but we can assume Poisson statistics based on the output from the frequency-count converter to form this equation:

$$\alpha_Z = Z\sqrt{\frac{1}{I}+\frac{1}{I_0}} \tag{5.8}$$

where α_z is the error on the normalised intensity, Z is the normalised intensity, I is the intensity and I_0 is the beam monitor. For example for the Pb 111 peak height in Figure 5.15 (coated lead) the values for Z, I and I_0 are 200 x 10^{-4}, 7355.74 and 367787 respectively. This gives an error of 2.35 x 10^{-4}, thus Z = (200 ± 2) x 10^{-4}. However, this error analysis for the beam measurements is somewhat oversimplified. As discussed in Chapter 2 there are multiple events which could contribute errors during the measurement of the beam monitor, which are not taken into account with simply Poisson statistics.

The error in beam measurements can also be approximated to the fractional beam measurement between any given beam monitor value and the mean beam monitor. Using data from one refill (Figure 5.3) fitted to an exponential curve, this can be calculated as follows:

$$\text{fractional mean difference} = \frac{\sqrt{\text{sum of the residual squares}}}{(\text{number of points})(\text{mean value})^{-1}} \tag{5.9}$$

which is equal to 0.004% or, using the same peak height example as above, Z = (200 ± 0.008) x 10^{-4}.

However, in these measurements errors arise from other sources in addition to those introduced by the beam monitor: there are thermal fluctuations from the Mar camera, fluctuations induced by the dark field correction, read-out noise, statistics from x-ray scattering and conversion probabilities incurred by the esaProject software. Equation 5.9 can also be used to estimate the fractional error from the Mar camera and data processing, as demonstrated in Figure 5.16. This data was normalised to the beam monitor in order to avoid the error incurred by beam decay and data was not background-corrected in order to preserve the Poisson statistics. The peak area of the Pb 111 ‘peak’ is 0.07, which is the fractional error on the peak area. Given a peak area from a Pb 111 reflection in this dataset, this equates to (5.85 ± 0.43) x 10^{-4}.

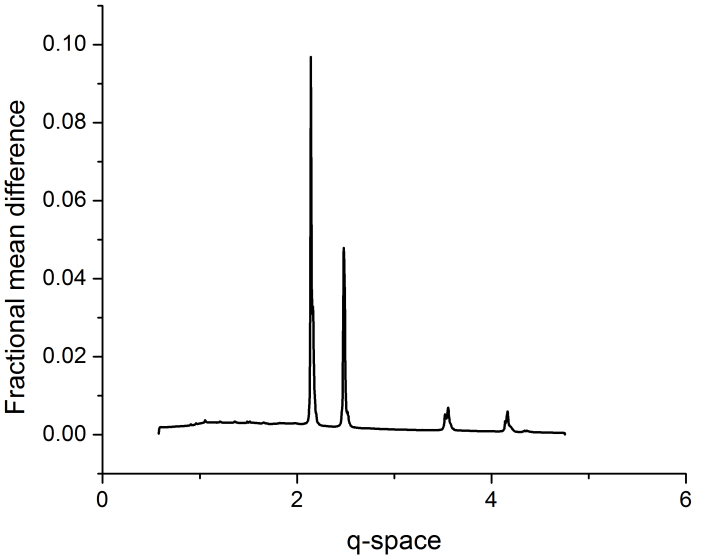

Figure 5.16 Fractional mean difference calculated from raw data from DUBBLE, normalised to the beam monitor. The raw data used in this example is three consecutive time-lapse patterns from the Mar camera.

5.4 Conclusions

In this chapter the effect of exposing a conservation coating to VOCs released from oak was studied in a variety of ways: in time-resolution for 12 hours in a high oak VOC concentration, over a long period of time (one month) in a high oak VOC concentration environment, and for 7 months in a real museum environment.

A study of the effectiveness of a lead ditetradecanoate coating on lead to protect against harmful VOCs emitted from oak was conducted using time-lapse SR-XRD *in situ* and laboratory XRD in a high concentration oak environment.

SPME and thermal desorption GC-MS were used to characterize the VOCs themselves.

Acetic acid was confirmed as the most predominant VOC emitted from oak (*Quercus sp.*), being three times more prevalent than any other. Acetic acid was also the only reactive VOC detected, reacting with lead to produce lead acetate oxide hydrate as a precursor to other corrosion products such as hydrocessurite. There was no evidence to show that other VOCs such as long-chain aldehydes reacted with the bare lead. The laboratory experiments showed that the coating was still present after 30 days in a model oak environment, but became visibly patchy, or covered with corrosion products.

By studying the growth of corrosion products it was found that the coating reduces the growth rates of some corrosion products by up to 75% compared with bare lead, and generally inhibits attack from the VOCs. However corrosion products still form, possibly at the metal-coating interface. This information could be obtained directly from sample cross sections. From the time-lapse XRD data it was also possible to estimate the thickness of hydrocerussite growing as a function of time on the bare and coated coupons.

In order to relate this study to conservation practice, lead samples were conserved with two long-chain carboxylic acids (from ethanolic solution) and microcrystalline wax and placed in a museum display case in order to study the effect of the VOCs. Thermal desorption GC-MS was also used to characterize the VOCs. Acetic acid was found to be the VOC with the greatest concentration although quantification (and therefore comparison with other results) could not be achieved. After 7 months of residence, the carboxylate-coated samples had ‘self-healed’ as unreacted carboxylic acid present on the surface had continued to react in the VOC-rich museum environment to product the lead carboxylate layer. Microcrystalline wax samples showed no change and bare lead reference samples had shown some initial corrosion by oak VOCs. Due to the lack of corrosion product formation on the carboxylate-coated samples during the placement (at close-to standard environmental conditions) it can be suggested that these coatings would be suitable for use as a conservation treatment in the short-term (up to 1 year).

Errors in this study are mostly accountable to the detectors used in analysis and the data processing software. The detectors in the lab XRD, GC-MS and ion chamber (the method of measuring the beam monitor on beamlines) in these experiments are subject to (approximately) Poisson noise due to the counting method of detection. For the synchrotron experiments, other sources of error were introduced (e.g. thermal fluctuations in the Mar camera). These errors can be approximately quantified by calculating the fractional mean difference between raw data and the mean pattern, although there is room for improvement in the calculation of beam measurement errors. Random errors were reduced in laboratory XRD experiments by measuring duplicate and triplicates of the samples but the time-limitations during beam time do not allow for multiple samples to be measured.

5.5 Acknowledgements

Picreator Enterprises Ltd. is thanked for the microcrystalline wax which was provided free-of-charge to this project. Thames Restek UK Ltd. is also thanked for the IceBlue® septa which were also provided free-of-charge.

5.6 References

[1] D. Watkinson, Preservation of Metallic Cultural Heritage, in: T.J.A. Richardson, B.R.A. Cottis, R. Lindsay, S. Lyon, D.J.D. Scantlebury, H. Stott, M. Graham (Eds.), Shreir's Corrosion, Volume 4, Elsevier, Amsterdam, 2009: pp. 3307–3340.

[2] J. Tétreault, E. Stamatopoulou, Determination of concentrations of acetic acid emitted from wood coatings in enclosures, Studies in Conservation. 42 (1997) 141–156.

[3] A. Fenech, M. Strlič, I. Kralj Cigić, A. Levart, L.T. Gibson, G. de Bruin, K. Ntanos, J. Kolar, M. Cassar, Volatile aldehydes in libraries and archives, Atmospheric Environment. 44 (2010) 2067–2073.

[4] T. Oikawa, T. Matsui, Y. Matsuda, T. Takayama, H. Niinuma, Y. Nishida, K. Hoshi, M. Yatagai, Volatile organic compounds from wood and their influences on museum artifact materials I. Differences in wood species and analyses of causal substances of deterioration, Journal of Wood Science. 51 (2005) 363–369.

[5] T. Oikawa, T. Matsui, Y. Matsuda, T. Takayama, H. Niinuma, Y. Nishida, K. Hoshi, M. Yatagai, Volatile organic compounds from wood and their influences on museum artifact materials II: Inference of causal substances of deterioration based on intercomparison of laser Raman spectra of deteriorated products, Journal of Wood Science. 52 (2006) 140–146.

[6] R. Wiesinger, R. Grayburn, M. Dowsett, P.J. Sabbe, P. Thompson, A. Adriaens, M. Schreiner, In-situ time-lapse synchrotron radiation X-ray diffraction of silver corrosion, J. Anal. At. Spectrom. (2015).

[7] A. Niklasson, S. Langer, K. Arrhenius, Air pollutant concentrations and atmospheric corrosion of organ pipes in European church environments, Studies in Conservation. 53 (2008) 24–40.

[8] R. Wiesinger, I. Martina, C. Kleber, M. Schreiner, Influence of relative humidity and ozone on atmospheric silver corrosion, Corrosion Science. 77 (2013) 69–76.

[9] J.M. Eargle, Acoustics of Brass Instruments, in: Music, Sound, and Technology, Springer US, Boston, MA, 1995: pp. 125–146.

[10] H. Yano, Chemical treatment of wood for musical instruments, The Journal of the Acoustical Society of America. 96 (1994) 3380.

[11] J. Kesselmeier, M. Staudt, Biogenic volatile organic compounds (VOC): an overview on emission, physiology and ecology, Journal of Atmospheric Chemistry. 33 (1999) 23–88.

[12] E. Roffael, Volatile organic compounds and formaldehyde in nature, wood and wood based panels, Holz Als Roh- Und Werkstoff. 64 (2006) 144–149.

[13] C. Chiavari, C. Martini, D. Prandstraller, A. Niklasson, L.-G. Johansson, J.-E. Svensson, A. Åslund, C.J. Bergsten, Atmospheric corrosion of historical organ pipes: The influence of environment and materials, Corrosion Science. 50 (2008) 2444–2455.

[14] A. Niklasson, L.-G. Johansson, J.-E. Svensson, Influence of Acetic Acid Vapor on the Atmospheric Corrosion of Lead, Journal of the Electrochemical Society. 152 (2005) B519.

[15] F. Deflorian, M. Fedel, Electrochemical analysis of the degradation of lead alloy organ-pipes due to acetic acid, Journal of Cultural Heritage. 14 (2013) 254–260.

[16] A. Åslund, J. Speedstra, The COLLAPSE Project: Corrosion of organ pipes - causes and recommendations, Publications Office of the European Union, Luxembourg, 2011.

[17] C. Degrigny, R. Le Gall, Conservation of Ancient Lead Artifacts Corroded in Organic Acid Environments: Electrolytic Stabilization/Consolidation, Studies in Conservation. 44 (1999) 157–169.

[18] D. Martin, High-performance display cases, Museum Practice. 2 (1999) 42–45.

[19] N.H. Tennent, J. Tate, L. Cannon, The corrosion of lead artifacts in wooden storage cabinets, S.S.C.R. Journal. 4 (1993) 8–11.

[20] D. Wegner, Lead Corrosion in Exhibition Ship Models, Nautical Research Journal. 43 (1996) 32–40.

[21] P. Donovan, T. Moynehan, The corrosion of metals by vapours from air-drying paints, Corrosion Science. 5 (1965) 803–814.

[22] M. Strlič, J. Thomas, T. Trafela, L. Cséfalvayová, I. Kralj Cigić, J. Kolar, M. Cassar, Material degradomics: on the smell of old books., Analytical Chemistry. 81 (2009) 8617–22.

[23] T. Prosek, M. Kouril, M. Dubus, M. Taube, V. Hubert, B. Scheffel, Y. Degres, M. Jouannic, D. Thierry, Real-time monitoring of indoor air corrosivity in cultural heritage institutions with metallic electrical resistance sensors, Studies in Conservation. 58 (2013) 117–128.

[24] L.T. Gibson, B.G. Cooksey, D. Littlejohn, N.H. Tennent, A diffusion tube sampler for the determination of acetic acid and formic acid vapours in museum cabinets, Analytica Chimica Acta. 341 (1997) 11–19.

[25] M. Ryhl-Svendsen, J. Glastrup, Acetic acid and formic acid concentrations in the museum environment measured by SPME-GC/MS, Atmospheric Environment. 36 (2002) 3909–3916.

[26] P. Sacco, F. Quaglio, Validation of the Radiello® Diffusive Sampler for the Measurement of Formic and Acetic Acids in Museum Environments, The Reporter. 26 (2008) 22–23.

[27] B. Schotte, A study of the electrolytic reduction of corroded lead objects and the application, characterization and testing of a protective lead carboxylate coating, PhD Thesis, Universiteit Gent, Belgium, 2007.

[28] M. Dowsett, A. Adriaens, B. Schotte, G. Jones, Real time spectroelectrochemical growth and corrosion resistance monitoring of lead carboxylate coatings in an environmental cell (eCell), in: C. Degrigny, R. van Langth, I. Joosten, B. Ankersmit (Eds.), Metal 07: Proceedings of the Interim Meeting of the ICOM-CC Metal Working Group, Rijksmuseum, Amsterdam, 2007: pp. 26–31.

[29] Picreator, Renaissance Wax, http://www.picreator.co.uk/articles/3_renaissance_wax.htm, Date accessed: August 15, 2014.

[30] L. Greenspan, Humidity fixed points of binary saturated aqueous solutions, Journal of Research of the National Bureau of Standards. Section A: Physics and Chemistry. 81 (1977) 89–96.

[31] Personal Communication from Kristel Wautier, (2014).

[32] K. Curran, A. Možir, M. Underhill, L.T. Gibson, T. Fearn, M. Strlič, Cross-infection effect of polymers of historic and heritage significance on the degradation of a cellulose reference test material, Polymer Degradation and Stability. 107 (2014) 294–306.

[33] M.G. Dowsett, A. Adriaens, Cell for simultaneous synchrotron radiation X-ray and electrochemical corrosion measurements on cultural heritage metals and other materials., Analytical Chemistry. 78 (2006) 3360–5.

[34] S. Nikitenko, A.M. Beale, A.M.J. van der Eerden, S.D.M. Jacques, O. Leynaud, M.G. O'Brien, D. Detollenaere, R. Kaptein, B.M. Weckhuysen, W. Bras, Implementation of a combined SAXS/WAXS/QEXAFS set-up for time-resolved in situexperiments., Journal of Synchrotron Radiation. 15 (2008) 632–40.

[35] A. Adriaens, M. Dowsett, K. Leyssens, B. Van Gasse, Insights into electrolytic stabilization with weak polarization as treatment for archaeological copper objects., Analytical and Bioanalytical Chemistry. 387 (2007) 861–8.

[36] G. Konig, Relative contribution of oxygenated hydrocarbons to the total biogenic VOC emissions of selected mid-European agricultural and natural plant species, Atmospheric Environment. 29 (1995) 861–874.

[37] M.S. Pérez-Coello, J. Sanz, M.D. Cabezudo, Gas chromatographic-mass spectrometric analysis of volatile compounds in oak wood used for ageing of wines and spirits, Chromatographia. 47 (1998) 427–432.

[38] M. Risholm-Sundman, M. Lundgren, E. Vestin, P. Herder, Emissions of acetic acid and other volatile organic compounds from different species of solid wood, Holz Als Roh-Und Werkstoff. 56 (1998) 125–129.

[39] D.F. Packman, The Acidity of Wood, Holzforschung. 14 (1960) 178–183.

[40] B.F. Tjeerdsma, M. Boonstra, A. Pizzi, P. Tekely, H. Militz, Characterisation of thermally modified wood: molecular reasons for wood performance improvement, Holz Als Roh- Und Werkstoff. 56 (1998) 149–153.

[41] A.M. Emsley, G.C. Stevens, Kinetics and mechanisms of the low-temperature degradation of cellulose, Cellulose. 1 (1994) 26–56.

[42] D. Fengel, G. Wegener, eds., Wood: chemistry, ultrastructure, reactions, De Gruyter, 1983.

[43] M. Dowsett, A. Adriaens, B. Schotte, G. Jones, L. Bouchenoire, In-situ spectroelectrochemical study of the growth process of a lead decanoate coating as corrosion inhibitor for lead surfaces, Surface and Interface Analysis. 41 (2009) 565–572.

[44] A. Niklasson, L.-G. Johansson, J.-E. Svensson, The influence of relative humidity and temperature on the acetic acid vapour-induced atmospheric corrosion of lead, Corrosion Science. 50 (2008) 3031–3037.

[45] J. Tètreault, J. Sirois, E. Stamatopoulou, Studies of lead corrosion in acetic acid environments, Studies in Conservation. 43 (1998) 17–32.

[46] L.T. Gibson, C.M. Watt, Acetic and formic acids emitted from wood samples and their effect on selected materials in museum environments, Corrosion Science. 52 (2010) 172–178.

[47] J.-O. Fechter, F. Englund, A. Lundin, Association between temperature, relative humidity and concentration of volatile organic compounds from wooden furniture in a model room, Wood Material Science and Engineering. 1 (2006) 69–75.

[48] A. van Loon, Color Changes and Chemical Reactivity in Seventeenth-century Oil Paintings, PhD Thesis, Amsterdam, The Netherlands, 2008.

[49] P. Ratnasamy, K.S. Anand, D.C. Gupta, Structure and properties of microcrystalline waxes, Journal of Applied Chemistry and Biotechnology. 23 (1973) 183–187.

[50] A. Niklasson, L.-G. Johansson, J.-E. Svensson, Atmospheric Corrosion of Lead, Journal of the Electrochemical Society. 154 (2007) C618.

[51] C.T. Chantler, K. Olsen, R.A. Dragoset, J. Chang, A.R. Kishore, S.A. Kotochigova, D.S. Zucker, Detailed Tabulation of Atomic Form Factors, Photoelectric Absorption and Scattering Cross Section, and Mass Attenuation Coefficients for Z = 1-92 from E = 1-10 eV to E = 0.4-1.0 MeV, http://www.nist.gov/pml/data/ffast/index.cfm, Date accessed: August 05, 2013.

[52] I.G. Hughes, T.P.A. Hase, Measurements and their uncertainties : a practical guide to modern error analysis, Oxford University Press, Oxford, 2010.

Chapter 6 – A Portable Cell (peCell) for spectroelectroelectrochemical studies of heritage metals

6.1 Introduction

Information regarding the long-term effects of conservation treatments is vital for the understanding of how the material will react during and after treatment. Chapter 5 addressed the idea of tracking corrosion processes *in situ* on conserved and unconserved samples using SR-XRD and *ex situ* for longer periods using laboratory XRD. To improve the long-term *ex situ* results, constant monitoring of the surface and environment would be necessary. In this chapter, the design of a new instrument for the long-term monitoring of corrosion processes is described.

In the same way that corrosion and corrosion inhibition studies are key to the understanding of conservation practices, many other materials (such as those in an architectural, engineering or industrial environment) require protection to prevent corrosion and preserve their usefulness. Therefore any new instrumentation designed to study corrosion with a heritage context in mind has a far wider application.

In this chapter the design of a portable electrochemical/environmental cell (peCell) for spectroelectrochemical measurements is described. The design brief was to create a platform for long-term corrosion studies of heritage materials and conservation techniques. However due to beam time pressures, the prototype cell was spectroelectrochemically tested using a biomaterial-based system, described in Chapter 7. In this chapter the design of the portable cell is detailed and analysed.

6.2 Design

The portable cell was designed using Alibre Design (3D Systems, USA), a computer-aided design program.

6.2.1 Design brief

The brief was to design a new type of eCell [1] which could be used for long term experiments to test the longevity of conservation techniques, for example. The portability of the cell from the lab to the synchrotron beamline (where surface analysis takes place) whilst experiments continue uninterrupted is an essential feature.

Possible uses of the cell would be:

- An electrochemical cell to test long-term effects of electrochemical conservation methods;
- A cell to mimic conservation treatments over the long-term e.g. soaking of iron in sesquicarbonate solution [2];
- To sustain a constant atmosphere for heritage samples e.g. temperature, humidity for modelling an organ windchest.

Design features of the cell must therefore include:

- Water tightness and air tightness to prevent leakage during experimentation;
- Combining water tightness with moving parts;
- Adaptability to accommodate different types of sensors (e.g. for temperature, humidity, corrosion potential);
- A compact design for portability;
- Remote filling of the cell during beamtime.

6.2.2 Design history

Several iterations of peCell were designed prior to manufacture of the current prototype. The details of some designs are given below, with explanations as to why the design process was discontinued.

Design 1

The first design was based on the current eCell shape [1], but with the working electrode motor separated from the environmental chamber. This feature would have allowed multiple environmental chambers to run simultaneously perhaps attached to a 'dock', which would monitor electrochemical parameters such as corrosion potential (E_{corr}). When the sample was ready for surface analysis, the chamber would be dismounted from the 'dock' and attached to a motor part, which would move the sample to the X-ray transparent window. The footprint of the sample chambers was designed to be small for mounting the equipment on a beamline. The design problems encountered were as follows:

- The volume compensation of electrolytes during movement of the sample was not accounted for in initial designs: this was eventually accounted for using an external passive piston attached to a cell port. The same port could be used to attach bellows [3] to maintain pressure for atmospheric samples. However, there was difficulty in ensuring that these accessories were more flexible than the window seal. In addition a supplementary piston to each cell was costly and bulky, compared to the amount of time in use;
- The water tightness of the environmental chamber during docking and movement was not robust;

- The electrochemical contact between the environmental chamber and dock was not thought to be secure enough through the dovetail joint connection;
- The major design flaw was the breaking of electrochemical contact during surface analysis, since the environmental chamber part would no longer be in contact with the dock. Maintaining electrical contact in other ways was too difficult to incorporate, bearing in mind the small footprint of the individual environmental chambers.

Design 2

A second design was a single-environment multicell, whereby samples were moved on a circular, undulating track up to the X-ray transparent window and then submersed in the electrolyte/other environmental conditions. The counter electrode would consist of embedded Pt within the interior cell wall and a miniaturised reference electrode would be attached to an external port. This design would avoid the need for volume compensation accessories. However, the maintenance of electrical connection to all samples proved too big a design challenge.

Design 3

The third design was a small single-sample cell, based on a ‘click-pen’ solenoid mechanism to switch the sample between surface analysis and ‘dwelling’ modes. Similar miniature electrodes would be used, as per Design 2. However, this design was not deemed suitable for remote use on a beamline due to the large size of solenoid motor required for moving seals. Additionally, high temperatures sometimes result from these motors, which could disrupt sample-environment interaction. Additionally, the downward pressure of gravity within the spectroscopic part of the cell would cause the window to be permanently bowed. However this design could be revisited for non-electrochemical experiments.

6.2.3 Design of the peCell

From lessons learned during preliminary designs, it was decided to remain close to the initial eCell concept regarding the mechanism (© M. G. Dowsett). The eCell contains a cam movement within the cell so that no volume compensation device is required (except for fine-tuning the window flatness). It was decided to design a Bragg-type multicell from this starting point in order to benefit from testing multiple samples during one beamtime, thus saving on material costs for multiple single cells.

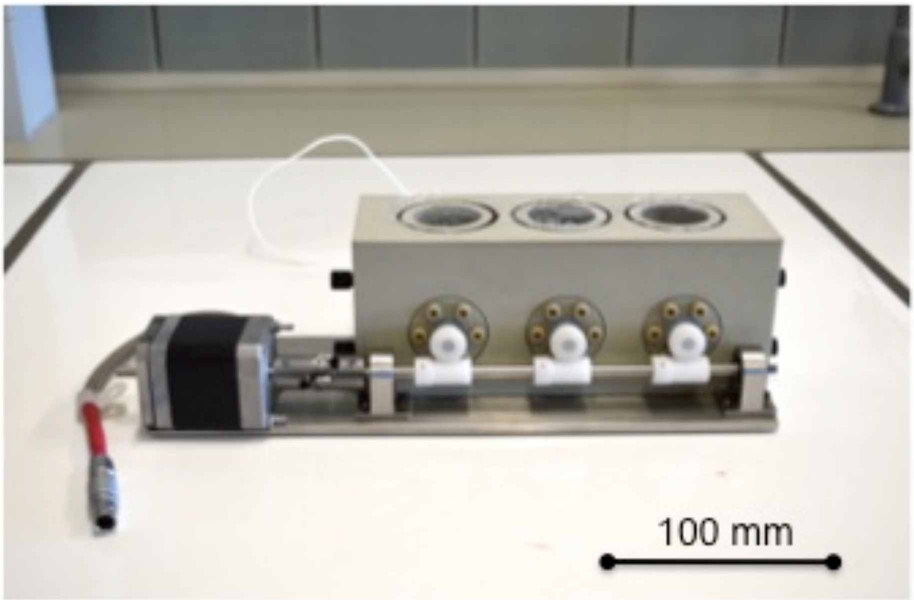

Figure 6.1 The assembled peCell, with motor. See Figure 6.2 and Table 6.1 for an explanation of parts.

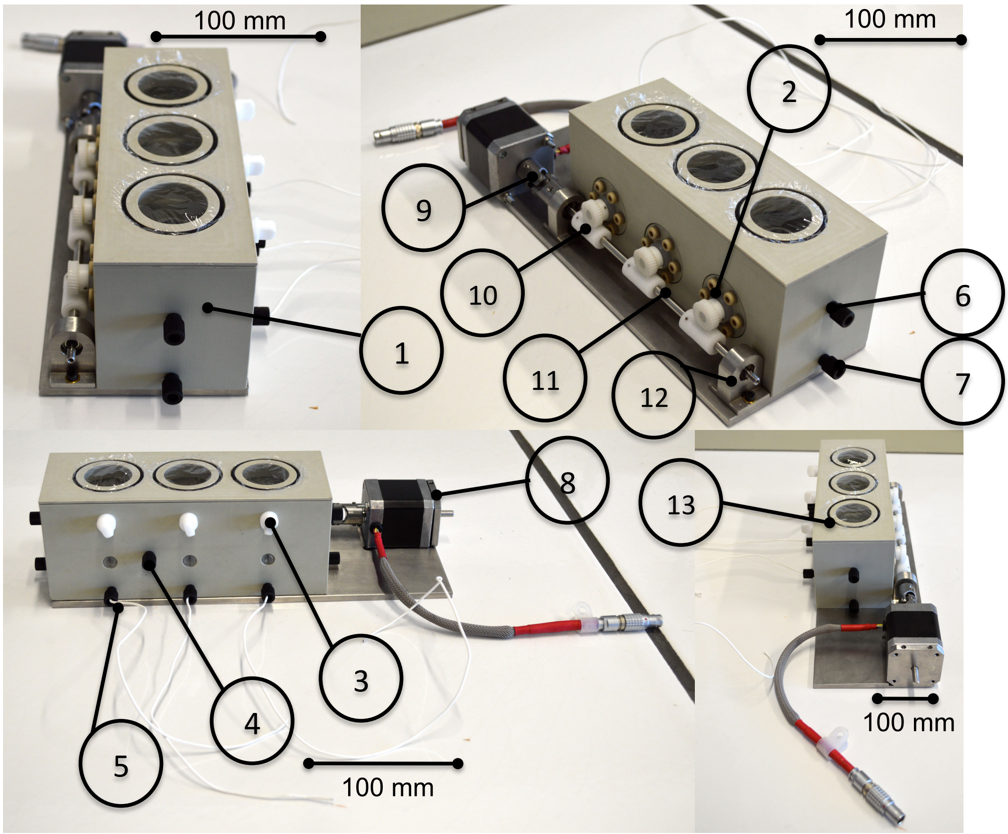

Figure 6.2 The assembled cell body with all attached parts

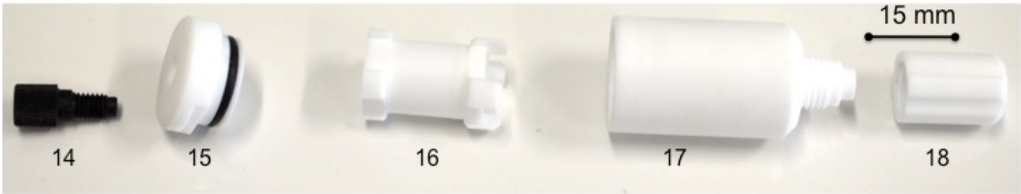

Figure 6.3 The environment generator for containing acetic acid or saturated salts [4], which create a desired environment away from the main cell body. See Chapter 5 for a description of its use with the eCell.

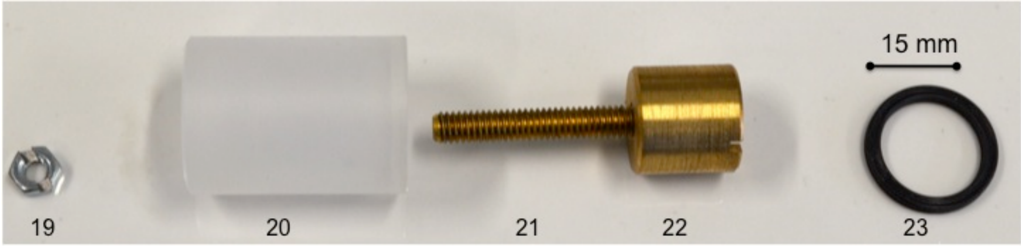

Figure 6.4 The eCell working electrode (© M. G. Dowsett). Later the PCTFE holder was redesigned – it was shortened by 1 cm and remade from PTFE.

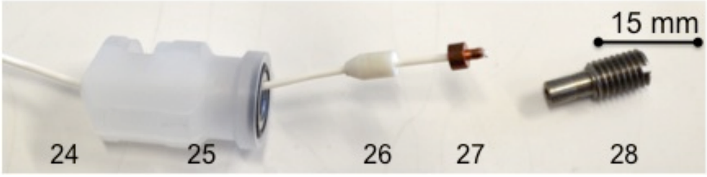

Figure 6.5 Working electrode piston parts, showing electrode connection through piston (© M. G. Dowsett)

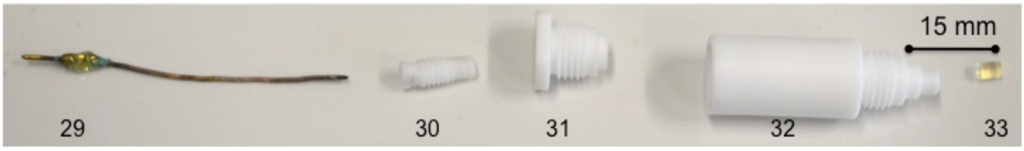

Figure 6.6 Reference electrode parts for Ag/AgCl electrode (© M. G. Dowsett)

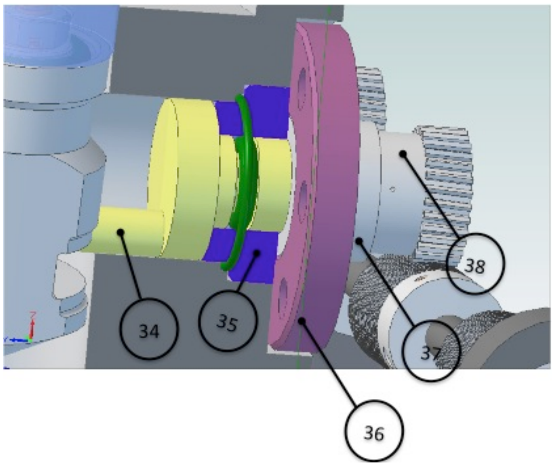

Figure 6.7 3D drawing of Cam assembly

Table 6.1 Labels for numbered parts, with material (if made) or supplier (if bought) details and details of associated seals/screws

#	Part	Material or Supplier
1	Cell body	Polypropylene (Polystone P, Röchling, Germany)
2	Port for cam movement	See Figure 6.7
3	Reference electrode/environment generator port	See Figure 6.6
4	Counter electrode (CE) port	Fits an M6 nut, sleeve and 1/16 inch ferrule (all Upchurch) on CE output
5	Working electrode (WE) outlet port	Fits an M6 nut and 1/16 inch ferrule (all Upchurch Scientific, USA) on WE output
6	Filling port (lower)	Detail in Figure 6.1 drawing
7	Filling port (upper)	Detail in Figure 6.1 drawing
8	Motor for worm gearing	Portescap type 17H218D05B-D
9	Universal joint	Eriks and Baudoin, Belgium
10	Worm	HPC Gears, UK
11	Shaft	Unhardened stainless steel; manufactured by Mark Dowsett, EVA Analysis
12	Plummer block	Stainless steel; fits 4 mm circlip and 4 x 10 x 4 mm bearing (both Simply Bearings Ltd.)
13	Window	Polypropylene; fits 41 x 2 Viton® O-ring (MEA bvba, Belgium) and Kapton® or Ultralene® film
14	M6 nut	Upchurch Scientific, USA
15	Environment generator cap	PTFE; fits a 16x2 Viton® O-ring (Brammer Ltd. UK)
16	Cup	PTFE
17	Environment generator body	PTFE
18	Environment generator lid	PTFE
19	Nut	Stainless steel
20	WE body	PCTFE
21	Working electrode contact	Brass
22	Electrode support	Brass
23	Quad ring 12.42 x 1.78	Viton® (Brammer Ltd. UK)
24	WE output	1.6 mm⌀ PTFE coated silver plated copper wire
25	Piston	PCTFE; fits an 11 x 2 Viton® O-ring (Brammer Ltd. UK)
26	Wire compression seal	PTFE
27	Wire Connector Nipple	Copper
28	WE Connector	Stainless steel 316
29	Reference electrode wire	Silver (Goodfellow Ltd, UK), coated with AgCl electrochemically
30	Wire seal gland	PTFE
31	Electrode cap	PTFE
32	Reference electrode body	PCTFE; to be filled with 3 mol L^{-1} KCl
33	Vycor tip	Bioanalytical Systems Inc., USA
34	Cam	PCTFE; fits a 6 x 2 Viton® O-ring (Brammer Ltd. UK)
35	Cam sleeve	PCTFE, fits a 17 x 1 Viton® O-ring (Brammer Ltd. UK)
36	Cam flange	Polypropylene, fits 6 x M4 PEEK cap head screws
37	Cam tail hula hoop	PCTFE
38	Worm wheel	HPC Gears, UK; fits a 1.5 mm dowel pin (AccuScrews, UK)

6.2.4 Materials

All materials were chosen for their chemical resistivity. The cell body and other non-moving parts were made from polypropylene. Polypropylene has a high chemical resistivity towards a range of chemicals which are commonly found in our test systems (e.g. acetic acid) [5]. In addition the cost of polypropylene is significantly lower than PCTFE (polychlorotrifluoroeythylene, the material from which the eCells are made), which has a cost per weight similar to that of gold. The cell body was made from polypropylene containing an inorganic dye (i.e. non-white polypropylene). It is presumed that the dye has no adverse effects on peCell experiments. However, if the prototype works well and there were a requirement for another generation of peCells, they would be made from PCTFE in order to maintain similar thermal expansion properties between parts [6].

All moving parts were to be made from PCTFE. PCTFE is highly chemically resistive to all possible chemicals planned for use in the peCell [7]. An important factor for moving parts: PCTFE has low thermal expansion (70-100 ppm/C) and is relatively hard (> 70 Shore) compared to PTFE (~55 Shore) [8]. The hardness of the material is an important factor in the ability to accurately and easily machine these parts: threads are stronger, and components are more rigid and will deform less easily. The compatibility of the PCTFE and polypropylene in the peCell will be evaluated in Chapter 7.

All seals (O-rings) are made from Viton®, a fluorocarbon rubber. This material was chosen due to Viton's high chemical resistivity, therefore being suitable for long-term contact with chemicals in the peCell.

6.2.5 Fittings

Like the eCell, the peCell has two types of threaded port for the attachment of accessories, and for electrical and liquid feedthroughs. The larger port is custom (Port Type A, Figure 6.1), and fits an M12 x 1.25-threaded screw with an O-ring seal. This port is designed to fit the reference electrode (Figure 6.6) or environment generator (Figure 6.3) at three different positions adjacent to the working electrode axes (e.g. Part 3, Figure 6.2). The smaller port type (8 in total) fits standard M6 x 1-threaded HPLC fittings. Electrical feedthroughs (working electrode, counter electrode) fit a nut and ferrule (both 1/16”) (Part 5, Figure 6.2). Fluid feedthroughs take the same fittings for Teflon tubing or use an M6 x 1 barbed adapter to fit soft Tygon ® tubing (⌀1.6 mm, inner) (Parts 6 and 7, Figure 6.2).

6.2.6 Windows

Each sample bay has its own elastomer window, which is held in place by an O-ring (Part 13, Figure 6.2). Kapton® (DuPont, USA), which has a thickness of 6 – 12 μm, is used as the window material for XRD measurements due to its X-ray transparent properties. Ultralene® (Spex UK Ltd.) can also be used as a window material if optical emission is to be measured. The long-term properties of the window are unknown. For example, ion adsorption onto the polymer film from the electrolyte could introduce errors over time. In addition, the thickness of the polymer could make it vulnerable to puncture during transportation and use. To prevent this, the windows were covered with a solid plastic lid for transportation. The O-ring seal is relatively strong and can prevent electrolyte leakage from a full cell. The O-ring is put in place by stretching it over the groove while the film is in place (Figure 6.8).

Figure 6.8 Window assembly using Ultralene® film

6.2.7 Filling

The cell can be filled from the ports furthest from the window (Part 7, Figure 6.2) using a peristaltic pump (Watson Marlow 502S, UK) or using a syringe filled with electrolyte, similar to the current eCell filling system [9]. The uppermost ports act as the fluid/air vent (Part 6, Figure 6.2). They are joined to the cell by bores (Port type E, Figure 6.1) which connect two short lengths of ⌀3 mm Teflon tubing to the windows. This ensures that the very top of the cell is filled last.

The type of tubing used for filling depends on which filling mechanism is chosen. For the prototype testing Tygon® tubing (VWR, Belgium) was used to fill the cell from the peristaltic pump and Teflon FEP tubing (VWR, Belgium) was used to empty the cell. Three mm diameter Tygon® tubing was used with the peristaltic pump because it is soft and therefore allows the peristaltic action. It is also resistant to the kinds of environments expected within the peCell [10]. The Teflon tubing used for emptying the cell had a larger bore diameter than Tygon® to reduce build-up of hydrostatic pressure within the cell.

6.2.8 Electrodes

The peCell can function as a three-electrode electrochemical cell. The designs of the working (Figure 6.4) and reference electrodes (Figure 6.6) make them interoperable with the eCell (© M. G. Dowsett). A ⌀1 mm platinum counter electrode (Figure 7.1) stretches along one of the long sides of the cell, adjacent to the working electrodes. The electrode is attached to the outside of the cell through a small Pt connection block and a length of 1 mm ⌀ wire.

The working electrode sample is encapsulated within the working electrode holder using a 12.42 x 1.78 mm Viton® quad ring (Brammer UK Ltd.) to ensure the electrical connection behind the working electrode stays dry (Figure 6.4). The working electrode holder is simply screwed into the piston (Figure 6.5) and sealed using the O-ring on the top face of the piston.

The reference electrode is an Ag/AgCl electrode (Figure 6.6), which is mounted onto the M12 x 1.25 ports (Part 7, Figure 6.2). The Vycor tip keeps the 3 mol L^{-1} KCl within the electrode while still allowing ion transfer. The electrode is sealed using multiple O-rings and can be kept for several years once conditioned. The electrode is conditioned by roughening the silver wire with P1200 SiC grit paper and, after rinsing with DI water, dipping the wire into a 3 mol L^{-1} KCl solution (the same used in the reference electrode). The silver wire is then attached to the positive terminal of a 9 V battery through a 56k resistor. The negative terminal is attached to a length of platinum wire, also immersed in the solution. After 1 hour the silver is coated in AgCl and ready for use after assembly.

6.2.9 Electrochemical measurements

When the peCell is used as an electrochemical cell, the corrosion potential can be monitored using a voltage data logger (Matchtech Volt 101A, USA). These devices are designed for long-term voltage monitoring. The Matchtech Volt 101A can measure continuously for 300 days (1 measurement every 10 minutes). The working electrode output and reference electrode are attached to the voltage logger. This device was chosen for its portability and voltage detection range (± 3 V). However, the input impedance of the device had to be buffered, as shown in the results section.

For shorter measurements and not during transportation, a Palmsens handheld potentiometer (Palmsens, The Netherlands) can be used. This device can conduct a wider range of electrochemical measurements, such as cyclic voltammetry, chronopotentiometry and OCP, at the working electrodes to collect other electrochemical data [11].

6.2.10 Motors and movement

The three working electrodes are moved between surface analysis and electrochemical/environmental exposure positions using a stepper motor (Part 8, Figure 6.2), which drives three worms on a common shaft. The worms drive the cams of the working electrodes synchronously through worm wheels (Figure 6.7 and Part 2, Figure 6.2). The rotation of the shaft can be remote controlled from outside the experimental hutch on a synchrotron.

The shaft is mounted in stainless steel flanged ball bearings (4 x 10 x 4 mm, Simply Bearings Ltd., UK) mounted so as to take up any thermal expansion (Part 12, Figure 6.2).

6.2.11 A working electrode position sensor for the eCell or peCell

The reproducibility of SR-XRD results from the working electrode can be affected by inconsistent sample height therefore the implementation of a position sensor was expected to improve results. A position sensor utilising the Hall effect was designed for the detection of the position of the working electrode with respect to the window. It was prototyped for the eCell with the intention of adding to the peCell at a later time.

A Hall sensor returns a voltage proportional to the magnetic field thus acting as a contactless transducer of magnetic field strength to current or voltage [12]. Equation 6.1 shows the Hall effect equation: V_H (Hall Voltage), R_H (Hall coefficient), I (current), B (magnetic field), t (thickness of sample).

$$V_H = R_H \frac{IB}{t} \tag{6.1}$$

An op-amp test circuit for the sensors (Figure 6.9) was powered by 15 V via a regulator from the power supply within the electronics for the eCell. The Hall sensors were provided with a ±5 V power supply via a 15 V low voltage regulator from the op-amp circuit.

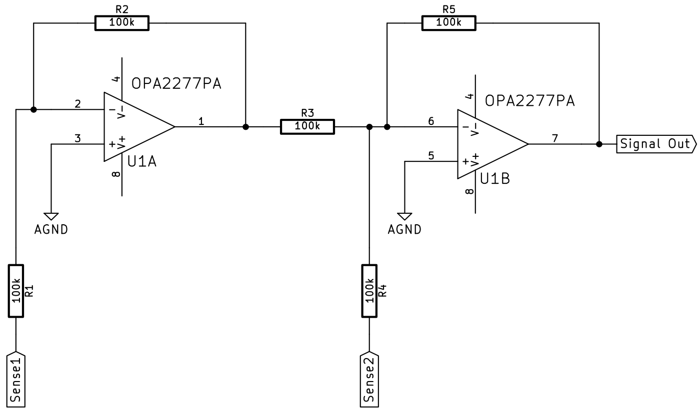

Figure 6.9 Test Circuit 1: Hall sensor op amp circuit diagram. ‘Sense 1’ and ‘Sense 2’ refer to the Hall sensors.

6.3 Experimental

6.3.1 Measuring the system impedance

In order to calculate the buffer required for the voltage logger, the output impedance of the eCell was tested. The output impedance of the eCell was recorded as an accurate estimate of the peCell impedance due to the similar electrodes used. The eCell MkIV was set-up with the Pt counter electrode as the working electrode and the Ag/AgCl reference electrode. A perspex dummy working electrode was put in place of the working electrode holder. A high impedance voltmeter (Keighley 616 Electrometer, USA) was used to measure the open circuit potential and a cascade of resistors from 50 GΩ to 21 kΩ were sequentially loaded onto the circuit (50 GΩ, 10 GΩ, 5 GΩ, 1 GΩ, 500 MΩ, 100 MΩ from Vishay Inc., USA; others from RS Components, UK). The output impedance is equal to the load which halves the E_{corr} [13]. The E_{corr} was left to equilibrate for at least 5 minutes in between each measurement. The E_{corr} of the loaded circuit was recorded every 10 seconds until the value had stabilised.

6.3.2 Optimising a working electrode position sensor for the eCell or peCell

The circuit shown in Figure 6.9 was tested prior to building of the custom eCell parts in order to check the range of the Hall sensor was appropriate for the eCell. This was done very simply using different numbers of SmCo magnets and a plastic ruler. The range of position sensing required by the eCell is 17 mm, which is equal to the range of movement of the piston. Presuming the magnet is placed in the base of the piston and the Hall sensors are housed in the base of the cell, the Hall sensors must be able to detect this range from 16 – 33 mm away from the sensor.

After this trial, two Hall Sensors (Honeywell SS495A) were incorporated into a custom-made base (Figure 6.10). The final version of the Hall sensor setup included neodymium iron boron magnets because the magnetic energy of these is 1.5 – 2 times greater compared to SmCo [14]. Three ⌀3 mm x 3 mm magnets were housed in a modified working electrode connector (Part 28, Figure 6.5) to avoid modification of the piston.

The Hall sensor circuit was then constructed on a breadboard. The amplification was increased from 100 kΩ by changing the resistor over the feedback resistor (R5, Figure 6.9); the piston was moved from its highest position to lowest position, and the output was measured between each point at various amplifications.

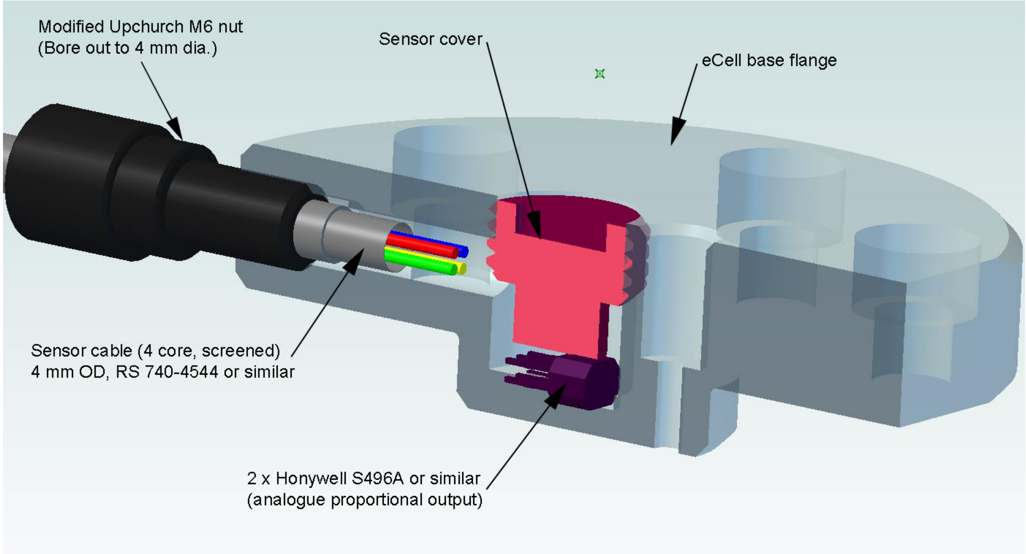

Figure 6.10 3D assembly of new eCell base, incorporating the Hall sensor modification (© Mark Dowsett)

6.4 Results and discussion

6.4.1 Analysis of the peCell design

The first peCell prototype was manufactured in house at the Department of Analytical Chemistry, UGent and by an external workshop (Verschuren

Hugo NV, Belgium; cell body and window only). It was assembled as shown in the Section 6.2 and tested fully – mechanically and electrochemically. During this process several design flaws were highlighted and are discussed below. These issues can be addressed if a second prototype is made.

The worm gearing, although a neat solution to the problem of moving three electrodes simultaneously and in phase, caused problems during assembly due to the intricate alignment of the worms and worm wheels. Correct alignment is necessary for uniform movement to the window of all electrodes, and therefore is essential for surface analysis. Additional problems with the worm gearing are addressed in Chapter 7.

The combined height of the piston and original working electrode design did not allow a full cam rotation, and therefore only a small movement range of the sample was achieved. A complete cam rotation would cause the sample to be pressed up against the window resulting in the window becoming detached. As a result the working electrode was redesigned to shorten it from 25 mm (Figure 6.4) to 15 mm in length to allow a full working range of the electrode without contact with the window. The piston cannot be shortened for mechanical reasons. The new electrodes were manufactured from PTFE due to a lack of PCTFE supply. These electrodes are tested in Chapter 7.

During initial testing, the biggest problem was that of electrolyte leakage leading to incomplete filling. It was found that all the ports intended to take the M6 Upchurch fittings (Port types C and E, Figure 6.1) were designed incorrectly - the port depth was longer than the original eCell design meaning there was no surface on which the seal could rest. As a consequence the ferrules were not sealing and the ports were leaking. In order to produce a seal, hard PCTFE tubes with the outer diameter equal to the inner diameter of the bore were placed inside the ports. This simple addition successfully sealed these openings. As an additional measure PTFE tape was wrapped around the threads to prevent further leakage. Once the seals were improved, filling could be achieved if the cell was simply tipped vertically to allow air bubbles to escape through the uppermost port.

6.4.2 A long-term voltage logger for OCP measurements

In order to measure the E_{corr} of samples using the OCP method within the peCell over long periods of time and during transportation, a voltage logger was purchased. Such data loggers are designed for long term use. Data is stored on the logger and downloaded into relevant software when required. A handheld PalmSens potentiostat (PalmSens, The Netherlands) was also trialled but was deemed unsuitable for long-term use due to the limited number of data points stored by the software and the need for constant attachment of the potentiostat to the cell and to the software on a PC. Simultaneous attachment to the peCell and a PC would be especially difficult during transportation. (A PalmSens application for OS X- and Android-based mobile devices was in development at the time of writing [15]: the PalmSens would be connected to the electrodes of the cell and data would be transmitted to the app on a mobile device via Bluetooth, thus avoiding the need for connection to a PC.)

The voltage logger of choice, MadgeTech Volt101A, has a 10 year battery life, a 10^6 reading storage capacity (± 0.05%) and a suitable voltage range for our purposes (±2.5 V). In order to keep the error of measured potential values below 0.1% the voltage logger needed to have an input impedance of 100 times the output impedance of the peCell. The input impedance of the voltage logger is

125 kΩ. The output impedance of the eCell was recorded as an accurate estimate of the peCell impedance due to the similar electrodes used.

The output impedance is equal to the load which halves the E_{corr} [13]. The E_{corr} was measured to be between -0.0342 V and -0.0210 V depending on how long the system was left to equilibrate in between loads. Loading the circuit with upwards of 10 MΩ gave no change in E_{corr}. Loading the circuit with resistors of 1 kΩ and below gave a voltage reading of 0 V. The E_{corr} for the remaining intermediate resistor loads are shown in Figure 6.11.

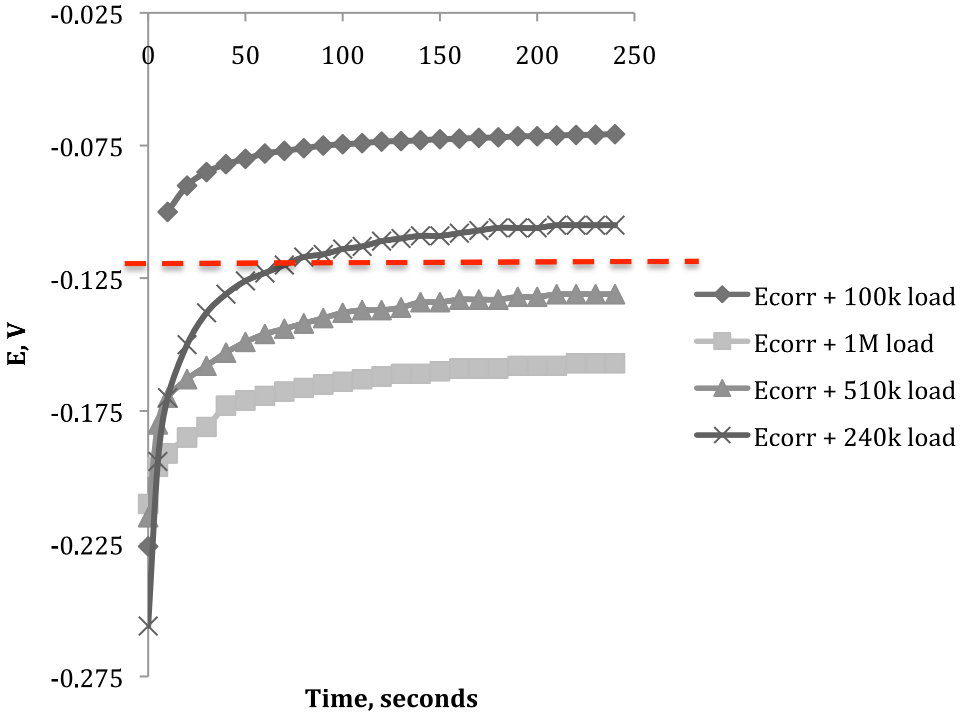

Figure 6.11 Finding the output impedance of the eCell MkIV. The red-dotted line shows the average E_{corr} value.

The average E_{corr} for the measurements is 0.227 V (Figure 6.11). The output impedance of the cell therefore lies between 510 and 240 kΩ. The median value for the output impedance is 375 kΩ. Therefore, if the input impedance of the data logger is to be at least 100 x that of the output of the peCell it will require an input impedance of at least 300 MΩ to be added using a follower op-amp. Figure 6.12 shows the circuit diagram for the buffer (OPA347, Texas Instruments, USA) which was integrated with the Volt101A to give the required input impedance. An alternative to this would have been to purchase a pH logger, similar to the Volt101A - pH loggers also have a high input impedance. Spectroelectrochemical testing using this logger is shown in Chapter 7.

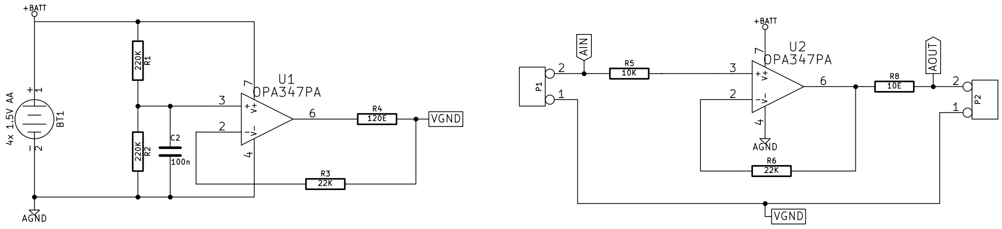

Figure 6.12 Circuit diagram of the battery-powered buffer integrated into the Volt101A logger, designed and built by Jorge Anjos (Department of Analytical Chemistry, UGent).

6.4.3 Optimising a working electrode position sensor for the eCell or peCell

In initial testing using Test Circuit 1 (Figure 6.9), a range of 0 – 120 mV was detected using a multimeter over a separation distance of 40 mm between the Hall sensor and the magnet. These results are shown in Figure 6.13. In order to improve the Hall voltage range, the test circuit was altered to give a gain of 4 and 10 and the number of magnets was increased. The new test circuits delivered an offset of 9.82 V which was subtracted from the recorded voltages to give the results shown in Figure 6.13. The test circuit with a gain of 4 and using 2 magnets gave the greatest improvement to the voltage range.

To conduct further optimisation, Test Circuit 1 was mounted on a breadboard and the Hall sensors positioned inside the custom-made eCell base (Figure 6.10). Feedback resistors were changed to amplify the signal. Results from these tests to find the optimal parameters for the Hall sensor in the eCell are found in Table 6.2.

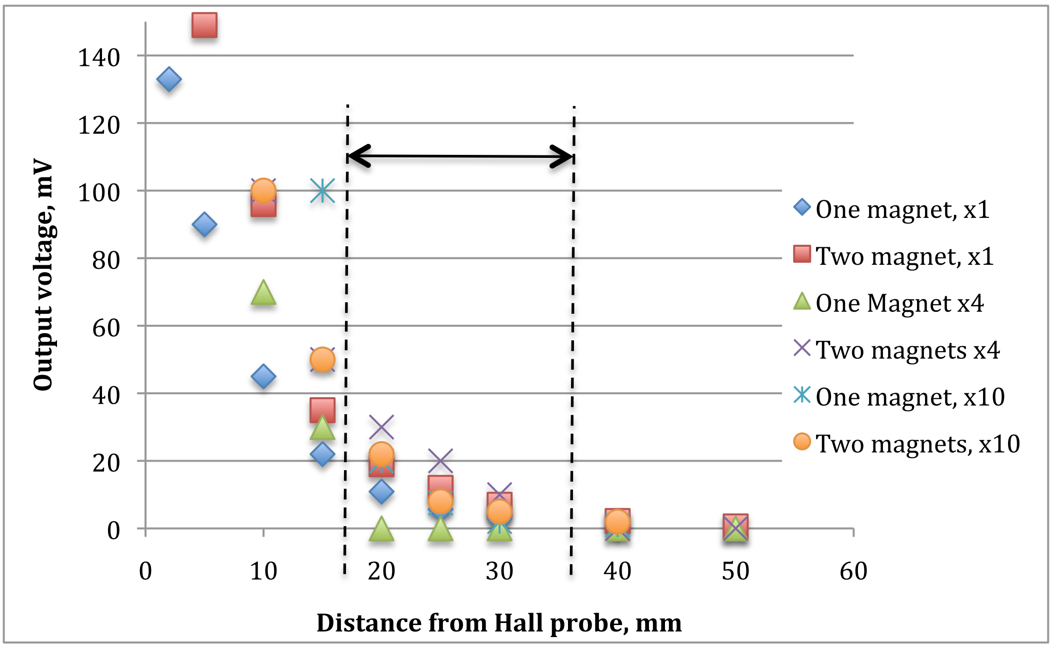

Figure 6.13 Measuring the output voltage of the Hall sensor with distance from the Hall probe to the magnetic field.

Table 6.2 Optimisation of the voltage difference and noise

Amplification	**ΔV ($V_{closest\ to\ sensor} - V_{furthest\ from\ sensor}$), mV**	**Noise, mV**
560 kΩ	201	35
100 kΩ	*125 kHz oscillation*	
220 kΩ	82	22
1 MΩ + 22 nF capacitor across	**365**	**10**

The results show that the introduction of an integrator (capacitor across the resistor) into the circuit improved the noise and delivered the greatest difference in potential between the extremities of piston movement due to the high resistance amplifying the signal. This setup of Hall sensor circuitry and modified eCell parts will now be implemented into normal eCell use in order to improve sample height reproducibility in the future.

6.5 Conclusions

A new multicell (peCell) was designed to accompany the eCell range of environmental/electrochemical cells currently in use. The aim of this new design was to act as a long-term portable cell for the preparation and analysis of samples ahead of beamtime.

The peCell prototype carries out the same functions as the latest eCell albeit with an increased sample capacity, increased volume and alternative movement mechanism. The shape of the peCell has some advantages regarding portability, being easy to pack and transport. However the seals were disimproved from the original eCell design. Sealing the cell is key to its success for use in long-term experiments, and the seals in the eCell design will set a precedent for this in future versions of the peCell. Some aspects of the mechanical design also did not function as planned. This will be discussed in Chapter 7.

In conclusion, the peCell prototype can be used for future long-term spectroelectrochemical experiments but some adjustments are required regarding sealing (to maintain a constant environment for longer timeframes) and movement.

6.6 References

[1] M.G. Dowsett, A. Adriaens, Cell for simultaneous synchrotron radiation X-ray and electrochemical corrosion measurements on cultural heritage metals and other materials., Analytical Chemistry. 78 (2006) 3360–5.

[2] D. Watkinson, Preservation of Metallic Cultural Heritage, in: T.J.A. Richardson, B.R.A. Cottis, R. Lindsay, S. Lyon, D.J.D. Scantlebury, H. Stott, M. Graham (Eds.), Shreir's Corrosion, Volume 4, Elsevier, Amsterdam, 2009: pp. 3307–3340.

[3] J.B. Crawford, James Crawford's Research Outline - Upgrading the passive display case, http://www2.warwick.ac.uk/fac/sci/physics/research/condensedmatt/sims/groupmembers/jamescrawford/, Date accessed: May 20, 2014.

[4] L. Greenspan, Humidity fixed points of binary saturated aqueous solutions, Journal of Research of the National Bureau of Standards. Section A: Physics and Chemistry. 81 (1977) 89–96.

[5] W. Wolshnis, S. Ebnesajjad, eds., Polypropylene, in: Chemical Resistance of Thermoplastics, Elsevier, 2011: pp. 1318–1624.

[6] DuPont, Teflon® PTFE fluoropolymer resin - Properties Handbook, USA, 2015.

[7] W. Wolshnis, S. Ebnesajjad, eds., Polychlorotrifluoroethylene (PCTFE), in: Chemical Resistance of Thermoplastics, Elsevier, 2011: pp. 105–127.

[8] Daikin, PCTFE Product Information Report, Osaka, Japan, 2003.

[9] M. Dowsett, A. Adriaens, EC188 Final Report: Time-resolved XRD and XAS for the conservation / protection of heritage and other metals using XMaS, 2011.

[10] Saint-Gobain Performance Plastics, Tygon® Flexible Tubing, http://www.processsystems.saint-gobain.com/flex-tubing-tygon.aspx, Date accessed: November 19, 2014.

[11] M. De Keersmaecker, M. Dowsett, R. Grayburn, D. Banerjee, A. Adriaens, In-situ spectroelectrochemical characterization of the electrochemical growth and breakdown of a lead dodecanoate coating on a lead substrate., Talanta. 132 (2015) 760–8.

[12] E.H. Hall, On a New Action of the Magnet on Electric Currents, American Journal of Mathematics. 2 (1879) 287.

[13] P. Horowitz, W. Hill, The Art of Electronics, 2nd ed., Cambridge University Press, 1989.

[14] P. Campbell, Permanent Magnet Materials and Their Application, Cambridge University Press, 1996.

[15] Personal Communications from Conrad Chapman and Niels van Veizen, PalmSens BV, (2014).

Chapter 7 Testing the peCell prototype – an SR-XRD study of a novel biomaterial

7.1 Introduction

The peCell concept described in Chapter 6 was tested at the XMaS beamline at the ESRF using a copper-based system.

Copper-bearing intrauterine devices (IUDs) are a very popular method for long-acting reversible contraception. The primary contraceptive effect of the IUD is the prevention of fertilization and implantation through the release of copper ions into the fluid medium of the uterus and their reaction with the endometrium [1,2]. The primary source of these ions is believed to be cuprite (Cu_2O) formed on the device surface through *in utero* reactions with the uterine environment [3–5]. However, without studying the reactions *in situ*, one can never be certain what surface condition gives rise to the release of copper ions. In addition, previous results have found that the treatment and storage of *in utero* samples after removal can provide misleading results during *ex situ* analysis [5,6]. Therefore there is a strong motivation for the study of this system using the peCell.

A new generation of frameless IUDs (Gynefix®, Contrel Research, Ghent, Belgium) aims to reduce the side effects of conventional IUDs such as bleeding, pain and expulsion [5]. The addition of gold to these devices should accelerate the copper release [7,8] and therefore improve anticonception rates for a smaller device and possibly provide protection against STDs [9–12]. Samples modelling this Cu/Au system resided within the peCell for one week while *in situ* spectroelectrochemical data was collected.

7.2 Experimental

Three samples with varying ratios of Cu/Au were made by Pieter-Jan Sabbe (UGent). Polished copper coupons of ⌀12.5 mm (99.99 %, Goodfellow, Cambridge) were sputter-coated with gold using a JEOL JFC – 1300 Auto Fine Coater (Department of Applied Physics, UGent). Coupons were covered with copper tape masks to create samples with 3 different sizes of gold spot – one sample recreated the Cu/Au surface area ratio of the IUD (⌀2.83 mm Au, sample 1), and the remaining samples recreated Cu/Au surface area ratios higher (⌀6.25 mm Au, sample 3) and lower (⌀1.5 mm Au, sample 2) than the Gynefix®. Masked coupons were then sputtered at 30 mA for 600 seconds to create 100 ± 50 nm of gold.

Samples were mounted within the peCell (Figure 7.1) two days prior to beamtime as the most interesting behaviour is said to occur in the 1st week [13,14]. The cell body was flooded with electrolyte modelling intrauterine fluid [3] (SUS) and a cartridge heater was used to keep samples at body temperature during transportation. SUS contains calcium, potassium and sodium chlorides, urea, glucose, monosodium phosphate, sodium bicarbonate (all < 1 g/l) and albumin (35 g/l). SUS has no associated biological hazard and has a pH of 6.2.

The cartridge heater was made by Jorge Anjos (UGent) and consisted of two 18 Ω carbon film resistors mounted in series to give a total power of 4 W at 12 V. The resistors were placed inside a custom-made PTFE nut (see Figure 7.1).

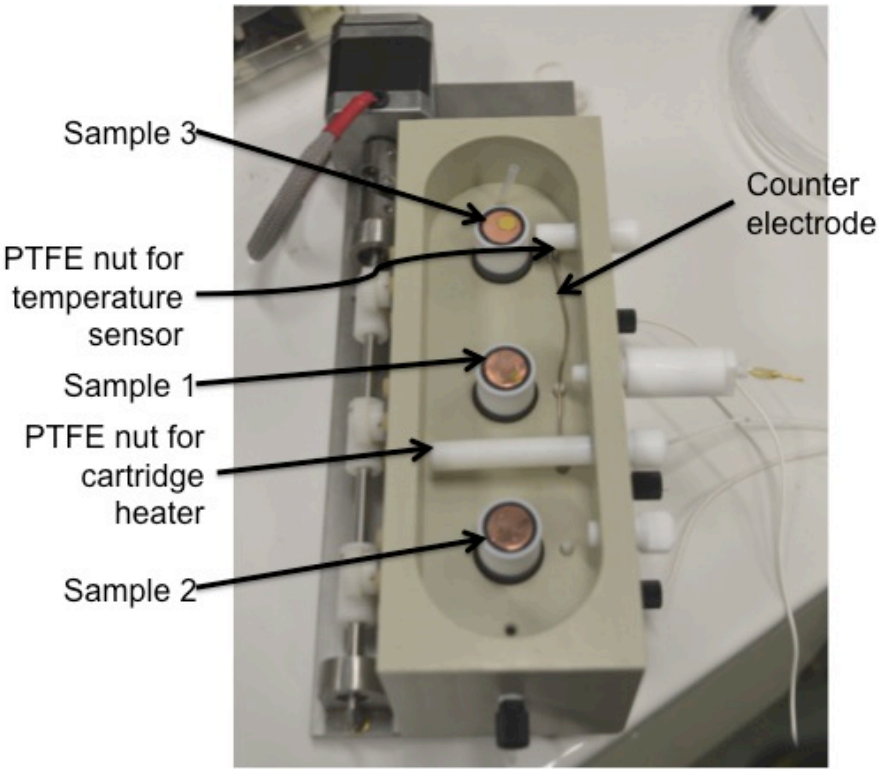

Figure 7.1 Cu/Au samples mounted within the peCell prior to filling with simulated uterine solution (SUS). A sensor records the electrolyte temperature closest to the electrolyte outlet port. The cartridge heater heats the electrolyte between samples 1 and 2, across the width of the cell.

The temperature was monitored using a silicone rubber-coated temperature sensor (model no. NTC-M5L20.K1.5) and controlled using an on/off temperature controller (model no. ESM-3710-N) (both RS Components, Belgium). Due to this heating requirement, changes were made to the peCell's ports to allow the heating element to have a larger surface-liquid contact area and thus heat the liquid more efficiently. As shown in Figure 7.1 an additional M12 port was tapped into the cell wall between samples 1 and 2 to allow the cartridge heater to be mounted.

When the cell was not being transported (for example, during surface analysis) (Figure 7.2), heated electrolyte was circulated through the cell by a peristaltic pump (Watson Marlow 502S) from a regulated hotplate (ESK Hei-Con, Heidolph Instruments, Germany) with a flow of 5.5 mL/min to allow slow and uniform flow into the cell from a reservoir of electrolyte. The electrolyte was heated to 52 °C in order that it was at body temperature on entering the cell. Three mm diameter Tygon® tubing was used to deliver the electrolyte to the cell from the pump. Barbed adapters (MedNet, Germany) reinforced with Teflon tape created the inlet to the cell. For the outlet, M6 ferruled nuts held Teflon FEP tubing, as described in Chapter 6.

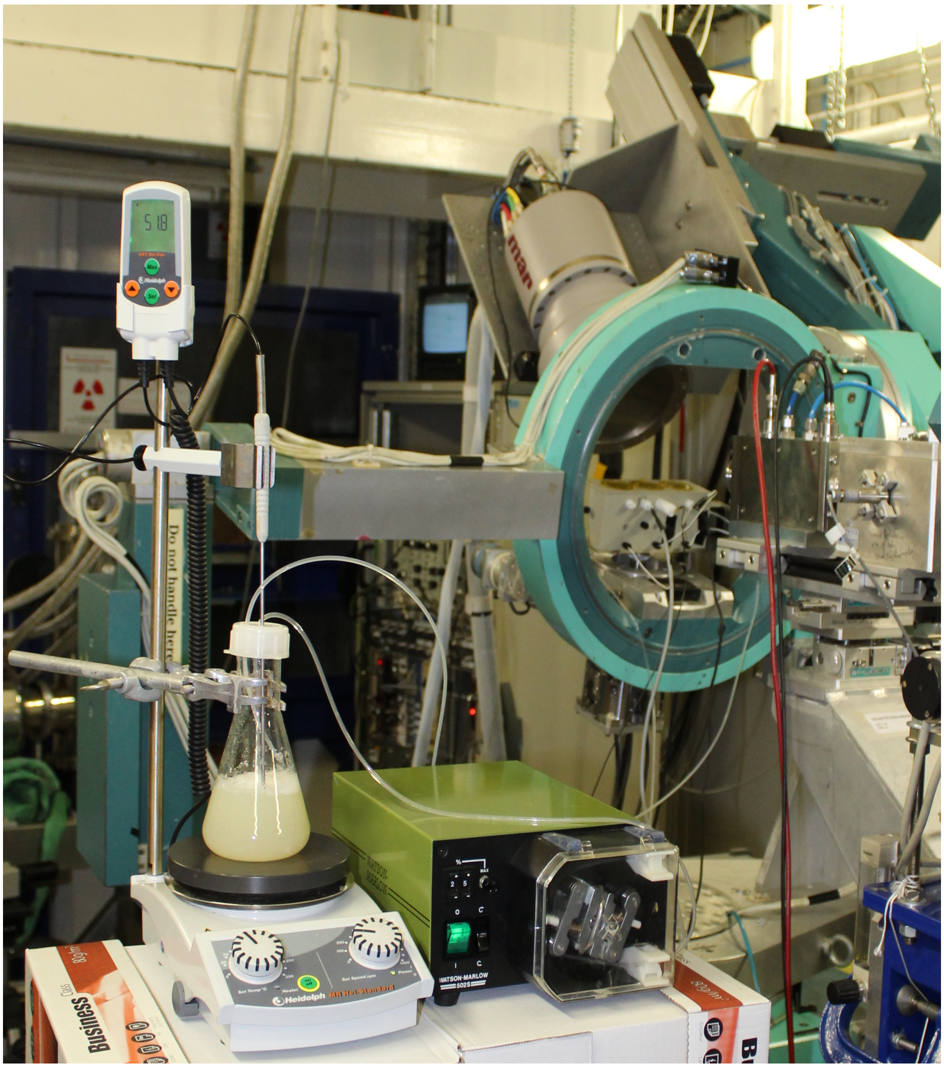

Figure 7.2 The pump-peCell setup on the XMaS beamline. Two meters of tubing were used to pump the electrolyte to and from the cell. A custom-made cap was fitted to the volumetric flask to reduce evaporation.

During the experiment (including transport to and from the beamline), the corrosion potential of sample 1 was constantly monitored using a custom voltage logger (as described in Chapter 6) thus completing the spectroelectrochemical dataset for the sample.

The peCell was transported by car to and from the ESRF. The setup (peCell and accompanying electronics box) was transported in an insulated plastic box and was equipped with a car-jack adapter in order that the cartridge heater could be constantly powered (Figure 7.3).

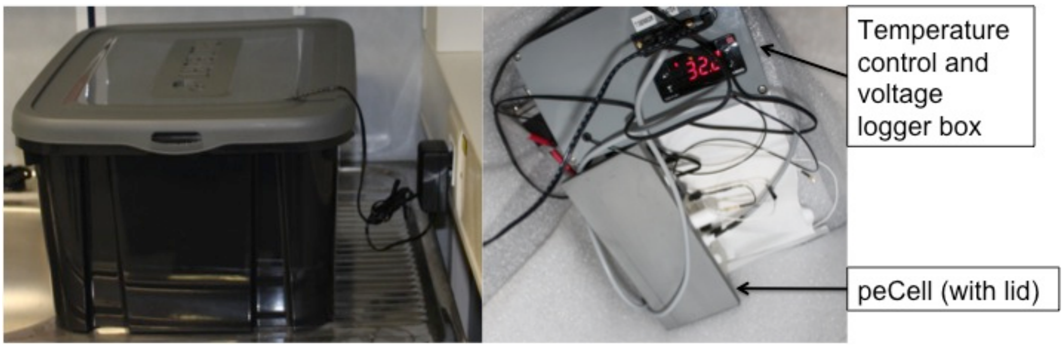

Figure 7.3 Insulated transportation box containing the peCell powered by the mains (left); the contents of the box (right).

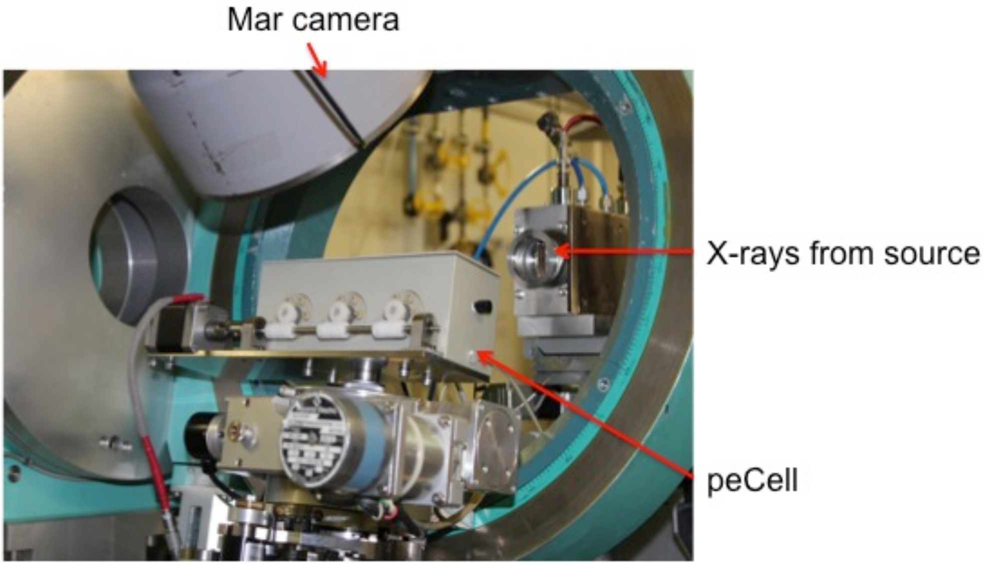

Figure 7.4 The peCell mounted on the XMaS beamline. The axis of the Mar CCD camera was at 44.5° to the incident X-ray beam. 8 keV X-rays were incident at 10° to the sample surface.

SR-XRD patterns were obtained from these samples *in situ* at time intervals of approximately 24 hours for 5 days. SR-XRD data were collected using a Mar

CCD 165 (Mar USA Inc.) 2D detector at XMaS (station BM28, ESRF). The camera was mounted at 44.5° to the incident X-ray beam (Figure 7.4) with a detector-sample distance of 132 mm.

The beam footprint was 3 x 0.5 mm and 9 images (exposure time 10 s) were recorded at 9 positions within a range of ± 2 mm from the centre of each sample. If there was a volume of electrolyte between the sample and the window, 10 images per position were taken to improve sensitivity. This data processing was carried out using the esaProject software [15]. A webcam mounted above the cell was used to record images of the samples.

7.3 Results and discussion

7.3.1 Open-circuit potential and temperature – monitoring the conditions inside the cell

Figure 7.5 shows the corrosion potential (E_{corr}) of sample 1 during the entire experiment alongside temperature data, which was recorded sporadically i.e. whenever there was access to the hutch and the temperature control box.

The E_{corr} has been recorded at -0.2 V for similar experiments with copper in this electrolyte [16]. From the start of the experiment to midnight on day 7, the E_{corr} steadily decreased to approximately -0.1 V from 0.1 V showing steady corrosion of the working electrode surface. Spikes in the data originate from the wiring becoming detached from the working electrode. A simple gold crimped connection was used, which was clearly not robust enough. Figure 7.5 shows that this mostly occurred when the temperature was being recorded, thus showing that these spikes occur due to human activity in the hutch when experiments were changed over.

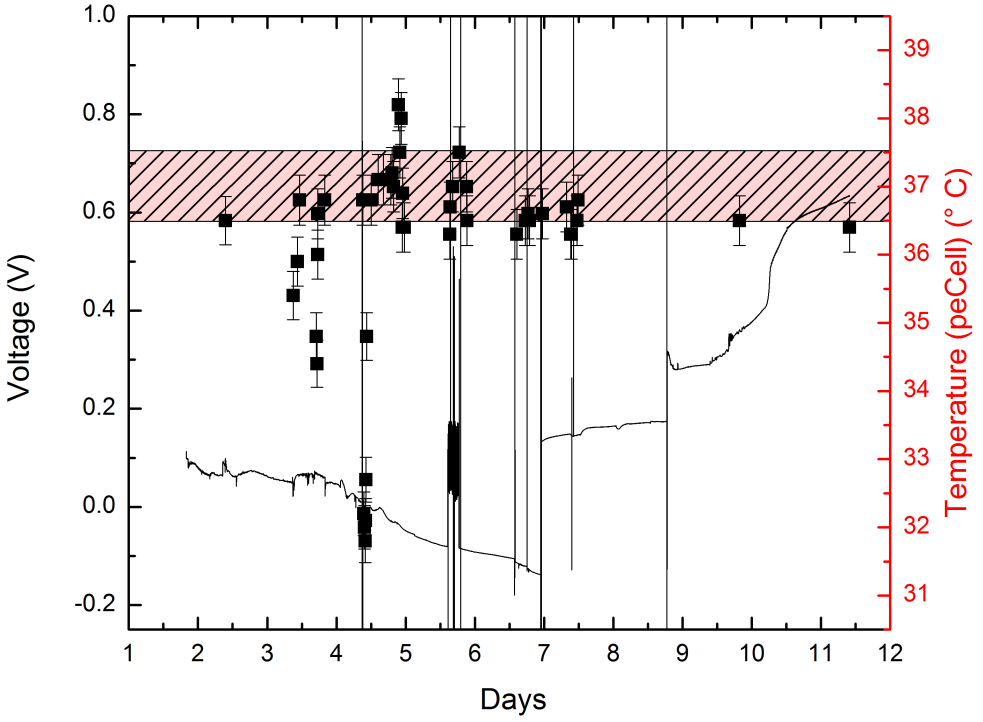

Figure 7.5 The E_{corr} of sample 1 and the temperature of the peCell during the experiment. The red shaded area indicates body temperature, the target temperature range. The cell was transported to the ESRF in an insulated box on day 2. The surface analysis started on day 4 and continued until midnight on day 9. The cell was then transported back to Ghent, Belgium and the experiment was completed at 10 am on day 11.

At midnight on the day 7 there was a spike in the E_{corr} followed by an increase in E_{corr} for the next two days, at a potential 0.2 V higher than before the spike. An increasing E_{corr} is a demonstration of the passivation of the surface [17]. This potential spike is associated with a problem that occurred with the peristaltic pump which was causing electrolyte to leak from the cell. While fixing the problem, 1/4 of the electrolyte reservoir for the peCell had to be refreshed. This could have caused the increasing E_{corr} recorded after this event. Similar data spikes occurred just before midnight on the day 9, when a 0.1 V jump of the stable E_{corr} was observed. This spike is not associated with any recorded event so it is unclear why it occurred. The error on the E_{corr} data is 0.05% according to the logger specifications. However this value does not take into account the error incorporated by the addition of the buffer amplifier – the systematic error is 0.04% and the noise at this frequency (< 1 kHz) is 12 μV_{pp}. Both sources of error are insignificant in this dataset.

Temperature was recorded sporadically during the experiment to check that it was within the range of body temperature. Extensive tests were carried out in the lab prior to the beamtime to check the uniform distribution of temperature within the cell. It was found that when electrolyte was circulating, there was an even distribution of heat through the cell. This also occurred when the cell was gently inverted or shaken to model transportation conditions. When the electrolyte and cell were static (for example on a bench top for 1 hour or in the ESRF guesthouse overnight prior to beamtime) there was a difference of 5 °C between the cartridge heater and the opposite end of the peCell. Therefore the cell was kept static for as little time as possible.

Seventy percent of the temperature values recorded were within the required temperature range. The temperature dropped below 36 °C only during the setting up of the experiment at the ESRF when the cell was removed from its insulated box and the electrolyte pumping was initiated on day 3. The lowest temperatures were recorded when the cell was moved into the hutch from a neighbouring laboratory on day 4. This could be due to a change in ambient temperature. However once electrolyte pumping was restarted body temperature was reinstated over the course of 2 hours and remained within range for the rest of the experiment. Overall, the data show that the temperature was mostly kept in range, aside from some isolated events during setup.

7.3.2 Corrosion product evolution – SR-XRD analysis

Nine XRD patterns (exposure time 10 s) were recorded across a range of ± 2 mm from a central point on each of the samples. Measurements were carried out in this way in order to probe the corrosion products at varying distances from the gold spot. This data will be further processed as part of another thesis to see which corrosion products form at different points on the surface in relation to the gold. However in this thesis the 4 mm range was summed so that the total corrosion products at 24-hour intervals and the main differences between the three samples could be observed, thus testing the efficacy of the peCell.

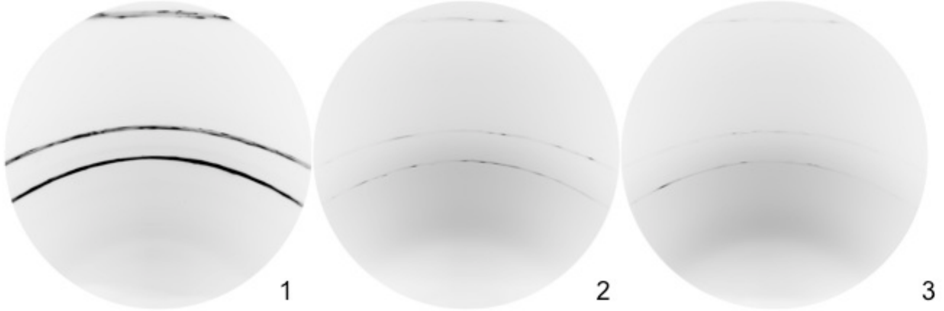

Figure 7.6 Raw diffraction patterns from samples 1 -3 within the peCell after 10 s exposure to X-rays when samples were as close to the surface analysis position in the peCell as possible.

As mentioned previously, for some samples the counts recorded in the diffraction patterns were not as high as others. Therefore 10 consecutive images were recorded per position in order to improve resolution. Figure 7.6 shows the difference in intensity between the three samples. For sample 1 the broad, darkly coloured bands originate from the copper. These bands have a granular appearance due to the large grain polycrystallinity of the copper. The same bands in samples 2 and 3 are faint due to a volume of electrolyte between the sample and the window attenuating the X-ray signal. The dark grey area in the lower half of the patterns shows the scatter from the electrolyte: sample 1 shows little or no electrolyte scatter. The reason for the difference in intensity between sample 1, sample 2 and 3 is due to a fault in the working electrode and window design, which is elaborated on in Section 7.3.3. Therefore the intensity of the peaks across samples cannot be compared – we can only identify and compare corrosion products.

Figure 7.7 shows the data obtained from the three samples within the peCell over the course of the 5-day surface analysis experiment. The aim was to take measurements from a surface area which included copper and the copper-gold boundary. This was difficult to achieve in practice because the cell height and x-y positioning changed when alternating between peCell and eCell experiments. Also, towards the end of the experiment black powdery corrosion products had covered the surface making it difficult to differentiate the gold and copper. However for most of the patterns, the area measured included gold and copper signals.

Sample 1 had the same Cu/Au ratio as the Gynefix®. Figure 7.7 shows that sample 1 had started corroding by day 4 of the experiment. This is in agreement with the OCP data. Over the following four days the main corrosion products were cuprite (Cu_2O) and copper (I)/(II) sulphides. From day 7, crystalline sodium chloride was also detected, which is a component of the SUS electrolyte. Cuprite has been observed previously [3–5] during ex situ analysis, but is liable to flake off over time and was recently suggested to be an artefact of the storage and sample preparation conditions [6]. Copper sulphides have been tentatively suggested to form [18] but this is the first time they have been observed in situ immersed in SUS. Sulphide salts were not added to the SUS, so it is presumed the source of sulphide ions is albumin which is known to contain disulphide bonds [19].

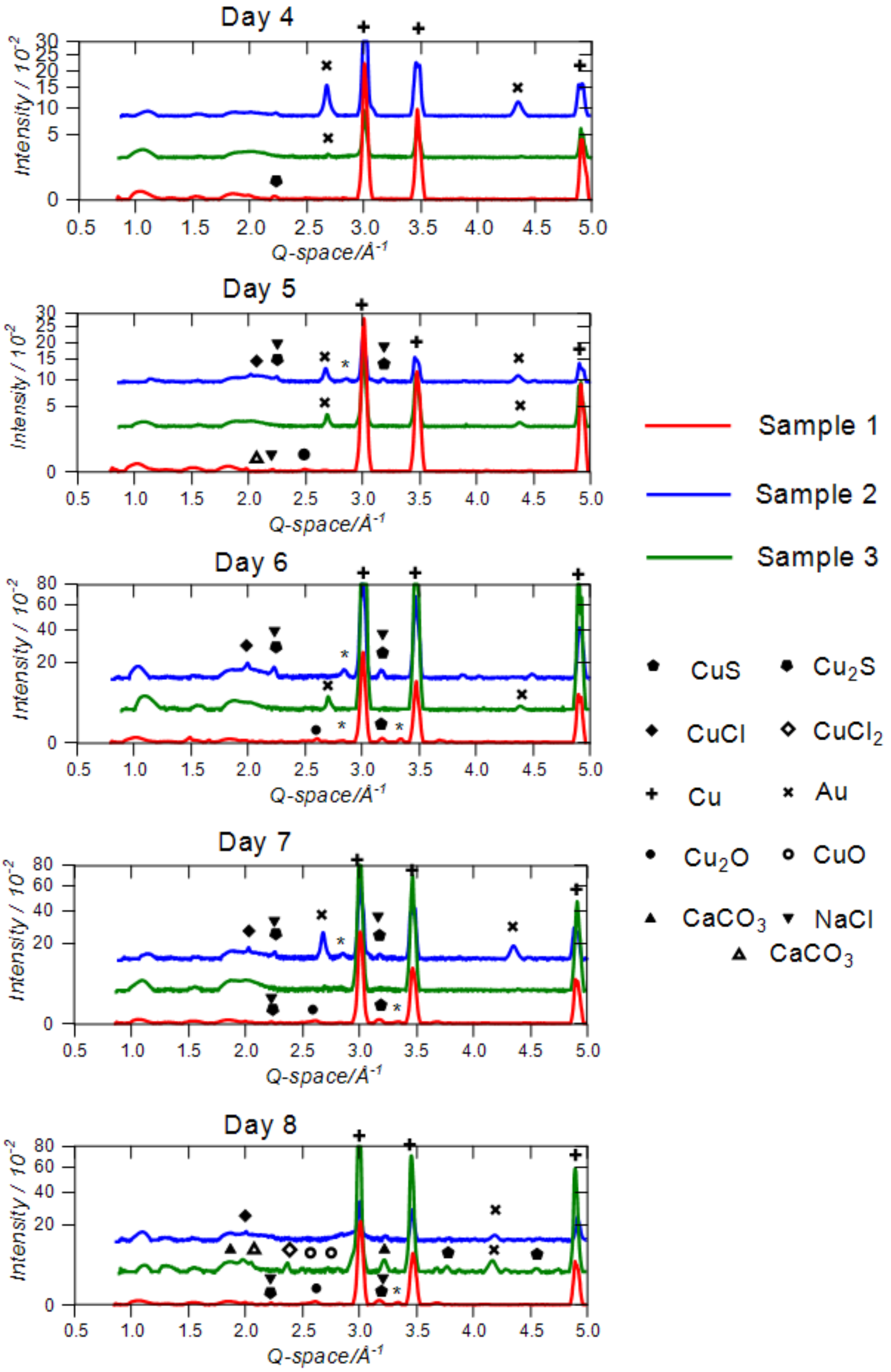

Figure 7.7 Summed diffraction patterns from across a 4 mm range on the surface of the samples 1-3 for five consecutive days. Corrosion products are labelled as shown. Unidentified peaks are marked with a *. Two polymorphs of calcium carbonate were indentified: ▲ is calcite, △ is aragonite.

Sample 2 had the least amount of gold on its surface. On day 5 copper (I)/(II) sulphides had already formed. On day 5 nantokite (CuCl) was also detected as well as sodium chloride. Nantokite has been previously observed in these conditions [4,16] and originates from the reaction of copper with chloride ions in solution (Equation 7.1), a reaction also seen in heritage contexts with archaeological copper and seawater [15,20–22].

$$\mathrm{Cu} + \mathrm{Cl}^{-} \longrightarrow \mathrm{CuCl} + \mathrm{e}^{-} \qquad (7.1)$$

By day 7, nantokite remained on the surface and sulphides were detected at 3.75 $Å^{-1}$ and 4.5 $Å^{-1}$. However it is possible that the copper (I)/(II) sulphides also remained on the surface in an amorphous state. It has been noted previously that the state of copper sulphide depends on the experimental conditions to inform the oxidation [23] and structure [24–27]. Nantokite is usually a precursor to cuprite (Equation 7.2) [28], so it could be suggested that the corrosion is occurring more slowly on this sample compared to sample 1 where cuprite was already present by day 5.

$$2\mathrm{CuCl} + \mathrm{H_2O} \longrightarrow \mathrm{Cu_2O} + 2\mathrm{HCl} \qquad (7.2)$$

Sample 3 had the most gold on its surface. No crystalline corrosion products were detected until day 8. On day 8 a range of crystalline copper (II) species was detected: $CuCl_2$ [4], CuO [1] and CuS [18]. These compounds have a range of solubilities in water: $CuCl_2$ is very soluble in water (76 g/100 mL at 25 °C), whereas CuO and CuS are both insoluble. It is possible that the $CuCl_2$ was formed before 8 days, had dissolved immediately and was a source of Cu^{2+} ions in solution. In other words, after 8 days the corrosion rate had increased and the $CuCl_2$ was being formed faster than it could dissolve. In addition calcite [3,4] and aragonite ($CaCO_3$ polymorphs) had been deposited from the SUS. The presence of solids deposited from the SUS is an unsurprising result because there was a substantial amount of solid material in the electrolyte which built up in the cell over the course of the experiment. In fact a ‘cloud’ of solid material billowed up from the base of the cell whenever the pistons were manoeuvred.

The results from the XRD are backed up by visual observations as shown in Figure 7.8. The surfaces of samples 1 and 2 were covered with a black powdery layer between day 5 and 6, which was loosely attached to the surface initially and was easily removed when simply moving the working electrode within the cell. However towards the end of the experiment and upon removal of the samples, this layer was more permanently attached to the surface. Sample 3 showed a black ring only around the gold spot but this did not appear until the final days of surface analysis, leaving a copper surface almost free of visible corrosion. It is clear from these data that there is a difference in the corrosion behaviour of the three samples in SUS, which is dependent on the surface area of gold.

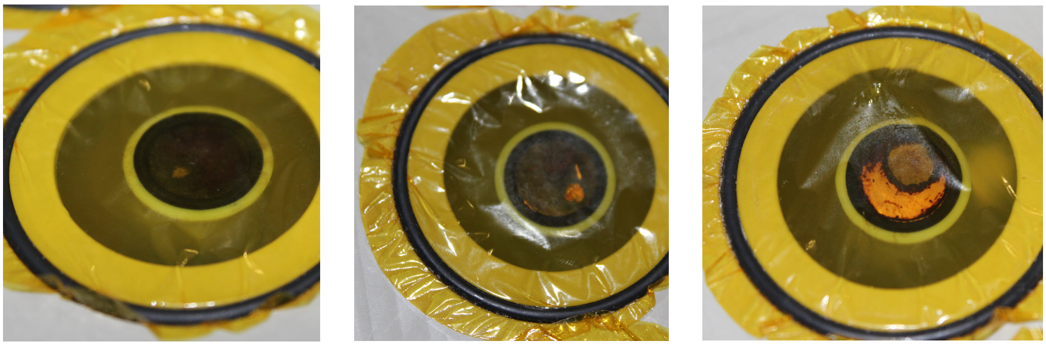

Sample 1 Sample 2 Sample 3

Figure 7.8 Photographs taken of the samples within the peCell after 7 days.

7.3.3 Analysis of the peCell design in use

During the weeklong experiment described in this chapter, no leaks occurred which demonstrates the robustness of the system. However some problems were encountered with the windows. In initial testing, the windows were kept flat when the cell was filled with electrolyte because the reservoir of electrolyte was kept at the same level as the cell. However, it was found that the windows had a range of possible curvatures when moving the cell between laboratory and beamline: if the reservoir was above the cell the windows would bow outwards; if the reservoir was below the cell the windows would curve inwards. The O-rings sealing the Kapton® windows were the incorrect size to hold the window tight (and therefore flat), which was necessary for surface analysis of the samples. Therefore in order to 'force' the window to flatten against the surface of the electrode, the electrolyte reservoir was placed on a jack which could be moved up or down (range 140 cm) to tune the hydrostatic pressure within the cell. This technique worked well for samples 1 and 2. However: sample 3 was adjacent to the electrolyte outlet. This Teflon tube, designed to be an vent for air bubbles at the very top of the cell, was too long and acted like a tent pole to slightly raise the window above the sample thus allowing a thicker layer of electrolyte to cover one half of the sample during surface analysis. This can be seen clearly in Figure 7.9. Signal attenuation by the electrolyte resulted in weaker signals in the diffraction patterns (see Figure 7.6).

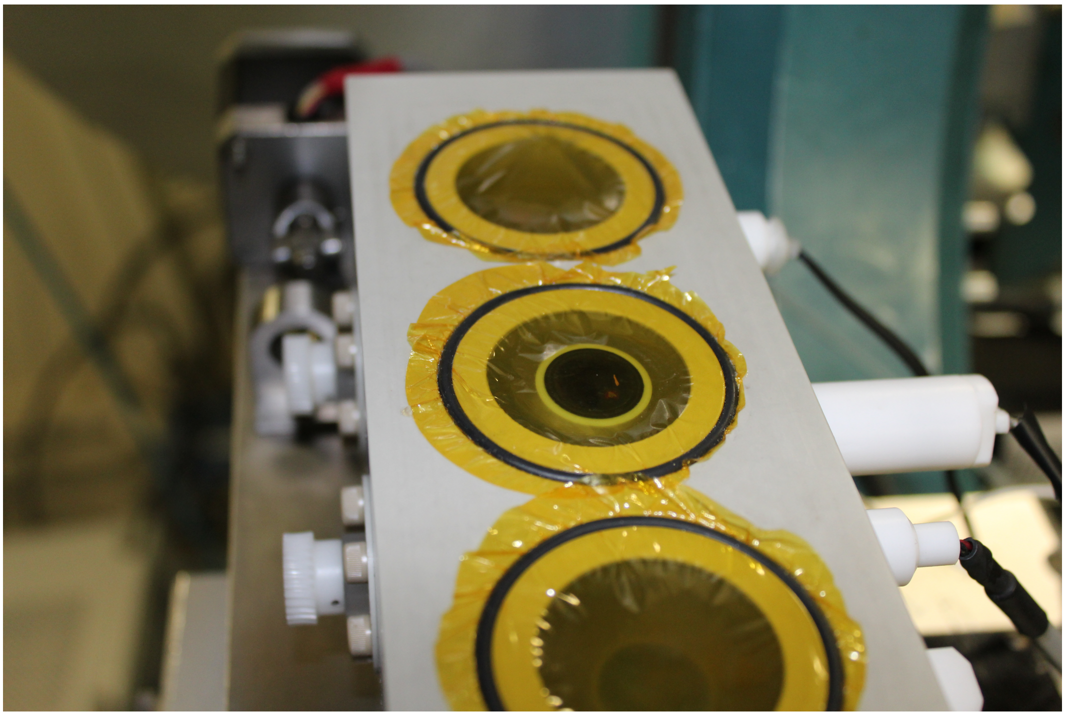

Figure 7.9 The peCell ready for XRD analysis on the XMaS beamline (sample 1 in position), concave windows caused by lowering the jack on which was placed the electrolyte reservoir. The rear sample is sample 3 and the near sample is sample 2.

In future prototypes, the correct O-ring must be used to secure the window and the outlet tubing needs to be trimmed. In the eCell design, a syringe attached to the cell is able to tune the window shape remotely in case of changes in atmospheric pressure [29]. It is uncertain if this feature could be translated to the peCell due to its rectangular shape and long-term experimental requirements. In addition this feature only works with a closed system, and could not have been applied in this particular experiment due to the open flask used to hold the electrolyte reservoir.

In the end it was possible to use the existing windows for surface analysis, but there were other problems in moving the working electrodes for samples 2 and 3 (the left- and right-hand samples) to the surface analysis position. It was noted soon after the first testing of the motors at the beamline that the working electrodes were not moving in alignment because the worm wheel controlling the height of sample 3 was jumping and its teeth being damaged as a result. When the shaft was removed in order to attempt manual movement of the worm wheel it was found that this irregular movement was caused by the piston jamming in the bore of the cell. Consequently the working electrode could not reach the analysis position and was covered with a thicker than usual layer of electrolyte. This weakened the signals in the diffraction patterns (again, see Figure 7.6).

There had been a full movement of the cam at the start of the experiment so this mechanical flaw must have developed during the experiment, possibly due to the heating. There are two materials used in this assembly: polypropylene (cell body) and PCTFE (piston and cam assembly). The coefficients of thermal expansion for these materials are 120-190 x 10^{-6}/°C [30] and 70-100 x 10^{-6}/°C [31], respectively. The difference in expansion coefficients between these materials could make them incompatible and therefore the following machining errors could have been exaggerated in the elevated temperature. Firstly, if there were steps in the bore created during machining this can cause irregular movements. Secondly, only the two end bores are affected (sample 1 in the central position enjoyed a full cam-movement). The geometry of the peCell makes it possible that the end bores became oval during machining. A second iteration of the peCell could be manufactured with PCTFE, making it more compatible with the moving parts.

7.4 Conclusions

This work highlights the importance of techniques which monitor corrosion processes *in situ*. The insoluble copper compounds, which do not provide the Cu^{2+} ions important for anti-conception, were identified and monitored during the course of a 9-day experiment.

Using the peCell, we were able to record SR-XRD patterns from three different samples every 24 hours for 5 consecutive days during which time the E_{corr} and temperature of the cell were also monitored. The cell was successfully transported to the beamline without losing heat or electrolyte whereupon surface analysis could commence.

The samples were copper coupons with different surface areas of gold. The sample with the highest surface area of gold showed the least amount of insoluble deposit on the surface but could have corroded to an unknown extent to form soluble corrosion products. The sample with the least amount of gold demonstrated a range of corrosion products during the experiment. Copper sulphides were formed initially but the final pattern showed just nantokite. The sample which was modelling the 'real' ratio of Cu/Au in the Gynefix® IUD formed cuprite before sulphides appeared, and these species coexisted until the end of the experiment.

The contraceptive action of copper depends on the copper ion release [1,3,11,16], and the 'capturing' of copper ions in corrosion products does not provide this information. Further tests will be done within the ESA research group (UGent) to study copper release from copper/gold samples using flame absorption atomic spectroscopy to correlate with the work described in this chapter. A simple weight loss measurements as a function of gold coating could also quantify the copper loss during exposure to SUS, without identifying soluble copper species. In addition, XAS could be performed on the SUS electrolyte to probe the coordination of the copper in solution.

In order to make a comment about the cell's performance as a multi-cell, the same experiments would have to be conducted in a single cell for the same periods of time. This experiment lasted just 9 days in total. To test the capabilities of the peCell further and fulfil its original design brief, a system would have to be devised to reside within the peCell for up to one year.

7.5 Acknowledgements

MedNet GmbH, Germany are thanked for the barbed adapter parts which were provide free of charge to this project. In addition, this experiment would not have gone so well (or at all!) without this fantastic beamteam: (r-l) Mark Dowsett, Michel De Keersmaeker, Didier Wermeille, Pieter-Jan Sabbe, Victoria Flexer and the author.

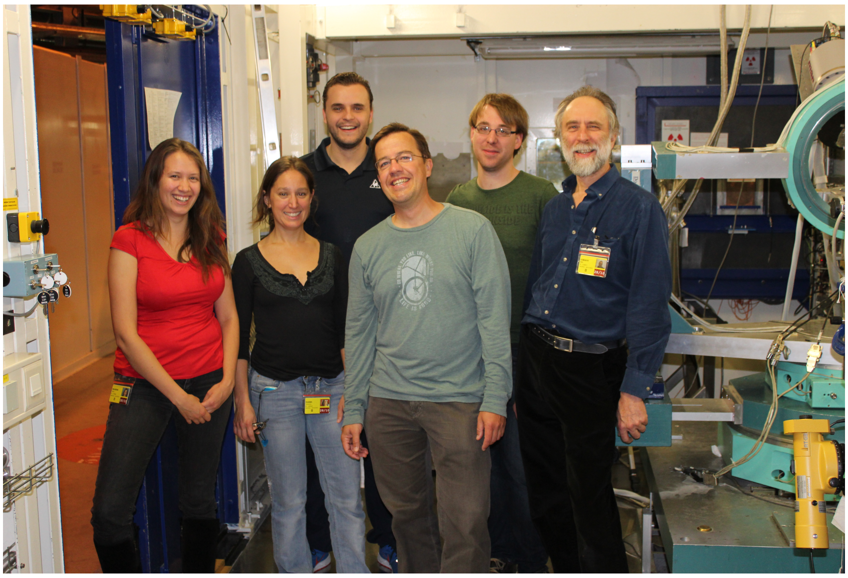

7.6 References

[1] K.M. Lewis, R.D. Archer, A.P. Ginsberg, A. Rosencwaig, The corrosion chemistry of copper intrauterine devices, Contraception. 15 (1977) 93–104.

[2] E. Chantler, Copper Loss From Copper IUDs, in: Intrauterine Contraception: Advances and Future Prospects, 1984: pp. 198–210.

[3] J.M. Bastidas, E. Cano, N. Mora, Copper corrosion-simulated uterine solutions., Contraception. 61 (2000) 395–9.

[4] N. Mora, E. Cano, E.M. Mora, J.M. Bastidas, Influence of pH and oxygen on copper corrosion in simulated uterine fluid., Biomaterials. 23 (2002) 667–71.

[5] D. Wildemeersch, P.-J. Sabbe, M.G. Dowsett, V. Flexer, P. Thompson, D. Walker, P.A. Thomas, A. Adriaens, Assessment of copper corrosion from frameless copper IUDs after long-term in utero residence., Contraception. 90 (2014) 454–9.

[6] P.-J. Sabbe, M. Dowsett, D. Wildemeersch, V. Flexer, P. Thompson, D. Walker, P.A. Thomas, A. Adriaens, Evaluation of site-specific corrosion behavior of copper tubes from a frameless intrauterine device, Paper Submitted to Corrosion Science. (2015).

[7] R. Gonen, L. Gal-Or, A. Zilberman, M. Scharf, A copper-based intrauterine device with gold or platinum core: in vitro and in vivo studies., Contraception. 24 (1981) 657–71.

[8] Personal Communication from Dirk Wildemeersch, (2013).

[9] J. Sagripanti, Mechanism of copper-mediated inactivation of herpes simplex virus, Antimicrobial Agents and Chemotherapy. 41 (1997) 812–817.

[10] G. Borkow, J. Gabbay, Putting copper into action: copper-impregnated products with potent biocidal activities., FASEB Journal : Official Publication of the Federation of American Societies for Experimental Biology. 18 (2004) 1728–30.

[11] A.R. Karlström, R.L. Levine, Copper inhibits the protease from human immunodeficiency virus 1 by both cysteine-dependent and cysteine-independent mechanisms., Proceedings of the National Academy of Sciences of the United States of America. 88 (1991) 5552–6.

[12] D. Wildemeersch, New frameless and framed intrauterine devices and systems - an overview., Contraception. 75 (2007) S82–92.

[13] J.M. Bastidas, E. Cano, N. Mora, J.L. Polo, Characterization of copper corrosion products originated in simulated uterine fluids and on packaged intrauterine devices, Journal of Materials Science: Materials in Medicine. 12 (2001) 391–397.

[14] H. Xue, N. Xu, C. Zhang, Corrosion behavior of copper in a copper bearing intrauterine device in the presence of indomethacin., Contraception. 57 (1998) 49–53.

[15] A. Adriaens, M. Dowsett, K. Leyssens, B. Van Gasse, Insights into electrolytic stabilization with weak polarization as treatment for archaeological copper objects., Analytical and Bioanalytical Chemistry. 387 (2007) 861–8.

[16] F. Alvarez, P.L. Schilardi, M.F.L. de Mele, Reduction of the “burst release” of copper ions from copper-based intrauterine devices by organic inhibitors., Contraception. 85 (2012) 91–8.

[17] A. Adriaens, M. Dowsett, The coordinated use of synchrotron spectroelectrochemistry for corrosion studies on heritage metals., Accounts of Chemical Research. 43 (2010) 927–35.

[18] E. Chantler, P. Kenway, Z. Larouk, E.B. Faragher, J. Morris, a Kosonen, H. Allonen, M. Elstein, An analysis of the corrosion process of the Nova-T IUD., Advances in Contraception : The Official Journal of the Society for the Advancement of Contraception. 10 (1994) 287–301.

[19] X.M. He, D.C. Carter, Atomic structure and chemistry of human serum albumin., Nature. 358 (1992) 209–15.

[20] D.A. Scott, Bronze disease: A review of some chemical problems and the role of relative humidity, Journal of the American Institute for Conservation. 29 (1990) 193–206.

[21] A.A.M. Pollard, R. Thomas, P. Williams, T. Drayman-Weisser, The copper(II) chloride system and corrosion: a complex interplay of kinetic and thermodynamic factors., in: T. Drayman-Weisser (Ed.), The Conservation of Bronze Sculpture in the Outdoor Environment: A Dialogue among Conservators, Curators, Environmental Scientists, and Corrosion Engineers. Edited by Terry Drayman-Weisser., National Association of Corrosion Engineers, Houston, Texas, United States, 1983: pp. 123–133.

[22] K. Leyssens, A. Adriaens, C. Degrigny, E. Pantos, Evaluation of corrosion potential measurements as a means to monitor the storage and stabilization processes of archaeological copper-based artifacts., Analytical Chemistry. 78 (2006) 2794–801.

[23] D. Scott, J. Podany, B.B. Considine, J.P.G. Museum, G.C. Institute, Ancient & Historic Metals: Conservation and Scientific Research: Proceedings of a Symposium Organized by the J. Paul Getty Museum and the Getty Conservation Institute, November 1991, Getty Conservation Institute, Los Angeles, 1994.

[24] R.W. Corkery, Artificial biomineralisation and metallic soaps, PhD thesis, Australian National University, 1998.

[25] H. Grijalva, M. Inoue, S. Boggavarapu, P. Calvert, Amorphous and crystalline copper sulfides, CuS, Journal of Materials Chemistry. 6 (1996) 1157.

[26] Y. Guo, J. Zhang, L. Yang, H. Wang, F. Wang, Z. Zheng, Syntheses of amorphous and crystalline cupric sulfide nanoparticles and study on the specific activities on different cells., Chemical Communications. 46 (2010) 3493–5.

[27] E. Güneri, A. Kariper, Optical properties of amorphous CuS thin films deposited chemically at different pH values, Journal of Alloys and Compounds. 516 (2012) 20–26.

[28] R. Grayburn, M. Dowsett, M. Hand, P.-J. Sabbe, P. Thompson, A. Adriaens, Tracking the progression of bronze disease – A synchrotron X-ray diffraction study of nantokite hydrolysis, Corrosion Science. 91 (2015) 220–223.

[29] M.G. Dowsett, A. Adriaens, Cell for simultaneous synchrotron radiation X-ray and electrochemical corrosion measurements on cultural heritage metals and other materials., Analytical Chemistry. 78 (2006) 3360–5.

[30] Röchling-Group, Technical data sheet Polystone® P homopolymer, Haren, Germany, 2015.

[31] Daikin, PCTFE Product Information Report, Osaka, Japan, 2003.

Chapter 8 – Conclusions

8.1 Project summary

The work described herein had the objective of studying the deposition and corrosion resistance of heritage lead coatings (specifically lead carboxylates) in high concentration VOC and more natural environments, and was principally concerned with using and developing synchrotron XRD based and electrochemical techniques to do this. A significant amount of effort was devoted to the design and testing of a new portable electrochemical/environmental cell (the peCell), and although this was tested using a copper corrosion system it's suitability for a wide range of applications (including the long-term testing of conservation coatings) was proven.

Chapter 3 introduced lead carboxylates from two points of view: as friend or foe to the conservator depending on whether they are used as a coating or are a product of unwanted reaction between oil paint and lead pigments in a painting. The compounds of interest (lead ditetra-, dihexa- and dioctadecanoate) were synthesised and fully characterised. In order to explore the 'unfriendly' side of these compounds, the voltammetric fingerprints were measured and compared with lead pigments to test the viability of using this method to detect lead carboxylates in paint fragments. These initial tests could pave the way for further work in developing this technique and its capabilities compared to other analytical techniques currently used for the analysis of works of art.

The next two chapters focussed on the behaviour of these compounds as coatings on lead. The deposition of the layer from ethanolic solution was studied using time-lapse XRD and was found to occur immediately on evaporation of the solvent due to the increased solubility of the lead carboxylate in ethanol: crystallisation of the coating to form a layer could only occur when the solvent was removed from the system. This was in contrast with the deposition of the layer from aqueous solution. Previous work carried out within the ASP/ESA research group showed that the layer forms via a dissolution-precipitation cycle due to the insolubility of the coating in aqueous solution. Although both solvents are polar, ethanol has a non-polar moiety which aids solvation of the aliphatic chain of the lead carboxylate.

The mass thickness of the layer was also optimised for the ethanol deposition method by changing the concentration of tetradecanoic acid in the coating solution. The lowest concentration solutions, 0.1 and 0.5 mol L^{-1}, afforded the thickest layer of 0.045 g cm^{-2} or 40 μm. At higher concentrations, the acid did not fully react with the lead and white crystals of carboxylic acid remained on the surface. The optimum coating solution concentration could be limited by the dissolution of lead carboxylate and carboxylic acid in ethanol because at higher concentrations the carboxylic acid saturates the solution and lead carboxylate forms less easily. Coating solution concentration is not as relevant for aqueous deposition due to the cyclic nature of the coating mechanism.

Electrochemical impedance tests were carried out using $Pb(C14)_2$ and $Pb(C18)_2$ coated samples in electrolyte modelling a corrosive atmosphere to gauge coating performance. Compared to uncoated samples, there was a 75% improvement in coating effectiveness for $Pb(C_{18})_2$ coated samples. These samples also performed 20% better than the shorter-chain $Pb(C_{14})_2$ samples, thus demonstrating the benefit of using a longer carbon chain. However, coating effectiveness against the corrosive electrolyte improved by 80% when a pre-corroded coupon was used as a substrate. This served as a much more accurate representation of objects likely to require conservation. The results from pre-corroded coated samples were comparable with an existing conservation wax coating. The natural progression of this work would be the use of the coating on lead artefacts, although the surface of the artefacts would require significant surface analysis prior to the application of the coating in order to determine the suitability and reactivity of the surface for carboxylic acid deposition.

The performance of the coatings was tested in two environments containing VOCs from oak. In the first, an *in situ* environmental cell was used to track the corrosion of the samples over time using SR-XRD while exposed to these VOCs. In the second, samples were placed inside an oak display case for 7-months in an 'exhibition'. Firstly, the VOC environments of both the museum and the cell were qualified using GCMS. Acetic acid was found to be the VOC with the highest concentration in both cases; long-chain aldehydes and other common oak-VOCs such as furfural were also detected but played no role in corrosion of lead. In the cell and the museum display case, the coating was found to reduce corrosion by acetic acid compared to bare lead. It was assumed that the *in situ* SR-XRD tests using the cell contained a higher concentration of VOCs compared to the museum environment. Here, coated samples showed a corrosion resistance improvement of 75% compared to bare lead. This was calculated by quantifying the amount of corrosion product growth on both samples. Within the museum environment, no corrosion products were detected on the 'conserved' samples, whereas 'unconserved' samples showed signs of corrosion by formic acid. By conducting tests in a 'real' museum environment the use of carboxylic acids deposited from ethanol were demonstrated for short-term conservation of lead objects for up to one year. The reduction in coating performance was also quantified electrochemically before and after exposure to acetic acid solution: coating performance was reduced by 15% in these conditions.

Chapters 6 and 7 described the design and use of a portable cell which was designed for long term spectroelectrochemical testing of conserved samples. The cell was tested using a copper corrosion system and was found to produce reliable data from three different samples residing within the same environment.

8.2 Future work

There are three main areas of work which could be continued from this research: 1) improvement of the VMP technique for lead carboxylates in oil paintings, 2) a review of lead carboxylate coatings, and 3) the further development of the peCell.

The initial VMP trial shown in Chapter 3 could lead to further work in developing this technique and testing its capabilities compared to other analytical techniques currently used for the analysis of works of art. The detection of pure lead soaps and some lead-containing pigments was possible using this method but the addition of the oil matrix prevented the redox reactions from taking place. Sample preparation requires improvement in order to increase the availability of electroactive species. Specifically, the deposition of the paint facsimile could be improved to remove or partition the insulating oil layer while still being able to monitor the effects of binding to the lead ions during voltammetry. The synthesised lead soap or pigment mixtures could be dispersed in the oil matrix in order to test the effectiveness of new deposition techniques. In addition, the detection by VMP of pigment/soap mixtures could be tested with or without the oil matrix as the eventual differentiation of these compounds is key for the success of this technique applied to paint samples.

A significant amount of investigation into lead carboxylate coatings had been carried out prior to this research and is still being carried out by ESA group members (UGent). Some of the work in this thesis also adds to this body of work, particularly in the elucidation of the ethanolic lead carboxylate coating mechanism and the effectiveness of the resulting coating. Crucially, no exhaustive review or comparison between deposition methods (use of aqueous and ethanolic coating solutions, direct application of melted carboxylates, deposition from micro-emulsions) exists. The corrosion inhibition performance of all coatings in an acetic acid or oak environment could be evaluated using the techniques described in this thesis. An evaluation of the various coating mechanisms and physical properties could explain the differences in corrosion inhibition performance. For example, from ethanolic solution it was found that a thin layer is formed by a single crystallisation step and the coating successfully inhibits corrosion, possibly because it has low porosity. An investigation of coating microstructure using SEM could be carried out on sample cross-sections in order to elucidate defect density, which could be correlated with corrosion performance across all deposition methods. In addition further elucidation of the deposition mechanisms is needed regarding the role and concentration of Pb^{2+} ions in ethanolic solution.

As mentioned in the previous section, encouraging results were obtained from the coating of a pre-corroded lead sample. In order to understand this fully, the reactivity of a range of lead corrosion products with carboxylic acids to produce lead carboxylates could be tested. This would enable us to deduce (after analysis of the sample surface) whether the treatment would be successful on an artefact, for example.

A significant amount of time was devoted to the design and testing of the peCell prototype. It is hoped that this new instrument can be used for further long-term corrosion studies after some alterations have been made to the mechanics and materials: As suggested in Chapter 7, the incomplete movement of the cam was possibly a result of the incompatibility of the expansion coefficients of the material of the moving parts (PCTFE) and the cell body (polypropylene). Furthermore, several seals require improvement (the window and filling ports, for example) to reduce possibility of leakages and to ensure the sample is at the correct distance from the window for data analysis. If the cell is to be used at temperatures above ambient in the future, the peCell heating system needs to be upgraded. Prototype testing showed that the cell is sensitive to ambient temperature changes when outside its insulated transportation box. The current cartridge heater works well, but the peCell requires permanent external insulation in order to minimise heat loss from the cell.

The peCell has several advantages in terms of shape and size for portability, but its effectiveness for long term *in situ* measurements should be compared against current eCells to check the added value of the multi-sample capacity. For example, the corrosion tests performed using the prototype could be repeated using single-sample cells to check the corrosion rates are consistent for single- and multi-sample instrumentation.

The capability of the cell to maintain environmental conditions (VOCs, high humidity, temperature range) could be trialled over a long period of time, for example to model a museum display case or organ wind chest conditions for interesting samples. Also, the electrochemical facilities of the cell could be developed: voltage logging or multi-channel potentiostat capability could be extended to all three working electrodes so electrochemical measurements can be conducted simultaneously. To facilitate future peCell use on a beamline, a motorised stage could be designed to remote control the movement of the cell across the beam axis. This movement could be synchronised with surface analysis and would require updated software control. Although laboratory XRD is not suitable for such time-sensitive tests, other analytical techniques could be implemented with the peCell, such as Raman or IR spectroscopy. This further increases the possibilities for peCell uses.

8.3 Final thoughts

The ongoing study of conservation processes is vital to the long-term survival of cultural heritage materials. In this research a suite of complimentary corrosion inhibition tests was carried out on a new conservation technique alongside the development of a new instrument for long-term spectroelectrochemical monitoring. The peCell is an addition to the existing eCell family. *In situ* SR-XRD using this instrumentation is an incredibly valuable tool and the research shown in this thesis using these techniques is an example for a wide range of studies which might be of use in other heritage contexts and, indeed in other contexts than heritage.

List of publications

- **R. Grayburn**, M. Dowsett, M. De Keersmaecker, E. Westenbrink, J.A. Covington, J.B. Crawford, M. Hand, D. Walker, P.A. Thomas, D. Banerjee, A. Adriaens, Time-lapse synchrotron X-ray diffraction to monitor conservation coatings for heritage lead in atmospheres polluted with oak-emitted volatile organic compounds, Corrosion Science. 82 (2014) 280–289. http://dx.doi.org/10.1016/j.corsci.2014.01.027
- **R. Grayburn**, M. Dowsett, M. De Keersmaecker, D. Banerjee, S. Brown, A. Adriaens, Towards a new method for coating heritage lead, Heritage Science. 2:14 (2014). http://www.heritagesciencejournal.com/content/2/1/14
- **R. Grayburn**, M. Dowsett, P. Sabbe, M. Hand, P. Thompson, A. Adriaens, Tracking bronze disease progression – a synchrotron XRD study of nantokite hydrolysis. Corrosion Science 91 (2014) 220-223. http://dx.doi.org/10.1016/j.corsci.2014.11.021
- P. Sabbe, M. Dowsett, M. Hand, **R. Grayburn**, P. Thompson, W. Bras, A. Adriaens, Evaluation of a X-ray-excited optical microscope (XEOM) for the chemical imaging of metal and other surfaces. Analytical Chemistry 86 (2014) (23) 11789-11796. http://pubs.acs.org/doi/abs/10.1021/ac503284r

- M. De Keersmaecker, M. Dowsett, **R. Grayburn**, D. Banerjee, A. Adriaens, *In situ* spectroelectrochemical characterisation method for the electrochemical growth and breakdown of a lead dodecanoate coating on lead, Talanta 132 (2015) 760-768. http://dx.doi.org/10.1016/j.talanta.2014.10.035
- R. Wiesinger, **R. Grayburn**, M. Dowsett, A. Adriaens, M. Schreiner, *In situ* time-lapse SR-XRD of silver corrosion, Journal for Analytical Atomic Spectroscopy 30 (2015) 694-701. http://dx.doi.org/10.1039/C4JA00392F
- V. Flexer, **R. Grayburn**, M. De Keersmaeker, M. Dowsett, A. Adriaens, A new strategy for corrosion inhibition coatings for heritage lead objects, Electrochimica Acta (2015). http://dx.doi.org/10.1016/j.electacta.2015.05.022
- **R. Grayburn**, M. Dowsett, A. Adriaens, A natural fatty acid coating for unprimed heritage lead. (2015). *Submitted to Talanta*
- **R. Grayburn**, M. Dowsett, Pieter-Jan Sabbe, Jorge Anjos, Didier Wermeille, A. Adriaens, A portable cell for long-term spectroelectrochemical analysis of corroding materials. (2015). *Submitted to Analytical Chemistry*

Conference attendance

Sept 2014	Synchrotron Radiation in Art and Archaeology, Paris. '*In situ* time-lapse X-ray diffraction of silver corrosion', oral presentation
Sept 2014	Preserving our history: Cultural Heritage and the Science behind it, Mary Rose Museum, Portsmouth.
July 2014	3rd International Congress Chemistry for Cultural Heritage, Vienna. 'A time-lapse SR-XRD study of the corrosion of silver by H_2S and O_3' poster presentation
Jan 2014	Surface Science with Synchrotron Radiation, RSC, London.
Sept 2013	Technart, Rijksmuseum, Amsterdam. 'Lead soaps: friend or foe?' poster presentation.
Sept 2013	International Symposium on Painting Techniques, Rijksmuseum, Amsterdam.
Jan 2013	ESRF User's Meeting, Grenoble. 'A portable cell for spectroelectrochemistry' and 'An X-ray imaging/cultural heritage collaboration', double poster presentation
Sept 2012	iCorr Corrosion Science Symposium, London. 'Towards a portable cell for spectroelectrochemical studies of heritage metals', oral presentation (Winner of Best Presentation Prize)
Nov 2011	ICON Metals group Symposium, London.
Sept 2011	Cultural Heritage meets Science: The Interface, Mary Rose Museum, Portsmouth. 'Beauty and the Synchrotron', poster presentation.

Synchrotron experiments at XMaS, BM28, ESRF, Grenoble

28-01/1060	Testing the peCell; corrosion of Cu/Au mixtures in interuterine fluid; time-lapse XRD
28-01/1002	Silver corrosion by anthropogenic gases; XEOL and time-lapse XRD
28-01/988	Testing the XEOM 1 with a new Andor camera
28-01/952	Testing the XEOM; XRD of Mary Rose artefacts; time-lapse XRD of nantokite hydrolysis

Synchrotron experiments at DUBBLE, BM26A, ESRF, Grenoble

26-01/1014	Time-lapse coating formation of molten carboxylates (at BM01A, Swiss-Norwegian beamline)
26-01/945	Spectroelectrochemistry of lead carboxylate corrosion in oak and corrosive electrolytes; time-lapse XRD
26-01/926	Testing the XEOM 1